



Tailoring complex heterogeneous metal-organic framework structures

Sudarat Yadnum

► To cite this version:

Sudarat Yadnum. Tailoring complex heterogeneous metal-organic framework structures. Chemical Physics [physics.chem-ph]. Université de Bordeaux; Mahāwitthayālai Kasētsāt (Thaïlande), 2014. English. NNT : 2014BORD0299 . tel-01200746

HAL Id: tel-01200746

<https://theses.hal.science/tel-01200746>

Submitted on 17 Sep 2015

HAL is a multi-disciplinary open access archive for the deposit and dissemination of scientific research documents, whether they are published or not. The documents may come from teaching and research institutions in France or abroad, or from public or private research centers.

L'archive ouverte pluridisciplinaire **HAL**, est destinée au dépôt et à la diffusion de documents scientifiques de niveau recherche, publiés ou non, émanant des établissements d'enseignement et de recherche français ou étrangers, des laboratoires publics ou privés.

THÈSE EN COTUTELLE PRÉSENTÉE
POUR OBTENIR LE GRADE DE
DOCTEUR DE
L'UNIVERSITÉ DE BORDEAUX
ET DE L'UNIVERSITÉ DE KASETSART

ÉCOLE DOCTORALE SCIENCES CHIMIQUES

SPÉCIALITÉ : CHIMIE-PHYSIQUE

Par Sudarat YADNUM

**TAILORING COMPLEX HETEROGENEOUS METAL-ORGANIC FRAMEWORK
STRUCTURES**

Sous la direction du Prof. Alexander KUHN
et du Prof. Jumras LIMTRAKUL

Soutenue le : 02.12.2014

Membres du jury :

M. BOPP, Philippe,	Professeur, Université de Bordeaux	Président
M. SCHULTE, Albert	Associate Professor, Suranaree University of Technology	Rapporteur
M. PHOMPHRAI, Khamphoe	Assistant Professor, Mahidol University	Rapporteur
M. PAVASANT, Prasert	Associate Professor, Chulalongkorn University	Examineur
M. KUHN, Alexander,	Professeur, Institut Polytechnique de Bordeaux	Examineur
M. LIMTRAKUL, Jumras,	Professor, Kasetsart University	Examineur
MMe. WARAKULWIT, Chompunuch,	Lecturer, Kasetsart University	Membre invité

Tailoring Complex Heterogeneous Metal-Organic Framework Structures

Abstract:

In this thesis, new strategies for the preparation of Metal Organic Frameworks (MOF) materials with designed structures were studied and developed. Indirect bipolar electrodeposition (IBED) was used to prepare ZIF-8 and HKUST-1 on metal substrates in a straightforward and site-selective way. This concept is expected to be able to be generalized for the synthesis of many other MOF compounds, thus allowing a cheap and green synthesis, leading to new generations of MOF-based Janus-type composites. Furthermore, rationally designed hierarchical macro-/microporous HKUST-1 electrodes were prepared via an electrochemical dissolution-deposition technique. The developed synthesis approach is very practical in terms of the time consumption, and opens up MOFs for various applications. Finally, MIL-101-supported noble metal nanoparticles were prepared as the last part of the experimental studies via a simple colloidal deposition technique. This concept might be generalized for the synthesis of other metal nanoparticle/MOF composites, and might improve the catalytic activity of MOFs. Apart from the experimental study, in order to gain a deeper insight into the catalysis of MOF materials, the catalytic behavior of Cu(II) in the paddle-wheel unit of MOF-505 was theoretically investigated for the Mukaiyama aldol reaction via the density functional theory and compared to that of another catalyst, Cu-ZSM-5 zeolite. Besides, the catalytic behavior of homo-metallic clusters and hetero-bimetallic clusters, that are the metal complexes representing the metal clusters in MOFs, were also theoretically investigated for the cycloaddition reaction of carbon dioxide and ethylene oxides.

Resumé en français:

Dans cette thèse, de nouvelles stratégies pour la préparation de matériaux de type Metal-Organic-Frameworks (MOF) ont été étudiés et développés. L'électrodeposition bipolaire indirecte (IBED) a été utilisée pour préparer ZIF-8 et HKUST-1 sur des substrats métalliques de façon simple et avec une sélectivité spatiale. Ce concept devrait pouvoir être généralisée pour la synthèse de nombreux autres composés MOF, permettant ainsi une synthèse pas chère et verte, conduisant à de nouvelles générations de composites de type Janus basés sur des MOFs. En outre, des électrodes avec une structure hiérarchique macro-/ microporeux de HKUST-1 ont été préparées par une technique de dissolution-dépôt électrochimique. L'approche de synthèse mis au point est très pratique en ce qui concerne la durée des expériences, et ouvre diverses applications pour les MOFs. Enfin des nanoparticules de métaux nobles sur un substrat à base de MIL-101 ont été préparées comme la dernière partie de l'étude expérimentale par dépôt colloïdal. Ce concept peut être généralisé pour la synthèse d'autres composites nanoparticules métalliques / MOF, et pourrait améliorer l'activité catalytique des MOFs. En dehors de l'étude expérimentale, afin de comprendre mieux la catalyse de matériaux MOF, le comportement catalytique de Cu (II) dans le MOF-505 a été théoriquement étudié pour la réaction d'aldolisation Mukaiyama par la théorie de densité fonctionnelle et comparé à celui d'un autre catalyseur, Cu-ZSM-5. En outre, le comportement catalytique d'amas homo- et hétéro-bimétalliques, qui sont des complexes métalliques qui représentent les agrégats métalliques dans les MOFs, a également été étudié théoriquement pour la réaction de cycloaddition de dioxyde de carbone et des oxydes d'éthylène.

Keywords : Metal-Organic Frameworks, Bipolar Electrochemistry, Electrodeposition, Hierarchical micro/macroporous MOFs, Colloidal template, Stabilizing agent, Density Functional Theory (DFT), Reaction mechanism, Mukaiyama aldol reaction, Cycloaddition reaction

Unité de recherche

Chemistry Department and Center of Nanotechnology
Kasetsart University, 50 Ngamwongwan Road, Chatuchak, Bangkok, 10900 Thailand

Institut des Sciences Moléculaires (ISM) UMR 5255 CNRS Université de Bordeaux
351 cours de la libération 33405 Talence Cedex - France

ACKNOWLEDGEMENTS

First of all I would like to take this opportunity to thank all members of the jury for having accepted to evaluate my thesis and for their useful comments and suggestions, particularly, Assoc. Prof. Dr. Albert Schulte and Asst. Prof. Khamphoe Phomphrai for accepting the invitation as examiners in the jury.

I would like to express my sincere gratitude to Prof. Jumras Limtrakul, my supervisor in Thailand (Kasetsart University), for the continuous support of my Ph.D research and beyond, for his patience, motivation, enthusiasm, and wide scientific knowledge. The confidence that he gave motivated me during all the time of research and writing. He showed me different ways to approach a research problem and the need to be persistent to accomplish any goal. He carefully guided me throughout the pursuit of my Ph.D degree at Kasetsart University, so that I was able to change my life for the better and improve my future prospects. A special thank you goes to my co-advisors, Dr. Pipat Khongpracha and Dr. Chompunuch Warakulwit, for their big help to develop my skill in computational chemistry and experiment and also for their insightful advices as well as patient corrections of my writing.

I also would like to express a big thank to Professor Alexander Kuhn, my supervisor in France (Université de Bordeaux), for the patient guidance, encouragement and advice he has provided throughout my time as his student. I have been extremely lucky to have a supervisor who cared so much about my work, and who responded to my questions and queries so promptly. My deep thanks for Dr. Darren Bradshaw from University of Southampton for his kind challenging ideas and encouragement to accomplish my work.

I would like to thank the Thailand Research Fund (TRF) for the financial support from the Royal Golden Jubilee Ph.D. fellowship program (3.C.KU/51/A.1), the French Government for giving me an opportunity to be a part of RGJ-Ph.D program and to spend until one year of my research in France, the French Ministry of Research, CNRS, and ENSCBP for supporting the project in France. The National Science and Technology Development Agency (NSTDA Chair Professor), the National Nanotechnology Center (NANOTEC Center of Excellence), Kasetsart University Research and Development Institute (KURDI), the Commission on Higher Education, Ministry of Education (The “National Research University Project of Thailand (NRU)” and the

“National Center of Excellence for Petroleum, Petrochemical and Advanced Materials (NCE-PPAM)”) are also acknowledged for their support.

Grateful thanks are also due to the following people for their help: Dr. Jakkapan Sirijaraensre, Dr. Winyoo Sangthong, Dr. Bundet Boekfa, Dr. Panvika Pannopard, Dr. Boonruen Sunpetch, Dr. Chularat Watanakit, Dr. Thana Maihom, Sombat Ketrat, Saowapak Choomwattana, Chaiyan Boonyuen at Kasetsart University and Dr. Jérôme Roche, Dr. Dodzi Zigah Patrick, Garrigue, Veronique Lapeyre, Aline Simon-Lalande, Dr. Bertrand Goudeau, Eric Lebraud, Philippe Négrier at University of Bordeaux.

I gratefully thank all my friends and colleagues at Kasetsart and Bordeaux University for their kind help, in particular, Teeranan Nongnual, Patanachai Janthon. Sarawoot Impeng, Anawat Thivasasith, Veerachart Paluka, Oranit Phuakkong, Chawanwit Kumsapaya, Malinee Niemlaem, Sippakorn Wannakao, Wasinee Panjan, Kanokwan Kongpatpanich, Dr. Zahra Fattah, Dr. Salem Ben-Amor, Dr. Catherine Adam, Dr. Léa Messenger, Dr. Suresh Reddy Vajrала, Florent Pinaud, Eugenio Gianessi, Aleksandar Karajic, Milica Sentic.

Last, but not least, I thank my family for giving me life in the first place, for educating me, for their unconditional support and encouragement to pursue my interests and for believing in me. Finally, I am grateful for the support, confidence and cordiality of my husband, the man who, without his patience, I could not have completed this thesis.

Sudarat Yadnum
December, 2014

LIST OF CONTENTS

	Page
TABLE OF CONTENTS	i
LIST OF TABLES	vi
LIST OF FIGURES	viii
LIST OF ABBREVIATIONS	xxiv
CHAPTER I. HISTORY AND CHALLENGES OF MOF CHEMISTRY	1
1. Introduction of metal-organic frameworks (MOFs)	1
2. Synthetic approaches for MOFs	6
3. Potential applications of MOFs	10
CHAPTER II. SYNTHESIS OF HETEROGENEOUS MOF STRUCTURES	14
1. Site-Selective Synthesis of Janus-type Metal-Organic Framework Composites	14
1.1 Introduction	14
1.2 Experimental section	28
1.2.1 Bipolar electrochemical synthesis of ZIF-8	28
1.2.2 Bipolar electrochemical synthesis of HKUST-1	30
1.2.3 Control Experiments	32
1.2.3.1 Synthesis of ZIF-8 by normal electrochemistry	32
1.2.3.2 Synthesis of HKUST-1 by normal electrochemistry	32
1.2.4 Characterization of ZIF-8 and HKUST-1	33
1.3 Results and discussions	33
1.3.1 Bipolar electrochemical synthesis of ZIF-8 on zinc wire	33

LIST OF CONTENTS (Continued)

	Page
1.3.1.1 Influence of the applied potential on the synthesis of ZIF-8 via the IBED technique	38
1.3.1.2 Influence of the electrodeposition time on the synthesis of ZIF-8 via the IBED technique	42
1.3.1.3 Influence of the concentration of organic linker (2-MeIm) on the synthesis of ZIF-8 via the IBED technique	44
1.3.2 Bipolar electrochemical synthesis of HKUST-1 on copper bead	48
1.4 Conclusions	54
2. Fabrication of Hierarchical Macroporous Electrodes of HKUST-1 via an Electrochemical-Dissolution-Deposition technique	55
2.1 Introduction	55
2.2 Experimental section	58
2.2.1 Preparation of silica colloidal template	58
2.2.2 Preparation of the surface of the gold slide	59
2.2.3 Fabrication of silica colloidal crystals by Langmuir-Blodgett (LB) trough technique	60
2.2.4 Fabrication of 3D ordered macroporous Cu electrode	62
2.2.5 Transformation of ordered macroporous Cu electrodes into HKUST-1	62
2.2.6 Characterizations	63
2.3 Results and discussion	64
2.4 Conclusions	78

LIST OF CONTENTS (Continued)

	Page
3. Preparation of Metal-Organic Framework (MOF)-Supported Metal Nanoparticles (Au, Pd and Pt)	79
3.1 Introduction	79
3.2 Experimental section	85
3.2.1 Materials	85
3.2.2 Synthesis of MIL-101	85
3.2.3 Preparation of Au:PVP, Pd:PVP and Pt:PVP nanoparticles	85
3.2.4 Synthesis of metal NPs@MIL-101 by colloidal deposition of the metal nanoparticles stabilized by PVP	86
3.2.5 Characterization	86
3.3 Results and discussion	87
3.3.1 Characteristics of the prepared MIL-101	87
3.3.2 Characteristics of the synthesized metal nanoparticles	90
3.3.3 Characteristics of the prepared metal NPs@MIL-101	92
3.4 Conclusions	99
CHAPTER III. THEORETICAL STUDY OF METAL-ORGANIC FRAMEWORKS STRUCTURE	100
1. Comparison of Cu-ZSM-5 Zeolites and Cu-MOF-505 Metal-Organic Frameworks as Heterogeneous Catalysts for the Mukaiyama Aldol Reaction: A DFT Mechanistic Study	100
1.1. Introduction	100
1.2. Models and Computational Methods	103
1.3. Results and discussions	105

LIST OF CONTENTS (Continued)

	Page
1.3.1. MOF-505-Encapsulated Formaldehyde (HCOH@MOF-505) and Its Mukaiyama Aldol Reaction with Silyl Enol Ether (HCOH@MOF-505/H ₃ SiOHC=CH ₂)	105
1.3.2. Cu-ZSM5-Encapsulated Formaldehyde (HCOH@Cu-ZSM5) and Its Mukaiyama Aldol Reaction with Silyl Enol Ether (HCOH@Cu-ZSM5/H ₃ SiOHC=CH ₂)	109
1.3.3. Comparison of the Two Catalyzed Cases with the Reaction without any Lewis Acid Catalyst	112
1.4. Conclusions	116
2. Cycloaddition Reaction of Carbon Dioxide and Ethylene Oxides over Homo-metallic and Hetero-metallic Paddlewheel Clusters: A Mechanistic DFT Study	118
2.1. Introduction	118
2.2. Models and Computational Methods	120
2.3. Results and discussions	121
2.3.1. Structure of the homo-metallic (MoMo and RhRh) and hetero- metallic trifluoroacetate (MoRh and RhMo)	121
2.3.2. The uncatalyzed cycloaddition reaction	123
2.3.3. Reaction mechanisms of carbon dioxide cycloaddition with ethylene oxide	125
2.3.3.1. Concerted Pathway	127
2.3.3.2. Stepwise Pathway	129
2.4. Conclusions	136

LIST OF CONTENTS (Continued)

	Page
CHAPTER IV. CONCLUDING REMARKS	138
REFERENCES	140
APPENDIX	168
CURRICULUM VITAE	174

LIST OF TABLES

Table		Page
1	Optimized geometric parameters of the isolated state, formaldehyde adsorption, coadsorption complex, transition state, and product of the Mukaiyama aldol reaction between formaldehyde and silyl enol ether on MOF-505 using the ONIOM (M06L/6-31G(d,p):UFF) method.	107
2	Optimized geometric parameters of the isolated state, formaldehyde adsorption, coadsorption complex, transition state, and product of the Mukaiyama aldol reaction between formaldehyde and silyl enol ether on Cu-ZSM-5 using the ONIOM (M06L/6-31G(d,p):UFF) method.	110
3	NBO-Wiberg bond orders of reactants, transition states and products in Mukaiyama aldol reaction catalyzed by MOF-505. Values obtained at M06L/6-31G(d,p) level	113
4	NBO-Wiberg bond orders of reactants, transition states and products in Mukaiyama aldol reaction catalyzed by Cu-ZSM-5. Values obtained at M06L/6-31G(d,p) level.	114
5	Structural Parameters, Bond Distances (Å), Angles (deg) and NPA charge analysis for Homo-metallic and Hetero-metallic, [M1M2(O ₂ CCF ₃) ₄] (M = Mo, Rh)	122
6	Optimized geometric parameters of isolated state, coadsorption complex, transition state, and product of the cycloaddition between CO ₂ and ethylene oxide using M06L/6-31G(d,p) method (bond lengths in Å)	124

LIST OF TABLES (Continued)

Table		Page
7	Optimized geometrical parameters and adsorption energies for the CO ₂ and ethylene oxide adsorption over the homo-metallic, MoMo(O ₂ CCF ₃) ₄ and RhRh(O ₂ CCF ₃) ₄ , and hetero-metallic ,MoRh(O ₂ CCF ₃) ₄ and RhMo(O ₂ CCF ₃) ₄ .. Bond distances are in Å and energies are in kcal/mol.	126
8	Optimized geometrical parameter of cycloaddition reaction between CO ₂ and ethylene oxide over the hetero-metallic (MoRh(O ₂ CCF ₃) ₄). Bond distances are in Å.	134

LIST OF FIGURES

Figure		Page
1	Schematic illustrations of the 1D, 2D and 3D structure of coordination polymers. M represents the metal cluster and L represents the organic bridging ligand	2
2	Chemical structures of examples of organic bridging ligands used for MOFs	3
3	Schematic illustrations showing MOFs constructed from linear dicarboxylate linkers with various molecular lengths. The pore sizes of the obtained materials depend on the molecular length of the linkers. Blue polyhedrals, red and black spheres represent Zn, O and C, respectively. The large yellow spheres represent the MOF cavities	4
4	Scheme illustrating the copper acetate paddlewheel units, which are connected and form a 3D framework with uniform pore structure of Cu-BTC. Orange, red, gray, and white spheres represent Cu, O, C, and H atoms, respectively	5
5	Schematic illustration showing the angles of the (a) Si-O-Si and (b) M-IM-M bridges in zeolites and zeolitic imidazolate frameworks (ZIFs) respectively. M represents the metal site and IM represents imidazolate derivative	6
6	Schematic illustration showing the steps involved in the conventional solvothermal or hydrothermal synthesis of MOFs	7

LIST OF FIGURES (Continued)

Figure		Page
7	Schematic illustration showing the newly developed routes for the preparation of MOFs: (a) microwave-assisted solvothermal, (b) sonochemical, (c) electrochemical, and (d) mechanochemical syntheses.	10
8	Schematic illustration showing different ways to create the catalytically active sites in MOFs. (a) The metal species, (b) the functionalized organic ligand or (c) the additional encapsulated species act as the active catalytic sites	12
9	Schematic illustration showing the process of the site-specific growth of MOFs on polymer particles prepared via electrohydrodynamic co-jetting of two distinct polymer solutions with differently functionalized polymers	16
10	Schematic illustration of a typical bipolar system with a conducting object immersed between two feeder electrodes in an electrolytic solution	17
11	Schematic illustrations showing the polarization of conducting substrates under the influence of an external electric field: (a) linear and (b) spherical conducting substrates	18
12	Schematic illustration of the linear conductive substrate acting as the bipolar electrode for a redox couple reaction when the substrate is exposed to an electric field and immersed in a solution containing the electroactive species	20

LIST OF FIGURES (Continued)

Figure		Page
13	(a) Schematic illustration showing the principle of the indirect bipolar electrodeposition (IBED). (b) Visualization of the pH evolution at a bipolar electrode, revealed by using a universal pH indicator. Blue corresponds to basic pH, and red corresponds to acid pH.	22
14	(a-d) SEM images of glassy carbon beads modified with different materials including (a) silica, (b) silicone (c)-(d) titanate (using an electric field of (c) 71 and (d) 214 Vcm ⁻¹) and (e) EDP. (f) Optical micrograph showing a glassy carbon bead modified with EDP. All hybrid materials were obtained via the IBED technique.	24
15	Schematic illustration of the formation of ZIF-8 from Zn metal centers and 2-methylimidazolate ligands. Zn, C, N and H atoms are represented by red, gray, blue and white spheres, respectively.	25
16	Schematic illustration of the formation of HKUST-1 or Cu-BTC from Cu metal centers and benzenetricarboxylic acid (btc) ligands. Cu, C, O and H atoms are represented by orange, gray, red and white spheres, respectively.	27
17	(a) Schematic illustration and (b) photo showing the experimental setup of equipment for the synthesis of ZIF-8. A zinc wire was introduced in the bipolar electrochemical cell containing a solution of 2-methylimidazole in ultrapure water (18.2 MΩ.cm) and 0.05M Na ₂ SO ₄ supporting electrolyte. The electrode compartments were filled only with 0.05 M Na ₂ SO ₄ electrolyte to facilitate the current flow in the cell.	29

LIST OF FIGURES (Continued)

Figure		Page
18	(a) Schematic illustration showing the principle of the indirect bipolar electrodeposition (IBED). (b) Visualization of the pH evolution at a bipolar electrode, revealed by using a universal pH indicator. Blue corresponds to basic pH, and red corresponds to acid pH.	30
19	(a) Schematic illustration and (b) photo showing the experimental setup of equipment for the synthesis of HKUST-1. A copper sphere was introduced in the bipolar electrochemical cell composed of a centered inner reaction compartment ($d = 2.0$ cm between both separators) and two outer electrode compartments ($d = 3.5$ cm). The solution contained 1,3,5-benzenetricarboxylic acid in ethanol and 0.05M MTBS supporting electrolyte. The electrode compartments were filled only with 0.05 M MTBS electrolyte in order to facilitate the current flow in the system.	31
20	Photos showing the setup of normal electrochemical cells used for the synthesis of (a) ZIF-8 and (b) HKUST-1.	33
21	Schematic illustration showing the mechanism of the formation of Zeolitic Imidazolate Framework (ZIF-8). The crystal growth on the anodically polarized side of a zinc wire is triggered by indirect bipolar electrodeposition	35
22	Cyclic Voltammogram of a zinc wire in 0.05 M Na_2SO_4 supporting electrolyte in ultrapure water obtained at a scan rate of 100 mV/s. The voltammogram was obtained at room temperature using a zinc wire as a working electrode, Pt mesh as a counter electrode, and Ag/AgCl as a reference electrode.	36

LIST OF FIGURES (Continued)

Figure		Page
23	Schematic illustration showing the reaction of the 2-methylimidazole linker with the Zn^{2+} ions at the surface of the bipolar electrode to form the basic building unit of ZIF-8 crystals.	37
24	Site-selective modification of a zinc wire with ZIF-8: a) Control experiment without electric field after three days in a solution containing 2-MeIm (1.376 M) and Na_2SO_4 (0.05 M). b) Synthesized by the IBED method (6 V, 60 min, 1.376 M 2-MeIm, 0.05m Na_2SO_4).	37
25	SEM image showing the site-selective modification of a zinc wire with ZIF-8 by the IBED method. The crystals were obtained by using 1.376 M 2-MeIm, 60 min reaction time and different external potential differences of (a) 5 V, (b) 6 V, (c) 7 V, and (d) 8 V.	38
26	SEM images showing the ZIF-8 structure obtained under unfavorable voltage conditions (of 8 V). Morphologies that can be attributed to the crystal phases other than ZIF-8 are clearly seen.	40
27	PXRD patterns of ZIF-8 obtained from the IBED synthesis using either 6 V (black line) or 8 V (red line), 1.376 M 2-methylimidazole in ultrapure water containing 0.05 M Na_2SO_4 as supporting electrolyte and 60 min electrodeposition time.	40
28	The diffraction patterns of ZIF-8 taken from (Kida, K. <i>et al.</i> , 2013), which illustrates in the different impurity phases that can be observed in ZIF-8 prepared at Hmim/Zn molar ratios: (a) 20, (b) 40, (c) 60, (d) 80, and (e) 100.	41

LIST OF FIGURES (Continued)

Figure		Page
29	Infrared spectra of (a) pure 2-methylimidazole, (b-d) the IBED-synthesized ZIF-8 by using 1.376 M 2-methylimidazole in ultrapure water containing 0.05 M Na ₂ SO ₄ as supporting electrolyte, 60 min electrodeposition time and applying different potentials ((b) 8 V, (c) 7 V, (d) 6 V), and (e) ZIF-8 from the literature (Du, Y. <i>et al.</i> , 2013).	42
30	SEM images showing the site-selective modification of a zinc wire with ZIF-8 by the IBED method. The deposits were prepared by using 1.376 M 2-MeIm and 6 V between the external feeder electrodes but different electrodeposition times of: (a) 2 min, (b) 10 min, (c) 30 min, and (d) 60 min.	43
31	Infrared spectra of (a) pure 2-methylimidazole and (b-d) ZIF-8 prepared via the IBED technique by using 1.376 M 2-MeIm in ultrapure water containing 0.05 M Na ₂ SO ₄ as supporting electrolyte and 6 V between the external feeder electrodes but with different electrodeposition times of: (a) 2 min, (b) 10 min, (c) 30 min, and (d) 60 min	44
32	SEM images showing the site-selective modification of a zinc wire with ZIF-8 by the IBED method. The deposits were prepared by using 60 min deposition time and 6 V between the external feeder electrodes but with different concentrations of 2-MeIm of (a) 0.344 M, (b) 0.688 M, (c) 1.032 M and (d) 1.376 M.	45
33	(Top) Structure of the ZIF-8 sodalite cage refined from the powder data of IBED deposited material. (Below) PXRD patterns illustrating the structural evolution of ZIF-8 prepared via the IBED technique when applying an electric field of 6 V for 60 min as a function of the concentration of 2-methylimidazole: (a) 0.688M, (b) 1.032M and (c) 1.376M. (d) XRD	46

LIST OF FIGURES (Continued)

Figure		Page
34	Infrared spectra of (a) pure 2-methylimidazole and (b-d) the IBED-synthesized ZIF-8 by applying a potential of 6 V and using 60 min electrodeposition time in ultrapure water containing 0.05 M Na ₂ SO ₄ as supporting electrolyte with various concentrations of 2-methylimidazole: (b) 0.344 M, (c) 0.688 M, (d) 1.032M, and (d) 1.376 M.	47
35	Photo showing the formation of ZIF-8 on a zinc wire via a classic electrochemical approach under the experimental conditions of 0 V vs Ag/AgCl, 10 min deposition time, 1.376 M 2-MeIm linker solution, and 0.05m Na ₂ SO ₄ supporting electrolyte. (a) Zinc wire glued on gold slide. (b) The wire after removing from the gold slide.	48
36	Optical micrographs showing the site-selective modification of a copper bead (3 mm in diameter) with HKUST-1. (a) Bead before modification, (b) after applying an external potential difference of 10 V for 60 min in the absence of 1,3,5-benzenetricarboxylic acid. (c ,d) Bead obtained after the modification by applying (c) 10 and (d) 20 V, respectively in the presence of 0.08 M 1,3,5-benzenetricarboxylic acid in ethanol for 60 min.	49
37	SEM images of HKUST-1 prepared via the IBED technique by applying an external electric potential of 10 V for 60 min in 0.08 M 1,3,5-benzenetricarboxylic acid in ethanol containing 0.05 M MTBS supporting electrolyte.	50

LIST OF FIGURES (Continued)

Figure		Page
38	SEM images of HKUST-1 prepared via the IBED technique by applying an external electric potential of 20 V for 60 min in 0.08 M 1,3,5-benzenetricarboxylic acid in ethanol containing 0.05 M MTBS supporting electrolyte.	50
39	(a) XRD pattern of HKUST-1 taken from the literature (Mao, Y. <i>et al.</i> , 2013) (b) PXRD pattern of HKUST-1 prepared via the IBED technique by applying an external electric potential of 20 V for 60 min in 0.08 M 1,3,5-benzenetricarboxylic acid in ethanol containing 0.05 M MTBS supporting electrolyte. The red bars are the standard XRD patterns of HKUST-1.	51
40	Infrared spectra of (a) pure-1,3,5-benzenetricarboxylic acid (b) HKUST-1 prepared via the IBED technique by applying an external electric potential of 20 V for 60 min in 0.08 M 1,3,5-benzenetricarboxylic acid in ethanol containing 0.05 M MTBS supporting electrolyte and (c) HKUST-1 is taken from the literature (Jeremias, F. <i>et al.</i> , 2012).	52
41	Optical micrographs for the Cu beads obtained from the control experiments (without applying any electric field) performed in 0.08 M 1,3,5-benzenetricarboxylic acid in ethanol containing 0.05 M tributylmethylammonium methyl sulfate as supporting electrolyte for (a) 1 h and (b) 3 days.	53
42	Optical images of HKUST-1 prepared on copper beads by a classic electrochemical approach (using 1.5 V vs Ag/AgCl, 60 min deposition time, 0.08M of 1,3,5-benzenetricarboxylic acid solution and 0.05M of tributylmethylammonium methyl sulfate electrolyte) (a) top-view, (b) on the right side and (c) on the left side.	54

LIST OF FIGURES (Continued)

Figure		Page
43	Schematic illustration showing the experimental steps for the fabrication of the hierarchical macro-/microporous HKUST-1 of this work.	58
44	Schematic illustration showing the functionalization with APTES of the surface of silica spheres prepared via the modified Stöber sol-gel process employed in this work.	59
45	Schematic illustration showing the functionalization with cysteamine of the surface of the gold slides employed in this work to improve the hydrophilicity of the gold surface, and leading to a good attachment of the silica spheres onto the Au surface.	60
46	Photo showing the side view of the LB trough instrument used in this work (NIMA Technology, model 622).	61
47	Schematic illustration showing the steps involved in the Langmuir-Blodgett experiment including the generation of a Langmuir film of silica spheres and the dipping-raising process to transfer the silica bead layer to the surface of a gold slide.	61
48	Schematic illustration showing the steps for the fabrication of the macroporous copper electrode.	62
49	Photograph showing the experimental set up for the transformation of the Cu surface of the 3D ordered macroporous Cu electrodes into HKUST-1 via the electrochemical dissolution of Cu in the presence of the organic ligand.	63

LIST OF FIGURES (Continued)

Figure		Page
50	(a-b) SEM images and (c) the corresponded particle size distribution of the silica spheres prepared in this study according to the Stöber method.	64
51	Surface pressure-area isotherms obtained during a) the compression of the film of 1 μm -silica particles until the surface pressure reached the target pressure of 4 mN/m and b) the deposition of 7 layers of the Langmuir film of silica spheres onto gold-coated glass slides at a constant surface pressure of 4 mN/m.	65
52	Photos of the gold-coated glass slides (a) before and (b) after the deposition of 7 layers of the silica spheres via the LB technique.	65
53	Cyclic voltammogram of the Cu plating bath (CUBRAC 660) with a flat Au-coated glass slide as working electrode recorded at a scan rate of 100 mV/s and at room temperature in the potential range of -1.00 to 0.50 V. A Pt mesh and Ag/AgCl electrodes were used as the counter and reference electrodes, respectively.	66
54	(a-d) SEM images of the top-surface of the Au-coated glass slides modified by Cu at different potentials: (a) -0.35, (b) -0.30, (c) -0.25 and (d) -0.20 V by using a Cu plating bath (CUBRAC 660) as the working solution. The deposition time was 300 s. (e-f) Typical SEM images of the (e) top-surface and (f) section of the Au-coated glass slides modified by Cu at various potentials in the range of -0.05 to -0.00625 V.	67

LIST OF FIGURES (Continued)

Figure		Page
55	Low and high magnifications SEM images of the top-surface of the ordered macroporous Cu electrodes obtained after the removal of 1 μm -silica colloidal crystal template (fabricated by the LB technique) by using an applied potential of -0.05 V but with various deposition times of (a-b) 300 s, (c-d) 700 s, (e-f) 900 s, and (g-h) 2300s.	69
56	SEM images of section of the ordered macroporous Cu electrodes obtained after the removal of 1 μm -silica colloidal crystal template (fabricated by the LB technique) by using an applied potential of -0.05 V but with different deposition times of (a) 900 s and (b) 2300s.	70
57	SEM images of HKUST-1 formed on the surface of the flat Cu-modified slides with 1.5 μm thickness via the electrochemical dissolution-deposition process at different potentials: (a-b) 0.125, (c-d) 0.25 and (e-f) 0.5 V and the same deposition time of 300 s in a solution of 0.05 M BTC in ethanol containing 0.2 M MTBS supporting electrolyte.	71
58	SEM images of HKUST-1 formed on the surface of the flat Cu-modified slides with 1.5 μm thickness via the electrochemical dissolution-deposition process at a constant potential of 0.5 V but for various deposition times: (a-b) 30, (c-d) 60, (e-f) 300, (g-h) 600, and (i-j) 1800 s in a solution of 0.05 M BTC in ethanol containing 0.2 M MTBS supporting electrolyte.	73
59	Infrared (IR) spectra of (a) pure BTC linker and (b) the sample prepared via the electrochemical dissolution-deposition process at a constant potential of 0.5 V and a deposition time of 60 min in the solution of 0.05 M BTC in ethanol containing 0.2 M MTBS supporting electrolyte.	74

LIST OF FIGURES (Continued)

Figure		Page
60	SEM images of the top-surface and various magnifications of the 3D ordered macroporous Cu electrodes with 3/2 layer thickness before (left-hand side) and after (right-hand side) the dissolution-deposition process at a constant potential of 0.5 V and a deposition time of 60 min in the solution of 0.05 M BTC in ethanol containing 0.2 M MTBS supporting electrolyte.	76
61	SEM images of the top-surface and various magnifications of the 3D ordered macroporous Cu electrodes with 3/2 layer thickness before (left-hand side) and after (right-hand side) the dissolution-deposition process at a constant potential of 0.125 V but various deposition times of (a-b) 30 s, (c-d) 60 s and (e-f) 120 s in a solution of 0.05 M BTC in ethanol containing 0.2 M MTBS supporting electrolyte.	77
62	Three proposed cases of metal nanostructures supported by a MOF. (a) the metal nanostructures are deposited at the outer surface of the MOF, (b) the nanostructures are introduced into the pore of the MOF, but they still have a broad size distribution, and (c) the nanostructures are embedded into the pores of MOFs with a uniform size distribution as their sizes matches well with the pore dimensions of MOF.	82
63	(a) Inorganic trimer; (b) 1,4-Benzenedicarboxylic acid; (c) ST made from the linkage of inorganic trimers and 1,4-BDC; (d) schematic view of the MIL-101 structure; and (e) schematic 3D representation of the MTN zeotype architecture : source from reference (Férey, G. <i>et al.</i> , 2005)	83
64	(a) Low- and (b) high-angle XRD patterns of the MIL-101 sample prepared in this work.	87

LIST OF FIGURES (Continued)

Figure		Page
65	(a) Low and (b) high magnification SEM images and (c) the corresponding particle size distribution of the prepared MIL-101.	88
66	(a,b) Low- and (c) high-resolution TEM images of the synthesized MIL-101.	89
67	(a) N ₂ adsorption/desorption isotherms and (b) the corresponded pore size distribution of the prepared MIL-101 sample.	90
68	Graphs showing particles size distribution of the Pd:PVP, Au:PVP and Pt:PVP nanoparticles, synthesized at 0°C in the presence of PVP using NaBH ₄ as the reducing agent, obtained from the DLS analysis.	91
69	TEM image of the prepared Au:PVP nanoparticles and their related particle size distribution.	92
70	Infrared spectra of (a) MIL-101, (b) PtNPs@MIL-101, (c) PdNPs@MIL-101, and (d) AuNPs@MIL-101.	93
71	N ₂ adsorption/desorption isotherms of the as-synthesized MIL-101 (black line), AuNPs@MIL-101 (blue line), PdNPs@MIL-101 (red line), and PtNPs@MIL-101 (green line).	94
72	(a) SEM and (b-d) TEM images of the prepared AuNPs@MIL-101.	95
73	(a) SEM and (b-d) TEM images of the prepared PdNPs@MIL-101.	96
74	(a) SEM and (b-d) TEM images of the prepared PtNPs@MIL-101.	97

LIST OF FIGURES (Continued)

Figure		Page
75	(a) BF- and (b) HAADF-STEM and (c) SE images taken at the same area of the prepared PtNPs@MIL-101.	98
76	Mechanism for Lewis-acid (LA) catalyzed Mukaiyama aldol reaction of an aldehyde and silyl enol ether.	100
77	The carbonyl-ene reaction of various olefins and formaldehyde incorporated zeolite.	101
78	The structures representation of catalytic active sites of (a) Cu-MOF-505 and (b) Cu-ZSM-5	103
79	The computational models of (a) MOF-505 and (b) Cu-ZSM-5 in which the high layer (DFT region) is represented in ball-bond style and the low layer (UFF) is represented by line style.	104
80	Optimized structures of the HCOH@MOF505/ H ₃ SiOHC=CH ₂ (a) HCOH@MOF-505; (b) HCOH@MOF505 /H ₃ SiOHC=CH ₂ complex; (c) transition state structure and (d) H ₃ SiOCH ₂ CH ₂ CHO@MOF-505 structure (distances in Å).	108
81	Optimized structures of the HCOH@Cu-ZSM-5/H ₃ SiOHC=CH ₂ (a) HCOH@Cu-ZSM-5; (b) HCOH@Cu-ZSM-5/H ₃ SiOHC=CH ₂ complex; (c) transition state structure and (d) H ₃ SiOCH ₂ CH ₂ CHO@Cu-ZSM-5 structure (distances in Å).	111
82	Calculation energy profiles (kJ/mol) for the Mukaiyama aldol reaction between formaldehyde and silyl enol ether in the MOF-505 system (solid line), the Cu-ZSM-5 system (dotted line) and the gas phase system (dashed line).	112

LIST OF FIGURES (Continued)

Figure		Page
83	Shows the natural population analysis (NPA) of the total charge of the reacting species and Wiberg bond order of the important bonds along with the Mukaiyama aldol reaction catalyzed by MOF-505 and Cu-ZSM-5.	116
84	A summary of organic chemicals produced from carbon dioxide utilization.	119
85	Schematic drawing of the homo-metallic and hetero-metallic compounds used in this investigation (a) Mo/Mo trifluoroacetate $[\text{MoMo}(\text{O}_2\text{CCF}_3)_4]$; (b) Rh/Rh trifluoroacetate $[\text{RhRh}(\text{O}_2\text{CCF}_3)_4]$; (c) Mo/Rh trifluoroacetate $[\text{MoRh}(\text{O}_2\text{CCF}_3)_4]$; and (d) Rh/Mo trifluoroacetate $[\text{RhMo}(\text{O}_2\text{CCF}_3)_4]$.	121
86	Optimized structures of (a) Mo/Mo trifluoroacetate $[\text{MoMo}(\text{O}_2\text{CCF}_3)_4]$, (b) Rh/Rh trifluoroacetate $[\text{RhRh}(\text{O}_2\text{CCF}_3)_4]$, and (c) Mo/Rh trifluoroacetate $[\text{MoRh}(\text{O}_2\text{CCF}_3)_4]$.	123
87	Energy profile for the uncatalyzed cycloaddition of CO_2 with ethylene oxide to give ethylene carbonate. Energies are in kJ/mol.	124
88	Reaction pathways for CO_2 with epoxides on homo-metallic and hetero-metallic systems which CO_2 activation as the first step (a) or with epoxide activation as the first step (b).	125
89	Optimized structures of the CO_2 and ethylene oxide over the Mo/Rh trifluoroacetate $[\text{MoRh}(\text{O}_2\text{CCF}_3)_4]$	126

LIST OF FIGURES (Continued)

Figure		Page
90	Optimized structures of (a) ethylene oxide adsorption (Ads) (b) the co-adsorption complex of CO ₂ and ethylene oxide (Coads), (c) transition state (TS_C) and ethylene carbonate product (Prod_C) of concerted mechanism over Mo/Rh trifluoroacetate [MoRh(O ₂ CCF ₃) ₄].	128
91	Energy profile (in kJ/mol) for concerted pathway mechanisms of the cycloaddition of carbon dioxide with ethylene oxide over Mo/Mo trifluoroacetate (green line), Rh/Rh trifluoroacetate (blue line), Rh/Mo trifluoroacetate (black line), and MoRh trifluoroacetate (red line).	129
92	Possible mechanisms of the MoRh trifluoroacetate catalyzed cycloaddition of CO ₂ and ethylene oxide.	130
93	Optimized structures of (a) transition state (TS1_S) (b) intermediate (Int1_S) (c) complex of Int_S and CO ₂ (Int_C/CO ₂) and (d) transition state (TS2_S) of step mechanism A over Mo/Rh trifluoroacetate [MoRh(O ₂ CCF ₃) ₄].	132
94	Optimized structures of (a) transition state (TS2_S) (b) intermediate (Int2_S) (c) transition state (TS3_S) and (d) product of step mechanism B over Mo/Rh trifluoroacetate [MoRh(O ₂ CCF ₃) ₄].	135
95	Energy profile (in kJ/mol) of the cycloaddition of carbon dioxide with ethylene oxide over Mo/Rh trifluoroacetate [MoRh(O ₂ CCF ₃) ₄] : stepwise pathway A (red line) and stepwise pathway B (black line).	136

LIST OF ABBREVIATIONS

Abbreviation	Meaning
1D	one-dimensional
2D	two-dimensional
3D	three-dimensional
Ads	adsorption
APTES	aminopropyltriethoxysilane
AuNPs	gold nanoparticles
BDC	Benzenedicarboxylic acid
BET	Brunauer, Emmett and Teller
BPE	bipolar electrode
BSSE	basis set superposition error
BTC	benzenetricarboxylic acid
CABED	capillary assisted bipolar electrodeposition
CPs	coordination polymers
CNFs	carbon nanofibers
CNTs	carbon nanotubes
Coads	coadsorption
CTAB	cetyltrimethylammonium bromide
DBA	dodecyloxy benzoic acid
DBED	direct bipolar electrodeposition
DC	direct current
DDA	dodecanoic acid
DI	deionize
DLS	dynamic light scattering
DMF	N, N-Dimethylformamide
E_a	activation energy
E_a	anode potential
E_{Arr}	Arrhenius activation energy
EC	electrochemical
E_c	cathode potential
EDPs	electrophoretic paints
EDS	energy-dispersive spectroscopy

LIST OF ABBREVIATIONS (Continued)

Abbreviation	Meaning
EPD	electrophoretic deposition
EXAFS	x-ray adsorption fine structure
FE-SEM	field emission scanning electron microscopy
FMO	frontier molecular orbital
GC	glassy carbon
HKUST	Hong Kong University of Science and Technology
HOMO	highest occupied molecular orbital
HPW	keggin-type phosphotungstate
IBED	indirect bipolar electrocrodeposition
IR	infrared spectroscopy
IRMOF	isorecticular metal–organic framework
LA	Lewis-acid
LAG	Liquid-Assisted Grinding
LB	langmuir–blodgett
LUMO	lowest unoccupied molecular orbital
MC	mechanochemical
MIL	materials from institute lavoisier
MMMs	mixed-matrix membranes
MTBS	methyltributylammonium methylsulfates
MW	microwave
NBO	natural bond orbital
NCs	nanoclusters
NHE	normal hydrogen electrode
NPA	natural population analysis
ONIOM	our own n-layered integrated molecular orbital and molecular mechanics
PDMS	polydimethylsiloxane
PdNPs	paladium nanoparticles

LIST OF ABBREVIATIONS (Continued)

Abbreviation	Meaning
PS	polystyrene
PSD	pore size distribution
PtNPs	Platinum nanoparticles
PVP	poly(N-vinyl-2-pyrrolidone)
QM	Quantum mechanics
S	spin
SAM	self-assembled monolayer
SBU _s	secondary building units
SDA	structure directing agents
SE	secondary electron
SEM	Scanning electron microscope
SPR	surface plasmon resonance
STEM	scanning transmission electron microscope
TEOS	tetraethyl orthosilicate
TMB	trimethylbenzene
TST	transition state theory
UFF	Universal force field
UV-vis	ultraviolet–visible spectroscopy
V _{min}	minimum potential value
XAFS	x-ray absorption fine structure
XRD	Powder X-ray diffraction
ZIF	zeolitic imidazolate framework
ZSM	zeolite socony mobil
ΔG^\ddagger	free energy
ΔV	maximum polarization potential
Θ	angular position
Å	Angstrom
cm	centimeter
cm ⁻³	cubic centimeter
C°	degree Celsius

LIST OF ABBREVIATIONS (Continued)

Abbreviation	Meaning
eV	electron volt
K	Kelvin
kJ	kilojoules
kV	kilovolts
kVm ⁻¹	kilovolts per meter
MΩ.cm	megaohm-centimeter
μm	micrometre
mA	milliampere
mg	milligram
mL	milliliter
mm	millimetre
mN/m	millinewton per meter
min	minute
M	molar
nm	nanometer
m ² g ⁻¹	square meter per gram
V	volt
Vcm ⁻¹	volts per centimeter

CHAPTER I. HISTORY AND CHALLENGES OF MOF CHEMISTRY

1. Introduction of metal-organic frameworks (MOFs)

Coordination polymers (CPs) are inorganic or organometallic polymers containing metal cation centers linked together with organic ligands. CPs can be categorized into one-dimensional (1D), two-dimensional (2D) and three-dimensional (3D) structure types depending on the number of dimensions of their organization structure (see Figure 1) (Batten Stuart, R. *et al.*, 2013). The CP structure may extend in one dimension by repeating the coordination entities with or without the cross-links, which are formed by repeating coordination entities, extending the structure to two or three dimensions. An important subclass of CPs is metal-organic frameworks (MOFs), which represent a new generation of porous crystalline materials.

MOFs are 3D porous materials in which the structure is constructed by assembling metal-containing clusters, known as secondary building units (SBUs), with multidentate organic ligands (such as carboxylates, imidazole, tetrazolates, sulfonates) via coordination bonds (Eddaoudi, M. *et al.*, 2001; Tranchemontagne, D. J. *et al.*, 2009). Generally, the metal clusters in the MOF structure are composed of transition metal cations (e.g. zinc, iron, copper, chromium, cobalt, or nickel), p-block metals (e.g. aluminium or gallium) or rare earth metals (e.g. scandium or yttrium) and organic bridging ligands, which are bi-, tri or tetra-dentate anions (see Figure 2).

MOFs exhibit relatively large pore sizes ($\sim 0.3\text{-}3.5$ nm), higher surface areas (Langmuir surface areas of up to ~ 5000 m² g⁻¹) and low densities ($\sim 1.00\text{-}0.20$ g cm⁻³) compared to those of zeolites, which are traditional inorganic adsorbents and catalysts, and those of the conventional porous carbon materials (Dhakshinamoorthy, A. *et al.*, 2011; Kitagawa, S. *et al.*, 2004). These remarkable properties make MOFs suitable for a wide range of applications including gas storage (Morris, R. E. and P. S. Wheatley, 2008), adsorption and separation (Li, J.-R. *et al.*, 2009), sensors (Allendorf, M. D. *et al.*, 2009; Kreno, L. E. *et al.*, 2011), size-, shape-, and enantio-selective catalysis (Ma, L. *et al.*, 2009), and drug delivery (Huxford, R. C. *et al.*, 2010). Due to their unique and tunable structures, and consequently also their properties, MOFs have attracted a great deal of research interest and benefit from an increasing attention in various industries, especially the chemical one.

The names of MOF materials are typically represented by a three-letter symbol, which demonstrates the molecular compositions or institution that prepared it for the first time. After

the three-letter symbol, a number is typically added. This number typically indicates the order of discovery. For instance, G. Férey and co-workers synthesized a series of MOFs and gave the symbol “MIL-n” where the “MIL” stands for "Materials from Institute Lavoisier" and followed by a number (Millange, F. *et al.*, 2002). In addition, MOFs synthesized by Yaghi and co-workers are represented with the symbol “ZIF” followed by a number in which “ZIF” stands for “Zeolitic Imidazolate Framework” (Park, K. S. *et al.*, 2006). In 1995, Yaghi and co-worker published for very first time research work dealing with MOFs. Meanwhile, Kitagawa and coworkers reported the 3D structure of porous coordination networks of MOFs and their fascinate properties concerning the gas sorption at room temperature. Subsequently, the materials have become very popular.

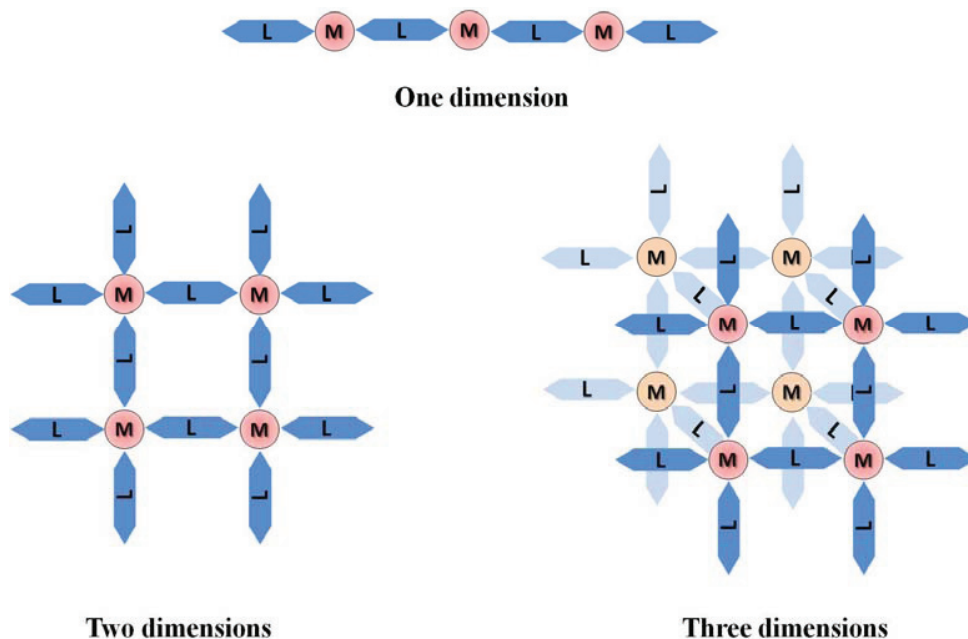


Figure 1. Schematic illustrations of the 1D, 2D and 3D structure of coordination polymers. M represents the metal cluster and L represents the organic bridging ligand.

The structural design of MOFs can be performed in several ways. The variation of metal clusters and type of organic linkers is the basic strategy to obtain MOFs with various characteristics (Eddaoudi, M. *et al.*, 2002). For example, various isorecticular MOFs (IRMOFs) can be prepared based on the same skeleton called MOF-5 (IRMOF-1), which is composed of

zinc oxide clusters (Zn_4O) linked together with terephthalate (1,4-benzenedicarboxylic acid, H_2BDC) ligands forming a cubic network of $\text{Zn}_4\text{O}(\text{BDC})_3$, but with different carboxylate linkers, having different molecular lengths (see Figure 3 for example). The physicochemical properties of the obtained MOFs are varied by the nature of this linker. The obtained IRMOFs have various pore sizes, ranging from several angstroms to a few nanometers (3.8 Å- 2.9 nm), pore volumes and crystal densities.

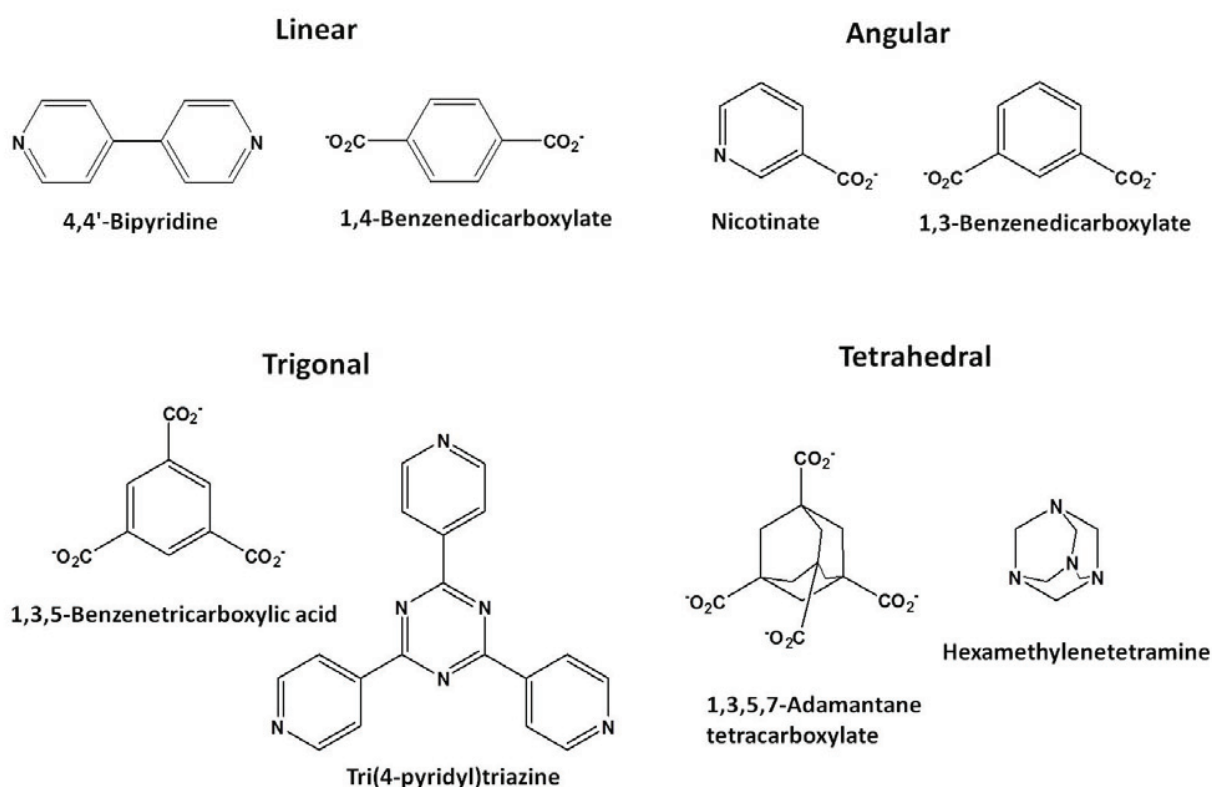


Figure 2. Chemical structures of examples of organic bridging ligands used for MOFs.

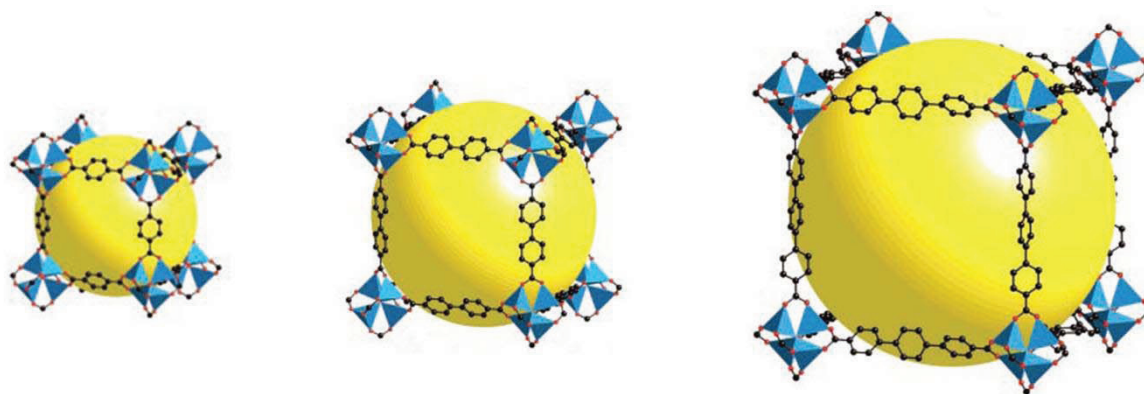


Figure 3. Schematic illustrations showing MOFs constructed from linear dicarboxylate linkers with various molecular lengths. The pore sizes of the obtained materials depend on the molecular length of the linkers. Blue polyhedra, red and black spheres represent Zn, O and C, respectively. The large yellow spheres represent the MOF cavities. Source from reference (Eddaoudi, M. *et al.*, 2002)

Apart from the variation of the molecular length of the dicarboxylic linkers as in the case of the IRMOF series, changing of the type of metal centers also creates diversity in the MOF structure. Different cationic secondary building units, called paddlewheels, of copper acetate ($\text{Cu}_2(\text{OAc})_4$) are used to create a new series of MOFs. The paddlewheel structure is composed of the $\text{Cu}_2(\text{CO}_2)_4$ moiety and four carboxylate carbon atoms located at the vertices of a square, as shown in Figure 4. One of MOFs in this series is copper-benzene-1,3,5-tricarboxylate (Cu-BTC or HKUST-1), owing to the 1,3,5-tricarboxylate linkers (Chui, S. S.-Y. *et al.*, 1999). Cu-BTC is one of the most studied MOFs. This is due to its various potential applications including adsorption (Bordiga, S. *et al.*, 2007), gas separation (Mao, Y. *et al.*, 2013), and hydrogen storage (Krawiec, P. *et al.*, 2006). The discovery of Cu-BTC was firstly reported in 1999 by Chui and coworker (Chui, S. S.-Y. *et al.*, 1999).

In 2002, another MOF series, MIL-n, was designed and developed by Férey's group (Millange, F. *et al.*, 2002). The strategy used for this structural design is the variation of the metal center atom. The structure of MIL-n is composed of trivalent cations, such as vanadium(III), chromium(III) or iron(III), extended with p-elements such as aluminium(III), gallium(III) or indium(III), and linked by derivatives of carboxylic acid. These materials have been studied for CO_2 capture (Stavitski, E. *et al.*, 2011), adsorption (Boutin, A. *et al.*, 2010) and

catalysis (Suresh, M. *et al.*, 2014). MIL-101 is one of the most studied MOFs in this series. It is a chromium terephthalate-based mesoscopic MOF. The crystal structure of MIL-101 is assembled by corner-sharing of supertetrahedra, which consist of the Cr_3O trimer and 1,4-benzenedicarboxylic acid moieties. It is stable in air, boiling water and organic solvents. For this reason, it has attracted a great interest for various applications including gas storage, catalysis and drug delivery.

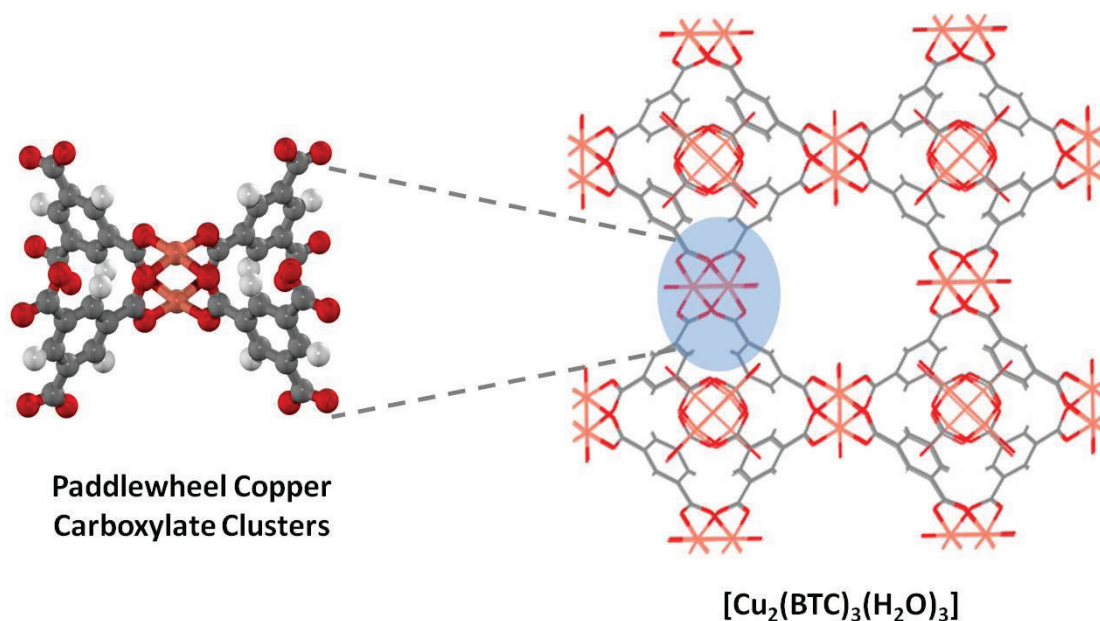


Figure 4. Scheme illustrating the copper acetate paddlewheel units, which are connected and form a 3D framework with uniform pore structure of Cu-BTC. Orange, red, gray, and white spheres represent Cu, O, C, and H atoms, respectively.

Apart from the mentioned strategies, zeolitic imidazolate frameworks or ZIFs were developed by Yaghi and co-workers via the use of different kinds of organic linkers, imidazolate derivatives. These MOFs have structures close to those of zeolites, which are aluminosilicate materials. ZIFs have attracted much attention due to their high porosity and high specific surface area, making them suitable for many applications including catalysis (Zhu, M. *et al.*, 2013), gas separation (Hara, N. *et al.*, 2014), gas storage (Hu, Y. *et al.*, 2013), and chemical sensors (Lu, G. and J. T. Hupp, 2010). The crystal structures of ZIFs are close to those of zeolites, which consist of tetrahedral Si (or Al) atoms and the bridging O atoms, but they are constructed with transition

metals (Zn or Co) as metal centers and imidazolate derivatives as organic linkers (see Figure 5). ZIF-8 is one of the most studied ZIFs. This is because it has large pores with a diameter of 11.6 Å that are very accessible for molecules. The presence of these large pores thus facilitates the diffusion of the molecules into the MOF structure. In addition, ZIF-8 has a high thermal stability and high surface area (1630 m²g⁻¹ for BET surface area). It has the combined highly desirable properties of zeolites and MOFs, such as high crystallinity, high surface area, as well as good thermal and chemical stability. Furthermore, its surface can be modified in order to obtain materials with the desired properties. ZIF-8 has been considered as a good candidate material for many technological applications such as membranes for gas separation, capillary coatings for the chromatographic separation and catalysis.

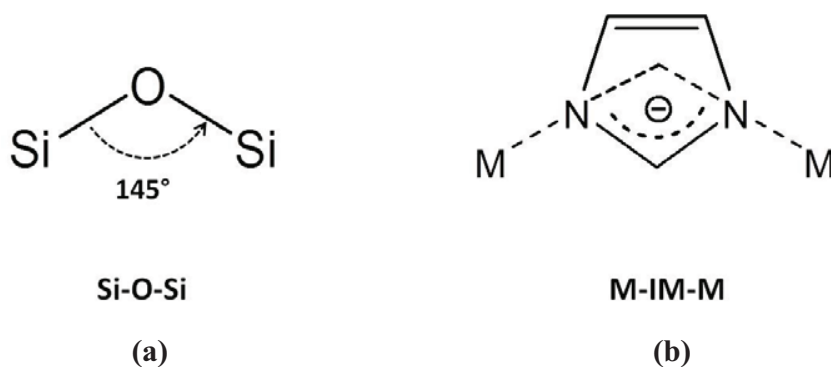


Figure 5. Schematic illustration showing the angles of the (a) Si-O-Si and (b) M-IM-M bridges in zeolites and zeolitic imidazolate frameworks (ZIFs) respectively. M represents the metal site and IM represents imidazolate derivative.

2. Synthetic approaches for MOFs

Depending on the type of MOFs, the suitable synthetic methods are varied. Some MOFs such as MOF-5, MOF-74, MOF-177, MOF-199, and ZIF-8 can be formed easily by only mixing metal salts and organic ligands at room temperature while some MOFs can only be formed under relatively drastic conditions. The typical methods used for the synthesis of MOFs can be divided into two main groups, the solvothermal and non-solvothermal methods. For the solvothermal method (when the solvent is water this method is called hydrothermal method), the MOF formation takes place in a closed vessel at the temperature higher than or at the boiling point of the used solvent. Thus, the reaction occurs under the pressure generated by the boiling of the

solvent (see Figure 6). For the non-solvothermal method, the reaction takes place below the boiling point of the solvent. Thus, it occurs at ambient pressure. Because the reaction in the case of the non-solvothermal method takes place under relatively mild conditions compared to that in the case of solvothermal one, the synthesis is more straight forward. The important parameters regarding the MOF formation are the reaction temperature, the concentrations of metal source and organic ligand, the solubility of the reactants in the solvent, and the pH of the solution (Tranchemontagne, D. J. *et al.*, 2008); (Cravillon, J. *et al.*, 2009).

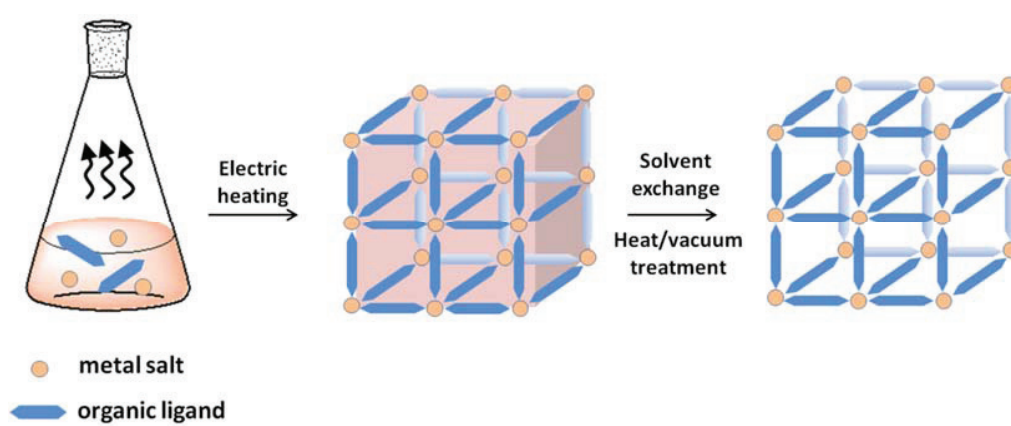


Figure 6. Schematic illustration showing the steps involved in the conventional solvothermal or hydrothermal synthesis of MOFs

Although, some MOFs can be formed under mild conditions, their industrial or large scale production is often limited. This is because the reaction under mild conditions is often slow and less effective or requires high quantities of solvent, which is typically toxic, and thus impacting the environment. Currently, new strategies for synthesizing MOFs have been developed. These routes include the electrochemical (EC), microwave-assisted heating (MW), mechanochemical (MC), and sonochemical (US) routes. These methods utilize electrical energy, microwave radiation, mechanical energy, and ultrasonic radiation, respectively (see Figure 7). As an advantage, these methods are not only more rapid and green (environmentally-friendly) compared to the conventional methods but also scalable, and thus allow industrial scale production. Furthermore they also often produce new MOF compounds that cannot be obtained with the conventional methods.

The MW synthesis is one of the most frequently used processes for the MOF preparation (Klinowski, J. *et al.*, 2011). This method has several advantages over other methods namely (i) an accelerated crystallization, (ii) nanoscale products and (iii) high product purity. In addition, the morphology of the products formed by this method is controllable. For this synthesis method, the reactants are dissolved in a solvent and transferred to a vessel, placed in the microwave unit, and then heated for a desired time (see Figure 7a). During the application of an oscillating electric field, the permanent dipole moment of the molecules in the synthesis medium is coupled. This induces molecular rotations, which lead to an increase in kinetic energy of molecules, and thus increasing the temperature of the system. The important synthesis parameters in the microwave approach are the type of solvent, the irradiation time, the reaction temperature, the power of the microwaves, and the molar (or concentration) ratio of the reactants. Normally, microwave irradiation allows faster synthesis compared to conventional heating. The reaction is typically carried out with reaction times below 1 h. As an example, Cr-MIL-101 could be synthesized at 210 C° with microwave irradiation. The reaction time for such a synthesis was less than 1 hour. This duration is much less than in the case of the conventional synthesis that yields the final product with comparable characteristics and properties (Jhung, S. H. *et al.*, 2007; Khan, N. A. *et al.*, 2011). Until recently, the MW synthesis has been applied to many MOFs including HKUST-1 (Schlesinger, M. *et al.*, 2010) and Fe-MIL-101 (Taylor-Pashow, K. M. L. *et al.*, 2009). Nevertheless, as a major drawback of this synthesis method, the scale-up process is limited by using typical microwave reactors. For this purpose, reactors with a more complicated design such as continuous flow microwave reactors are required.

The sonochemical synthesis of MOFs takes place under the influence of high-energy ultrasound. Ultrasound is cyclic mechanical vibration with frequencies greater than the upper limit of human hearing, which is approximately 25 kilohertz. The application of ultrasound to the synthesis system leads to a homogeneous and accelerated nucleation process, which results in shorter crystallization times and smaller particle sizes compared to those obtained via the conventional synthesis method. In this method, the solution containing metal salt and organic ligand substances are introduced in a reactor, which is fitted with a sonicator bar for applying ultrasonic waves (see Figure 7b). During this application, the formation and collapse of bubbles occurring in the solution produce very high temperatures (~5000 K) and high pressures (~1000 bar). The heating and cooling rates are very high. Fine crystallites of the product are produced.

The sonochemical synthesis is easily carried out. It is considered as a green route. The reaction time for this method is quite short. Furthermore, additional heating is not required. $\text{Zn}_3(\text{BTC})_2$ is an example of MOFs that can be prepared via this sonochemical method (Qiu, L.-G. *et al.*, 2008a).

The electrochemical synthesis of MOFs was first reported in 2005 by researchers at BASF Cooperation (a chemical company) (Müller, U. *et al.*, 2005). In this method, the metal ions are produced by an anodic dissolution (the dissolution of metal or the oxidation of metal to metal ions occurs at the anodic side of an electrochemical cell) in a mixture containing the organic ligand and conducting salt (electrolyte) species (see Figure 7c). As this process can be run as a continuous process and it provides the possibility to produce the products in relatively high amounts compared to the conventional methods, it can be used for large scale production of MOFs. The important parameters that play a role for the product characteristics and yield are the solvent, the conducting salt, voltage, current and temperature. Recently, the syntheses of HKUST-1, ZIF-8, MOF-5, Al-MIL-100, Al-MIL-53, and Al-MIL-53-NH₂ via the anodic dissolution in an electrochemical cell were reported (Stock, N. and S. Biswas, 2011). The main drawback of the electrochemical synthesis of MOFs is that typically organic solvents are required. As organic solvents have a higher resistivity than aqueous solutions, the synthesis requires a relatively high concentration of supporting electrolyte, and thus becomes somewhat costly.

In 2006, the mechanochemical synthesis of MOFs was initially reported (Pichon, A. *et al.*, 2006). In this approach, mechanical force is used to break the intramolecular bonds within the reactant molecules and create the bonds of the product molecules. In this method, the MOF formation can take place with or without the use of solvent. With the addition of small amounts of solvent the synthesis efficiency was found to be improved. This is due to the acceleration of mechanochemical reactions derived from the increase in mobility of the reactants in the presence of solvent molecules (Frisic, T. and L. Fabian, 2009). This method is called as liquid-assisted grinding (LAG). The biggest drawback of the mechanochemical synthesis is the difficulty of the product characterization because of the product obtained by grinding contains some impurities. Therefore the product is not suitable for characterization by conventional method.

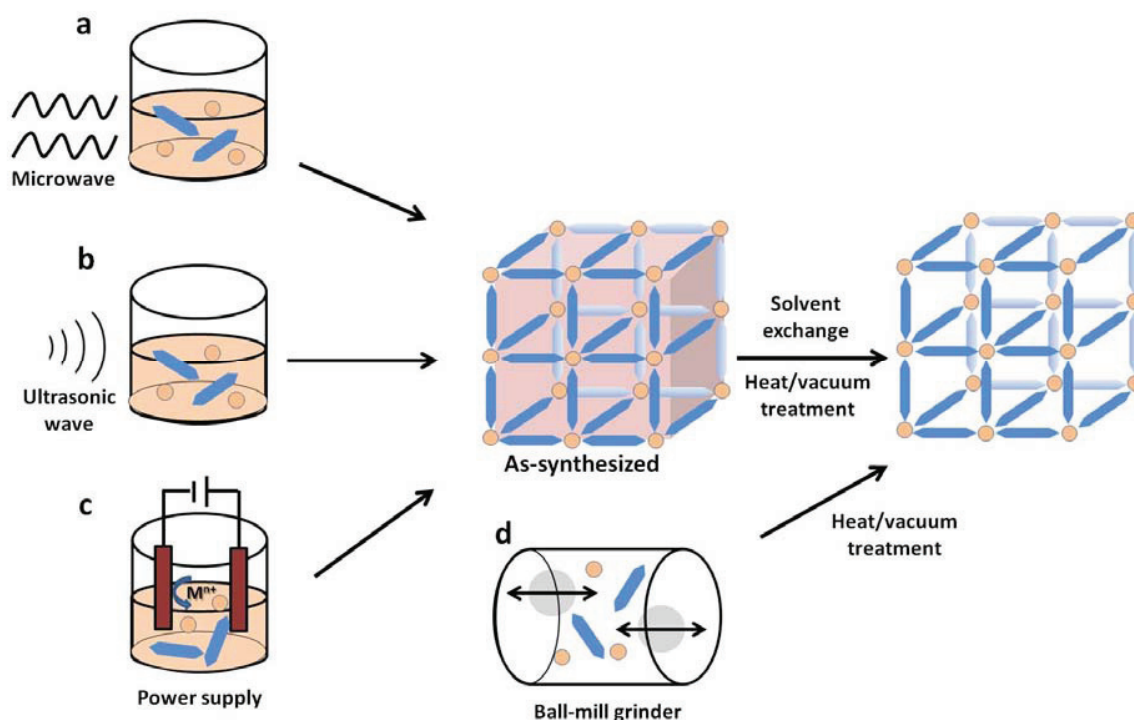


Figure 7. Schematic illustration showing the newly developed routes for the preparation of MOFs: (a) microwave-assisted solvothermal, (b) sonochemical, (c) electrochemical, and (d) mechanochemical syntheses.

3. Potential applications of MOFs

Recently, MOF materials have been widely used in many applications including gas storage (Morris, R. E. and P. S. Wheatley, 2008), gas adsorption and separation (Li, J.-R. *et al.*, 2009), drug delivery (Huxford, R. C. *et al.*, 2010), luminescence (Allendorf, M. D. *et al.*, 2009), electrode materials (Wu, D. *et al.*, 2014), and sensors (Kreno, L. E. *et al.*, 2011). Furthermore, they could be applied in heterogeneous catalysis, for example for alcohol oxidation (Dhakshinamoorthy, A. *et al.*, 2010), CO oxidation (Zhao, Y. *et al.*, 2011), cyanosilylation (Aguirre-Diaz, L. M. *et al.*, 2013), and Knoevenagel condensation (Burgoyne, A. and R. Meijboom, 2013) reactions. In this thesis, apart from the synthesis of MOFs, the catalytic activities of MOFs is also of interest.

The catalytic behavior of MOFs can be due to different mechanisms. In a first case, the MOF molecular species act as the active centers themselves for the reaction. A second way is

that external active species are introduced or encapsulated in the MOF structure. In the first approach, both metal and organic parts of MOFs can be the active sites. For the case of the metal sites, the sites can be available to react with the reactants by removal of the solvent molecules that coordinate to the metal species (see Figure 8a). In this case, the amount of the reactants interacting with them is limited. In the case of the organic parts, the active catalytic sites can be generated by functionalization of the linker molecules (see Figure 8b). In the second approach, catalytic active species, such as monometallic (e.g. Au, Pd, Pt, Ru, Cu, Ni, Ag), or bimetallic (e.g. AuPd, RuPt) nanoparticles, can be encapsulated in the MOF structure (see Figure 8c) via various methods including solvent-free gas-phase loading, solution impregnation, incipient wetness impregnation, and solid grinding (Meilikhov, M. *et al.*, 2010). The catalytic behavior of the obtained composites does not only depend on the characteristics of the encapsulated species (clusters or particles) such as the chemical compositions, size, shape, and electronic properties (such as oxidation state) (Cuenya, B. R., 2010), but also depends on the nature of the supporting materials (MOFs) and the stabilizers of the particles (such as ligands or polymers) (Tsunoyama, H. *et al.*, 2009).

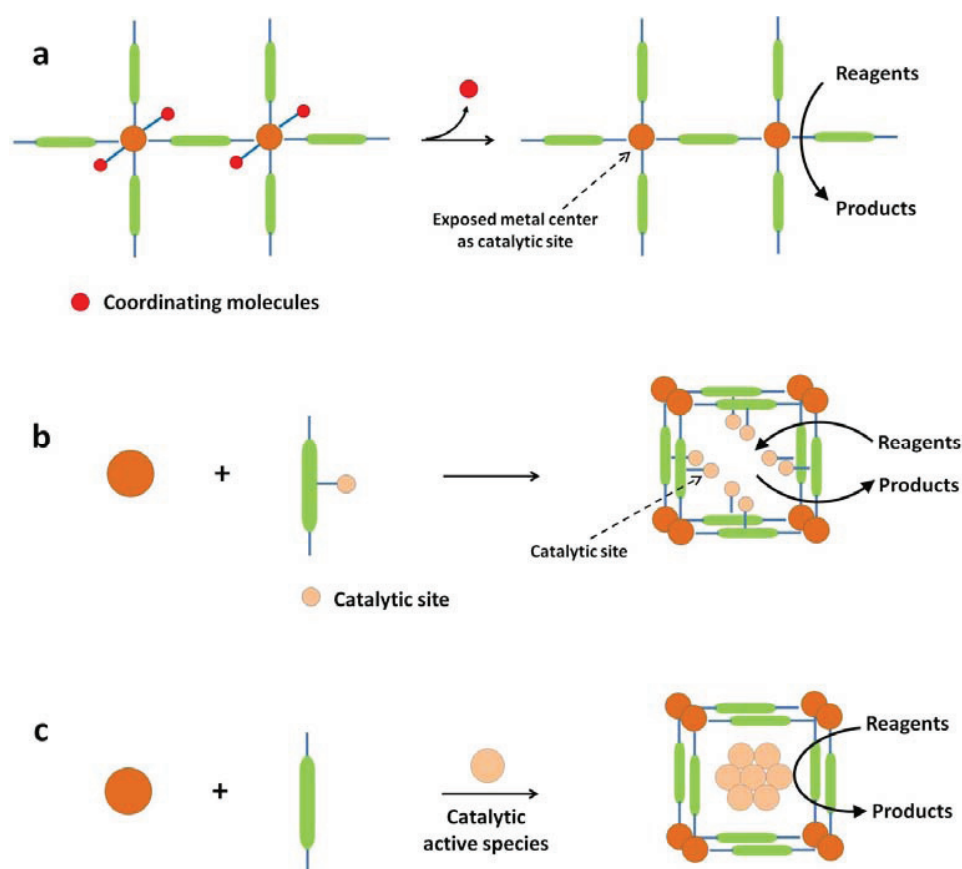


Figure 8. Schematic illustration showing different ways to create the catalytically active sites in MOFs. (a) The metal species, (b) the functionalized organic ligand or (c) the additional encapsulated species act as the active catalytic sites. Source from reference (Lee, J. *et al.*, 2009)

In the first part of this thesis, a new strategy for MOF synthesis was studied and developed. Indirect bipolar electrodeposition (IBED) was used to synthesize ZIF-8 and HKUST-1. The proof of principle experiments were performed for the asymmetric generation of MOFs. In the second part, we investigated the possibility to use an electrochemical route to prepare a well-designed hierarchical porous (macro- and micro-porous) electrode of Cu/MOF composites. In this regard, the Cu macroporous electrodes were first prepared by using colloidal silica particles as template materials. Then the synthesis of MOF was performed via the anodic dissolution of the copper surface of the prepared electrodes. We expect that the newly-developed composites should have interesting applications in the field of catalysis. In addition we studied the preparation of a MOF, MIL-101, and the deposition of noble metal nanoparticles of gold,

palladium, and platinum. These particles were prepared by a colloidal deposition of the precisely size-controlled nanoparticles stabilized by poly(N-vinyl-2-pyrrolidone) (PVP). This concept might be generalized for the synthesis of other metal nanoparticle/MOF composites and is supposed to lead to the improvement of the catalytic activity of MOFs.

Apart from the experimental study, in order to gain a deeper insight into the catalysis carried out with MOFs, the catalytic behavior of MOF-505 in the Mukaiyama aldol reaction of formaldehyde and silyl enol ether molecules was investigated. In addition, the reaction mechanism was explored. The progress of this reaction was examined both in a systems catalyzed with MOF-505 and also another catalyst, Cu-ZSM-5, and for an uncatalyzed system for the purpose of comparison. The catalytic activity of homo-metallic clusters (Mo/Mo trifluoroacetate and Rh/Rh trifluoroacetate) and hetero-bimetallic clusters (Mo/Rh trifluoroacetate), that are the metal complexes representing the metal clusters in MOFs, were also theoretically investigated for the cycloaddition reaction of carbon dioxide and ethylene oxides.

CHAPTER II. SYNTHESIS OF HETEROGENEOUS MOF STRUCTURES

1. Site-Selective Synthesis of Janus-type Metal-Organic Framework Composites

1.1 Introduction

MOFs with well-defined pores and excessive porosity are one of candidate materials that may find an importance in a wide range of future applications ranging from catalysis (Ma, L. *et al.*, 2009), to chemical separation (Li, J.-R. *et al.*, 2009) and drug delivery (Horcajada, P. *et al.*, 2011). For MOFs, in order to reach their full potential in these and other applications, it is necessary to prepare them with some specific configurations (Bradshaw, D. *et al.*, 2012) such as thin films and supported membranes (Shekhah, O. *et al.*, 2011). Nowadays, the selective growth of MOF crystals on substrates is a very interesting topic. The selective growth can be obtained via lithography and printing techniques, which can result in well-defined and two-dimensional MOF-patterned films (Ameloot, R. *et al.*, 2010; Doherty, C. M. *et al.*, 2013).

Ameloot and co-workers reported the preparation of HKUST-1 via a lithographic technique, which is based on the use of stable precursor solutions of MOF primary building blocks including metal ions and ligand molecules to deposit monodisperse crystals in patterns down to the single-crystallite level by in situ crystallization. The protrusions of a microlithographed polydimethylsiloxane (PDMS) stamp are inked with the MOF precursor solution. The stamp is subsequently placed on the target substrate, resulting in the patterned deposition of oriented MOF crystals on selected area (Ameloot, R. *et al.*, 2010). The area-selective deposition of MOFs has been reported by Guang Lu and co-workers. They prepared ZIF-8 thin films with photolithography, soft lithography, and sputter coating. They demonstrated the successful patterning of the films. A periodically vertically spaced ZIF-8/Pt hybrid material was successfully prepared. This obtained material is applicable for sensors for some selected vapors and gases, including H₂ (Lu, G. *et al.*, 2012).

Cara M. Doherty and co-workers used the combined technique of UV lithography and imprinting to prepare Al-based MOF crystals. This process involves the use of a common epoxy-based photoresist to pre-pattern the surface. The MOF crystals are imprinted into the pre-patterned surface. It was proposed that the protocol for the surface patterning does not affect the MOF properties. The fabricated MOFs show remarkable properties for bio-processing (Doherty,

C. M. *et al.*, 2013). Ldan-Hod and co-workers used the electrophoretic deposition (EPD) technique for the patterned growth of electroactive MOF thin films on conductive surfaces. Four representative MOFs including two Zr-based MOFs (NU-1000 and UiO-66), an ionic Cu-based MOF (HKUST-1) and an Al-based MOF (MIL-53) were successfully deposited (Hod, I. *et al.*, 2014). In addition, a combined EPD and photolithography technique was used to produce a patterned grid of MOF particles.

While significant progress has been made, the development of fast, cheap and scalable fabrication processes, which facilitate the integration of MOFs in functional devices (Allendorf, M. D. *et al.*, 2011), and the development of the spatio-selective preparation of MOF-based structures onto 3-dimensional substrates remain a challenge. Tae-Hong Park and co-workers reported a new type of hierarchically functionalized colloidal composite particles in which MOF nanocrystals are spatio-selectively grown on the surface of polymer particles (Park, T.-H. *et al.*, 2014). The patchy seed particles were prepared by electrohydrodynamic co-jetting of two distinct polymer solutions with differently functionalized polymers (see Figure 9). Then, MOFs were grown on one site of the polymer particles. The researchers suggested that due to the anisotropic 3D structure and the magnetically controllable properties of these Janus particles they may be used as catalysts (Crossley, S. *et al.*, 2010), microactuators (Lee, K. J. *et al.*, 2012), smart drug vehicles (Champion, J. A. *et al.*, 2007), and switchable displays (Kim, S.-H. *et al.*, 2010).

Nevertheless, there is currently a limit in growing of the MOF@MOF type structures in which a close degree of lattice matching between the two frameworks is required for an efficient epitaxial growth of one MOF crystal onto or around another (Furukawa, S. *et al.*, 2009a, 2009b). Until recently, there was no satisfactory method for the site-selective deposition of MOFs onto 3-dimensional metal substrates, forming in this way Janus-type architectures. Considering the advantages of combining the inherent porosity and tunable physical properties of MOFs with the applications of Janus structures in catalysis, drug delivery, optoelectronics and biomedical imaging, the development of strategies creating MOF composites is very interesting (Jiang, S and Granick, S. 2012).

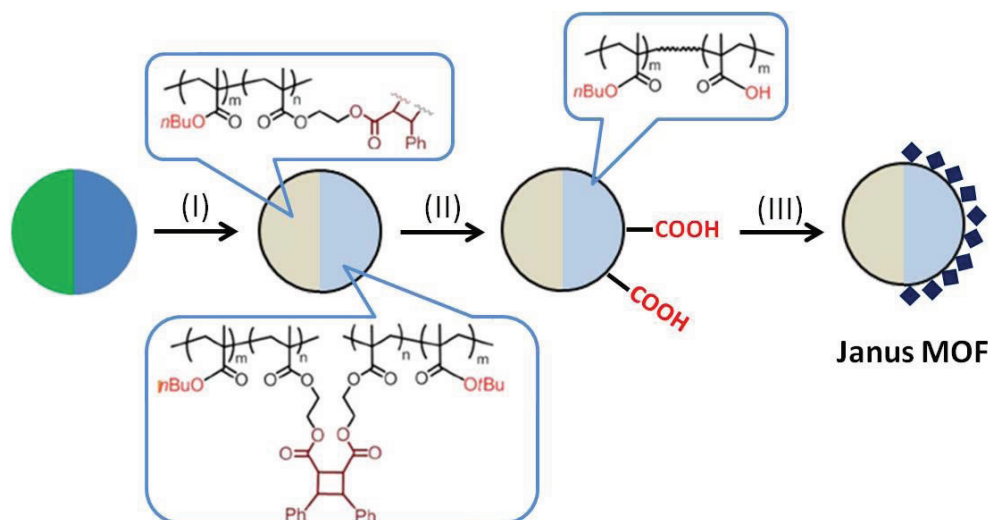


Figure 9. Schematic illustration showing the process of the site-specific growth of MOFs on polymer particles prepared via electrohydrodynamic co-jetting of two distinct polymer solutions with differently functionalized polymers (Park, T.-H. *et al.*, 2014).

Herein we investigated the application of bipolar electrodeposition for the wireless and selective deposition of prototypical MOFs onto metallic wires (zinc) and metallic particles (copper) to prepare Janus-type composite materials in a facile manner under mild conditions. This technique is considered to be a cheap and fast process and thus being an excellent candidate method for the industrial preparation.

Bipolar electrochemistry (BE) on microparticles was first described by Fleischmann *et al.* (Fleischmann, M. *et al.*, 1986). This technique is based on the polarization of conducting objects under the influence of an external electric field. When a conducting object is exposed to an electric field, established between two electrodes in a solution, a positive and negative polarization occurs between the two opposite sides of the object. Redox reactions can occur when the polarization is strong enough, which means that the same object becomes an anode and a cathode at the same time. The object is then called a bipolar electrode (BPE) (Loget, G. and A. Kuhn, 2011a; Mavr , F. o. *et al.*, 2010).

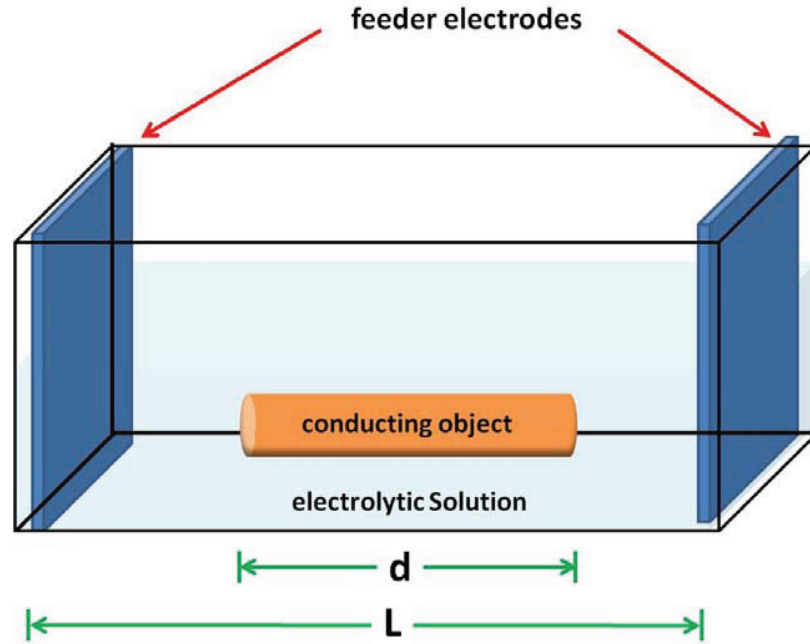


Figure 10. Schematic illustration of a typical bipolar system with a conducting object immersed between two feeder electrodes in an electrolytic solution.

In the normal case, a conductive object is suspended in a homogeneous electrolytic solution between feeder electrodes without a direct connection between the conducting object and the power source (see Figure 10). When a potential difference ($E_{\text{apply}} = E_a - E_c$ where E_a and E_c are the potential at the anode and the cathode, respectively) is applied to the cell (L is the distance between two feeder electrodes), the value of the electric field (\mathcal{E}) existing in the solution is given, in a first order approximation by Equation 1:

$$\mathcal{E} = \frac{E_a - E_c}{L} \quad (1)$$

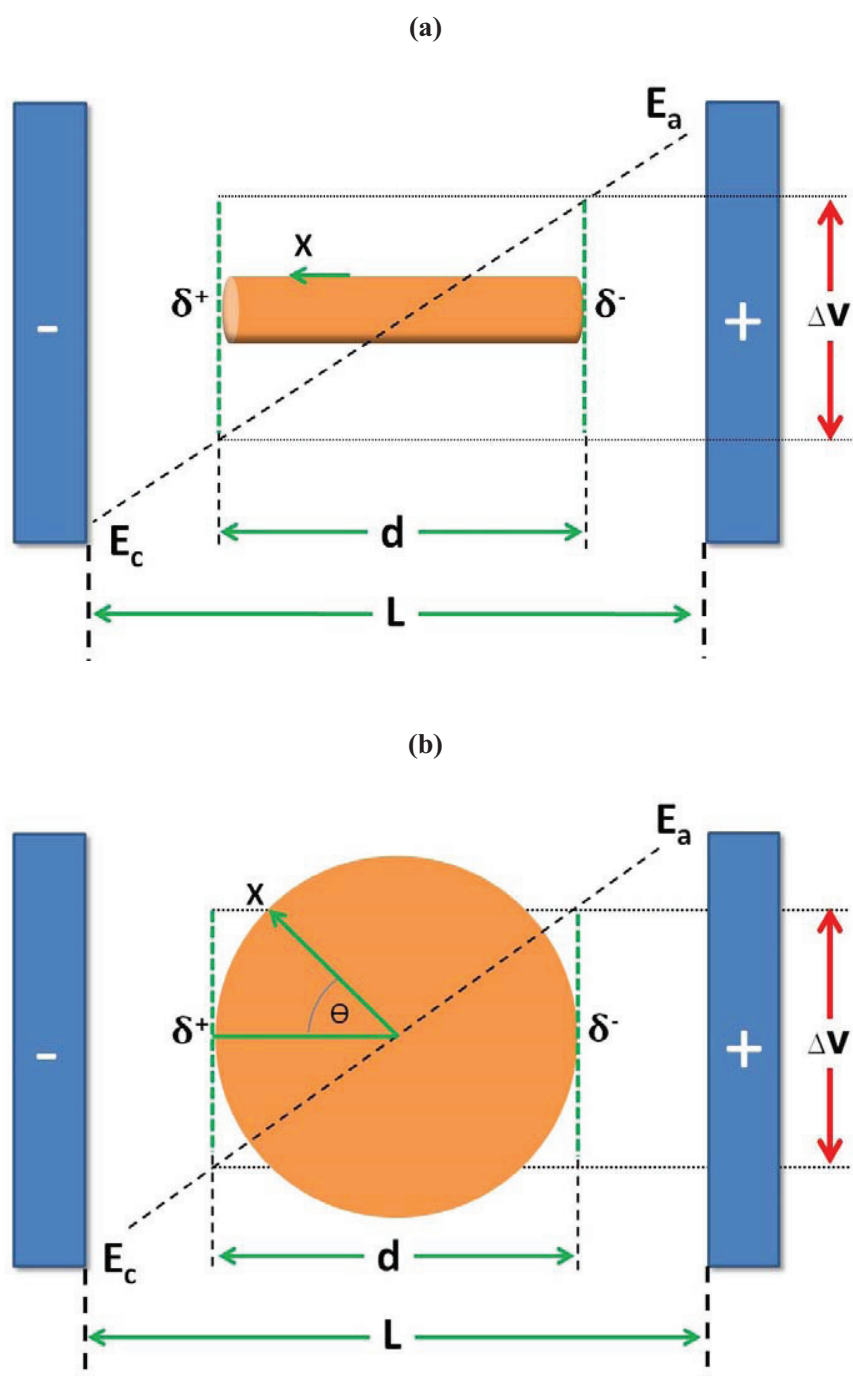


Figure 11. Schematic illustrations showing the polarization of conducting substrates under the influence of an external electric field: (a) linear and (b) spherical conducting substrates.

Figures 11a and 11b show the potential distribution in the solution of the cell for two conducting morphologies, linear and spherical ones, respectively. As a consequence, under the influence of the electric field, the polarization potential (E) is given by the difference of the solution potential with respect to the conducting substrate. The value of E varies linearly as a function of the position (x) along the solution and substrate interface. The E value can be calculated by using Equation 2 and Equation 3 for linear and spherical conducting substrates, respectively.

$$E = \mathcal{E} \cdot x \quad (2)$$

$$E = \mathcal{E} d/2 \cdot \cos\Theta \quad (3)$$

Parameter x in Equation 2 represents the length of the conductive substrate. Parameter d in Equation 3 represents the diameter of the conductive substrate.

The maximum polarization potential difference (ΔV) occurs between the ends of the conductive object. The value of ΔV can be calculated via Equation 4:

$$\Delta V = \mathcal{E} \cdot d \quad (4)$$

This value indicates the overall polarization between the ends of the conductive substrate.

When the solution contains the electroactive species, R_{ed} and O_x' , which undergo the following reactions:



where n and n' represent the number of electrons involved for each half-reaction and the two redox couples R_{ed}/O_x and R_{ed}'/O_x' having a standard potential with E_0^1 (Equation 5) and E_0^2 (Equation 6), we can assume that the minimum potential value (ΔV_{min}) needed to induce redox

reactions at the end of the substrate has to be approximately equal to the difference between the standard potentials of the two involved redox couples (Equation 7):

$$\Delta V_{\min} = |E_0^1 - E_0^2| \quad (7)$$

If $\Delta V > \Delta V_{\min}$, the electrochemical reactions can be carried out simultaneously at both ends of the substrate, the oxidation at the anodic pole (Equation 5) and the reduction at the cathodic pole (Equation 6) (see Figure 12).

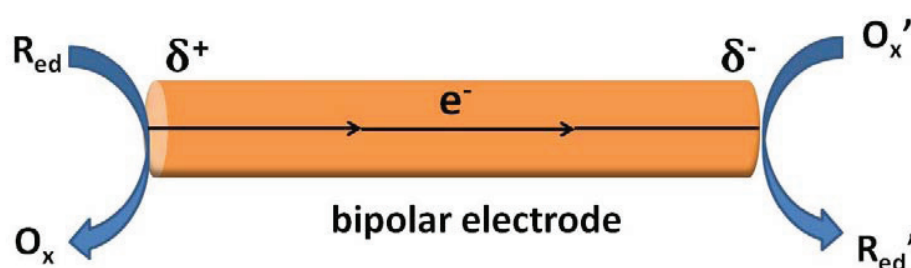


Figure 12. Schematic illustration of the linear conductive substrate acting as the bipolar electrode for a redox couple reaction when the substrate is exposed to an electric field and immersed in a solution containing the electroactive species.

Bipolar electrochemical techniques have been used in various areas including micro- and macroswimmer developments (Loget, G. and A. Kuhn, 2010, 2011b, 2012), electronics (Bradley, J.-C. *et al.*, 1997), analytical chemistry (Fosdick, S. E. *et al.*, 2013; Guerrette, J. P. *et al.*, 2012b; Guerrette, J. P. *et al.*, 2012a) and materials science (Loget, G. *et al.*, 2013; Ulrich, C. *et al.*, 2008a, 2008b). An asymmetric bipolar electrodeposition on micrometer-sized particles was first reported by Bradley and co-workers in 1999 (Bradley, J.-C. and Z. Ma, 1999). The modification of micrometer-sized amorphous graphite particles with Pd was performed. The Pd particles and solvent were reduced and oxidized at the cathodic and anodic poles of bipolar graphite electrodes, respectively. A hybrid Au/carbon/Pd material was prepared via the same technique (Bradley, J.-C. and Z. Ma, 1999). In addition, this technique was adopted for the modification of carbon substrates including carbon nanotubes (CNTs) and carbon nanofibers

(CNFs). CNTs and CNFs were modified at one end with Pd particles by applying electric fields of 1000 and 300 kVm^{-1} , respectively (Bradley, J. C. *et al.*, 2005).

Kuhn and co-workers have developed a new technique for the modification of micro-and nanoparticles in an aqueous bulk phase. This technique is based on the use of a capillary electrophoresis equipment. It is called capillary assisted bipolar electrodeposition (CABED). The first publication concerned the selective modification of multi-wall carbon nanotubes by gold nanoparticles (AuNPs) via the CABED technique (Warakulwit, C. *et al.*, 2008). The particle size of AuNPs was in the order of ten nanometers. It was found that the particle size increases with the length of the multi-wall carbon nanotubes. This finding evidences that the deposition occurs via bipolar electrochemistry. The same CABED technique was used to modify carbon tubes with a length at the micrometer-scale by gold (Loget, G. *et al.*, 2011), platinum (Fattah, Z. *et al.*, 2011), copper (Loget, G. *et al.*, 2011), and nickel (Loget, G. *et al.*, 2010). These bipolar electrodepositions involve the direct electron transfer from the substrate to the electroactive precursors that undergoes the electrodeposition on the substrate, and thus this is called direct bipolar electrodeposition (DBED). The DBED technique is usually limited to deposits obtained from electroactive precursors while many interesting materials cannot be obtained directly by electrodeposition or electropolymerization.

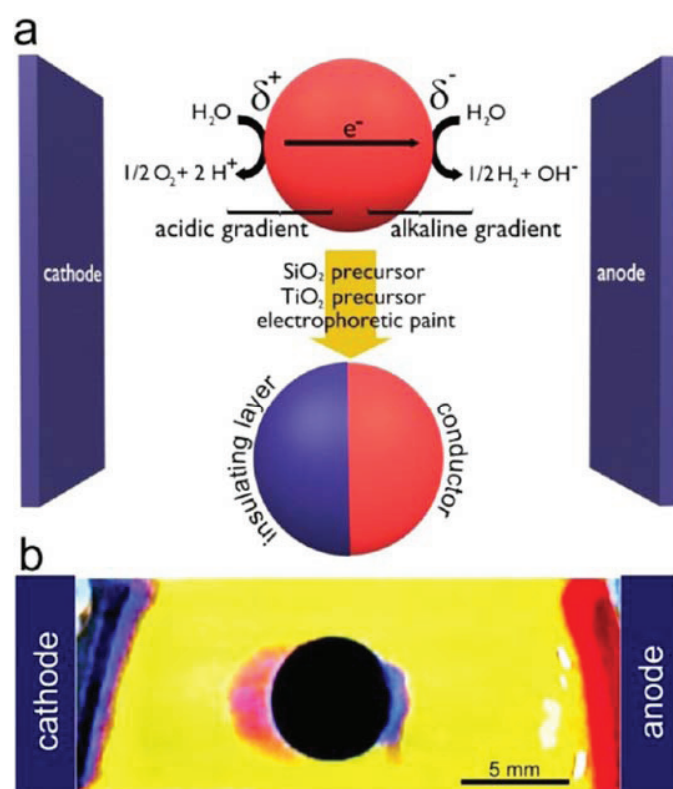


Figure 13. (a) Schematic illustration showing the principle of the indirect bipolar electrodeposition (IBED). (b) Visualization of the pH evolution at a bipolar electrode, revealed by using a universal pH indicator. Blue corresponds to basic pH, and red corresponds to acid pH. Source from reference (Loget, G. *et al.*, 2012)

Loget and co-workers recently reported that insulating materials including metal oxides and electrophoretic paints (EDPs) can be also generated from non-electroactive precursors at a bipolar electrode via an indirect bipolar electrodeposition (IBED) technique (Loget, G. *et al.*, 2012). This IBED technique does not involve a direct electron transfer between the substrate and the precursor of the deposit, but exploits a local pH change that is electrochemically triggered around the conducting objects. This pH change leads to the controlled polymerization or precipitation of an insulating deposit. The pH can be controlled at the reactive poles of bipolar electrodes. For this reason, the IBED technique is promising for the synthesis of various bifunctional objects from non-electroactive precursors (see Figure 13). These materials include

silica, silicone, titanate, crystalline titanium dioxide, and organic insulating polymers (Loget, G. *et al.*, 2012).

Bipolar electrodeposition of silica on glassy carbon beads via the IBED technique was investigated. Polycondensation of silica occurs at the cathodic pole of the bipolar electrode where the pH at the interface is strongly increased. The silica modification on glassy carbon is clearly observed as the brightest part of the Janus object from the SEM images (see Figures 14a-14b) (Loget, G. *et al.*, 2012). Other types of materials such as TiO_2 can be also electrodeposited via this strategy (Loget, G. *et al.*, 2012). For TiO_2 , by using the same procedure and cell used for the silica modification, it was found that the amount of titanate deposited on carbon beads depends on the value of the applied electric field. With an electric field of 71 V cm^{-1} , the resulting asymmetric object shows a small titanate deposit at one extremity of the particle. By using a higher electric field of 214 V cm^{-1} , a bigger deposit, which covers a relatively larger area on the GC particle, is obtained (see Figures 14c-14d). In addition, the modification of EDP on glassy carbon bead was also performed via the IBED technique (see Figures 14e-14f).

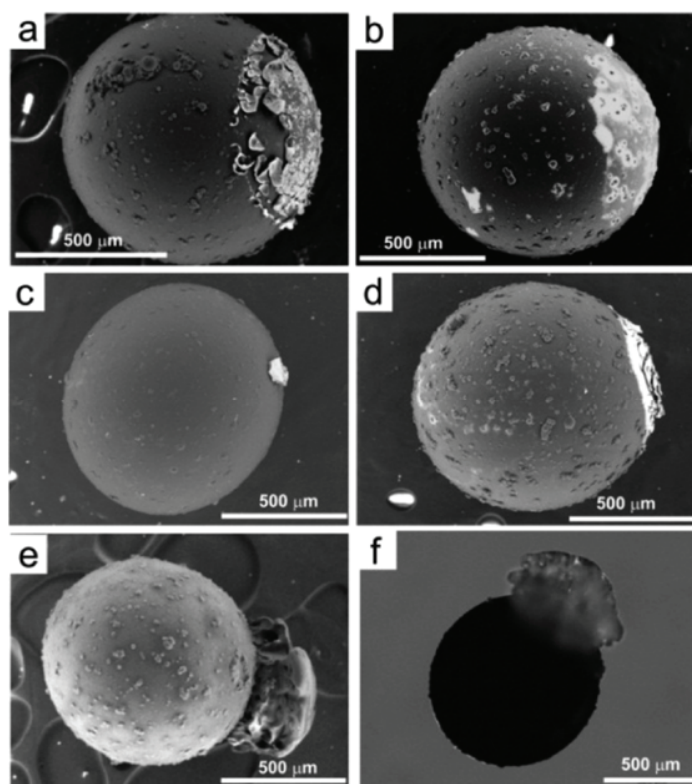


Figure 14. (a-d) SEM images of glassy carbon beads modified with different materials including (a) silica, (b) silicone (c)-(d) titanate (using an electric field of (c) 71 and (d) 214 Vcm^{-1}) and (e) EDP. (f) Optical micrograph showing a glassy carbon bead modified with EDP. All hybrid materials were obtained via the IBED technique. Source from reference (Loget, G. *et al.*, 2012)

As MOFs cannot be obtained by a direct electrochemical oxidation or reduction of a single electroactive precursor compound the idea emerged to use the IBED concept also for the site-selective generation of MOF deposits as mentioned above.

Among MOFs, two MOFs including “Zeolitic Imiazolate Frameworks-8” (ZIF-8) and “Hong Kong University of Science and Technology-1” (HKUST-1 or Cu-BTC) on metallic substrates are of our interests in this section. ZIF-8 was firstly synthesized by Park and co-workers (Park, K. S. *et al.*, 2006). Its structure is composed of zinc ions and 2-methylimidazolate (meIm-) ligands that form the cubic crystals with space group $I4^- 3m$ ($a=16.991 \text{ \AA}$) and the formula $\text{C}_8\text{H}_{12}\text{N}_4\text{Zn}$. For ZIF-8, each Zn^{2+} ion is tetrahedrally coordinated by four N atoms from

the bridging *meIm*- ligand (see Figure 15). This leads to the formation of the sodalite structure with large cavities (11.6 Å in diameter), which are connected with a small pore aperture (3.4 Å in diameter). ZIF-8 exhibits the highly desirable and combined properties of zeolites and MOFs such as high crystallinity, high surface areas (1630 m²/g (BET) and sufficient thermal and chemical stabilities. The ZIF-8 crystals, which were produced solvothermally in *N,N*-dimethylformamide (DMF) media, are thermally stable under ambient conditions up to 450 °C and chemically stable during boiling in benzene, methanol and water for up to a week (Park, K. S. *et al.*, 2006). Therefore, ZIF-8 is one of good candidate materials for many technological applications such as membranes for gas separation, sensors, and catalysis.

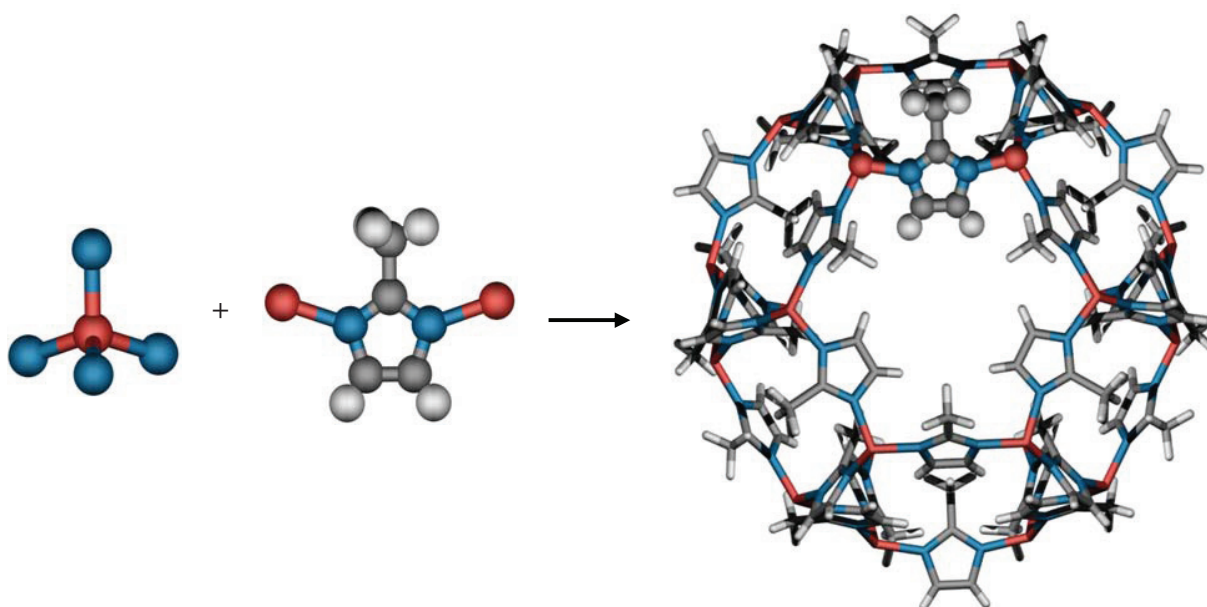


Figure 15. Schematic illustration of the formation of ZIF-8 from Zn metal centers and 2-methylimidazolate ligands. Zn, C, N and H atoms are represented by red, gray, blue and white spheres, respectively.

Ordóñez and co-workers fabricated the membranes made of ZIF-8 for gas separation applications. The membranes were further used as additives in mixed-matrix membranes (MMMs). The obtained ZIF-8 mixed-matrix membranes exhibit potential in the separation of small gas molecules including H₂ from H₂/CH₄ and H₂/C₃H₈ gas mixtures, and CO₂ from CO₂/CH₄, and CO₂/C₃H₈ gas mixtures due to the higher selectivity of transporting H₂ and CO₂, respectively (Ordóñez, M. J. C. *et al.*, 2010). Venna and co-workers also used ZIF-8 membranes

fabricated on titania and α -alumina supports for gas separation. ZIF-8 membranes exhibit a gas-separating ability with a higher selectivity for H_2 from H_2/N_2 , H_2/CH_4 , and H_2/C_3H_8 gas mixtures and for CO_2 from CO_2/CH_4 gas mixture (Venna, S. R. and M. A. Carreon, 2009). In addition, Lu and co-workers (Lu, G. and J. T. Hupp, 2010) prepared a thin film of ZIF-8 for sensor applications. The results show that the ZIF-8 based sensor is responsive to a range of vapors and gases, and exhibits selective responses to n-hexane and ethanol. Moreover, ZIF-8 was investigated for catalysis applications. Jiang and co-workers discovered that a fine mixture of ZIF-8 nanocrystals and a small amount of gold nanoparticles can convert CO to less toxic CO_2 at temperatures lower than 250 °C (Jiang, H.-L. *et al.*, 2009).

HKUST-1 or Cu-BTC consists of copper as the metal component and benzenetricarboxylic acid (btc) as the organic ligand. HKUST-1 with the formula $C_{18}H_6Cu_3O_{12}$ has a cubic framework structure with an open 3D pore system. Its framework $[Cu_3(btc)_2(H_2O)_3]$ (where BTC = 1,3,5-benzenetricarboxylate) is microporous (Chui, S. S.-Y. *et al.*, 1999). Two Cu(II) ions are linked to form a dimer. Each dimer further links with four 1,3,5-benzenetricarboxylic acid molecules to form a dimeric cupric tetracarboxylate unit or paddle-wheel unit. The paddle-wheel units are linked together and weakly bound with water molecules, or organic solvent molecules, (located at the centre of the main pores) creating the framework of HKUST-1. The open framework of HKUST-1 is obtained after the removal of the coordinated water molecules (in vacuum) from the structure in a post-synthesis treatment (see Figure 16). Lewis acidic Cu (II) sites are generated and are accessible for molecules, thus offering various applications including catalytic transformations, gas purification and separation, as well as hydrogen adsorption and storage. The pore network of HKUST-1 has a simple cubic symmetry. It consists of main channels of a square cross-section of ca. 0.9 nm in diameter and tetrahedral side pockets of ca. 0.5 nm, which are connected to the main channels by triangular windows of ca. 0.35 nm in diameter (Vishnyakov, A. *et al.*, 2003).

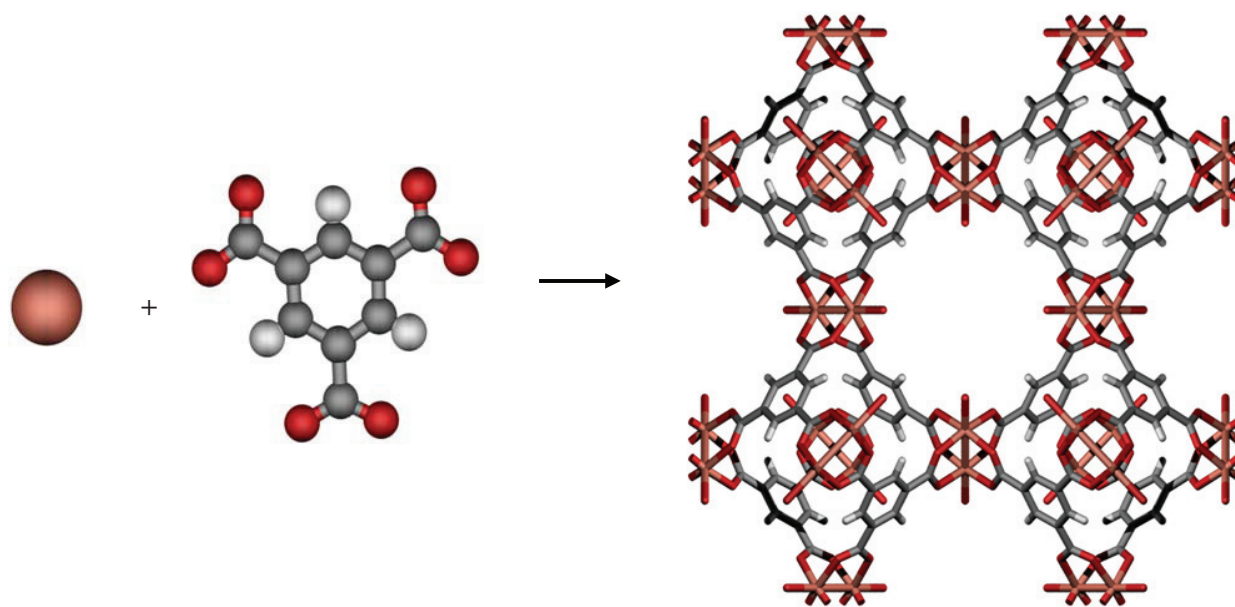


Figure 16. Schematic illustration of the formation of HKUST-1 or Cu-BTC from Cu metal centers and benzenetricarboxylic acid (btc) ligands. Cu, C, O and H atoms are represented by orange, gray, red and white spheres, respectively.

Pathan and co-workers used HKUST-1 for a green synthesis of pyrimidine chalcones via the Aldol condensation. As HKUST-1 behaves as a heterogeneous catalyst, it is easily separated from the reaction products and recycled. In addition, HKUST-1 provides a high product yield (Pathan, N. B. *et al.*, 2011). Sachse and co-workers successfully prepared an efficient catalytic material by introducing HKUST-1 nanoparticles inside the pores of hierarchical macro-mesoporous silica. The material exhibits high productivity for the Friedländer reaction (Sachse, A. *et al.*, 2012). The applicability of HKUST-1 for gas sensing was demonstrated by Davydovskaya and co-workers (Davydovskaya, P. *et al.*, 2013). HKUST-1 was used as a selective aldehyde sensing material for work function read-out based gas sensors at ambient conditions. It was shown that the HKUST-1 sensing layers allow distinguishing between hydrocarbon molecules with similar chemical properties but different molecular chain lengths. HKUST-1 was also examined for gas adsorption and separation. The study of HKUST-1 for the CO₂ adsorption and separation from flue gases (mixtures of CO₂/N₂/O₂) was carried out by Qingyuan Yang and co-workers (Yang, Q. *et al.*, 2007). The results show that HKUST-1 is a promising material for separating CO₂ from the flue gases. Furthermore, it was shown that the

electrostatic environment present inside the pores of HKUST-1 is very important for the selectivity in the case of mixtures composed of the quadrupolar molecules.

In this section, we prepared ZIF-8 and HKUST-1 (Cu-BTC) on metallic substrates via the IBED technique. The IBED technique was used to wirelessly generate reactive metal ions locally on the surface of the metallic substrates. These ions subsequently react with the ligand species in the solution, forming the extended coordination-based network structure of MOFs. Although there have been reports regarding the electrochemical preparation of MOFs either *via* anodic dissolution of ‘wired’ Cu electrodes (Martinez Joaristi, A. *et al.*, 2012; Mueller, U. *et al.*, 2006) for the selective deposition onto printed circuit boards) (Ameloot, R. *et al.*, 2009), or *via* the cathodic electroreduction (generation of base equivalents for ligand deprotonation) (Li, M. and M. Dincă, 2011), the IBED technique employed in this work is superior since it allows the wireless and selective deposition of MOFs at one end or hemisphere of a substrate. In this case the polarization simultaneously generates the metal ions required for the framework growth, and acts as a simple virtual mask without the need to chemically or physically block the areas where the deposition is not desired.

1.2 Experimental section

1.2.1 Bipolar electrochemical synthesis of ZIF-8

Zinc wires (1.0 mm in diameter, 99.999% trace metal basis) and 2-methylimidazole (99% purity) were purchased from Sigma-Aldrich. Anhydrous sodium sulfate with 99% purity was purchased from Acros Organics. 1M hydrochloric acid (HCl) aqueous solution was purchased from AVS TITRINORM. Nafion perfluorinated membranes (thickness = 0.005 in) were purchased from Sigma-Aldrich. Ultrapure water (18.2 MΩ.cm) was obtained from a Millipore Milli-Q system.

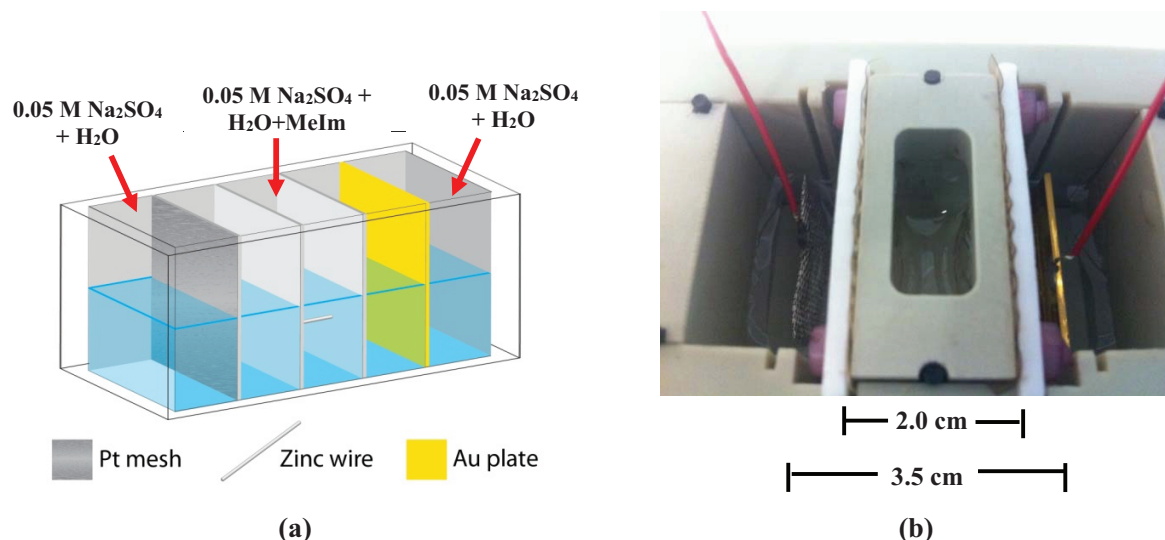
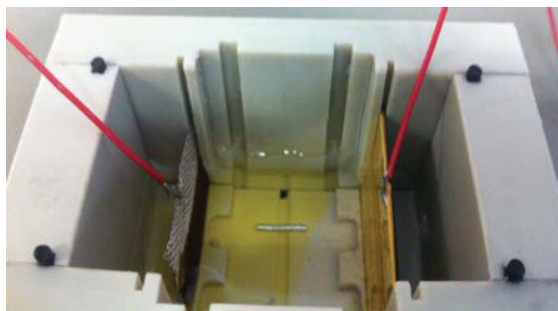
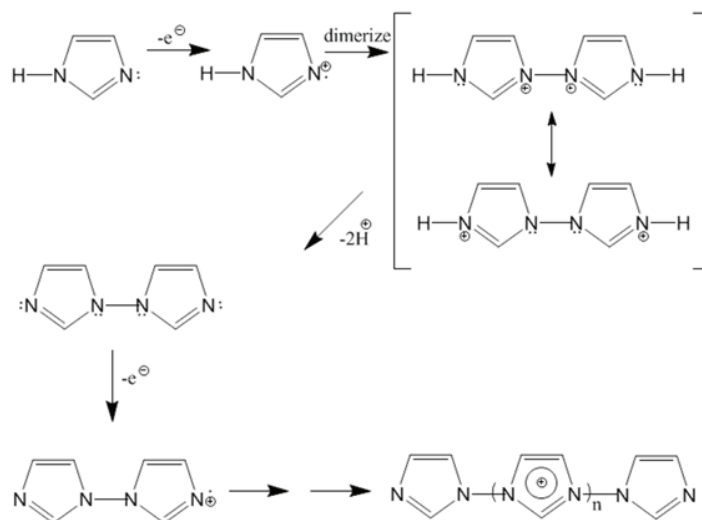


Figure 17. (a) Schematic illustration and (b) photo showing the experimental setup of equipment for the synthesis of ZIF-8. A zinc wire was introduced in the bipolar electrochemical cell containing a solution of 2-methylimidazole in ultrapure water (18.2 MΩ.cm) and 0.05M Na₂SO₄ supporting electrolyte. The electrode compartments were filled only with 0.05 M Na₂SO₄ electrolyte to facilitate the current flow in the cell.

All experiments were performed in a home-built electrochemical cell (see Figure 17) composed of a centered inner reaction compartment and two outer electrode compartments (distance (d) of 3.5 cm between both electrodes) separated by two Nafion membranes (distance (d) of 2.0 cm between both separators) for preventing the polymerization of 2-methylimidazole at the feeder electrodes (see Figure 18). A cathode (Pt mesh) and an anode (Au plate) were positioned in the outer compartments of the cell with an effective distance of 3.5 cm between both electrodes. The reaction compartment of the electrochemical cell contained a zinc wire (length = 1 cm) and a solution of 2-methylimidazole in ultrapure water (18.2 MΩ.cm) and 0.05M Na₂SO₄ supporting electrolyte. The zinc wire was pretreated by etching for 15 min in 1M hydrochloric acid before use. The electrode compartments were filled only with 0.05 M Na₂SO₄ electrolyte to facilitate the current flow in the cell.



(a)



(b)

Figure 18. (a) Picture of the experimental setup (without Nafion perfluorinated membranes) showing the position of the Zn wire introduced into the bipolar electrochemical cell. (b) Mechanism of the electrochemical polymerization of Imidazole derivatives that is prevented at the feeder electrodes in this work.

1.2.2 Bipolar electrochemical synthesis of HKUST-1

Copper spheres (3.0 mm in diameter) were purchased from Goodfellow Cambridge Limited. 1,3,5-benzenetricarboxylic acid with 95% purity of the organic linker and tributylmethylammonium methyl sulfate with $\geq 95\%$ purity of the supporting electrolyte were purchased from Aldrich. Absolute ethanol ($\geq 99.8\%$ purity) and sulfuric acid (95.0-98.0% purity) were purchased from Sigma-Aldrich. Nafion membranes (with the thickness of 0.005 inch) were

purchased from Sigma-Aldrich. Ultrapure water ($18.2 \text{ M}\Omega\cdot\text{cm}$) was obtained from a Millipore Milli-Q system.

All experiments were performed in a home-built electrochemical cell (see Figure 19) composed of a centered inner reaction compartment and two outer electrode compartments separated by two Nafion membranes ($d = 2.0 \text{ cm}$ between both separators) for preventing 1,3,5-benzenetricarboxylic acid polymerization at the electrodes. A cathode (platinum mesh) and an anode (gold plate) were positioned in the outer compartments of the cell with an effective distance of 3.5 cm between both electrodes. The reaction compartment of the electrochemical cell contained a copper bead (3 mm in diameter) and a solution of 1,3,5-benzenetricarboxylic acid in ethanol with 0.05M Tributylmethylammonium methyl sulfate. The copper bead was pretreated by etching for 15 min in 10% sulfuric acid before use. The electrode compartments were filled with 0.05 M Tributylmethylammonium methyl sulfate (MTBS) electrolyte in order to facilitate the current flow in the system.

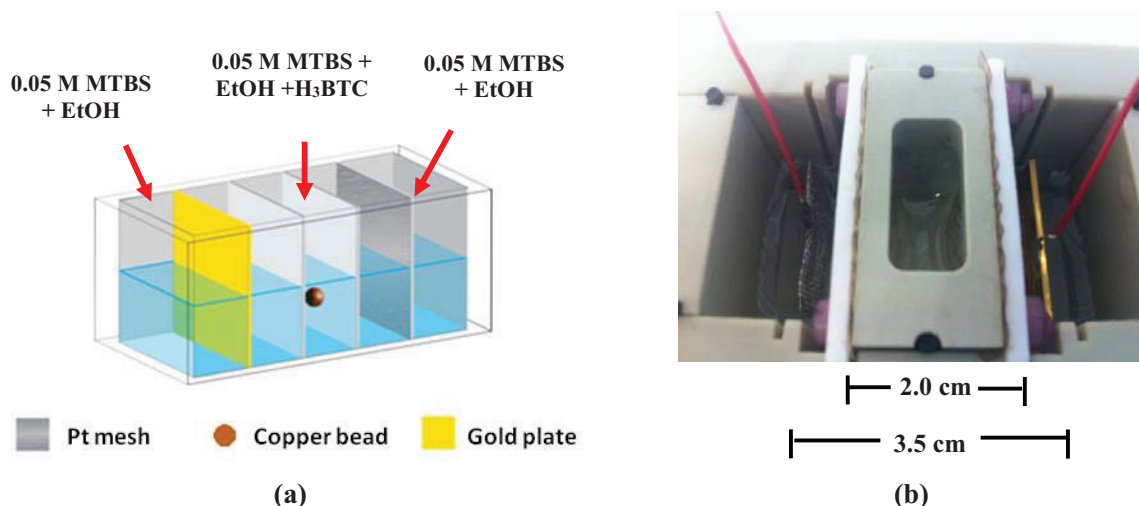


Figure 19. (a) Schematic illustration and (b) photo showing the experimental setup of equipment for the synthesis of HKUST-1. A copper sphere was introduced in the bipolar electrochemical cell composed of a centered inner reaction compartment ($d = 2.0 \text{ cm}$ between both separators) and two outer electrode compartments ($d = 3.5 \text{ cm}$). The solution contained 1,3,5-benzenetricarboxylic acid in ethanol and 0.05M MTBS supporting electrolyte. The electrode compartments were filled only with 0.05 M MTBS electrolyte in order to facilitate the current flow in the system.

1.2.3 Control Experiments

In order to demonstrate that the obtained Janus objects cannot be prepared via a classic electrochemical approach, which means by connecting the object physically to an electrode, we performed two control experiments for the zinc wire and the copper bead. The details of the control experiments are as follows.

1.2.3.1 Synthesis of ZIF-8 by normal electrochemistry

The reaction compartment of the normal electrochemical cell contained a zinc wire (1 cm in length) as the working electrode and a solution of 2-methylimidazole in ultrapure water (18.2 MΩ·cm) with 0.05M of Na₂SO₄ as the supporting electrolyte. The Zn wire was pretreated by etching for 15 min in 1M hydrochloric acid before use. The connection between the Au slide and the Zn wire was made by silver glue. Varnish was used for protecting the silver at the contact point (see Figure 20a). An Ag/AgCl electrode and a platinum mesh were used as reference and counter electrodes, respectively.

1.2.3.2 Synthesis of HKUST-1 by normal electrochemistry

The reaction compartment of the electrochemical cell contained a copper bead (3 mm in diameter) as a working electrode and a solution of 1,3,5-benzenetricarboxylic acid in ethanol with 0.05M tributylmethylammonium methyl sulfate as supporting electrolyte. The copper bead was pretreated by etching for 15 min in 10% sulfuric acid before use. A copper tape was used for the connection between the Au slide and the Cu bead (see Figure 20b). An Ag wire and a platinum mesh were used as pseudo-reference and counter electrodes, respectively.

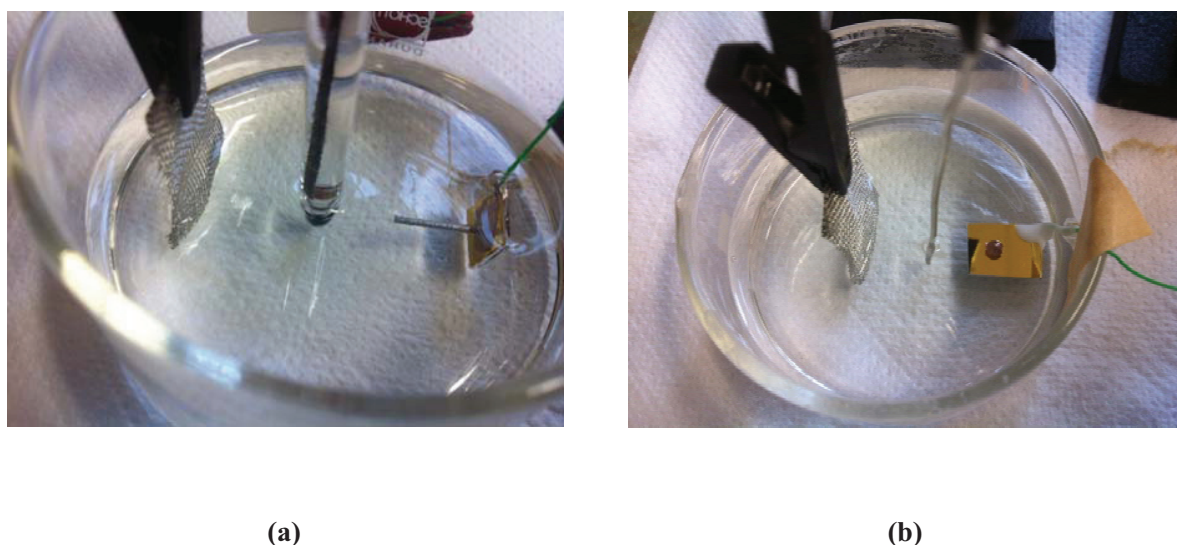


Figure 20. Photos showing the setup of normal electrochemical cells used for the synthesis of (a) ZIF-8 and (b) HKUST-1.

1.2.4 Characterization of ZIF-8 and HKUST-1

Powder X-ray diffraction (XRD) patterns of the samples were obtained by using a PANalitical X'pert MPD Bragg-Brentano θ - θ geometry diffractometer equipped with a secondary monochromator over an angular range of $2\theta = 5$ - 80° . Each acquisition lasted for 15 hours. The Cu- $K\alpha$ radiation was generated at 45 kV and 40 mA ($\lambda = 0.15418$ nm). The morphology of the ZIF-8 deposit was investigated by using a scanning electron microscope (SEM, Hitachi, TM-1000). The molecular composition of ZIF-8 and HKUST-1 was studied by infrared spectroscopy using a Thermo Nicolet iS10 FT-IR equipped with a Smart Orbit (Diamond) ATR accessory. Spectral analysis was performed over the range $4,000$ - 400 cm^{-1} with a resolution of 4 cm^{-1} .

1.3 Results and discussions

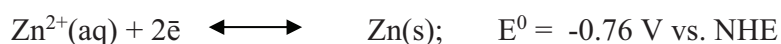
1.3.1 Bipolar electrochemical synthesis of ZIF-8 on zinc wire

To demonstrate the possibility to use the IBED technique for the preparation of MOFs, we initially selected for our study the chemically and thermally stable tetrahedrally coordinated Zn-imidazolate network $[\text{Zn}(2\text{-MeIm})_2]$ ZIF-8 (2-MeIm=2-methylimidazole) (Park, K. S. *et al.*, 2006). This is because of its reliable synthesis in a range of solvents under mild conditions

(Cravillon, J. *et al.*, 2009; Pan, Y. *et al.*, 2011). We employed a metallic Zn wire as both metal source and substrate for the selective deposition. To carry out these reactions, one has to consider that in bipolar electrochemistry the polarization voltage generated between the two sides of an object with respect to the surrounding solution is proportional to the external electric field (E) and the length of the object (l) as follow.

$$\Delta V = E \times l \quad (8)$$

In a first-order approximation, ΔV must be at least equal to the difference between the formal potentials of the two involved redox couples. In the present case, the oxidation of Zn metal occurs at the positively polarized side of a zinc wire (see Figure 21), based on the following redox couple.



At the opposite side of the wire, protons are simultaneously reduced.



Under standard conditions, the combination of these two redox couples leads, from a thermodynamic point of view, to a spontaneous reaction between both redox couples.

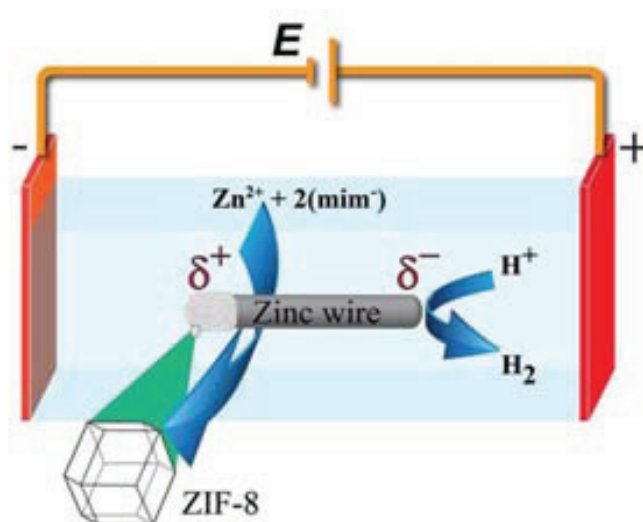


Figure 21. Schematic illustration showing the mechanism of the formation of Zeolitic Imidazolate Framework (ZIF-8). The crystal growth on the anodically polarized side of a zinc wire is triggered by indirect bipolar electrodeposition.

However, the variable overpotentials derived from the potential drops at the electrodes and in the solution as well as slow kinetics need to be considered, and especially in the case that the pH change will likewise impact on the potential difference. To experimentally estimate the potential difference required to drive the desired redox reactions simultaneously at both ends of the wire with sufficiently high kinetics, cyclic voltammetry has been used (see Figure 22). In order to estimate the order of magnitude of potential that needs to be applied to the bipolar electrochemistry cell for the synthesis of ZIF-8, a cyclic voltammogram of a Zn wire in water was recorded in the absence of ligand. It can be seen from the results that hydrogen evolution starts at around -1 V and reaches a maximum at -1.7 V, whereas the oxidation of zinc starts to be the dominant process at the potentials more positive than -1 V. One can therefore conclude that, in order to have a sufficient driving force, a polarization of the zinc wire of at least 0.7 V should be used (-1.7 V - (-1 V)). In order to be on the safe side and to ensure convenient reaction kinetics, potentials that are higher than the calculated threshold value were used.

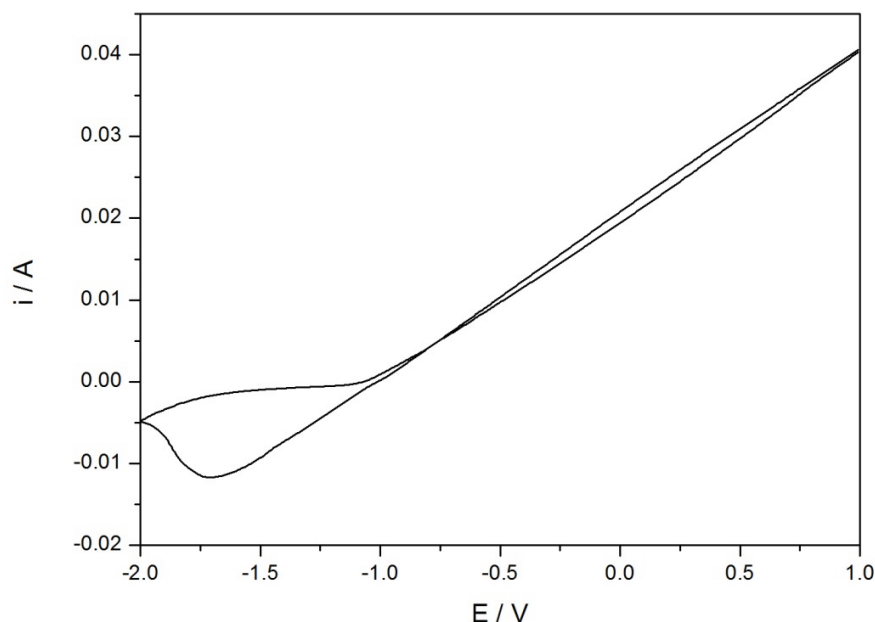


Figure 22. Cyclic Voltammogram of a zinc wire in 0.05 M Na_2SO_4 supporting electrolyte in ultrapure water obtained at a scan rate of 100 mV/s. The voltammogram was obtained at room temperature using a zinc wire as a working electrode, Pt mesh as a counter electrode, and Ag/AgCl as a reference electrode.

The electrochemical cell used for the ZIF-8 synthesis was composed of two electrodes and a 1 cm Zn wire, which was placed at the center between two Nafion membranes used in order to avoid the parasitic reactions of the ligand at the feeder electrodes. The distance between two electrodes was 3.5 cm. When applying a potential difference of 5V between them, one can calculate, based on Equation 8, that a potential drop of 1.4 V should occur between the two ends of the Zn wire. This is sufficient to overcome possible overpotentials and induce the required redox reactions at the opposite ends of the wire (according to the CV of Figure 22).

The Zn^{2+} ions produced at the positively polarized side of the wire undergo a chemical reaction with the 2-MeIm linker group (see Figure 23). In a control experiment where a Zn wire was left in an aqueous solution of the ligand for three days without applying a potential (see Figure 24a), almost no spontaneous reaction occurs, with only a few small deposits located at random positions along the wire. However, when applying the electric field, ZIF-8 is generated as a crystalline deposit exclusively at the positively polarized end of the wire (see Figure 24b).

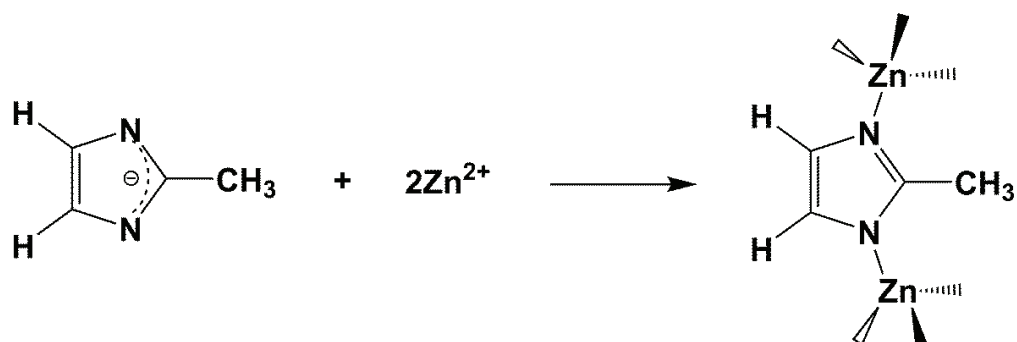


Figure 23. Schematic illustration showing the reaction of the 2-methylimidazole linker with the Zn^{2+} ions at the surface of the bipolar electrode to form the basic building unit of ZIF-8 crystals.

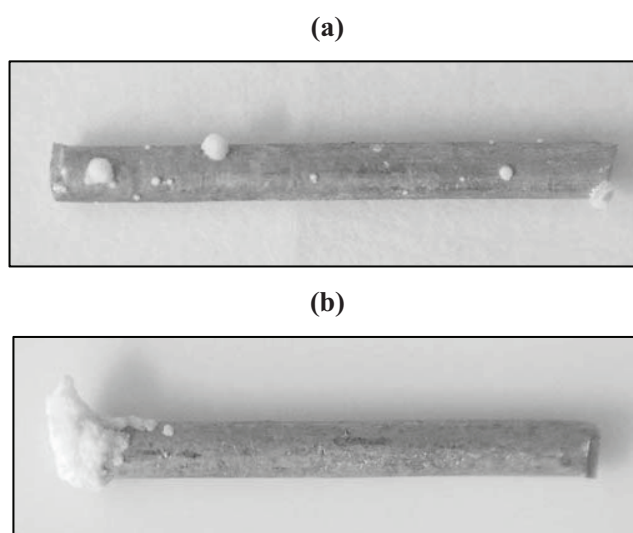


Figure 24. Site-selective modification of a zinc wire with ZIF-8: a) Control experiment without electric field after three days in a solution containing 2-MeIm (1.376 M) and Na_2SO_4 (0.05 M). b) Synthesized by the IBED method (6 V, 60 min, 1.376 M 2-MeIm, 0.05m Na_2SO_4).

The influence of the amplitude of the applied potentials, electrodeposition time and concentration of 2-MeIm on the preparation of ZIF-8 via the IBED technique were investigated as follows.

1.3.1.1 Influence of the applied potential on the synthesis of ZIF-8 via the IBED technique

The SEM images of the ZIF-8 samples prepared via the IBED technique using applied potentials of different amplitude are shown in Figure 25. In contrast to the previous reports where no ZIF-8 deposition occurred onto ‘wired’ Zn anodes (Martinez Joaristi, A. *et al.*, 2012), we clearly observe the formation of ZIF-8 crystals bound to the surface. As a consequence of the polarization of the substrate, the deposition continues at one end of the wire with increasing reaction time, rather than leading to even coverage as observed with the conventional electrochemical systems (Martinez Joaristi, A. *et al.*, 2012). This finding strongly suggests that the electrochemically generated Zn^{2+} ions can migrate through the porous deposits of ZIF-8 and/or the interstices between the crystals to continue the growth at its outer surface. Eventually the linker molecules could also diffuse through the deposit towards the inner interface between zinc and MOF (Li, M. and M. Dinca, 2014), but in a less efficient way than the positively charged Zn^{2+} ions attracted by the feeder cathode.

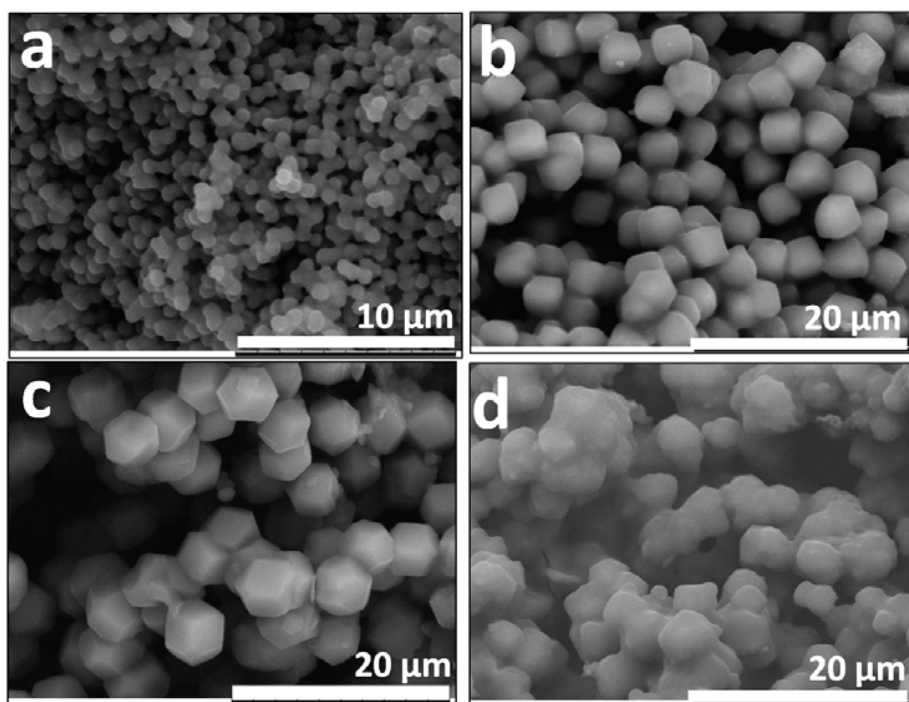


Figure 25. SEM image showing the site-selective modification of a zinc wire with ZIF-8 by the IBED method. The crystals were obtained by using 1.376 M 2-MeIm, 60 min reaction time and different external potential differences of (a) 5 V, (b) 6 V, (c) 7 V, and (d) 8 V.

As shown in Figure 25, the crystal size increases with the increase of the potential difference, at a fixed 2-MeIm concentration. In all cases, rhombic dodecahedral crystals are obtained, and the observed size increase is consistent with the decrease in the 2-MeIm/ Zn^{2+} ratio, as reported for the bulk ZIF-8 synthesis in water in the literature (Kida, K. *et al.*, 2013). Under the optimized synthesis conditions using 6 V of external potential for 60 min (Figure 25b), the obtained ZIF-8 is composed of crystals with a rhombic dodecahedral morphology and uniform size (of $\sim 4\mu\text{m}$), matching well the reported morphology for this zeotype extended network (Cravillon, J. *et al.*, 2009). For the generation of MOF ZIF-8 via the IBED technique, the external electric field applied during the synthesis plays an important role with respect to the MOF crystal size and morphology, under otherwise identical conditions.

However, the crystal morphology becomes less well-defined at too high potentials. For example, at 8 V (see Figure 25d) the particles appear to be fused together. This is probably because of the co-deposition of impurity phases, arising from the low 2-MeIm/ Zn^{2+} ratio (Kida, K. *et al.*, 2013) due to the relatively rapid release of Zn^{2+} at this potential. For such a relative deficiency of ligand, the zinc ions are more likely to form zinc hydroxides (see Figures 26-28). The finding strongly suggests that a close match between the release rate of metal ions that is readily controlled by the applied potential and the MOF nucleation and growth kinetics is required in order to obtain MOFs with well-defined crystals.

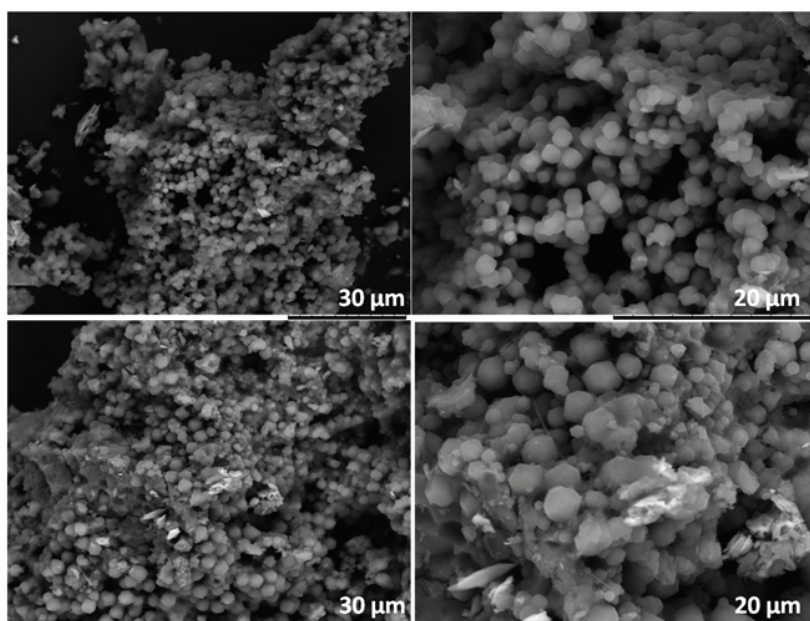


Figure 26. SEM images showing the ZIF-8 structure obtained under unfavorable voltage conditions (of 8 V). Morphologies that can be attributed to the crystal phases other than ZIF-8 are clearly seen.

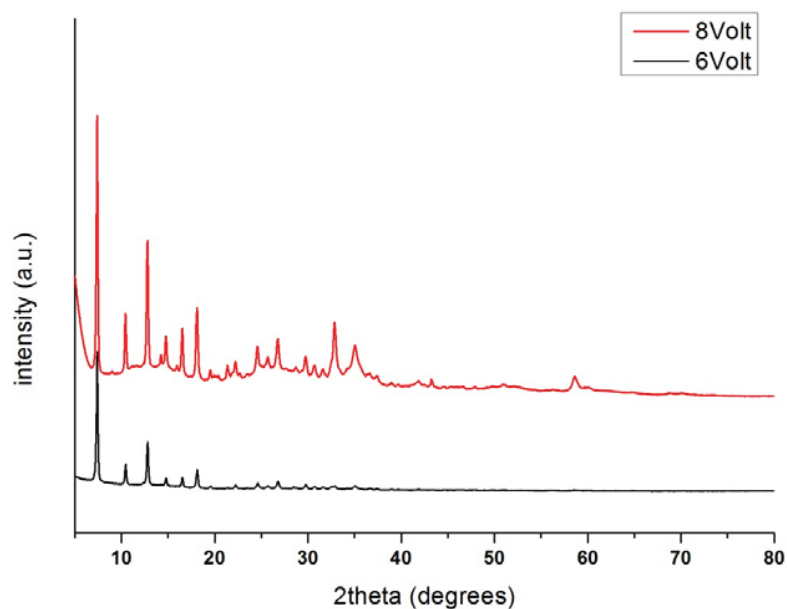


Figure 27. PXRD patterns of ZIF-8 obtained from the IBED synthesis using either 6 V (black line) or 8 V (red line), 1.376 M 2-methylimidazole in ultrapure water containing 0.05 M Na_2SO_4 as supporting electrolyte and 60 min electrodeposition time.

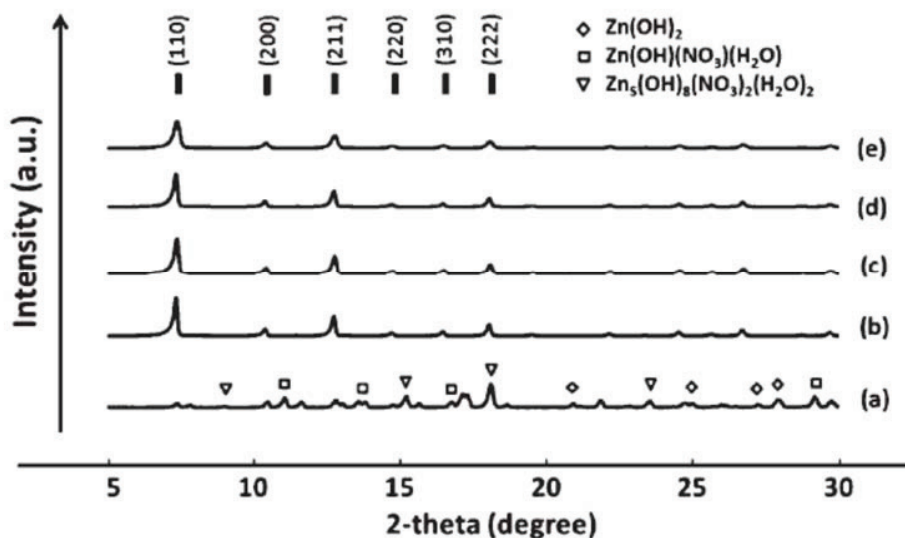


Figure 28. The diffraction patterns of ZIF-8 taken from (Kida, K. *et al.*, 2013), which illustrates in the different impurity phases that can be observed in ZIF-8 prepared at Hmim/Zn molar ratios: (a) 20, (b) 40, (c) 60, (d) 80, and (e) 100.

Figure 29 shows IR spectra of ZIF-8 obtained via bipolar electrochemical technique using different potentials. The IR spectra of ZIF-8 exhibit significant differences as compared to the one of pure 2-methylimidazole. The structure of ZIF-8 can be confirmed when comparing with literature values (Hu, Y. *et al.*, 2011; Hu, Y. *et al.*, 2013). The peak at about 1578 cm^{-1} is attributed to the C=N stretch mode, whereas the band at $1350\text{--}1500\text{ cm}^{-1}$ is associated with the ring stretching. The bands from $900\text{ to }1350\text{ cm}^{-1}$ correspond to the in-plane bending of the ring, while those below 800 cm^{-1} are assigned to the out-of-plane bending. The band at 420 cm^{-1} is very specific for the Zn-N stretching mode in the ZIF-8 structure, and obviously is not present in the case of pure 2-methylimidazole. The resonance of the N-H...N out-of-plane bending and the N-H stretching vibration is found in the case of pure 2-methylimidazole at 1846 cm^{-1} . This signal is not present in the spectra of ZIF-8, thus confirming that the 2-methylimidazole linkers were fully deprotonated during the formation of the ZIF structure.

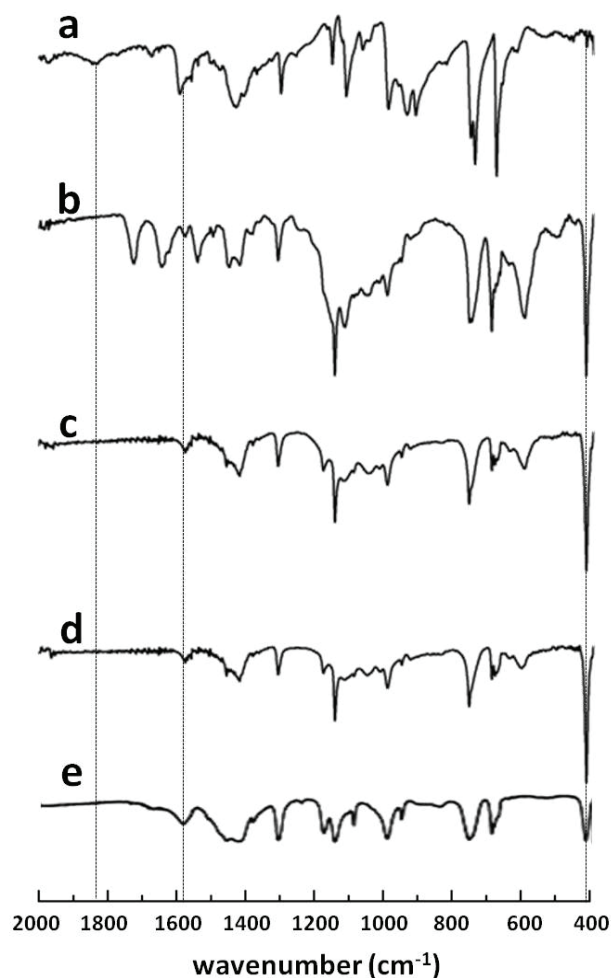


Figure 29. Infrared spectra of (a) pure 2-methylimidazole, (b-d) the IBED-synthesized ZIF-8 by using 1.376 M 2-methylimidazole in ultrapure water containing 0.05 M Na₂SO₄ as supporting electrolyte, 60 min electrodeposition time and applying different potentials ((b) 8 V, (c) 7 V, (d) 6 V), and (e) ZIF-8 from the literature (Du, Y. *et al.*, 2013).

1.3.1.2 Influence of the electrodeposition time on the synthesis of ZIF-8 via the IBED technique

Electrodeposition time also affects the amount and morphology of the products (see Figure 30), and as expected, the amount of products and their crystal size increase and the morphology becomes better defined with the increase of the reaction time. Recent reports based on the in-situ studies of early-stage ZIF-8 growth using SAXS (Cravillon, J. *et al.*, 2011a, 2011b)

and time-resolved static light-scattering (Cravillon, J. *et al.*, 2011c) indicate that the nucleation of ZIF-8 is a slow continuous process, whereas the crystal growth of ZIF-8 is more rapid. However, the growth mechanism of the coordination-based materials under the synthesis conditions presented around the bipolar electrodes is complex (Fattah, Z. *et al.*, 2013), and local effects such as pH and concentration gradients certainly play an important role. Figure 31 shows the IR spectra of ZIF-8 prepared via the IBED technique using different electrodeposition times. The spectra of the ZIF-8 exhibited a significant difference as compared to that of pure 2-methylimidazole. In addition, the structure of ZIF-8 can be confirmed when comparing with the literature (Hu, Y. *et al.*, 2011; Hu, Y. *et al.*, 2013).

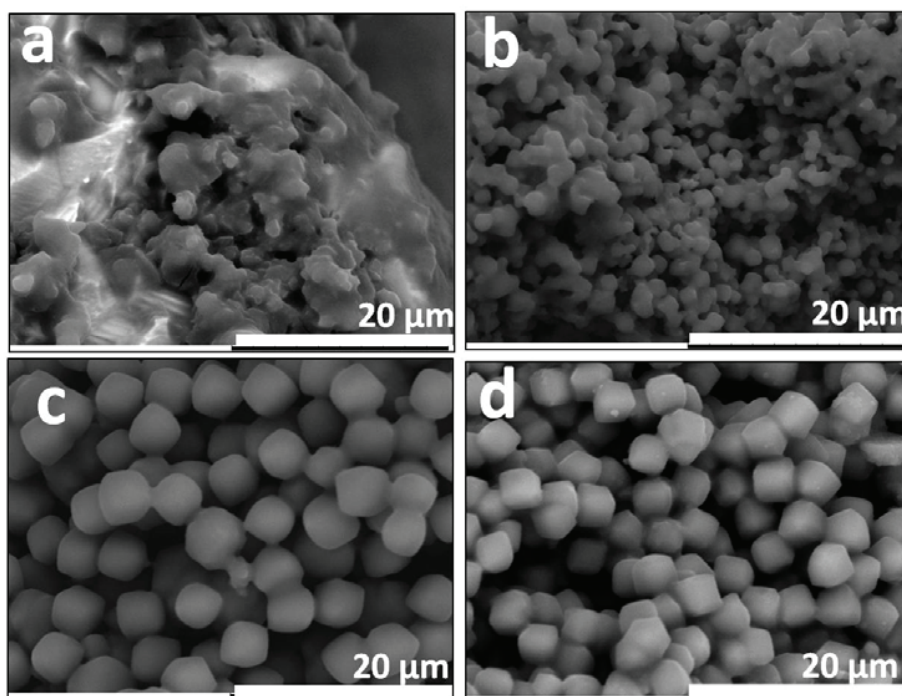


Figure 30. SEM images showing the site-selective modification of a zinc wire with ZIF-8 by the IBED method. The deposits were prepared by using 1.376 M 2-MeIm and 6 V between the external feeder electrodes but different electrodeposition times of: (a) 2 min, (b) 10 min, (c) 30 min, and (d) 60 min.

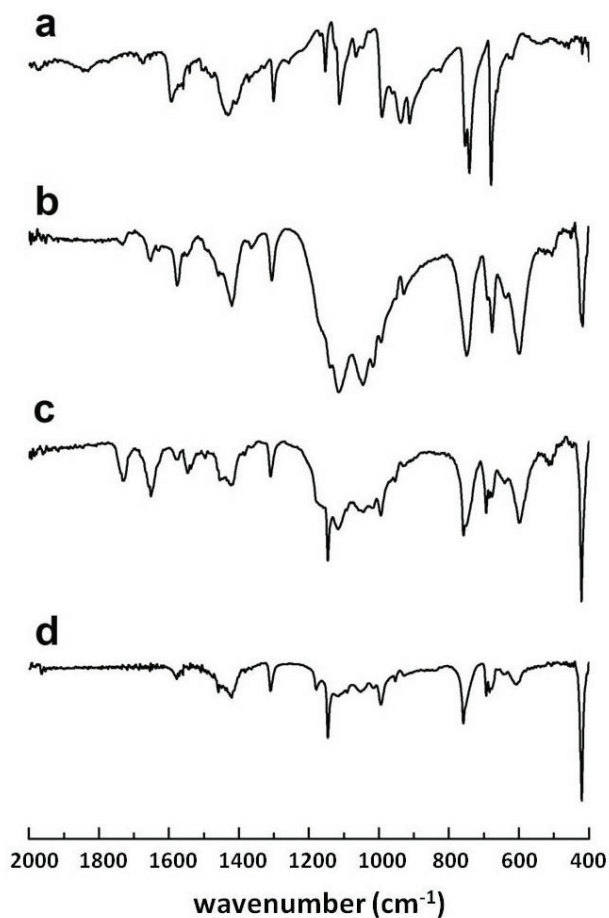


Figure 31. Infrared spectra of (a) pure 2-methylimidazole and (b-d) ZIF-8 prepared via the IBED technique by using 1.376 M 2-MeIm in ultrapure water containing 0.05 M Na₂SO₄ as supporting electrolyte and 6 V between the external feeder electrodes but with different electrodeposition times of: (a) 2 min, (b) 10 min, (c) 30 min, and (d) 60 min

1.3.1.3 Influence of the concentration of organic linker (2-MeIm) on the synthesis of ZIF-8 via the IBED technique

Figure 32 shows SEM images of ZIF-8 prepared with different concentrations of 2-MeIm, but keeping the electrodeposition time and the applied electric field constant at 60 min and 6 V, respectively. Increasing of the 2-MeIm/Zn²⁺ molar ratio also improves the crystal morphology. The highly faceted crystals are obtained at the highest concentrations of 2-MeIm. Under these conditions all the produced Zn²⁺ ions react with the organic linker, and the excess 2-MeIm could potentially act to stabilize and/or control the ZIF-8 crystal growth (Cravillon, J. *et*

al., 2011c). At lower 2-MeIm concentrations, however, the Zn wire is still oxidized at the same rate, but insufficient linker is available to lock all of the metal ions into the extended ZIF structure, leading to the formation of other Zn-containing species, including oxides and/or hydroxides, as previously observed for the aqueous synthesis of bulk ZIF-8 at low 2-MeIm/Zn ratios (Kida, K. *et al.*, 2013). This is an analogous situation to that occurring when high potentials are used as shown in Figure 25d.

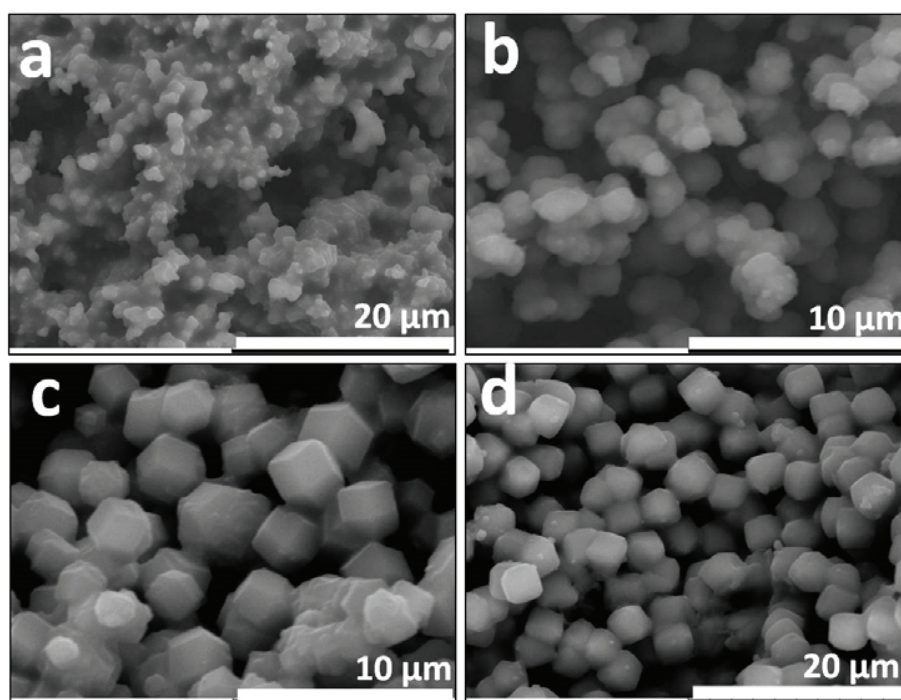


Figure 32. SEM images showing the site-selective modification of a zinc wire with ZIF-8 by the IBED method. The deposits were prepared by using 60 min deposition time and 6 V between the external feeder electrodes but with different concentrations of 2-MeIm of (a) 0.344 M, (b) 0.688 M, (c) 1.032 M and (d) 1.376 M.

The ZIF-8 crystals prepared via the IBED technique using different concentrations of 2-MeIm were characterized by powder X-ray diffraction (PXRD) (see Figure 33) and infrared (IR) spectroscopy (see Figure 34). Figure 33 shows the diffraction peak positions and the relative diffraction intensities of the ZIF-8 products recorded from three samples obtained from the solutions containing different concentrations of 2-MeIm after applying a potential of 6 V for 60

min. The products prepared at high concentrations of 2-MeIm are assigned to sodalite (SOD) network type structures. A typical reflection pattern for the synthesized ZIF-8 corresponding to the (011), (002), (112), (022), (013) and (222) planes was observed. This result is in excellent agreement with the one described in the literature (Venna, S. R. *et al.*, 2010). In addition, the structure of ZIF-8 can be confirmed when comparing with the literature (Hu, Y. *et al.*, 2011; Hu, Y. *et al.*, 2013) (see Figure 34).

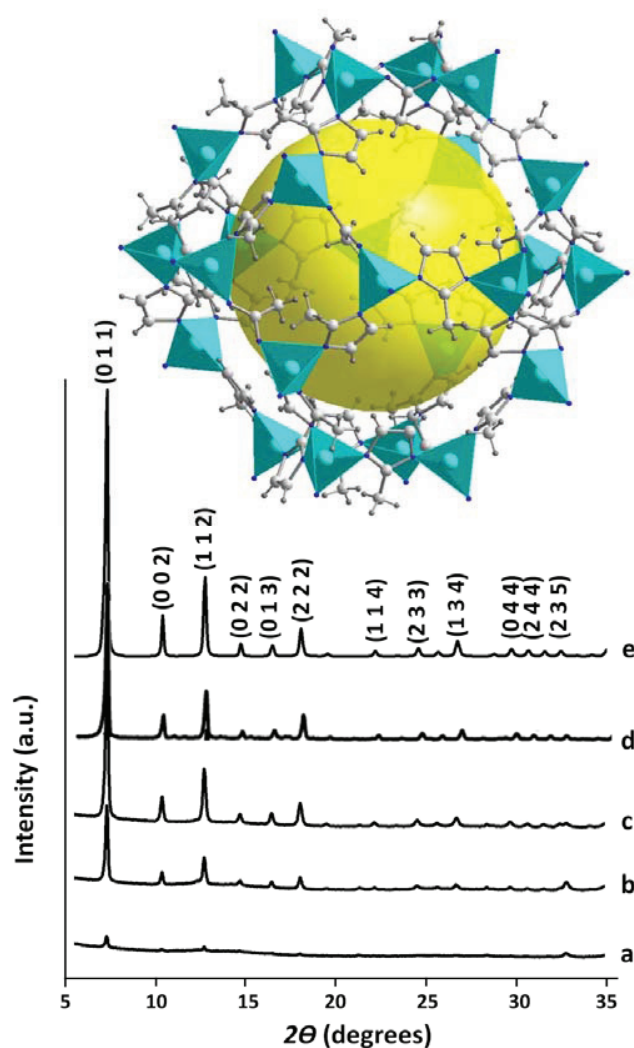


Figure 33. (Top) Structure of the ZIF-8 sodalite cage refined from the powder data of IBED deposited material. (Below) PXRD patterns illustrating the structural evolution of ZIF-8 prepared via the IBED technique when applying an electric field of 6 V for 60 min as a function of the concentration of 2-methylimidazole: (a) 0.688M, (b) 1.032M and (c) 1.376M. (d) XRD

pattern of ZIF-8 from the literature (Venna, S. R. *et al.*, 2010). (e) Simulated XRD pattern of the ZIF-8 powder.

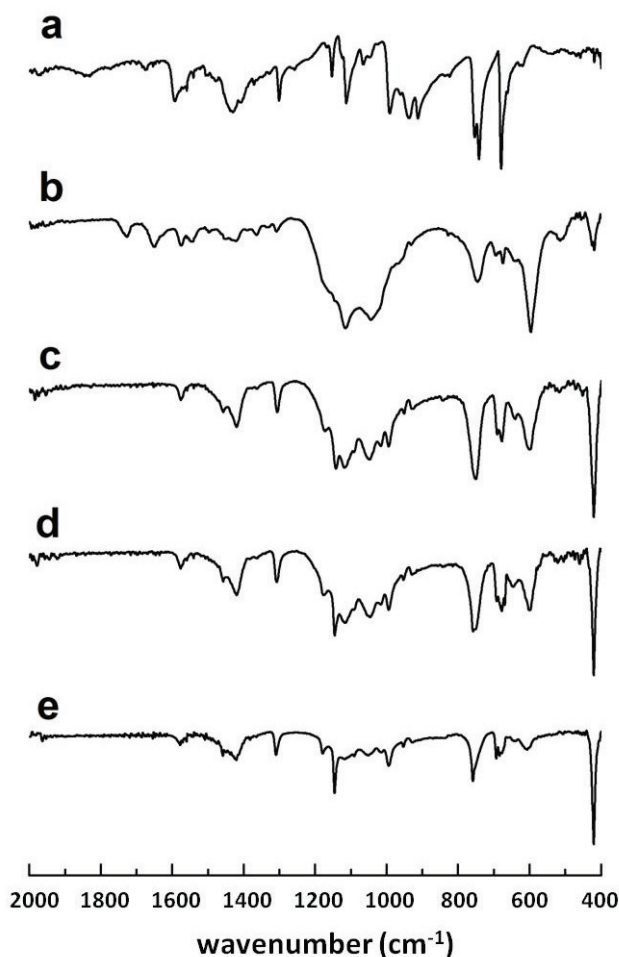


Figure 34. Infrared spectra of (a) pure 2-methylimidazole and (b-d) the IBED-synthesized ZIF-8 by applying a potential of 6 V and using 60 min electrodeposition time in ultrapure water containing 0.05 M Na₂SO₄ as supporting electrolyte with various concentrations of 2-methylimidazole: (b) 0.344 M, (c) 0.688 M, (d) 1.032M, and (e) 1.376 M.

The control experiments that were carried out with a zinc wire attached and electrically connected to the working electrode in a normal three-electrode set-up only result in a homogeneous coverage of the wire with the MOF, but never in a site selective way (see Figure 35). This clearly demonstrates that the proposed approach is unique in terms of the formation of

Janus-type objects. In order to demonstrate that the obtained Janus objects cannot be synthesized by a classic electrochemical approach that means by connecting the object physically to an electrode, the substrate is connected in a classic way to the electrode. Then, it is exposed to the horizontal electric field between the auxiliary and the working electrode. A completely homogenous coverage of the objects with the MOF deposit is obtained except at the very extreme point of contact where the object is glued to the electrode and then the contact is protected by varnish to avoid parasitic electrochemical reactions with the silver glue (see Figure 35).



Figure 35. Photo showing the formation of ZIF-8 on a zinc wire via a classic electrochemical approach under the experimental conditions of 0 V vs Ag/AgCl, 10 min deposition time, 1.376 M 2-MeIm linker solution, and 0.05m Na₂SO₄ supporting electrolyte. (a) Zinc wire glued on gold slide. (b) The wire after removing from the gold slide.

1.3.2 Bipolar electrochemical synthesis of HKUST-1 on copper bead

In order to illustrate the general validity of the IBED concept for the site-selective MOF deposition, we also investigated the formation of HKUST-1. In the current work, an isotropic Cu metal bead was employed as the substrate. The wireless oxidation of copper in ethanol (see Figure 36b) produces the Cu²⁺ ions that are necessary for the local formation of the MOF on one hemisphere only, and thus, leading to a well-defined Janus-type composite particle. The position and extension of the blue crystalline MOF deposits can be readily controlled by the applied external voltage due to the change of polarization (see Figures 36c and 36d). The SEM images of the material deposited on the anodic side of this Janus object (see Figures 37 and 38) show the

familiar octahedral block-like crystals of HKUST-1, further confirming the successful generation of the MOF under these conditions. As the applied potential increases from 10 to 20 V, the crystal size decreases. This finding is in a good agreement with that obtained in the previous study on the electrochemical deposition of HKUST-1 (Ameloot, R. *et al.*, 2009). The deposit has been further characterized by using XRD and FTIR spectroscopy (see Figures 39 and 40).

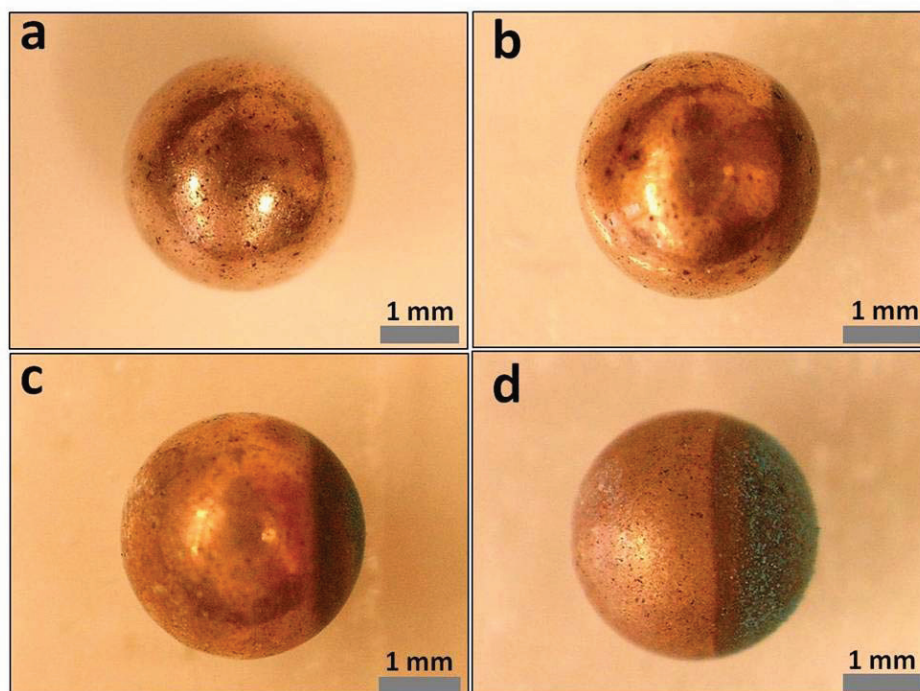


Figure 36. Optical micrographs showing the site-selective modification of a copper bead (3 mm in diameter) with HKUST-1. (a) Bead before modification, (b) after applying an external potential difference of 10 V for 60 min in the absence of 1,3,5-benzenetricarboxylic acid. (c ,d) Bead obtained after the modification by applying (c) 10 and (d) 20 V, respectively in the presence of 0.08 M 1,3,5-benzenetricarboxylic acid in ethanol for 60 min.

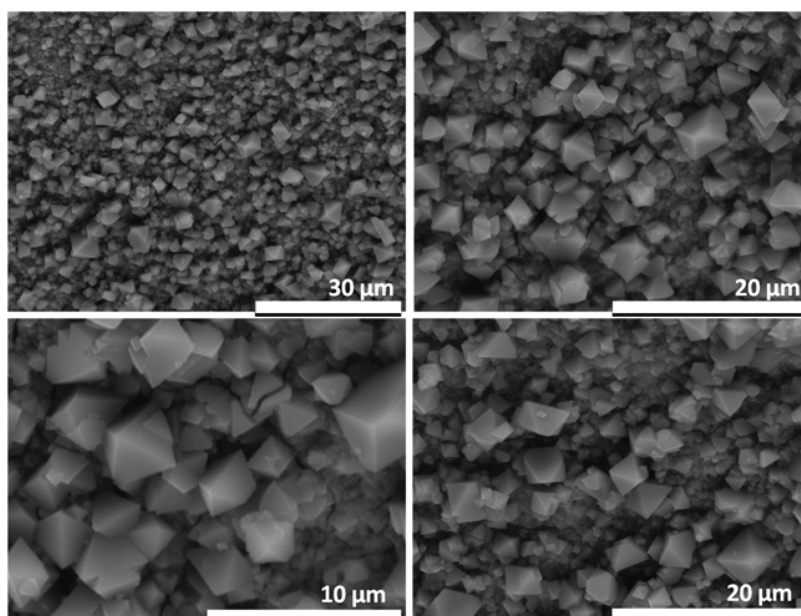


Figure 37. SEM images of HKUST-1 prepared via the IBED technique by applying an external electric potential of 10 V for 60 min in 0.08 M 1,3,5-benzenetricarboxylic acid in ethanol containing 0.05 M MTBS supporting electrolyte.

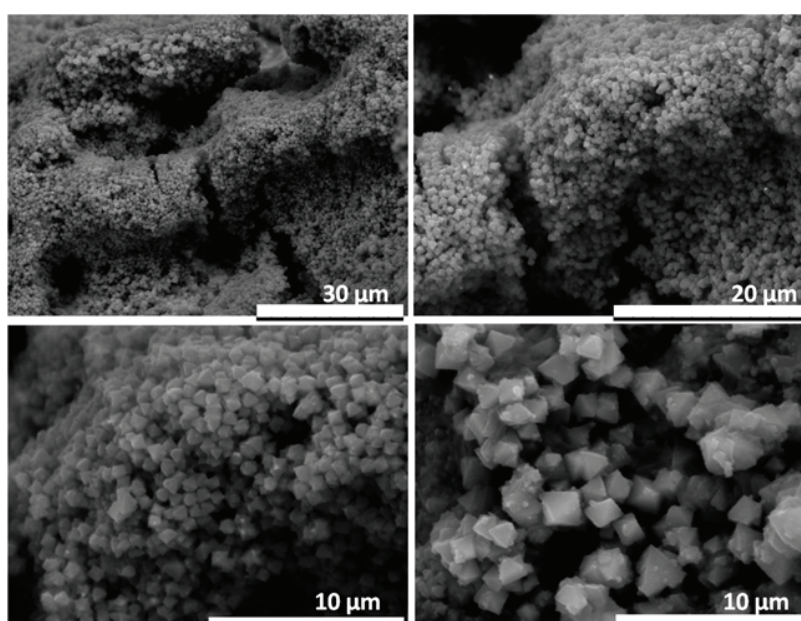


Figure 38. SEM images of HKUST-1 prepared via the IBED technique by applying an external electric potential of 20 V for 60 min in 0.08 M 1,3,5-benzenetricarboxylic acid in ethanol containing 0.05 M MTBS supporting electrolyte.

The HKUST-1 deposits were characterized by powder X-ray diffraction. Figure 39 shows the diffraction peak positions and the relative diffraction intensities of HKUST-1 prepared via the IBED technique by applying an external electric potential of 20 V for 60 min in 0.08 M 1,3,5-benzenetricarboxylic acid in ethanol containing 0.05 M MTBS supporting electrolyte. The PXRD patterns match with those reported in the literature for HKUST-1 (Mao, Y. *et al.*, 2013).

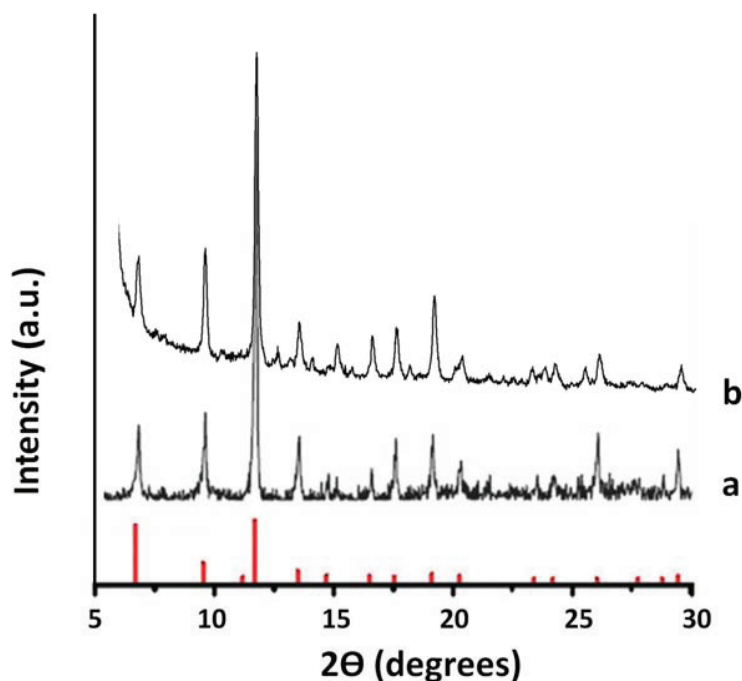


Figure 39. (a) XRD pattern of HKUST-1 taken from the literature (Mao, Y. *et al.*, 2013) (b) PXRD pattern of HKUST-1 prepared via the IBED technique by applying an external electric potential of 20 V for 60 min in 0.08 M 1,3,5-benzenetricarboxylic acid in ethanol containing 0.05 M MTBS supporting electrolyte. The red bars are the standard XRD patterns of HKUST-1.

The HKUST-1 samples were characterized by Infrared spectroscopy. Figure 40 shows the IR spectra of 1,3,5-benzenetricarboxylic acid and the HKUST-1 synthesized by IBED when applying the electric field to a solution of 0.08M 1,3,5-benzenetricarboxylic acid in ethanol containing 0.05M Tributylmethylammonium methyl sulfate for 60 min. The IR spectrum of the HKUST-1 corresponds well to the literature data (Wang, F. *et al.*, 2013; Zybailo, O. *et al.*, 2010). The band in the range of 1560-1440 cm^{-1} can be assigned to the asymmetric stretching vibrations of carboxylate groups. The symmetric vibrations are centered at 1370 cm^{-1} . The peaks

at 730 and 760 cm^{-1} can be assigned to the phenyl group in the HKUST-1 structure. Importantly, the band at 1690-1730 cm^{-1} , that can be assigned to the acidic C=O stretching vibration, present in 1,3,5-benzenetricarboxylic acid, starts to vanish after complexation with Cu^{2+} , suggesting that deprotonation has occurred.

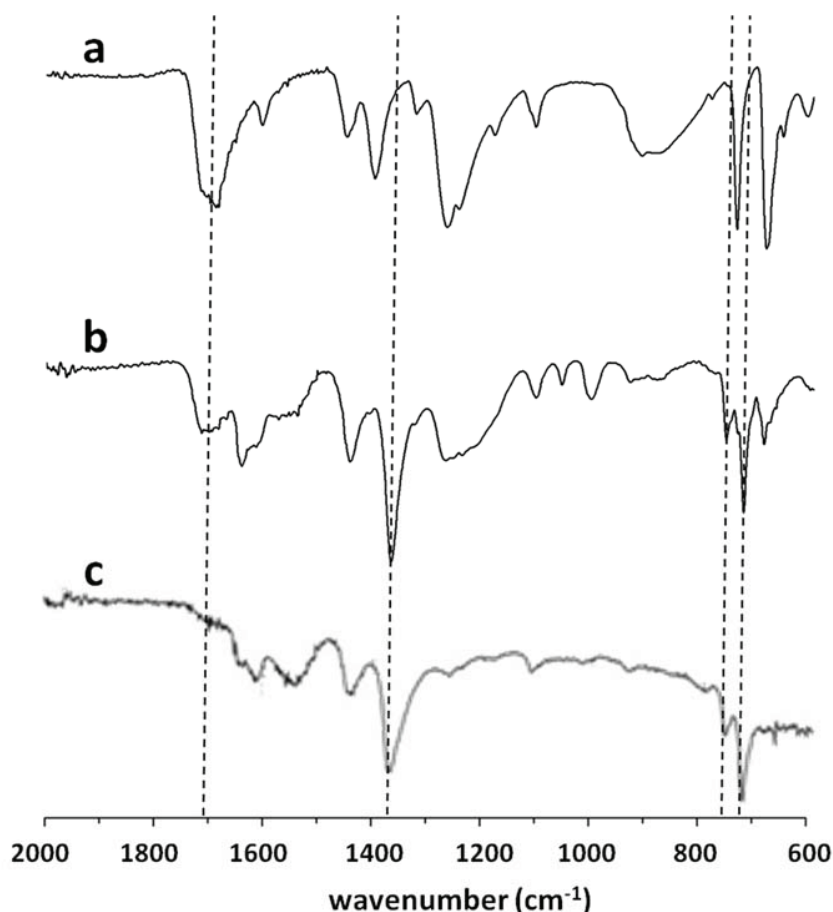


Figure 40. Infrared spectra of (a) pure-1,3,5-benzenetricarboxylic acid (b) HKUST-1 prepared via the IBED technique by applying an external electric potential of 20 V for 60 min in 0.08 M 1,3,5-benzenetricarboxylic acid in ethanol containing 0.05 M MTBS supporting electrolyte and (c) HKUST-1 is taken from the literature (Jeremias, F. *et al.*, 2012).

Control experiments with a copper bead immersed in the ligand solution without applying an electric field do not result in the formation of HKUST-1 even after three days (see Figure 41). Only some corrosion of the copper bead is visible but there is no deposition of MOF whereas in

the bipolar electrochemical experiment a highly asymmetric deposit is already visible after 60 min.



Figure 41. Optical micrographs for the Cu beads obtained from the control experiments (without applying any electric field) performed in 0.08 M 1,3,5-benzenetricarboxylic acid in ethanol containing 0.05 M tributylmethyammonium methyl sulfate as supporting electrolyte for (a) 1 h and (b) 3 days.

Furthermore, attaching the bead to the working electrode of a three-electrode set-up leads to a homogeneous and complete MOF coverage (see Figure 42), indicating that the bipolar set-up is absolutely crucial to produce the asymmetric composite particles. The electrochemical oxidation of the copper bead occurs everywhere on its surface in a homogeneous way. Therefore, the HKUST-1 is formed everywhere. This situation is completely different from the case with the bipolar electrochemical set-up where the substrate experiences a potential gradient along the electric field lines with respect to the surrounding solution. Therefore, from a thermodynamic point of view, MOF can only be formed in certain areas where the polarization is above a critical threshold value, and thus, leading to Janus particles.

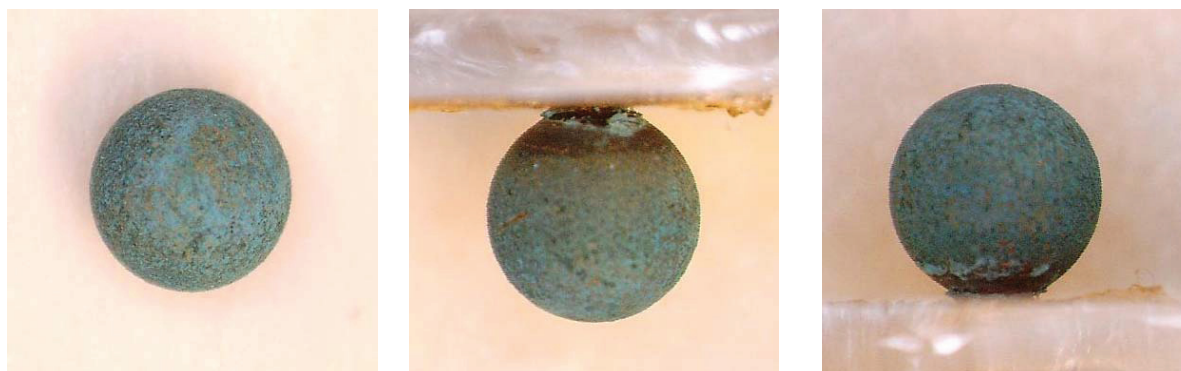


Figure 42. Optical images of HKUST-1 prepared on copper beads by a classic electrochemical approach (using 1.5 V vs Ag/AgCl, 60 min deposition time, 0.08M of 1,3,5-benzenetricarboxylic acid solution and 0.05M of tributylmethylammonium methyl sulfate electrolyte) (a) top-view, (b) on the right side and (c) on the left side.

1.4 Conclusions

In summary, we report here for the first time the straightforward and site selective synthesis of MOF compounds by indirect bipolar electrochemistry with two representative proof-of-principle experiments for the asymmetric generation of MOFs on the surface of isotropic and anisotropic substrates. Infrared spectroscopy, XRD and SEM characterizations of the obtained compounds confirm the successful synthesis for which the crystal size and morphology can be tuned in a facile manner through the modulation of linker concentration, electrodeposition time and the amplitude of the external electric field. This concept might be generalized for the synthesis of many other MOF compounds, thus allowing a cheap and green access to this important family of microporous materials and leading to new generations of MOF-based Janus-type composites with applications in catalysis, separation, storage and sensing.

2. Fabrication of Hierarchical Macroporous Electrodes of HKUST-1 via an Electrochemical-Dissolution-Deposition technique

2.1 Introduction

As MOFs are mainly composed of the micropores and form large crystals, there are limitations in the diffusion of i) bulky molecules with dimensions larger than the micropore dimension that cannot adsorb and perform any reactions within the MOF structure and ii) molecules with dimensions smaller than the micropore dimension that may be only slowly diffusing through the pores of MOF. These diffusion limitations prevent using MOFs for some applications. Although, some MOFs have mesoporous cages within their structure, however, the large cavities are accessed via much smaller apertures of the micropores. This limits the size of molecules that can diffuse through the MOF structure.

Until recently, various synthetic strategies have been employed to create MOFs with an increased pore size. However, there are still some limitations for each technique. For example, the strategy using organic linkers with a designed long chain length to create large voids is limited by the fact that the created MOFs show frequently framework breakdown. For this reason, the development of new strategies that are efficient to synthesize meso-/macroporous MOFs providing an improved mass transport of the molecules that can diffuse into the MOF crystal through the large pores (macropores and mesopores) to the small pores (micropores) remains a great challenge. In addition, the preparation of MOF nanocrystals with the aim to reduce the diffusion path length is of great interest. These developed approaches could open up MOFs for various applications including catalysis, separation and sensor. The synthesis methods that are mainly employed to generate meso- and macroporous MOFs are template-assisted methods. Both soft templates (surfactants) and hard templates (metal oxide and polystyrene) have been used. In the surfactant-assisted synthesis, the surfactant molecules (cationic, anionic, or non-ionic surfactants) first self-assemble into micelles, and then, the micelles act as templates for the formation of mesoporous MOFs. In the case of hard templates, the polymerization or cross-linking of the precursors at the interface causes phase separation. A continuous ordered template replica of the meso-macroporous MOF is formed.

Qiu and coworkers first designed and prepared a mesoporous MOF, HKUST-1, by using a supramolecular template, cetyltrimethylammonium bromide (CTAB) cationic surfactant (Qiu,

L.-G. *et al.*, 2008b). A hierarchical porous HKUST-1 was successfully prepared with controllable porosity derived from the CTAB micelles via a standard solvothermal synthesis. The obtained HKUST-1 has mesopores with an average diameter of 5.6 nm. The specific surface area due to the mesopores of the obtained HKUST-1 increases with the increase of the molar ratio of CTAB/metal (Cu^{2+}) ion in the synthesis solution. The addition of swelling agents such as 1,3,5-trimethylbenzene (TMB) could increase the mesopore size of the obtained materials (from 5.6 to 31.0 nm at the CTAB/TMB ratio of 0.5). Besides, hierarchically porous MIL-101 was prepared by the same research group using the same template system (CTAB/TMB) (Huang, X.-X. *et al.*, 2012).

Wee and coworkers prepared HKUST-1 with wide permanent mesopores, known as COK-15, by using a keggin-type phosphotungstate (HPW) anion alongside the cationic CTAB act as structure directing agent (SDA) (Wee, L. H. *et al.*, 2012). The synthesis was based on the concept that the Keggin ions act as molecular template for the MOF structure while the CTAB molecules direct the mesoporous structure. The hierarchically porous COK-15 exhibits excellent catalytic activity with 100% conversion of styrene oxide and 100% selectivity for 2-methoxy-2-phenylethanol in the methanolysis of styrene oxide under mild experimental conditions while the reference materials, HKUST-1 and HKUST-1 with incorporated Keggin ions, provide only 2 and 40% conversion of styrene oxide, respectively.

Anionic surfactants such as dodecanoic acid (DDA) and 4-(dodecyloxy) benzoic acid have been used for the preparation of mesoporous MOFs. (Bradshaw, D. *et al.*, 2014) Kitagawa and co-workers used DDA as the coordination modulator to control the size of HKUST-1 crystals that can be tuned from nanometers to micrometers. They found that the DDA molecules essentially bind to the metal ions controlling the nucleation rate of the MOF framework. Nucleation occurred very fast, and thus, small crystals formed and further aggregated, resulting in materials with a hierarchically porous phase with inter-particle mesoporosity. The hierarchically MOF-5 materials with sponge- and pomegranate-like meso- and macropores (with sizes ranging from 10 to 100 nm) were prepared by Choi and coworkers using 4-(dodecyloxy)benzoic acid (DBA) with controlled amounts of DBA (Choi, K. M. *et al.*, 2011) having i) a carboxyl functionality that binds to the Zn^{2+} ions, which is required for the MOF formation and ii) an alkyl chain for creating the cavities in the MOF structure. The macroporous

MOF-5 was obtained for equimolar amounts of DBA and the organic ligand, and microporous MOF-5 was obtained when the amount of DBA was reduced to 30%.

Non-ionic templates including block copolymers and neutral surfactant molecules have also been used for the preparation of hierarchically porous MOF materials Wan, Y. *et al.*, 2007. Pham and coworkers reported the synthesis of a new family of bimodal micro-mesoporous MOF nanocrystals via the coassembly of nanosized MOF building blocks with a nonionic triblock copolymer surfactant, F127 (EO₉₇PO₆₉EO₉₇), in the presence of acetic acid (Pham, M.-H. *et al.*, 2011b). F127 acts as template while the acetic acid controls the rate of the framework crystallization. This combination was also used by the same group to prepare a MOF, namely Fe-MIL-88B-NH₂ (Pham, M.-H. *et al.*, 2011a). Peng and coworker used N-ethyl perfluorooctylsulfonamide (N-EtFOSA), a non-ionic surfactant, to synthesize mesoporous HKUST-1 nanoplates in an ionic liquid solution (Peng, L. *et al.*, 2012). They proposed that the surfactant molecules play two roles in the assembly process. First of all, they stabilize the MOF building blocks, and lead to the formation of the mesopores within the MOF structure. Second, they adsorb on some crystal planes of the MOF and thus control kinetically the rate of framework extension, and therefore, the crystal growth in the form of platelets.

Wu and coworkers reported a new scheme for the fabrication of HKUST-1-based films with an ordered macroporous structure by using polystyrene (PS) as the template (Wu, Y.-n. *et al.*, 2011). The macroporous MOF was prepared in three steps. The first step is the fabrication of the polystyrene (PS) opal template. The second step is the infiltration of the colloidal crystal template with the MOF precursor solution, followed by the solvent evaporation to crystallize the MOF. The final step is the dissolution of the PS template to provide the 3D-ordered macroporous MOF. Apart from PS, metal oxide was also used as a template and metal source. The MOF material was obtained via the direct reaction between the metal and the organic ligand. Reboul and coworkers utilized aluminium oxide as the template to prepare a mesoscopic architecture of an aluminium dicarboxylate framework (Reboul, J. *et al.*, 2012). The alumina inverse opals were converted into MOF replicas via the direct reaction with the organic ligand under microwave irradiation. The resulting MOF materials were grown in the inverse opal architectures with 10-200 nm cubic crystals.

Herein, we report the fabrication of hierarchically macro-/microporous HKUST-1 via an electrochemical dissolution-deposition technique (see Figure 43). In the first step, silica particles

with a diameter of about 1 μm were prepared. Then, a colloidal crystal of the obtained silica particles was fabricated on a gold electrode by the Langmuir–Blodgett (LB) technique. In a second step, the voids of the template were filled with copper (Cu) with controlled numbers of porous layers via an electrochemical deposition. After that, the silica template was removed to provide the 3D ordered macroporous Cu electrode with the inverse opal structure. In the final step, the Cu surface was transformed into HKUST-1 via the electrochemical dissolution of Cu in the presence of the organic ligands leading to the crystallization of the MOF.

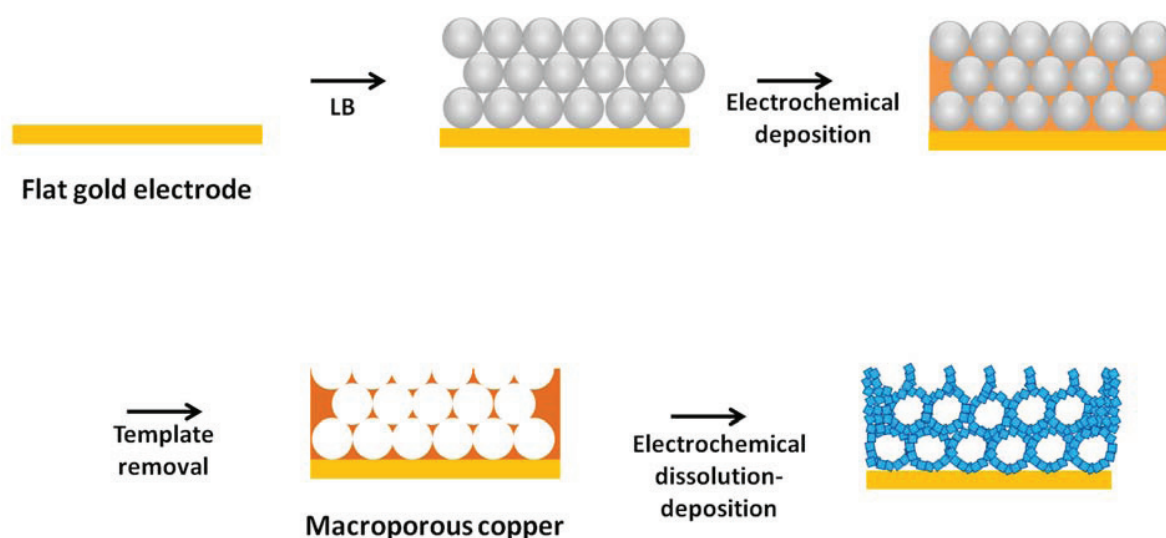


Figure 43. Schematic illustration showing the experimental steps for the fabrication of the hierarchical macro-/microporous HKUST-1 of this work.

2.2 Experimental section

2.2.1 Preparation of silica colloidal template

The synthesis of silica particles with monodisperse size distribution was reported for the first time by Fink and Stöber in 1968 (Stöber, W. *et al.*, 1968). They found that the hydrolysis and polycondensation of siloxane precursors such as tetraethyl orthosilicate (TEOS) (often used) in an alcoholic solution under basic conditions results in the formation of silica particles with a very narrow size distribution. By varying the synthesis conditions, particles with various average sizes can be prepared (Giesche, H., 1994; Tan, C. G. *et al.*, 1987). In this work, a colloidal

solution of the silica particles with an average diameter of $\sim 1\ \mu\text{m}$ and a monodisperse particle size distribution was prepared according to the batch or semi-continuous Stöber sol-gel process. TEOS and a 25% NH_3 solution were used as the silica source and the catalyst, respectively. A mixture of water (Millipore water) and ethanol (EtOH) was used as the solvent. Before coating the silica particles onto the gold substrate (Au-coated glass slide) via the Langmuir-Blodgett (LB) trough technique, the particles were functionalized with aminopropyltriethoxysilane (APTES) to create the NH_2 -terminated alkyl chains on the particles (see Figure 44). This functionalization is very important in order to improve the hydrophobicity of the particles, and providing stable Langmuir films of the particles.

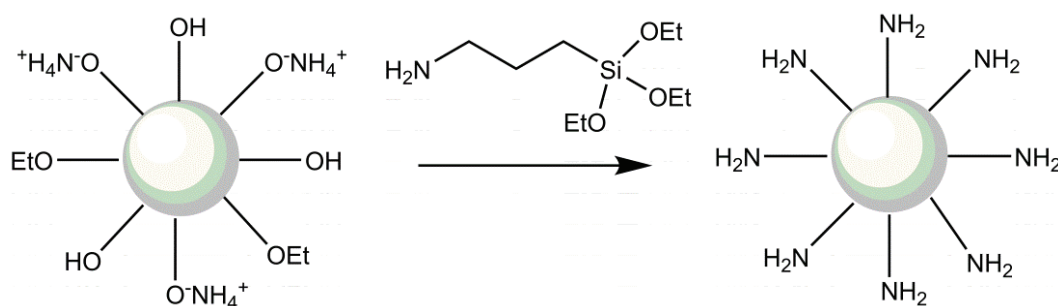


Figure 44. Schematic illustration showing the functionalization with APTES of the surface of silica spheres prepared via the modified Stöber sol-gel process employed in this work.

2.2.2 Preparation of the surface of the gold slide.

Au-coated glass slides were cut into small pieces and then treated twice in a piranha solution (a mixture containing concentrated sulfuric acid and hydrogen peroxide at the volume ratio of $\text{H}_2\text{SO}_4:\text{H}_2\text{O}_2$ 3:1 ($\text{H}_2\text{SO}_4 = 15\ \text{ml}$ and $\text{H}_2\text{O}_2 = 5\ \text{ml}$) for 15 min, to remove organic contaminants. The slides were then washed three times with water. They were further divided into two parts. The first part was used for the Langmuir-Blodgett (LB) experiment without any modification. The second part was soaked with 10 mM cysteamine (Cys) in absolute EtOH overnight to improve the hydrophilicity of the gold surface through the formation of self-assembled monolayer (SAM) of Cys, and allowing a good attachment of the silica spheres on the Au surface, and used for the LB experiment (see Figure 45). The results obtained from both parts are discussed and compared in the results and discussion section.

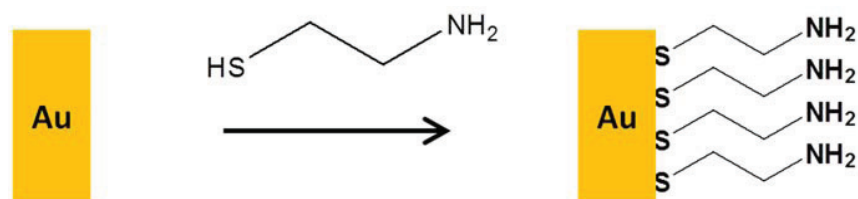


Figure 45. Schematic illustration showing the functionalization with cysteamine of the surface of the gold slides employed in this work to improve the hydrophilicity of the gold surface, and leading to a good attachment of the silica spheres onto the Au surface.

2.2.3 Fabrication of silica colloidal crystals by the Langmuir-Blodgett (LB) trough technique

A LB trough (NIMA Technology, model 622) equipped with two symmetrically barriers was used (see Figure 46). Prior to the experiment, the reservoir, barriers and dipping well of the instrument were cleaned with analytical grade chloroform (CHCl_3) for several times. Ultrapure water (resistivity $\geq 18 \text{ M}\Omega\cdot\text{cm}$) was filled into the reservoir. A certain amount of the functionalized silica beads was isolated from the synthesis solution and washed several times with absolute ethanol to remove the residues. The washed beads were redispersed in a solution of chloroform-ethanol 80-20 v/v. The obtained suspension was spread at the air-water interface drop by drop. After the solvent evaporation (chloroform and ethanol), the barriers were closed with a controlled slow rate. As a result, the silica particle layer was compressed forming a Langmuir film (see Figure 47). Along with this compression, surface pressure-area isotherms were observed. The compression was stopped when the surface pressure increased and reached the target pressure of 4 mN/m. The prepared slides were attached to the dipper well by using removable and re-usable glue pads and then dipped through the Langmuir film of silica with a controlled fast rate of 63 mm/min. Then, the slides were pulled up through the film with a controlled slow rate of 1 mm/min. During the dipping-raising process, the surface pressure was kept constant at 4 mN/m. During the raising step, a single silica layer was transferred to the surface of Au slides. The dipping-raising process was repeated until the desired numbers of layer of silica beads was obtained.

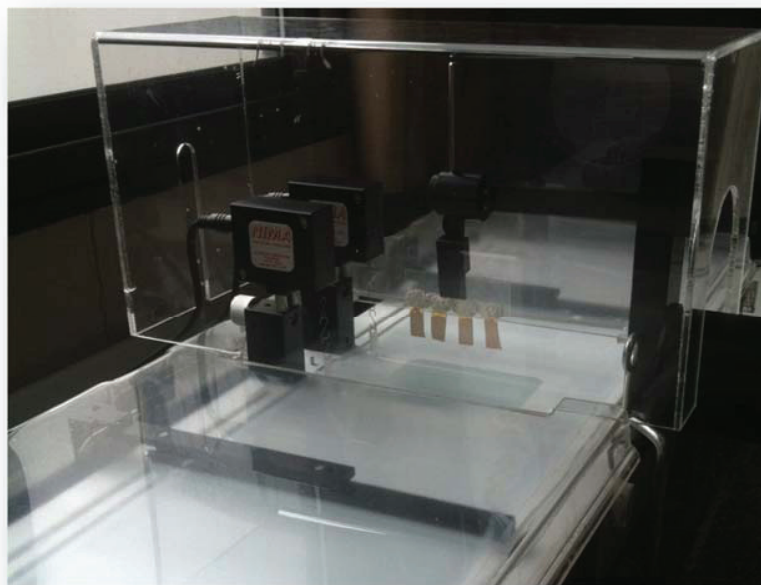


Figure 46. Photo showing the side view of the LB trough instrument used in this work (NIMA Technology, model 622).

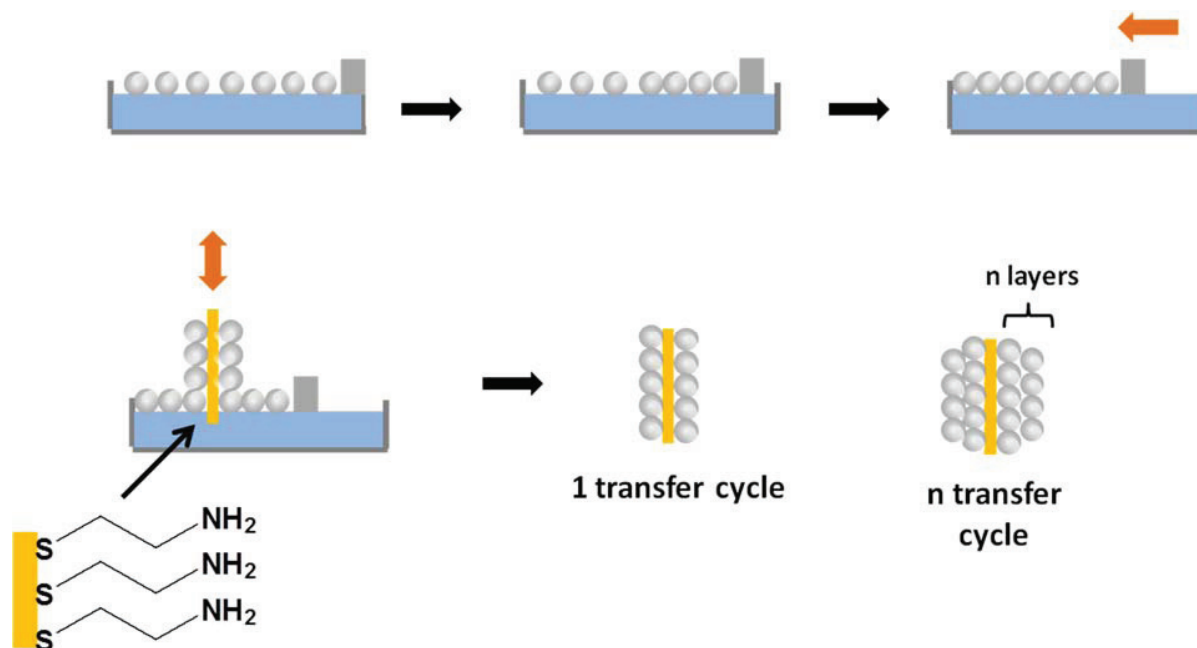


Figure 47. Schematic illustration showing the steps involved in the Langmuir-Blodgett experiment including the generation of a Langmuir film of silica spheres and the dipping-raising process to transfer the silica bead layer to the surface of a gold slide.

2.2.4 Fabrication of 3D ordered macroporous Cu electrode

The voids of the silica colloidal template were filled with Cu via electrochemical deposition (see Figure 48). The Au slide coated with the silica colloidal template was used as the working electrode in a 3-electrode cell. A Platinum mesh and a silver-silver chloride electrode (Ag/AgCl, sat. KCl) were used as the counter and reference electrodes, respectively. The electrodes were connected to a potentiostat/galvanostat instrument (μ -Autolab Type III equipped with the GPES software). The electrochemical deposition of copper was performed at a desired applied voltage and deposition time by using a commercial copper plating bath (CUBRAC 660) as the copper source. After the deposition, the Cu-coated slides were washed with ultrapure water and dried with air. Then, they were immersed into a 5% HF solution to remove the silica beads, resulting in a 3D ordered macroporous Cu electrodes.

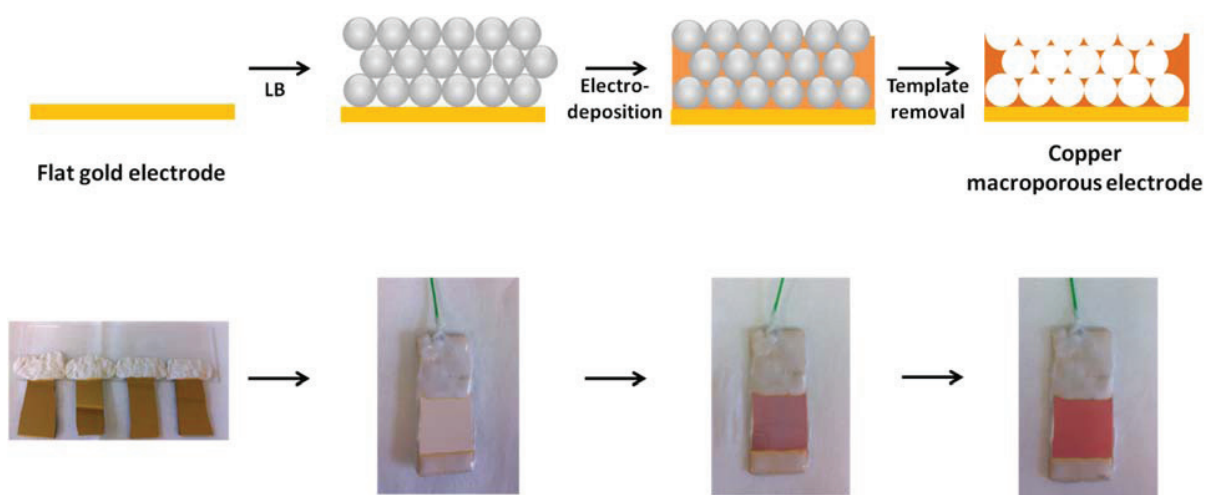


Figure 48. Schematic illustration showing the steps for the fabrication of the macroporous copper electrode.

2.2.5 Transformation of ordered macroporous Cu electrodes into HKUST-1

The transformation of the 3D ordered macroporous Cu electrodes into HKUST-1 was performed via the electrochemical dissolution of Cu in the presence of the organic ligand. A 3D ordered macroporous Cu electrode was used as the working electrode. Prior to each experiment, the electrode was pretreated for 15 min in 10% sulfuric acid solution to remove the copper oxide contamination that may occur via the air oxidation of the Cu surface. An Ag electrode and a

platinum mesh were used as pseudo reference and counter electrodes, respectively. All experiments were performed in a home-built electrochemical cell (see Figure 49) composed of a centered inner reaction compartment and two outer reaction compartments. These compartments are separated by two Nafion membranes. The objective of the use of the cells with the separated compartments is to prevent the polymerization of 1,3,5-benzenetricarboxylic acid (the organic ligand) causing an important loss of linker from the working solution and, perhaps, disturbing the reaction occurring at the working electrode. The inner cell compartment was filled with a solution of 1,3,5-benzenetricarboxylic acid in ethanol containing tributylmethylammonium methyl sulfate (MTBS) supporting electrolyte and the outer cell compartments were filled with a solution of MTBS supporting electrolyte in ethanol.

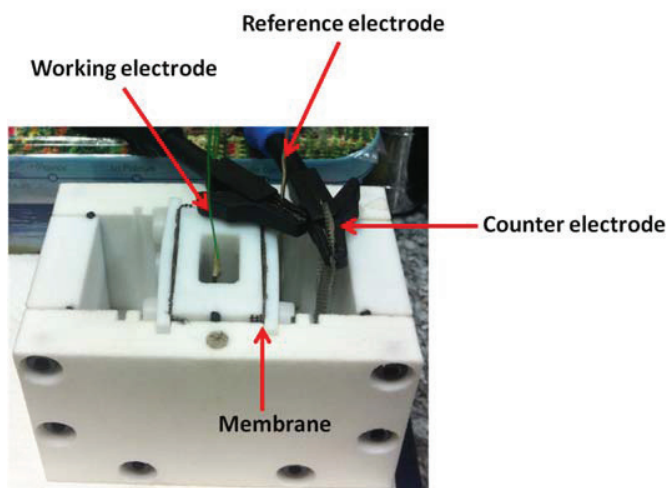


Figure 49. Photograph showing the experimental set up for the transformation of the Cu surface of the 3D ordered macroporous Cu electrodes into HKUST-1 via the electrochemical dissolution of Cu in the presence of the organic ligand.

2.2.6 Characterizations

The characteristics of the obtained materials were analyzed by FT-IR, FE-SEM and EDS analyses. The FT-IR spectra of the samples were recorded by using a TENSOR 27 (Bruker) FT-IR spectrometer (with KBr pellets) in the range $400\text{--}4000\text{ cm}^{-1}$ with a resolution of 4 cm^{-1} . The SEM images were taken with a HITACHI S4700 Field Emission scanning electron microscope

and HITACHI, TM-1000 scanning electron microscope equipped with an EDS2006 model 550i analyzer.

2.3 Results and discussion

Figures 50a-b show the SEM images of the as-prepared silica beads. The image shows that the particles have spherical shape and their size is quite uniform. Figure 50c shows the corresponded particle size distribution (PSD) suggesting a monodisperse and narrow PSD. The average diameter of the silica spheres is $1.029 \pm 0.045 \mu\text{m}$. The results indicate the successful preparation of the $1 \mu\text{m}$ -silica spheres with monodisperse and narrow PSD via the Stöber method.

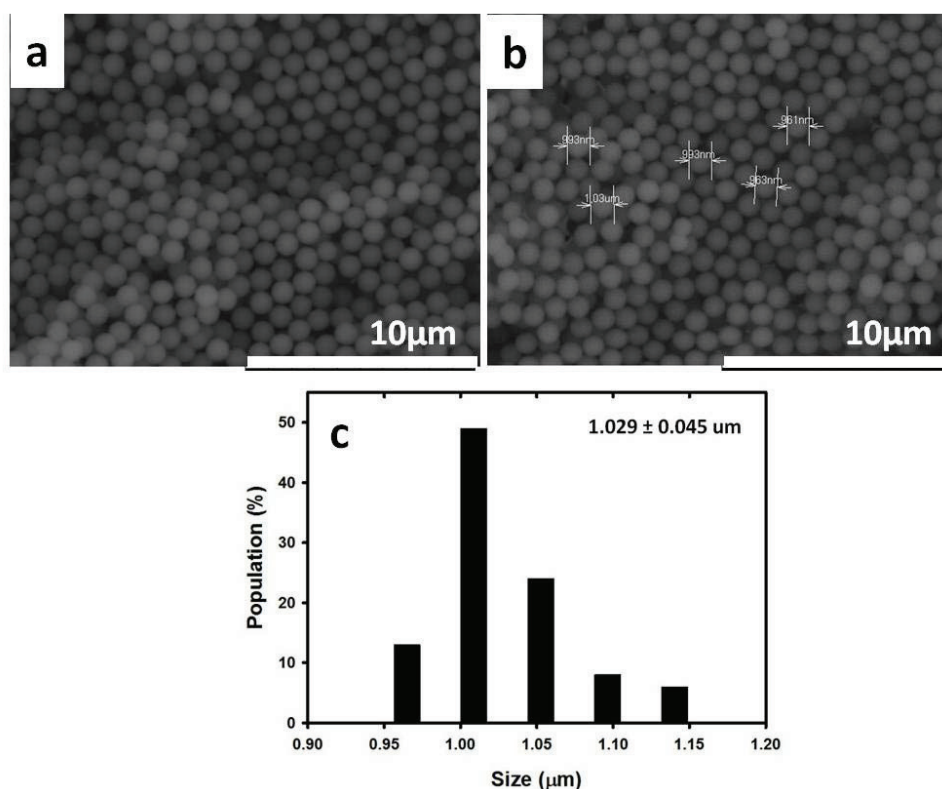


Figure 50. (a-b) SEM images and (c) the corresponded particle size distribution of the silica spheres prepared in this study according to the Stöber method.

Layers of the obtain silica spheres were transferred to the surface of Au-coated glass slide via the LB technique. In this process, the silica particle layer was compressed forming a Langmuir film. During the compression, the degree of the film compression was tuned by

controlling the surface pressure of the water as a function of film area or area per molecule. Figure 51 shows the surface pressure-area isotherms obtained during the compression of the film of 1 μm -silica particles. The compression was continued until the surface pressure reached the target pressure of 4 mN/m. Three distinct states can be distinguished from the isotherms corresponding to three different states of matter including solid, liquid and gas. 7 layers of the Langmuir film of silica spheres were transferred to the slides at a constant surface pressure of 4 mN/m (see Figure 51b). The photos of the substrates obtained before and after the deposition of silica spheres are shown in Figure 52. From the images, it is obvious that the silica spheres were transferred to the slide with a smooth and uniform surface.

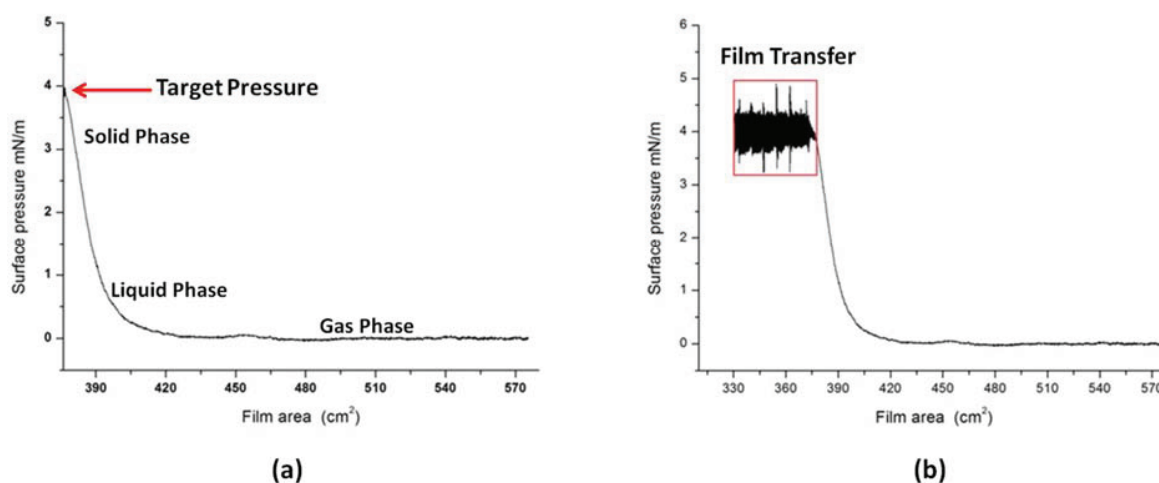
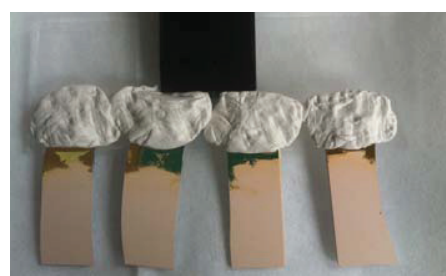


Figure 51. Surface pressure-area isotherms obtained during a) the compression of the film of 1 μm -silica particles until the surface pressure reached the target pressure of 4 mN/m and b) the deposition of 7 layers of the Langmuir film of silica spheres onto gold-coated glass slides at a constant surface pressure of 4 mN/m.



(a)



(b)

Figure 52. Photos of the gold-coated glass slides (a) before and (b) after the deposition of 7 layers of the silica spheres via the LB technique.

After the particle assembling process, the voids of the silica colloidal template were filled with Cu via electrochemical deposition. Before the deposition, a suitable potential was chosen by cyclic voltammetry. Figure 53 shows the cyclic voltammogram of the Cu plating bath (CUBRAC 660) with a flat Au-coated glass slide as working electrode. The voltammogram was recorded at a scan rate of 100 mV/s and at room temperature in the potential range of -1.00 to 0.50 V. The onset potential for the reduction of the copper ions was found to be +0.07 V corresponding to the reduction of Cu^{2+} to Cu^0 . The maximum peak potential is at -0.47 V. From the findings, we concluded that a potential in the range of 0.00 V to -0.47 V should be suitable for Cu deposition.

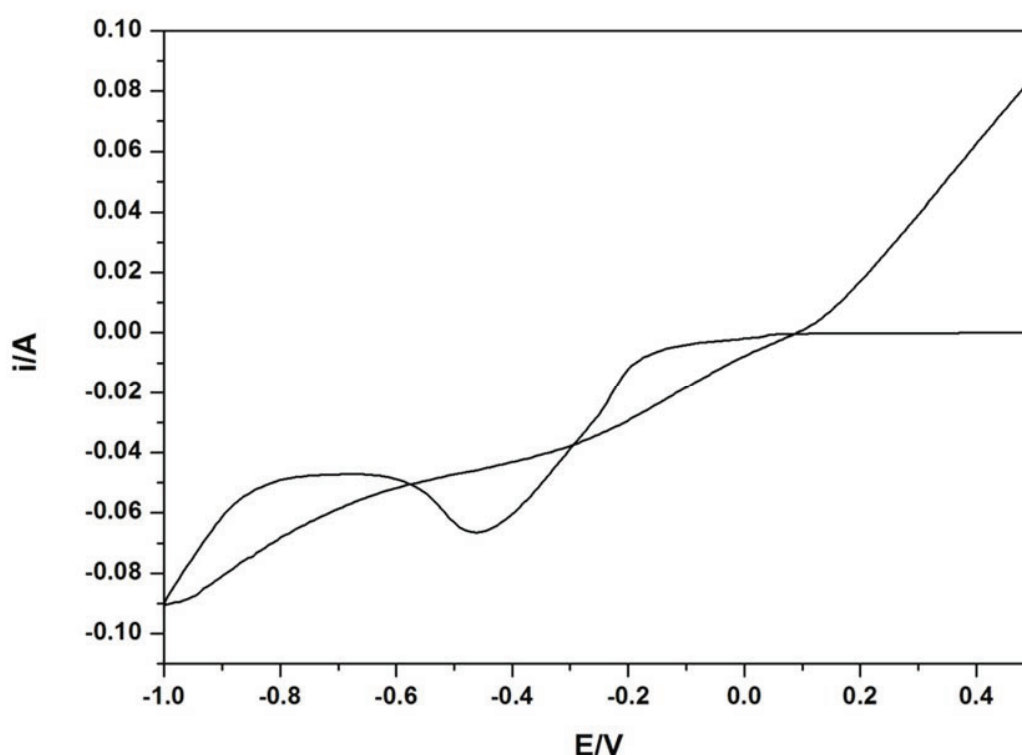


Figure 53. Cyclic voltammogram of the Cu plating bath (CUBRAC 660) with a flat Au-coated glass slide as working electrode recorded at a scan rate of 100 mV/s and at room temperature in the potential range of -1.00 to 0.50 V. A Pt mesh and Ag/AgCl electrodes were used as the counter and reference electrodes, respectively.

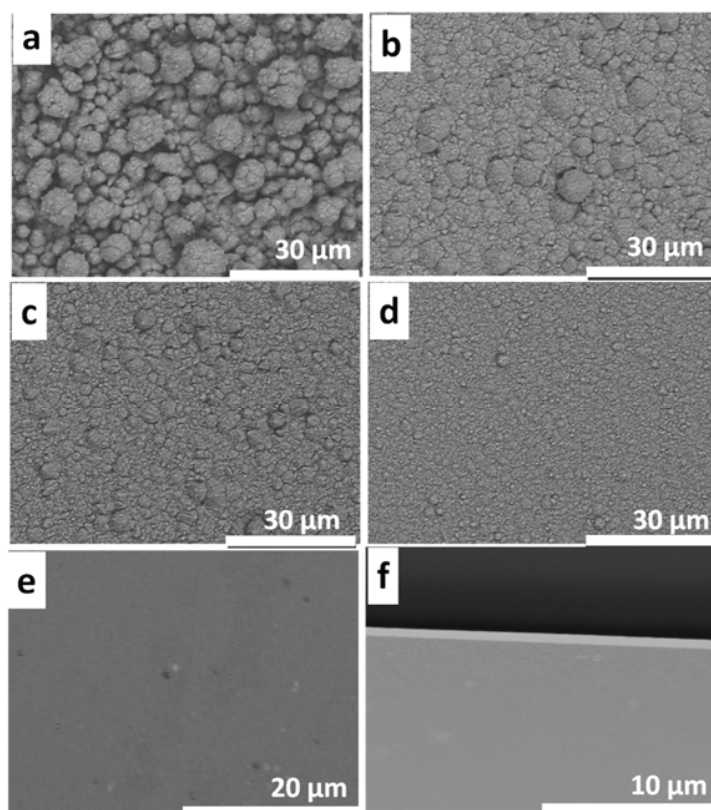


Figure 54. (a-d) SEM images of the top-surface of the Au-coated glass slides modified by Cu at different potentials: (a) -0.35, (b) -0.30, (c) -0.25 and (d) -0.20 V by using a Cu plating bath (CUBRAC 660) as the working solution. The deposition time was 300 s. (e-f) Typical SEM images of the (e) top-surface and (f) section of the Au-coated glass slides modified by Cu at various potentials in the range of -0.05 to -0.00625 V.

The SEM images of the top-surface and of the sections of the Au-coated glass slides modified with Cu at various potentials ranging from -0.35 to -0.00625 V (-0.35, -0.30, -0.25, -0.20, -0.05, -0.025, -0.0125, and -0.00625 V) are shown in Figure 54. At relatively high negative potential values in the range of -0.35 to -0.20 V, the Cu surfaces were not smooth. We suggest that in this potential range the Cu deposition is too fast to provide a smooth surface of Cu. When increasing the potential to -0.05 V, a smooth Cu surface is obtained (see Figure 54e). The side view image of the sample confirms again the smoothness of the Cu layer (see Figure 54f). An increase of the applied potentials to -0.025, -0.0125, and -0.00625 V does not result in a

significant change of the smoothness of the surface. The SEM images of the samples obtained by using potentials of -0.05, -0.025, -0.0125, and -0.00625 V look quite similar, only the thicknesses of the Cu layer is different. From the results, we have chosen the potentials at -0.05 V to deposition of copper into colloidal templates to generated macroporous electrode on next step. Before the deposition, the slides with the silica colloidal template were soaked in the plating bath for at least 10 min to ensure the penetration of the plating solution into the voids of the template. After the deposition, the silica template was dissolved by soaking the electrodes in 5% HF solution for ~10 min. It should be mentioned that the soaking time should not exceed 10 min in order to prevent the Cu surface from building oxides.

Figure 55 shows the SEM images of the ordered macroporous Cu electrodes, obtained after the removal of the silica colloidal crystal template, by using an applied potential of -0.05 V, but with various deposition times. It can be seen from the images that the thickness of the Cu layer is changing depending on the deposition time. The relatively short deposition time of 300 s was not long enough to create ordered macropores. With the increase of the deposition time to 700 s, although ordered macropores start to be observed, from the SEM image of the section, we found that the layer thickness of Cu was less than 1/2 silica bead layer (data is not shown). With a deposition time of 900 s, in addition to the ordered macropores, a complete 1/2 silica layer thickness of Cu was obtained (see the SEM image with the cross-section view in Figure 56a). Due to the presence of the macropores, the Cu surface area is increased compared to that of the flat Cu electrode. The macropores of the electrode were found to have the highly-organized hexagonal arrangement and an inverse opal structure. This finding agrees well with that typically found for macroporous metal electrodes fabricated via the LB technique using the silica colloidal crystal template. The pore diameter of the electrode corresponds to the diameter of the silica particles of 1 μm that were used as template. With a deposition time of 2300 s, the desirable ordered macropores with a 3/2 silica layer thickness of Cu was obtained (see the SEM image of the cross-section in Figure 56b). The macroporous Cu electrode with the complete 3/2 porous layer thickness is the most interesting for our purpose as we expect that this feature will allow the formation of MOF materials on the surface of macropores while maintaining the characteristics of the macroporous electrode. For this reason, we use a deposition time of 2300 s and a potential of -0.05 V to fabricate the Cu electrodes for the next experimental steps of the MOF preparation.

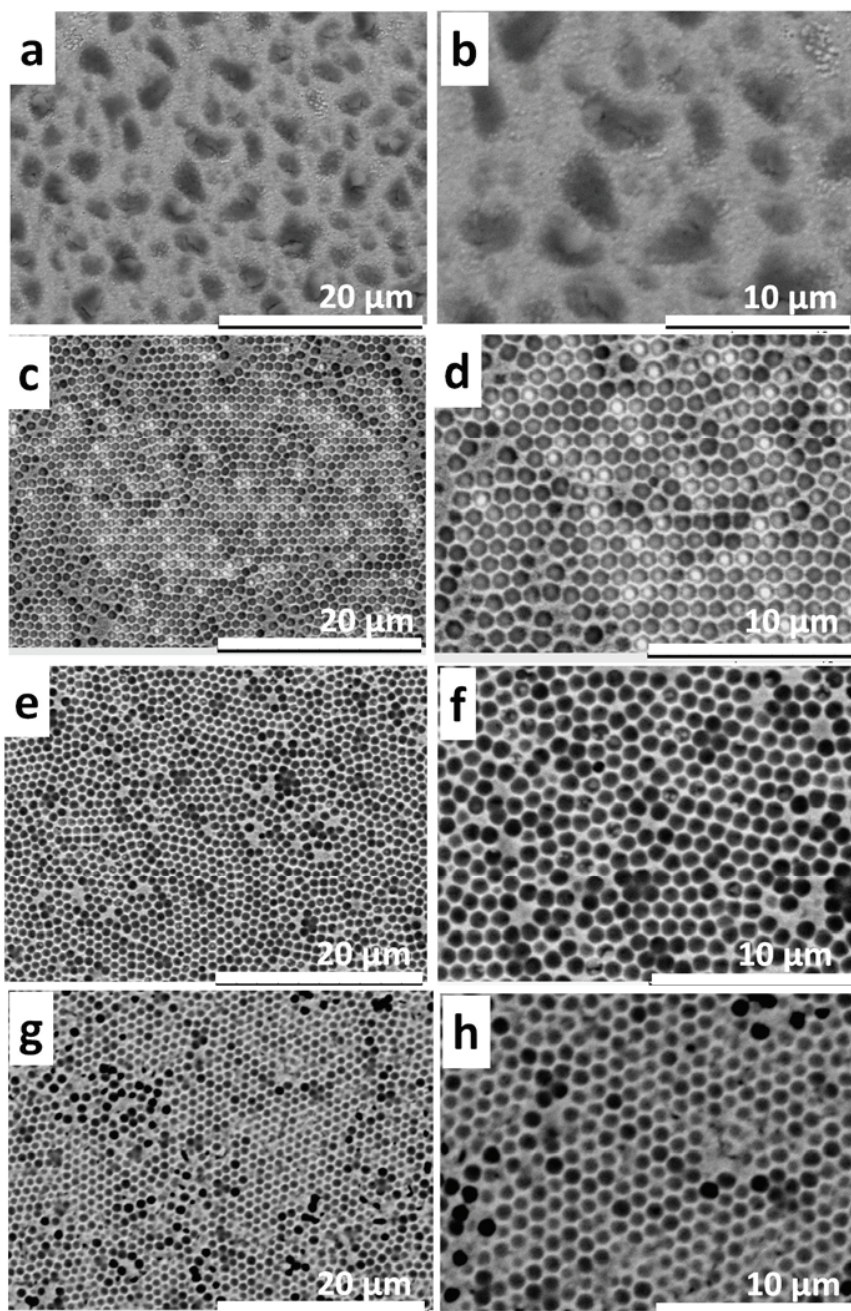


Figure 55. Low and high magnifications SEM images of the top-surface of the ordered macroporous Cu electrodes obtained after the removal of 1 μm -silica colloidal crystal template (fabricated by the LB technique) by using an applied potential of -0.05 V but with various deposition times of (a-b) 300 s, (c-d) 700 s, (e-f) 900 s, and (g-h) 2300s.

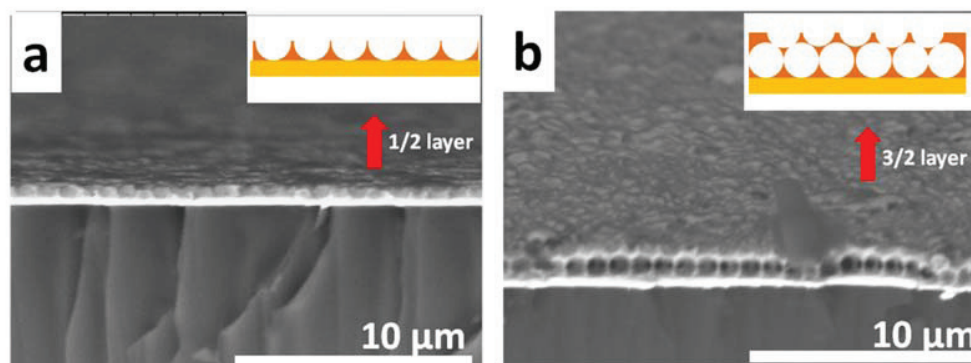


Figure 56. SEM images of cross-section of the ordered macroporous Cu electrodes obtained after the removal of 1 μm -silica colloidal crystal template (fabricated by the LB technique) by using an applied potential of -0.05 V but with different deposition times of (a) 900 s and (b) 2300s.

As the silica particles have an average diameter of $\sim 1\ \mu\text{m}$, the Cu layer with a thickness of 3/2 layers will have a thickness of 1.5 μm . To optimize the experimental conditions for the Cu deposition, flat Au-coated slides were coated with Cu. The thickness of the Cu layer coated on the flat electrodes was chosen to be 1.5 μm , equal to that of the porous electrodes. In order to obtain such a Cu layer, we varied the deposition time of Cu at a constant potential of -0.05 V and found that with a deposition time of 300 s, the desired thickness can be obtained.

To optimize the conditions for the transformation of the Cu surface into HKUST-1, the flat Cu-modified slides with a 1.5 μm Cu layer were used as the working electrode. The electrode was pretreated in 10% H_2SO_4 for 15 min before use. A silver wire and a platinum mesh were used as the pseudo reference and counter electrodes, respectively. A solution of 0.5 M 1,3,5-benzenetricarboxylic acid (BTC) in ethanol with 0.2 M tributylmethylammonium methyl sulfate (MTBS) supporting electrolyte was used as the working solution.

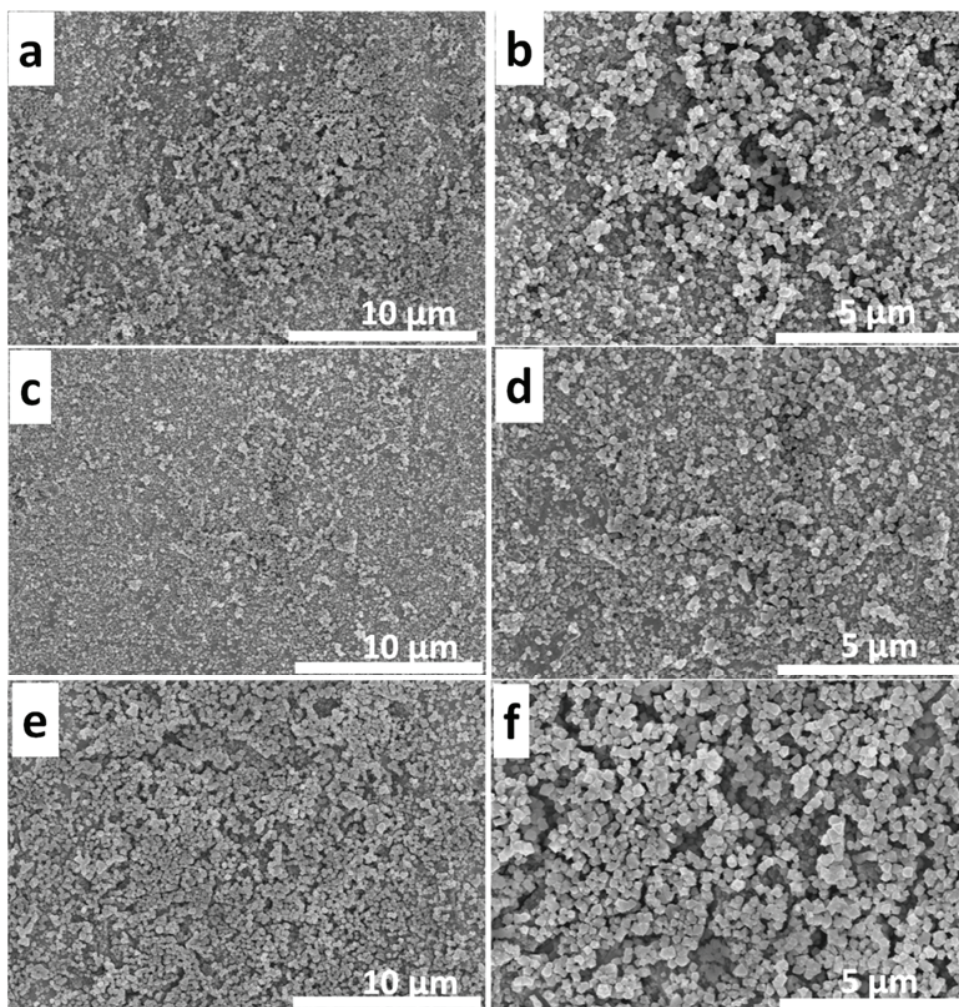


Figure 57. SEM images of HKUST-1 formed on the surface of the flat Cu-modified slides with 1.5 μm thickness via the electrochemical dissolution-deposition process at different potentials: (a-b) 0.125, (c-d) 0.25 and (e-f) 0.5 V and the same deposition time of 300 s in a solution of 0.05 M BTC in ethanol containing 0.2 M MTBS supporting electrolyte.

Figure 57 shows the SEM images of HKUST-1 formed on the surface of the flat Cu-modified slides at the constant deposition time of 300 s but for various potentials. By using a potential of 0.125 V, the obtained products look crystalline. Nevertheless, the amount of product is small compared to the total surface area of Cu. With the increase of the applied potential to 0.25 V and 0.5 V, the products look more crystalline with the octahedral block-like shape. This finding corresponds well with that reported in the literature for the HKUST-1 structure (Chui, S. S.-Y. *et al.*, 1999). Additionally, the yield of product increases with increasing potential.

Next, we used an applied potential of 0.5 V but with varying deposition times to understand the influence of the deposition time on the product characteristics. Figure 58 shows the SEM images of HKUST-1 formed on the surface of the flat Cu-modified slides at a constant potential of 0.5 V but for various deposition times. The products look more crystalline and the octahedral block-like crystal structure becomes better defined with increasing deposition time. The size of the crystals increases from one hundred nanometers to a few micrometers when increasing the deposition time from 30s to 1800s.

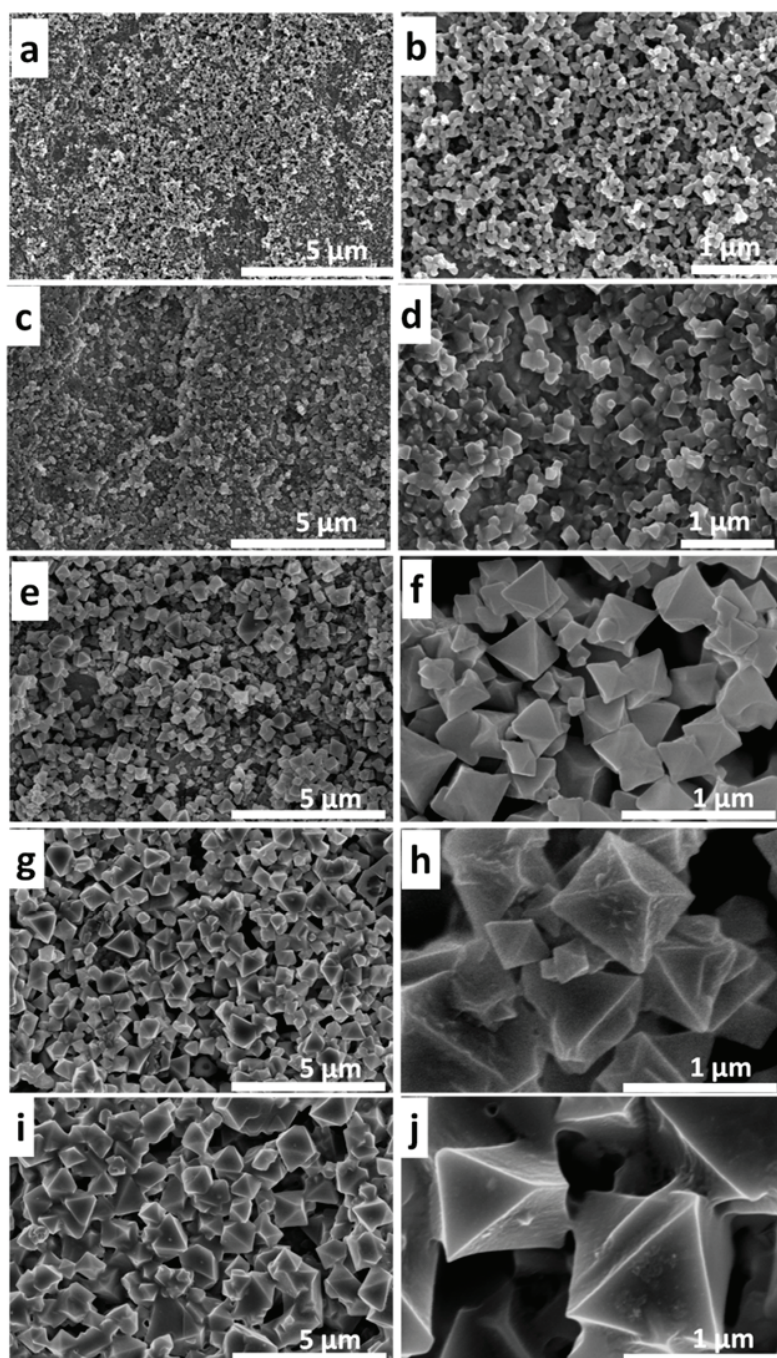


Figure 58. SEM images of HKUST-1 formed on the surface of the flat Cu-modified slides with 1.5 μm thickness via the electrochemical dissolution-deposition process at a constant potential of 0.5 V but for various deposition times: (a-b) 30, (c-d) 60, (e-f) 300, (g-h) 600, and (i-j) 1800 s in a solution of 0.05 M BTC in ethanol containing 0.2 M MTBS supporting electrolyte.

Figure 59 shows the IR spectra of pure BTC linker and the sample prepared via the electrochemical dissolution-deposition process at a constant potential of 0.5 V and a deposition time of 60 min in the solution of 0.05 M BTC in ethanol containing 0.2 M MTBS supporting electrolyte. The IR spectrum of the sample differs from that of the BTC linker indicating a difference in the functional groups contained in both materials. The band in the range of 1560-1440 cm^{-1} is assigned to the asymmetric stretching vibrations of carboxylate groups. The symmetric vibrations centered at 1370 cm^{-1} and the peaks at 730 and 760 cm^{-1} are assigned to the phenyl group in the HKUST-1 structure. Importantly, the band at 1690-1730 cm^{-1} , which is assigned to the acidic C=O stretching vibration, present in the case of the linker, vanishes in the case of the prepared product. This result suggests a deprotonation during the complexation of the linker molecules with the Cu^{2+} ions. The spectrum of the prepared material corresponds well with that reported for HKUST-1 in the literature confirming the successful preparation of HKUST-1 (Wang, F. *et al.*, 2013; Zybailo, O. *et al.*, 2010).

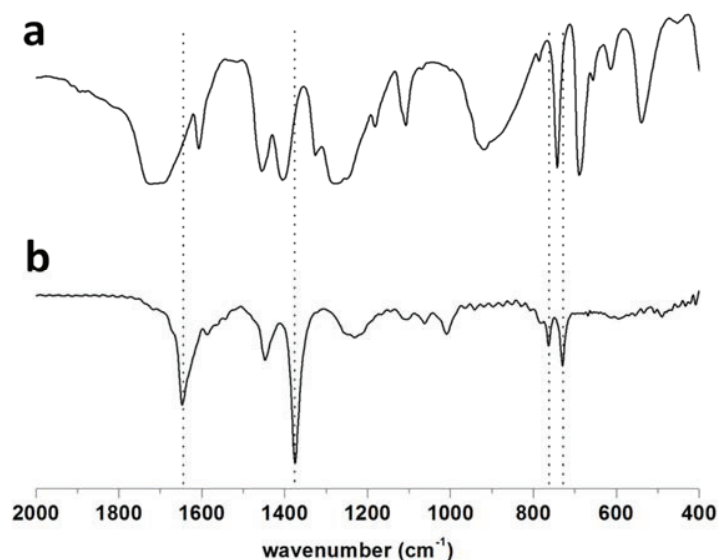


Figure 59. Infrared (IR) spectra of (a) pure BTC linker and (b) the sample prepared via the electrochemical dissolution-deposition process at a constant potential of 0.5 V and a deposition time of 60 min in the solution of 0.05 M BTC in ethanol containing 0.2 M MTBS supporting electrolyte.

In the next step, we prepared HKUST-1 on the Cu surface of the 3D ordered macroporous Cu electrodes with 3/2 porous layer thickness. First, we selected to use a voltage of 0.5 V (where the well-defined crystal structure of HKUST-1 was obtained) and a concentration of BTC in the working solution of 0.05 M. A relatively short deposition time of 60 s was chosen in order to make sure that the 3D ordered macroporous Cu electrodes will transform only partly into HKUST-1 and the designed macroporous architecture can be preserved. Prior to the application of the electric field, the electrode was soaked in the working solution for at least 5 min to ensure the penetration of the working solution into the macropores of the electrodes. Application of the potential of 0.5 V triggers the electrochemical dissolution of Cu^0 to Cu^{2+} . The dissolved Cu^{2+} ions immediately interact with the BTC molecules in the working solution in the front of the electrode surface leading to an observable precipitation of solid material with blue color.

The SEM images of the top-surface and various magnifications of the electrode before and after the dissolution-deposition process are shown in Figure 60. The low magnification image reveals the uniform distribution of HKUST-1 on the surface area of the macroporous electrode. Higher magnification images show the morphology of the prepared material corresponding to that obtained in the case of the flat Cu-coated electrodes that will further develop into the well-defined octahedral block-like crystals with an increase of the deposition time. Nevertheless, the image also reveals the alteration of the designed macropores due to the formation of the HKUST-1 aggregates. Additional pores originating from the voids between the MOF crystals in the aggregates can be seen. The obtained results support the successful preparation of the porous electrode of HKUST-1. Nevertheless, in order to better preserve the originally designed macropores, the applied potential was decreased to 0.125 V for the next experiments.

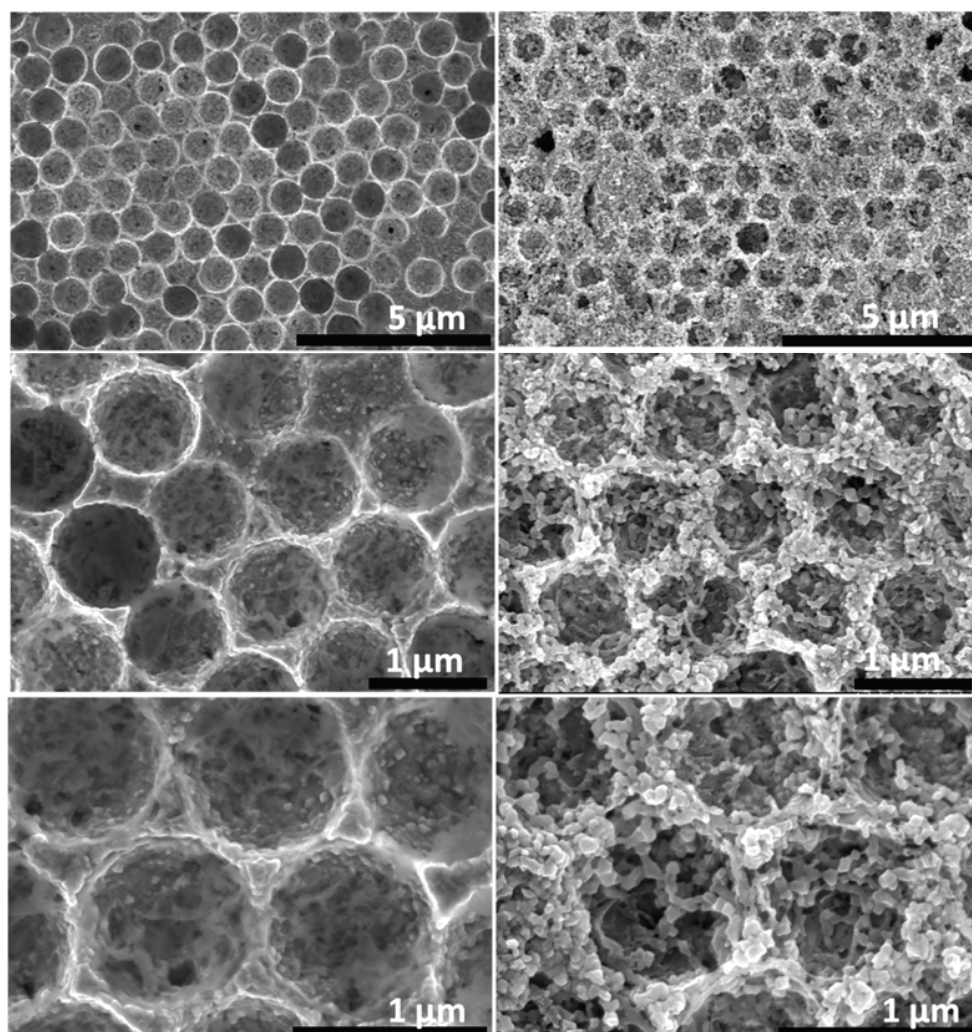


Figure 60. SEM images of the top-surface and various magnifications of the 3D ordered macroporous Cu electrodes with 3/2 layer thickness before (left-hand side) and after (right-hand side) the dissolution-deposition process at a constant potential of 0.5 V and a deposition time of 60s in the solution of 0.05 M BTC in ethanol containing 0.2 M MTBS supporting electrolyte.

Figure 61 shows the SEM images of the top-surface and various magnifications of the electrode after the dissolution-deposition process at a potential of 0.125 V. Here, the originally designed macroporous structure is mainly preserved. The amount of the MOF products and their morphology are varied by changing the deposition time, analog to what was obtained for the flat electrodes. The amount of the MOF products increases and the crystal structure is more well-defined with increasing deposition time. The obtained results indicate the successful preparation

of a hierarchical macroporous electrode of HKUST-1 via the currently employed technique. It should be noted that the desired hierarchical macroporous electrode of HKUST-1 can be obtained in a relatively short reaction time (<120 s). Thus, the employed technique is not time-consuming.

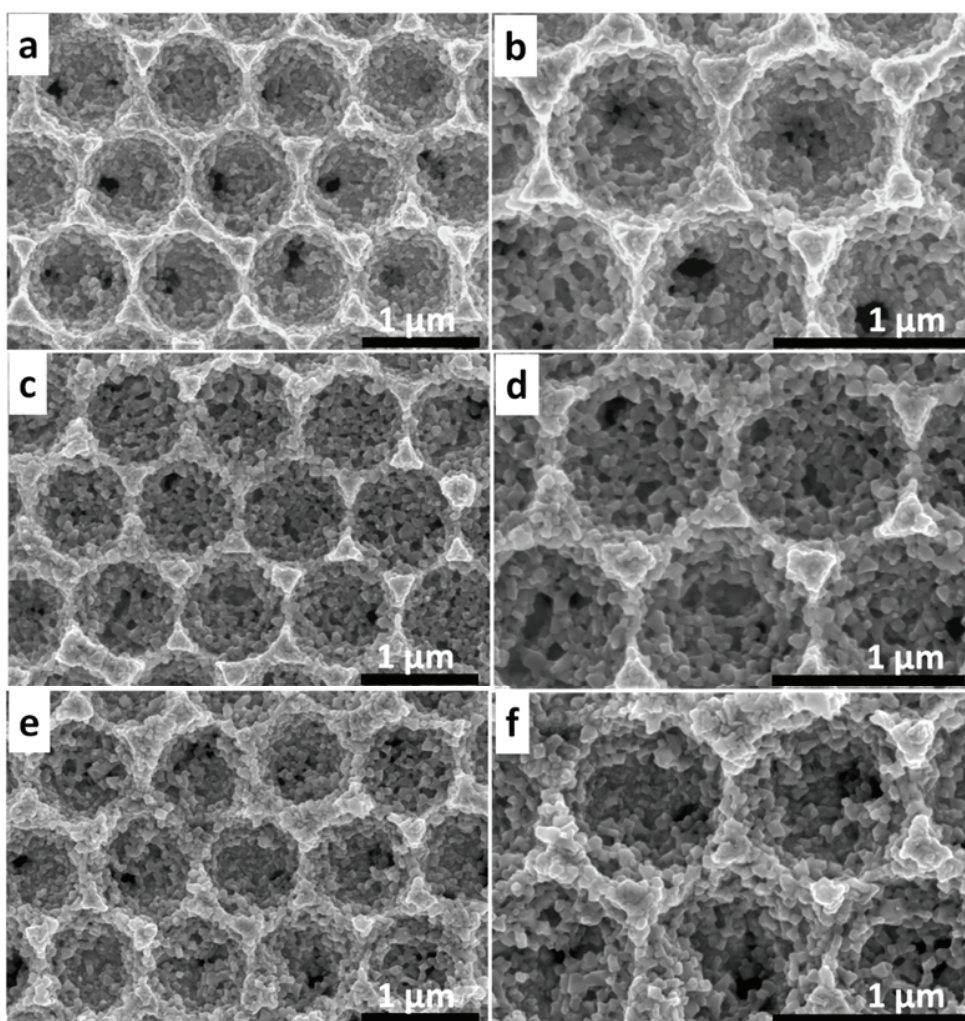


Figure 61. SEM images of the top-surface and various magnifications of the 3D ordered macroporous Cu electrodes with $3/2$ layer thickness before (left-hand side) and after (right-hand side) the dissolution-deposition process at a constant potential of 0.125 V but various deposition times of (a-b) 30 s, (c-d) 60 s and (e-f) 120 s in a solution of 0.05 M BTC in ethanol containing 0.2 M MTBS supporting electrolyte.

2.4 Conclusions

In summary, we have successfully fabricated hierarchical macro-/microporous HKUST-1 via an electrochemical dissolution-deposition technique. The 1 μm -silica particles with a monodisperse and narrow size distribution were prepared via the Stöber method. Then, a colloidal crystal template of the silica particles was deposited on gold-coated glass slide via the Langmuir-Blodgett technique. The voids of the crystal template were then filled with copper (Cu) by electrochemical deposition. The results show that with an applied potential of -0.05 V and potentials above (-0.025, -0.0125 and -0.00625 V), the obtained Cu surface was smooth (for a deposition time of 300 s). An optimized potential of -0.05 V was utilized for the Cu deposition. By fine-tuning the Cu deposition time, the 3D ordered macroporous Cu electrodes with an inverse opal structure were obtained with a controlled thickness of 3/2 porous layers after the dissolution of the silica template. The Cu surface of the obtained electrodes was directly transformed into HKUST-1 via the electrochemical dissolution of Cu in the presence of the organic ligands, leading to the crystallization of the MOF at the surface. As a result, a porous HKUST-1 electrode was obtained. The applied potential and deposition time were found to play important roles for the amount of product and its characteristics. With a relatively high applied potential of 0.05 V, the designed macroporous structure of the electrode was disturbed due to the formation of the HKUST-1 aggregates. With a relatively low applied potential of 0.0125 V, the originally designed macroporous structure was mainly preserved. As a result, hierarchically structured macro-/microporous HKUST-1 electrodes were successfully obtained. The deposition time was found to influence the amount of the MOF products and their morphology. The amount of the MOF products increases and the crystal structure is better defined when increasing the deposition time. The obtained results clearly indicate the successful preparation of a hierarchically structured macro-/microporous electrode of MOFs via the currently employed dissolution-deposition technique, opening up MOFs for various applications including catalysis, separation and sensor by ensuring improved transport properties in the MOF matrix.

3. Preparation of Metal-Organic Framework (MOF)-Supported Metal Nanoparticles (Au, Pd and Pt)

3.1 Introduction

Metal nanostructures are known as one of the most important advanced materials on which much research attention has been focused in the last two decades. This is due to their unique properties such as catalytic properties, magnetism and surface plasmon resonance (SPR) serving applications in various fields, such as catalysis (Burda, C. *et al.*, 2005; Tsunoyama, H. *et al.*, 2004), magnetic data storage (Xian-Wen, W. *et al.*, 2006), and biosensors (Yáñez-Sedeño, P. and J. M. Pingarrón, 2005). Among metal nanostructures, which are of interests for catalysis (Burda, C. *et al.*, 2005), noble metal nanostructures including gold (Au) (Hashmi, A. S. K. and G. J. Hutchings, 2006), palladium (Pd) (Reetz, M. T. *et al.*, 1996), and platinum (Pt) (Lordi, V. *et al.*, 2001) have attracted much consideration. This is because they are very reactive for many chemical reactions i.e. hydrogenation, oxidation, C–C coupling, and cleavage reactions that are important in the field of chemical manufacturing. Each metal nanostructure shows different catalytic behaviors for different chemical reactions. Au nanostructures have been reported to be reactive for oxidation reactions including CO and alcohol oxidation reactions. Pd nanostructures have been reported to be active for the Suzuki cross-coupling and Mizoroki-Heck reactions, while Pt nanoparticles (PtNPs) are active for the hydrogenation reactions.

For catalysis involving metal nanostructures, their size, composition, shape, and electronic properties such as oxidation state, are key parameters (Cuenya, B. R., 2010). In addition, the supporting materials and the stabilizers also play an important role with respect to their catalytic properties (Tsunoyama, H. *et al.*, 2004). It has been reported that metal nanoparticles with 1-10 nm in size or metal nanoclusters (NCs) exhibit good catalytic behaviors for various chemical reactions. This is because of their high surface area to volume ratio, which increases with the decrease of particle size, leading to a high amount of the active atoms present on the surface.

In this size regime, the number of the metal atoms plays important role for the chemical reactivity of the nanostructures. For example, Zhu and co-workers investigated the catalytic properties of three small gold nanoclusters (AuNCs or Au_n), Au₂₅, Au₃₈, and Au₁₄₄ (with a size of about 1.0, 1.3 and 1.6 nm, respectively) for the selective oxidation of styrene (Zhu, Y. *et al.*,

2010a; Zhu, Y. *et al.*, 2010b). They found that the catalytic activity of the catalysts strongly depends on the number of Au atoms (n) composing the clusters (corresponding to the size of the clusters). The clusters with a smaller number of Au atoms give rise to a much higher catalytic activity compared to those with a higher number of Au atoms. Among the investigated clusters, the smallest clusters (Au_{25}) show the highest activity for styrene conversion, followed by the Au_{38} and Au_{144} clusters, respectively.

Up to now, there have been many preparative techniques reported for the synthesis of metal nanoparticles. These methods include the chemical reduction (using some reducing agents) (Van Hyning, D. L. and C. F. Zukoski, 1998; Wang, H. *et al.*, 2005) such as dihydrogen, sodium borohydride, amineboranes, hydrazine, and alcohols), the electrochemical reduction (Zhang, D.-W. *et al.*, 2008) and the photochemical reduction of the metal ions/precursors (Maillard, M. *et al.*, 2003). Beside these reduction methods, the metal nanoparticles can also be synthesized by other techniques, for example, the evaporation of the metal atoms from the surface of bulk metals by using a high-energy laser, and then, cooling them (as a result, the nanoparticles are formed). Although, the particles can be prepared both via physical and chemical techniques, in order to obtain the nanoparticles with a small size, the chemical techniques are preferable to the physical ones. Because the physical techniques are based on the subdivision of bulk metals, for example, the mechanical crushing of bulk metals or the discharge between the metal electrodes, so the size of the produced metal NPs is usually large and widely distributed. While the chemical techniques are based on the reduction of metal ions or the decomposition of the metal precursors (to form the metal atoms followed by aggregation of the atoms in the presence of a stabilizer) so the size distribution of the prepared metal nanoparticles is typically narrow.

Apart from the generation of the metal nanostructures with the desirable small size, the formation of them with the precise size and size distribution is also one of the keys that one should concern for catalysis of metal catalysts. For this reason, much attention has focused onto the synthesis of the nanoclusters with precisely controlled and monodisperse size. Such NCs do not only exhibit potential in the field of catalysis but also in other fields, for example, in electrochemical quantized capacitance charging (Chen, S. *et al.*, 1998), single-electron transistor assembly (Philip, M., 2001) and advanced applications of thermal gradient optical imaging (Boyer, D. *et al.*, 2002).

A number of preparative methods which lead to metal NPs with a specific size and a narrow size distribution have been reported. Poly(N-vinyl-2-pyrrolidone) or PVP is one of the most effective stabilizing agent for metal nanoparticles. Poly(N-vinyl-2-pyrrolidone) or PVP is one of the most effective stabilizing agents that are used for the metal nanoparticles. Tsunoyama and co-worker (Tsunoyama, H. *et al.*, 2009; Tsunoyama, H. *et al.*, 2005) prepared the gold nanoclusters stabilized by PVP (Au:PVP NCs) via the reduction of metal ions in the presence of PVP. The correlation between the catalytic behaviors, the electronic structures of the Au:PVP NCs and the charge states of Au cores with different sizes and stabilized by different polymers was investigated. They found that the PVP-stabilized Au clusters show higher catalytic activity than the clusters stabilized by other stabilizer, polyacrylic acid. Besides, the catalytic behaviors of the Au:PVP NCs with the average sizes ranging from 1.3 to 10 nm were investigated for the aerobic oxidation of p-hydroxybenzyl alcohol. They found that the catalytic activity increases with the decrease of the Au:PVP size (Tsunoyama, H. *et al.*, 2006). This finding clearly indicates the importance of the size-controlled synthesis of metal nanostructures in the field of catalysis. For this reason, this topic is of our interests in this section.

Although the metal NPs have exhibited high potential for catalysis, there is also an obvious disadvantage that hinders this application. This is the difficulty in separation and recycling of the metal catalysts with small sizes behaving as homogeneous catalysts for liquid phase reactions. For this reason, it is necessary to find solid material candidates for supporting the particles. In addition to the ease of the catalyst separation and recycling, the stability of the NPs could be improved and the catalytic behavior could be enhanced by supporting them on solid substrates, opening up the possibility to carry out for example reactions that require a relatively high temperature.

Until recently, there have been many solid supporting materials used for metal nanostructures. These materials include metal oxides (Haruta, M., 1997; Sayle, D. C. *et al.*, 2003), carbonaceous materials (Castillejos, E. *et al.*, 2009; Lin, Y. *et al.*, 2005; Shao, Y. *et al.*, 2006), zeolites (Kato, H. *et al.*, 2004; Tosheva, L. and V. P. Valtchev, 2005) and metal organic frameworks (MOFs) (El-Shall, M. S. *et al.*, 2009). The unique structure of MOFs resulted from the combination of the long-range order of a solid-state template material with tunable dimensionalities, and the chemical tailoring of the inner surface of the MOF channels and

cavities makes them promising as a candidate materials for supporting the functional nanomaterials.

For the catalysis purpose, many functional nanostructures i.e. copper (Cu), ruthenium (Ru), silver (Ag), palladium (Pd), gold (Au) and platinum (Pt) nanostructures have been successfully embedded in the cavities or channels of MOFs via various preparation techniques. Typically, the particles can be embedded in the MOF structure in three ways (see Figure 62) (Meilikhov, M. *et al.*, 2010). A first possibility is to deposit them at the outer surface of MOFs. This situation usually occurs when the particle sizes are larger than the accessible pore dimension of MOFs (about less than a few nanometers) (Hermes, S. *et al.*, 2005). In a second case, the particles are introduced into the pore due to their smaller dimensions but they still have a broad size distribution (El-Shall, M. S. *et al.*, 2009). Last but not least, the particles can be embedded into the pores of MOFs with a uniform size distribution as their sizes match well with the pore dimensions of MOF (Yuan, B. *et al.*, 2010). This feature is desirable for the application in catalysis. In many cases, the resulting metal-embedded MOFs (abbreviated as metal@MOF) exhibit unique catalytic activity for some chemical reactions. The reported reactions include CO oxidation (Jiang, H.-L. *et al.*, 2009), alcohol oxidation (Liu, H. *et al.*, 2010), the ethyl cinnamate hydrogenation (Opelt, S. *et al.*, 2008), and the Heck reaction (Hwang, Y. K. *et al.*, 2008).

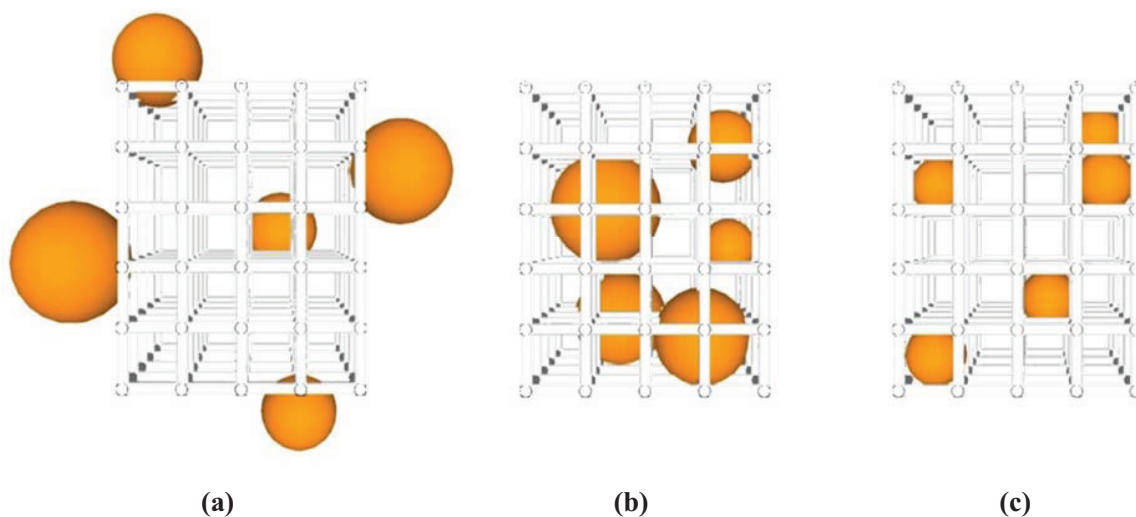


Figure 62. Three proposed cases of metal nanostructures supported by a MOF. (a) the metal nanostructures are deposited at the outer surface of the MOF, (b) the nanostructures are

introduced into the pore of the MOF, but they still have a broad size distribution, and (c) the nanostructures are embedded into the pores of MOFs with a uniform size distribution as their sizes matches well with the pore dimensions of MOF.

Among MOFs that have been previously reported as supporting materials for the metal catalysts one material of the Institute Lavoisier, MIL-101, is of special interests in this section. MIL-101 is constructed from $[\text{Cr}_3\text{O}]$ cluster nodes and 1,4-benzenedicarboxylate. The structure is based on supertetrahedra, which consist of trinuclear units linked by 1,4-benzenedicarboxylate. (see Figure 63) This type of MOF has a rigid zeotype (MTN type) crystal structure, consisting of quasi-spherical cages with two modes (2.9 and 3.4 nm). MIL-101 (Férey, G. *et al.*, 2005) possessing a large surface area (Brunauer-Emmett-Teller or BET surface area of ca. $3000 \text{ m}^2 \text{ g}^{-1}$), large pore size (ca. 29-34 Å) and good chemical resistance to water and organic solvents, have shown to be desirable supports for the metal catalysts.

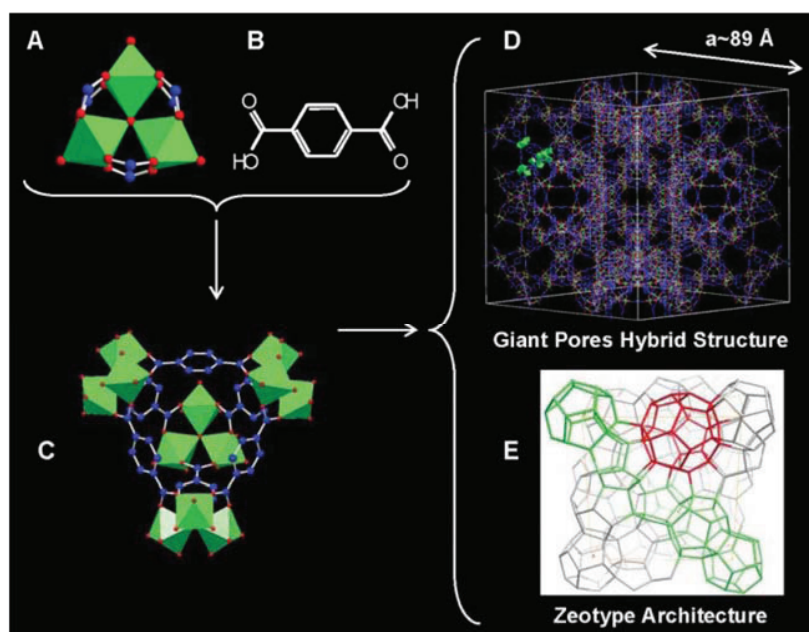


Figure 63. (a) Inorganic trimer; (b) 1,4-Benzenedicarboxylic acid; (c) ST made from the linkage of inorganic trimers and 1,4-BDC; (d) schematic view of the MIL-101 structure; and (e) schematic 3D representation of the MTN zeotype architecture : source from reference (Férey, G. *et al.*, 2005)

In the literature, the hybrid metal-MIL-101 materials were successfully prepared via a colloidal deposition technique. This technique includes the steps of the synthesis of the colloidal metal NPs, followed by the deposition of the obtained particles onto the supporting material (Pan, Y. *et al.*, 2010). The MIL-101-supported gold NPs (AuNPs@MIL-101) prepared via this colloidal deposition method show extremely high catalytic activities for the liquid-phase oxidation of a wide range of alcohols under ambient conditions in the absence of water or base (Liu, H. *et al.*, 2010), which is typically used to activate the reactions (Tsunoyama, H. *et al.*, 2005). This finding is in contrast to that obtained in the case of the unsupported AuNPs in which high amounts of base (about 300% of the reactants) is required to make the reaction occur. This difference is due to the electron donation effect of the aryl rings of the organic linker molecules on the particle surface through π -bond interactions. As a result, the Au particles are negatively charged resulting in the favorable activation of O₂ on the Au surface (Liu, H. *et al.*, 2010). The results from this study motivated us to fabricate AuNPs@MIL-101 and other MIL-101-supported metal NPs, PdNPs@MIL-101 and PtNPs@MIL-101, with the perspective to study the catalytic behavior of the obtained hybrid materials and to gain insight into the combined impact of an intrinsic catalytic activity of size-controlled metal nanoparticles (Au, Pd and Pt) and the electron donation effect from the organic linker of MOFs on the activity and selectivity of the reaction.

Herein, we prepared AuNPs@MIL-101, PdNPs@MIL-101 and PtNPs@MIL-101 via the colloidal deposition of size-controlled metal NPs stabilized by poly(N-vinyl-2-pyrrolidone) (PVP). This method was used for the preparation of AuNPs@MIL-101 in the previous work. We found that all metal NPs@MIL-101 samples were successfully prepared. The characterizations show a difference in behavior of the metal nanoparticles deposited onto the MIL-101. The observed differences are due to the difference in the intrinsic properties of the nanoparticles, which further leads to the difference in their catalytic activity and selectivity for a chemical reaction.

3.2 Experimental section

3.2.1 Materials

Chromium nitrate ($\text{Cr}(\text{NO}_3)_3 \cdot 9\text{H}_2\text{O}$, Sigma-Aldrich, 99%), terephthalic acid ($\text{C}_8\text{H}_6\text{O}_4$, Sigma-Aldrich, 98%), polyvinylpyrrolidone (K-30, wt~40,000, Fluka), sodium borohydride (NaBH_4 , Sigma-Aldrich, 99%), potassium tetrachloroplatinate (II) (K_2PtCl_4 , Sigma-Aldrich, 99.9%), gold (III) chloride trihydrate ($\text{HAuCl}_4 \cdot 3\text{H}_2\text{O}$, Sigma-Aldrich, 99.9%), palladium (II) chloride (PdCl_2 , Sigma-Aldrich, 99.9%), hydrofluoric acid (HF, 48%), ethanol ($\text{C}_2\text{H}_5\text{OH}$, 98%) were used as received. Deionized (DI) water was made in our laboratory.

3.2.2 Synthesis of MIL-101

MIL-101 was prepared by using the previously published hydrothermal technique (Férey, G. *et al.*, 2005). Briefly, $\text{Cr}(\text{NO}_3)_3 \cdot 9\text{H}_2\text{O}$ (5 mmol), HF (5 mmol), terephthalic acid (5 mmol), and DI water (24 mL) were mixed and reacted at 220 °C for 8 h in an autoclave. After that, the reaction mixture was allowed to cool down slowly to room temperature for 12 h. Next, in order to remove the residual organic linker, which was left in the form of large white crystals, the mixture was then filtered through a filter, a nylon membrane with an average pore diameter of 41 μm (Spectra/Mesh Nylon Macroporous filters). The MIL-101 product remained in the filtrate part and was isolated by using paper filter (Whatman, No. 1). The solid remaining on the filter paper was then washed with a solution of 95 % v/v ethanol in water, and then removed from the filter paper. The powder sample of MIL-101 was obtained after a washing step performed by soaking the obtained solid in a solution of 95 % v/v ethanol in water at 80 °C for 24 h followed by drying at 150 °C under vacuum overnight.

3.2.3 Preparation of Au:PVP, Pd:PVP and Pt:PVP nanoparticles

The metal colloids stabilized by PVP were synthesized by the technique reported by Tsunoyama and co-worker (Tsunoyama, H. *et al.*, 2005). Typically, $\text{HAuCl}_4 \cdot 3\text{H}_2\text{O}$, PdCl_2 and K_2PtCl_4 were used as the metal sources. PVP was used as the stabilizer. NaBH_4 was used as the reducing agent. 555.5 mg (0.0139 mmol) of PVP was added to the aqueous solution of each metal source (1 mM, 50 mL). The mixture was stirred. The resulting mixture was placed in an ice bath at 0 °C and stirred for 30 min. Then, an aqueous solution of NaBH_4 (100 mM, 5 mL)

was rapidly added to the mixture under vigorous stirring. After the addition of NaBH_4 , the mixture was further stirred for 1 h. In the case of Au:PVP, after the addition of NaBH_4 , the color of the reaction mixture immediately turned from pale yellow to dark brown, indicating the formation of small AuNCs. In the cases of Pd and Pt, there is no change in color of the reaction mixtures. The resulting mixtures of metal:PVP were used as starting materials for the next colloidal deposition step.

3.2.4 Synthesis of metal NPs@MIL-101 by colloidal deposition of the metal nanoparticles stabilized by PVP

Typically, in order to support the nanoparticles onto the MIL-101, 0.5 g of the synthesized MIL-101 was added to 4 mL of DI water and then dispersed by sonicating in an ultrasonic bath for 20 s. The as-prepared metal:PVP solution was also sonicated for 20 s before use. The two mixtures were then mixed and stirred in an ice bath at 0 °C for 4 h. The metal NPs@MIL-101 materials were obtained after filtration by using a normal paper filter (Whatman, No. 1). The metal NPs@MIL-101 sample was washed with DI water and then dried in a vacuum oven overnight.

3.2.5 Characterization

Powder X-ray diffraction (XRD) of the samples were performed by a Rigaku diffractometer (TTRAX III) using $\text{Cu K}\alpha$ radiation (for the low angle XRD pattern) operating at an accelerating voltage of 50 kV and a current of 300 mA and a Philips diffractometer (X'Pert Pro) with $\text{Cu-K}\alpha$ radiation (for the high angle XRD pattern) operating at an accelerating voltage of 40 kV and a current of 30 mA. The low angle powder X-ray diffraction pattern was recorded from 2 to 7 degrees of 2θ by using a step-size of 0.01 degrees and a scan speed of 0.5 degrees/minute. The high angle XRD pattern was recorded from 5 to 50 degrees using a step-size of 0.01 degrees and a scan speed of 0.5 degrees/minute. The size of the nanoparticles was measured by using a dynamic light scattering (DLS) technique (Malvern Zetasizer, Nano ZS-90, UK). The textural properties of the samples were obtained from the analysis of the N_2 adsorption/desorption isotherms performed at 77 K by a Micromeritics ASAP 2010 instrument. Prior to the measurement, the sample was degassed under vacuum overnight at 100 °C. The features of the MIL-101 crystals and the metal NPs@MIL-101 materials were observed by using

a transmission electron microscope (TEM, JEOL, JEM-2010), a scanning electron microscope (SEM, JEOL, JSM 6301F) and a scanning transmission electron microscope (STEM, JEOL, JEM-2100F STEM/TEM). For the TEM characterization, the dry powder of MIL-101 was dispersed in absolute ethanol for a few minutes by using an ultrasonic bath and then deposited on a carbon-coated copper (Cu) grid. Then the grid was left in air until it was dry. For the STEM characterization, different detectors were used for imaging the samples in the bright field (BF), dark field (high-angle, HA) and annular dark field (HA-ADF) modes. In addition, a secondary electron (SE) detector was used. This combination allowed us to visualize how the nanoparticles are located in the structure of MIL-101. The textural properties of the prepared materials were determined via the measurement of N₂ adsorption/desorption isotherms.

3.3 Results and discussion

3.3.1 Characteristics of the prepared MIL-101

The low-angle and high-angle powder X-ray diffraction patterns of the prepared MIL-101 are shown in Figure 64. The diffraction peak positions of the sample correspond well with those of MIL-101 in the literature and the standard data for MIL-101 (Férey, G. *et al.*, 2005). The main diffraction peaks of MIL-101 are at $2\theta = 3.25, 5.10, 8.41, 9.02, 16.49$, and 17.40 . The relative diffraction intensities of the sample are high indicating that the sample has a good crystallinity. The intensive peaks presented at small 2θ angles are the characteristics of materials that possess abundant pores or cavities. The results confirm the successful synthesis of porous MIL-101 with high crystallinity.

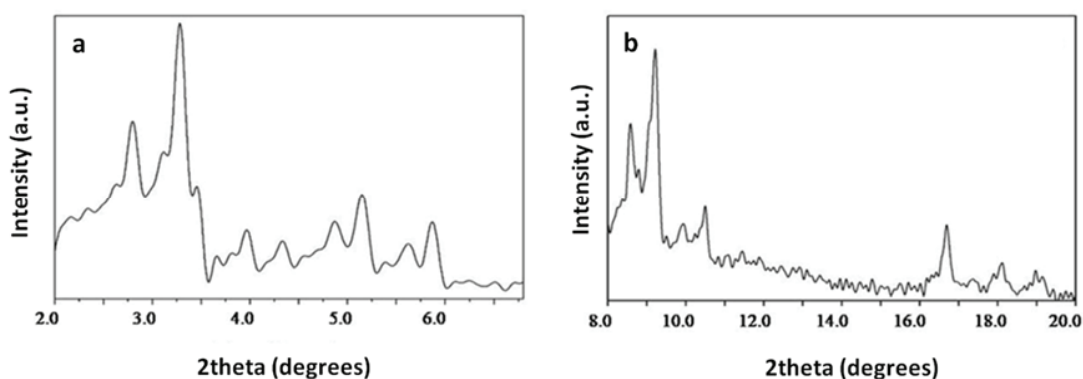


Figure 64. (a) Low- and (b) high-angle XRD patterns of the MIL-101 sample prepared in this work.

The SEM images with low and high magnifications of the synthesized MIL-101 are shown in Figures 65a and 65b, respectively. It can be seen from the images that the obtained material is composed of cubo-octahedral crystals with an average particle size of $1.2 \pm 0.2 \mu\text{m}$ (see in Figure 65c). This finding agrees well with that reported in the literature (Férey, G. *et al.*, 2005).

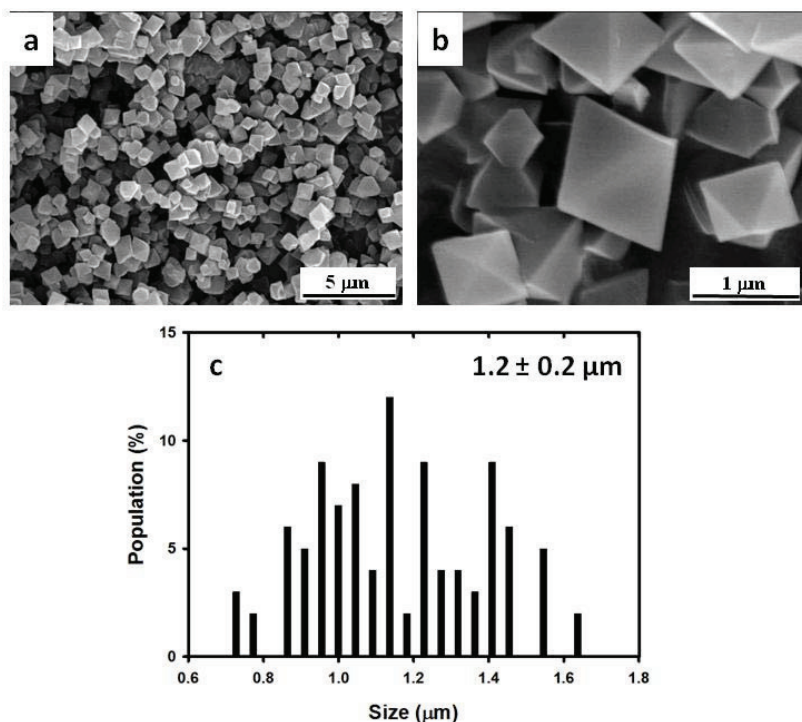


Figure 65. (a) Low and (b) high magnification SEM images and (c) the corresponding particle size distribution of the prepared MIL-101.

The TEM images confirm the nearly perfect cubo-octahedral crystal structure of the prepared MIL-101 (see Figures 66a and 66b). The high magnification TEM image shows the crystal arrangement with an interspacing distance of $\sim 2.5 \text{ nm}$ (see Figure 66c).

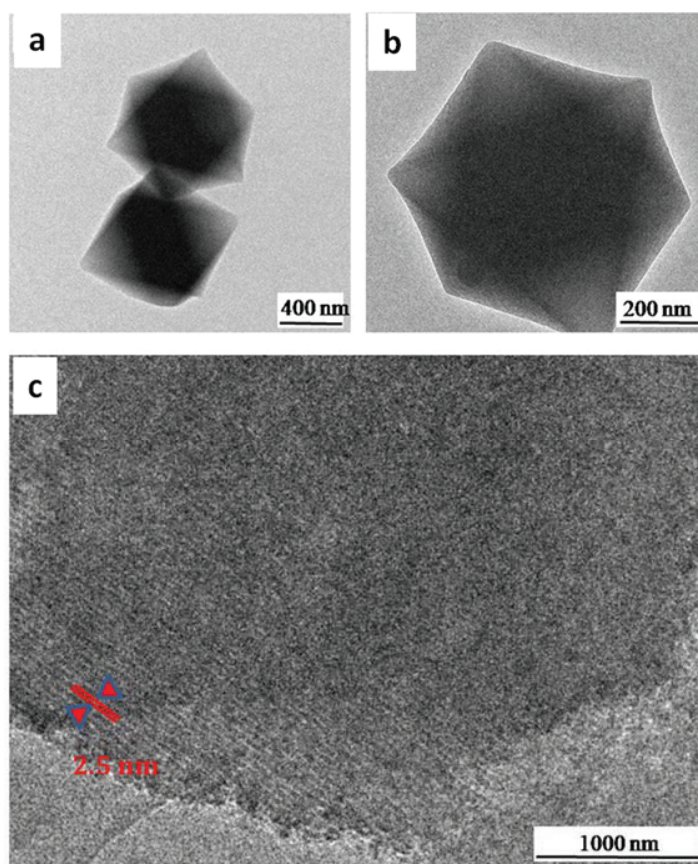


Figure 66. (a-b) Low- and (c) high-resolution TEM images of the synthesized MIL-101.

The N₂ adsorption/desorption isotherms of the sample corresponding to the type I isotherms (classified by IUPAC) are shown in Figure 67a. This type I isotherm is typically observed for microporous solids. The adsorptions at the relatively low pressure ($P/P_0 \sim 0.1$ and $P/P_0 \sim 0.2$, where P is gas pressure and P_0 is saturation pressure) are due to the micropore filling, indicating that there are two kinds of micropores contained in the material (see Figure 67a) (Férey, G. *et al.*, 2005). The BET surface area (S_{BET}) and pore volume (V_{pore}) of the prepared MIL-101 extracted from the isotherms are 3,384 m²/g and 1.611 cm³/g, respectively. The pore size distribution (PSD) derived from the adsorption branch of the isotherms is shown in Figure 67b. The highest PSD centers at ~ 2.54 nm. The obtained BET surface area, pore volume and pore size are in good agreement with those reported in the literature (Férey, G. *et al.*, 2005).

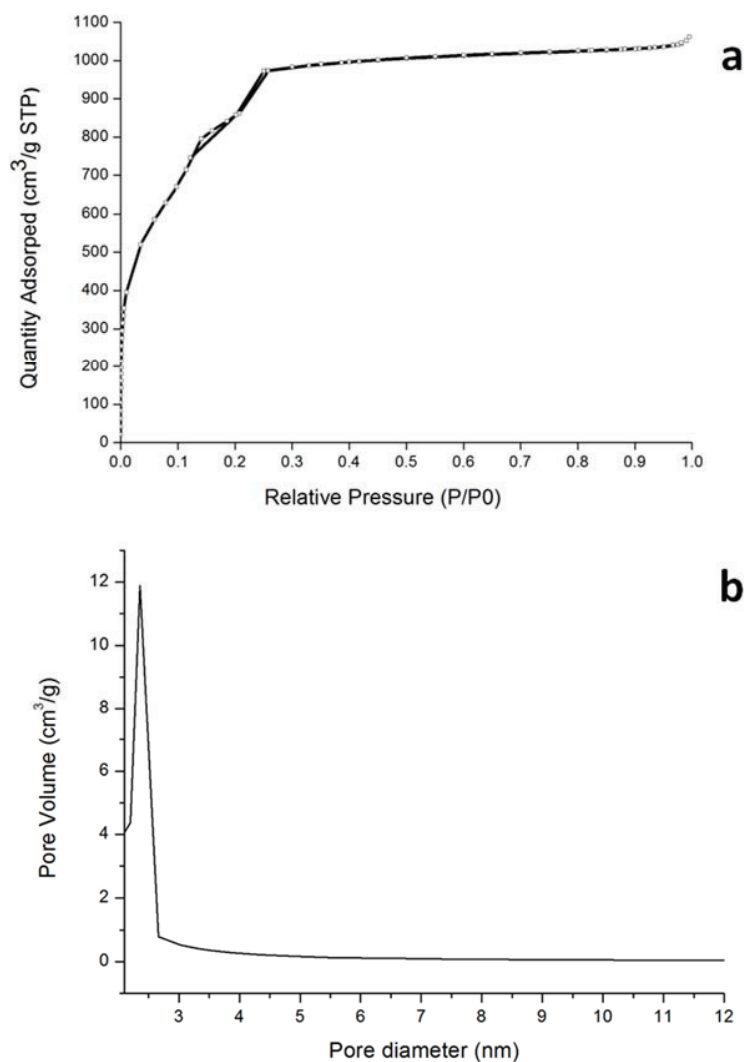


Figure 67. (a) N₂ adsorption/desorption isotherms and (b) the corresponded pore size distribution of the prepared MIL-101 sample.

3.3.2 Characteristics of the synthesized metal nanoparticles

Figures 68a-c show the particle-size distribution of the PVP-protected metal nanoparticles obtained from the DLS analysis showing the monodisperse size distribution for all metals. The average hydrodynamic diameters of the Pd:PVP, Au:PVP and Pt:PVP nanoparticles are ~ 10.5, 10.4 and 8.1 nm, respectively. The average diameter of metal cores estimated from the TEM images of the Pd:PVP, Au:PVP and Pt:PVP nanoparticles are 2.6, 2.4 and 1.5 nm, respectively. These diameters are much less than the hydrodynamic diameters in all cases due to the lack of

the large PVP polymer layer. It should be noted that the average hydrodynamic diameters of the particles (~8-10 nm) are much larger than the average pore size of the prepared MIL-101 (~2.5 nm). Therefore we expect that the particles will be deposited just onto the outer surface of MIL-101. An example TEM image of the prepared metal NPs (AuNPs) and their related PSD are shown in Figure 69.

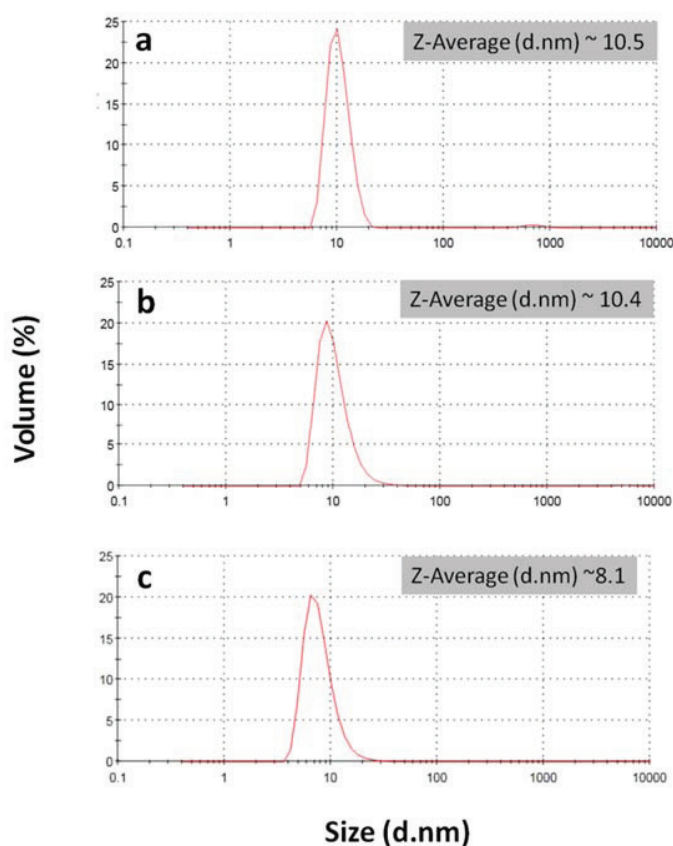


Figure 68. Graphs showing particles size distribution of the Pd:PVP, Au:PVP and Pt:PVP nanoparticles, synthesized at 0°C in the presence of PVP using NaBH₄ as the reducing agent, obtained from the DLS analysis.

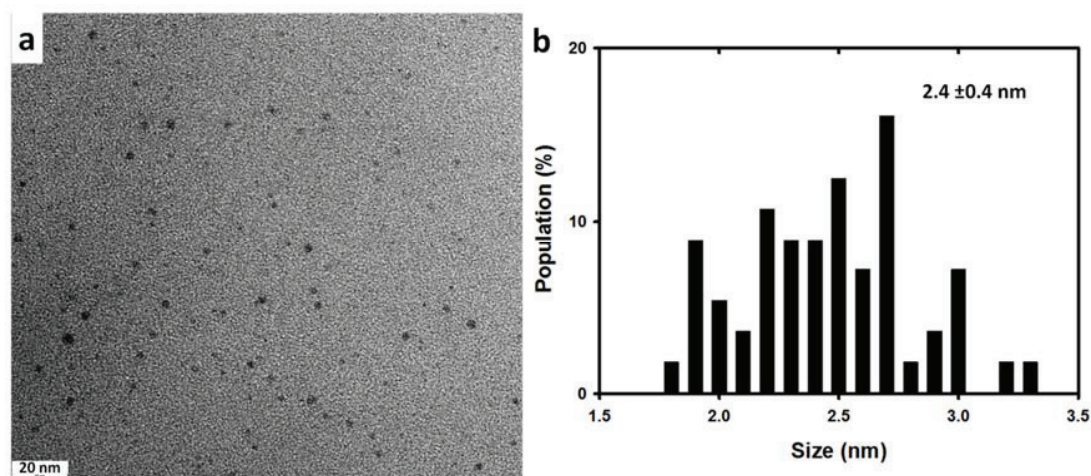


Figure 69. TEM image of the prepared Au:PVP nanoparticles and their related particle size distribution.

3.3.3 Characteristics of the prepared metal NPs@MIL-101

IR spectra of the MIL-101 samples obtained before and after the metal deposition are shown in Figure 70. Comparing them to the data in the literature (Liu, Q. *et al.*, 2013), the structure of MIL-101 can be confirmed. The band at 1627 cm^{-1} indicates the presence of adsorbed water. The band at 1406 cm^{-1} corresponds to the symmetric (O–C–O) vibration, implying the presence of dicarboxylate within the MIL-101 framework (Jhung, S. H. *et al.*, 2007; Zhang, Z. *et al.*, 2011). The peaks between 600 and 1600 cm^{-1} are attributed to the benzene ring. These peaks include the stretching vibration (C = C) at 1510 cm^{-1} and deformation vibration (C–H) at 1170 , 1018 , 885 , and 748 cm^{-1} . Additionally, the IR spectra of the MIL-101 samples obtained before and after the metal deposition are comparable indicating that the MIL-101 framework is preserved after the metal deposition process.

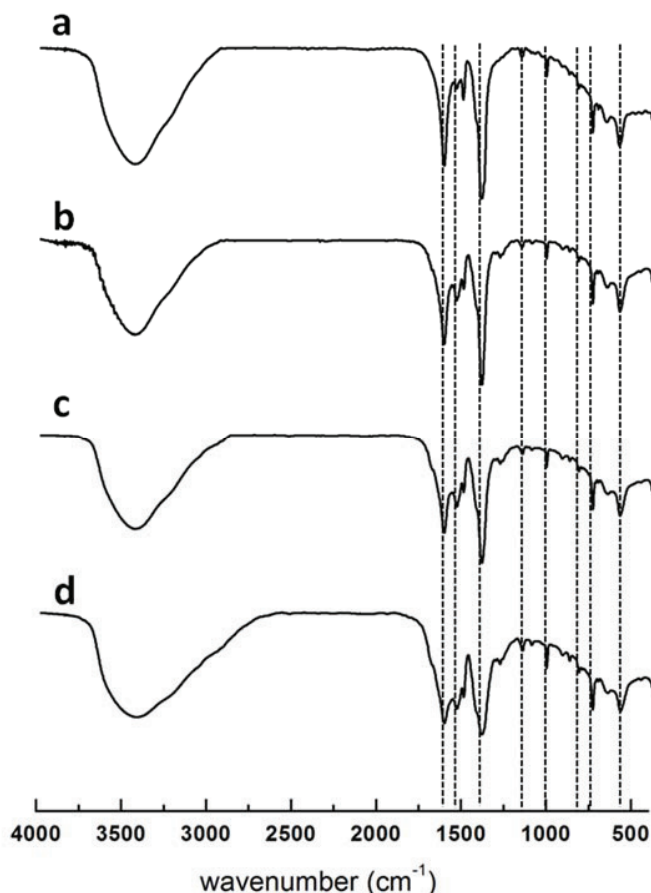


Figure 70. Infrared spectra of (a) MIL-101, (b) PtNPs@MIL-101, (c) PdNPs@MIL-101, and (d) AuNPs@MIL-101.

Due to the small size of the metal nanoparticles, the XRD patterns of the MIL-101 samples obtained before and after the metal deposition are expected to be comparable. For this reason, the XRD pattern of the MIL-101 samples obtained after the metal deposition was not recorded. The N_2 adsorption/desorption isotherms of the obtained AuNPs@MIL-101, PdNPs@MIL-101 and PtNPs@MIL-101 are shown in Figure 71. A difference in the isotherms of the samples obtained before and after the metal deposition is clearly observed. The BET surface area extracted from the N_2 sorption isotherms of the obtained AuNPs@MIL-101, PdNPs@MIL-101 and PtNPs@MIL-101 are 1236, 1098 and 1323 m^2/g , respectively. These values are much less than that of the as-synthesized sample (3384 m^2/g). The pore volume of the obtained AuNPs@MIL-101, PdNPs@MIL-101 and PtNPs@MIL-101 are 0.66, 0.72 and 0.77 cm^3/g , respectively. These values are much less than that of the as-synthesized sample (1.61

cm³/g). The appreciable decreases in surface area and pore volume could indicate that either the cavities of MIL-101 are occupied by highly dispersed metal NPs located in the pores of the material, or they are blocked by metal NPs deposited at the entrance of the MIL-101 pores. However, as mentioned before that the average hydrodynamic diameters of the particles are much larger than the average pore size of the prepared MIL-101, and thus, we suppose that the particles may not be able to penetrate into the pores of the material. Thus the second hypothesis is more reasonable.

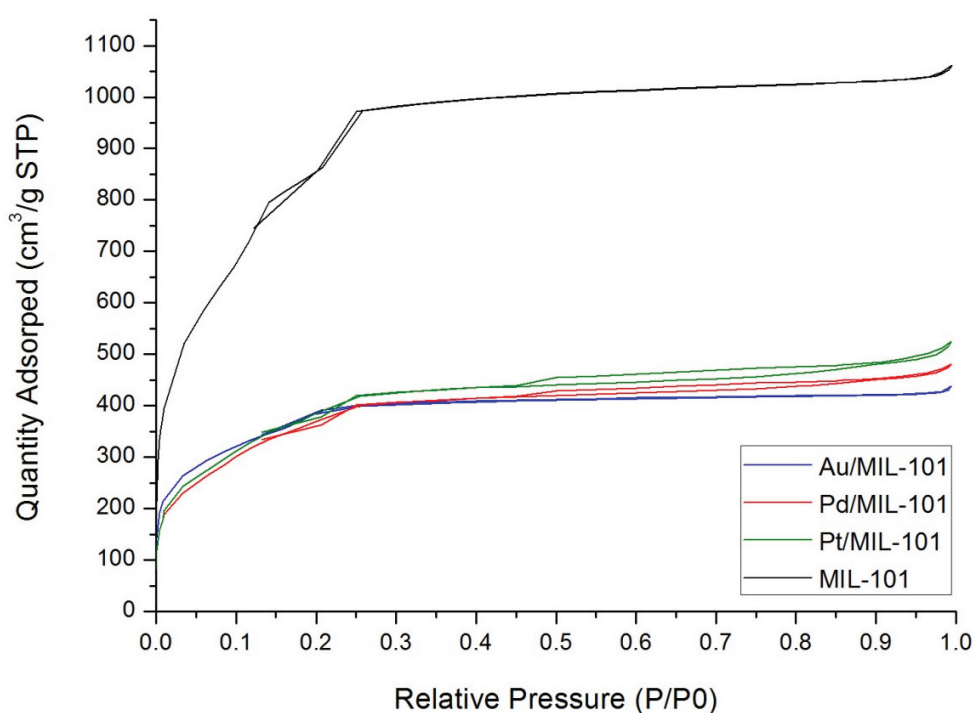


Figure 71. N₂ adsorption/desorption isotherms of the as-synthesized MIL-101 (black line), AuNPs@MIL-101 (blue line), PdNPs@MIL-101 (red line), and PtNPs@MIL-101 (green line).

The SEM and TEM images of the obtained AuNPs@MIL-101, PdNPs@MIL-101 and PtNPs@MIL-101 are shown in Figures 72, 73 and 74, respectively. It can be seen from the SEM images that the cubo-octahedral crystal structure of the MIL-101 still exists after the deposition of the metal NPs followed by the calcination at 200°C. The colloidal deposition technique used

for supporting the metal NPs onto the MIL-101 structure did not destroy the structure of MIL-101.

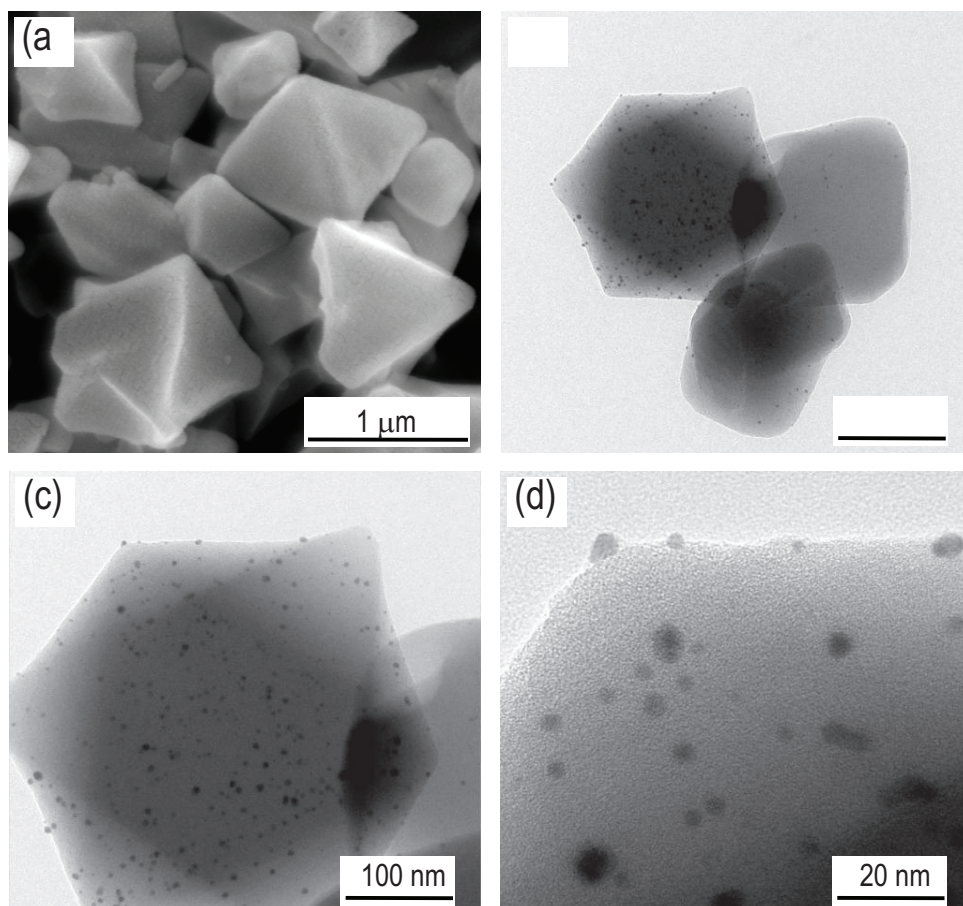


Figure 72. (a) SEM and (b-d) TEM images of the prepared AuNPs@MIL-101.

The average particle size of AuNPs in the AuNPs@MIL-101 estimated from the TEM image (see Figures 72b-d) is 2.6 ± 1.3 nm. This value is almost comparable to that of the as-prepared AuNPs, indicating that the particles do not aggregate during the deposition. We suggest that this is because the interactions of PVP and the AuNPs are strong enough to prevent the particles from aggregation. In addition, from the images, it seems that the particles are located only on the outer surface of the MIL-101 crystals.

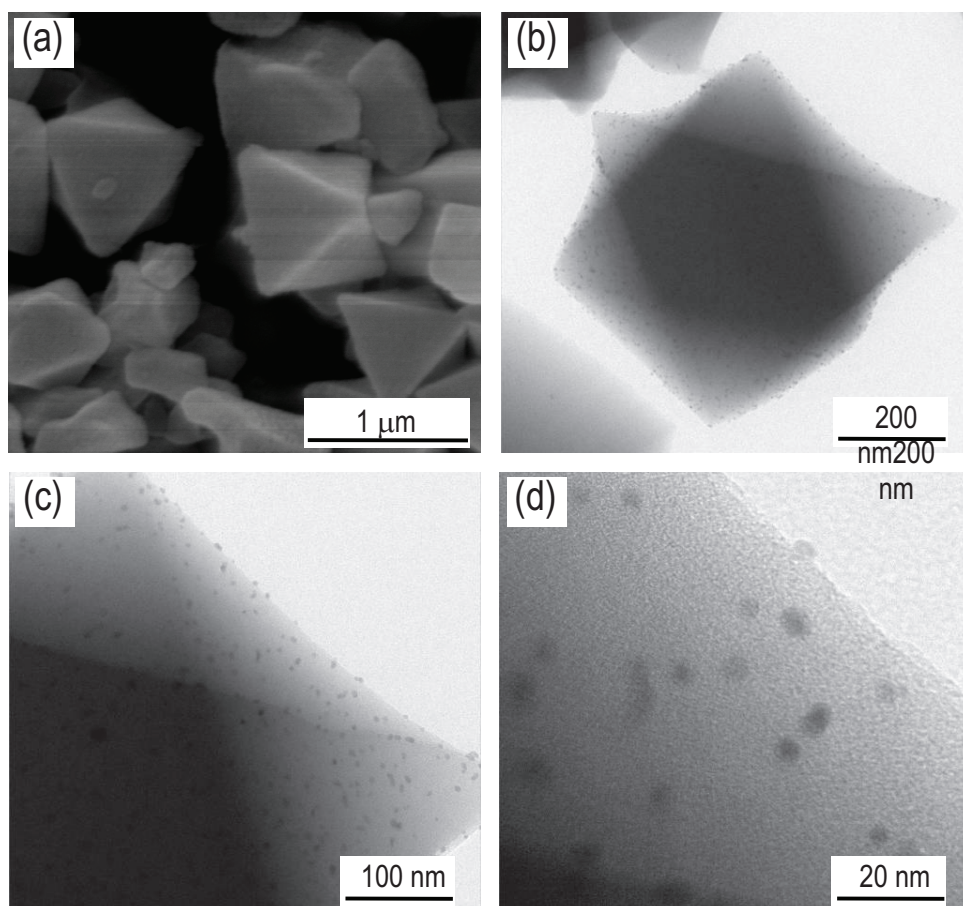


Figure 73. (a) SEM and (b-d) TEM images of the prepared PdNPs@MIL-101.

The average particle size of PdNPs in the PdNPs@MIL-101 estimated from the TEM image (see Figures 73b-d) is 2.8 ± 0.7 nm. Like in the case of AuNPs, this value is almost comparable to that of the as-prepared PdNPs indicating that the particles do not aggregate via the deposition. Thus, the interactions of PVP and the surface of PdNPs are also strong. From the TEM image, it is also likely that the particles are located only on the outer surface of the MIL-101 crystals.

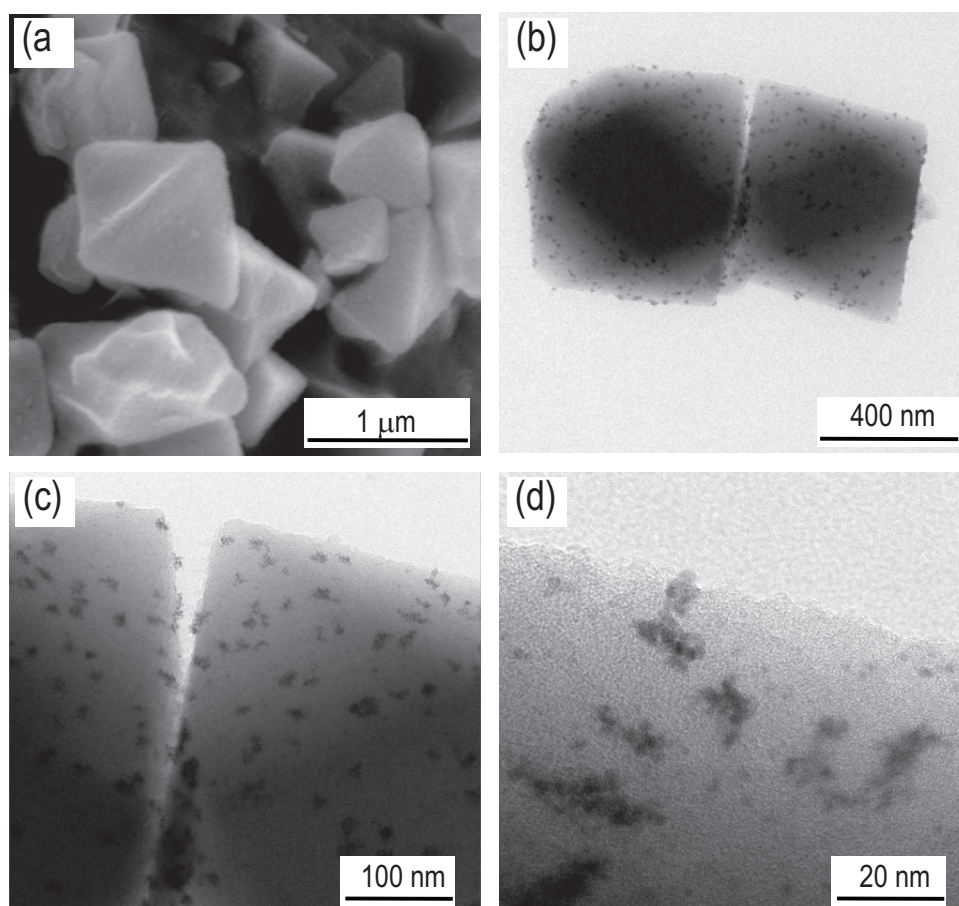


Figure 74. (a) SEM and (b-d) TEM images of the prepared PtNPs@MIL-101.

In the case of PtNPs@MIL-101, we clearly observed the aggregation of the particles from the TEM images (see Figures 74b-d), suggesting that the interactions of PVP and the PdNPs are not strong enough to prevent the particles from aggregation. Apart from the aggregates of the particles, isolated particles with a size of 1.6 ± 0.4 nm are also observed from the images. It seems that these particles are also located inside the MIL-101 crystals while the aggregates of the particles are located only onto the outer surface of the MIL-101 crystals. This suggestion will be confirmed again by using the STEM technique.

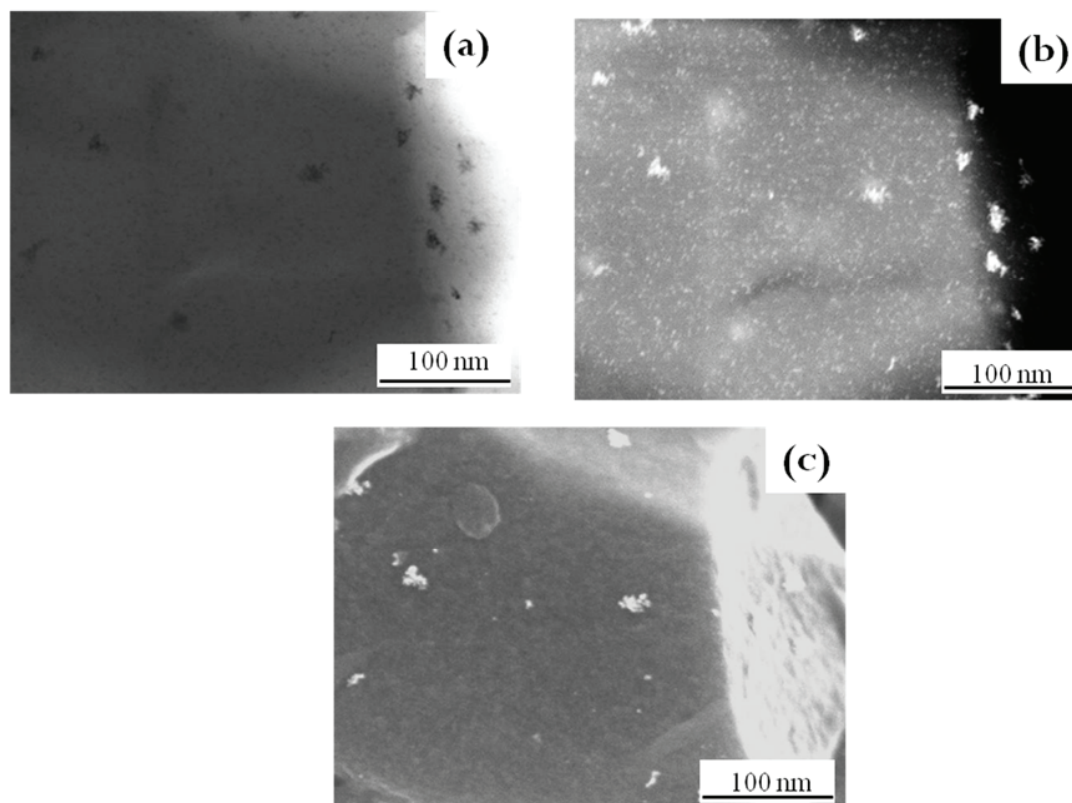


Figure 75. (a) BF- and (b) HAADF-STEM and (c) SE images taken at the same area of the prepared PtNPs@MIL-101.

Figure 75 shows the STEM images of the PtNPs@MIL-101 sample taken from the same area in three different modes, BF-, HAADF-STEM and SE. The aggregates of the Pt particles are observed in the images in three modes indicating that the particles are located on the outer surface of the MOF crystals. The Pt particles with the diameters of $\sim 1\text{-}3$ nm are clearly recognized in the BF- and HAADF-STEM images (Figures 75a-b) indicating that such small Pt nanoparticles were located inside the MIL-101 crystal. This finding supports our suggestion mentioned above about the location of the Pt particles (observed from TEM). The presence of PtNPs inside the MOF crystals leads us to suggest a weak interaction between PVP and the surface of PtNPs leading to an easy detachment of PVP from the surface of the particles during the deposition process. As the average particle size of the metal cores (~ 1.6 nm) is smaller than the pore dimension (~ 2.5 nm), the individual particles lacking the PVP stabilization can

penetrate into the pores of the MIL-101 while the aggregates of the particles (with relatively large sizes) can only adsorb onto the outer surface of the MIL-101 crystals.

3.4 Conclusions

In this work, we prepared MIL-101-supported noble metal nanoparticles (Au, Pd and Pt) by using a simple colloidal deposition followed by calcination of the metal nanoparticles stabilized by poly(N-vinyl-2-pyrrolidone) (PVP). The characterization of the as-synthesized MIL-101 confirms the characteristics of MIL-101 showing the successful synthesis achieved via a hydrothermal synthesis method. The characterization of the prepared Pd:PVP, Au:PVP and Pt:PVP nanoparticles confirm the successful synthesis of the particles with an average size of few nanometers indicating that the PVP stabilizer is efficient to provide particles with a controllable small size. The characterization of the metal NPs@MIL-101 samples reveals the successful deposition of the metal NPs onto the MIL-101 materials in all metal cases. The employed deposition technique does not destroy the original structure of MIL-101. The characterization of the obtained samples reveals that, in the case of the AuNPs@MIL-101 and PdNPs@MIL-101, the particles adsorb only at the external surface of the MIL-101 without particle aggregation. In the case of the PtNPs@MIL-101, the particles deposit mainly inside the MIL-101 crystal. Partly, they aggregate and locate onto the external surface of MIL-101. This difference might be due to the difference in the strength of the interactions between the surface of metal NPs and PVP. The interactions of PVP and the surface of AuNPs and PdNPs are strong enough to prevent the particles from the aggregation. Thus, the particles cannot penetrate inside to the pores of MIL-101 and are located at the external surface. The interactions of PVP and the surface of PtNPs are weak. Thus, PVP detaches from the surface of the particles. This allows the particles to penetrate into the pores of the MIL-101. Because PVP detaches from the surface of the particles, the particles partly aggregate, and thus a certain fraction is located at the outer surface of the MIL-101 crystals due to their large aggregate size. We expect that the preparation technique used in this case can be generalized for other metal NPs-MOF hybrid materials leading to final products that might have interesting applications in various fields including catalysis.

CHAPTER III. THEORETICAL STUDY OF METAL-ORGANIC FRAMEWORKS STRUCTURE

1. Comparison of Cu-ZSM-5 Zeolites and Cu-MOF-505 Metal-Organic Frameworks as Heterogeneous Catalysts for the Mukaiyama Aldol Reaction: A DFT Mechanistic Study

1.1 Introduction

The Mukaiyama aldol reaction is a reaction between a silyl enol ether and a carbonyl compounds which can be catalyzed by acid condition (see Figure 76). It is an important and versatile process in organic and biochemical domains (Mukaiyama, T. *et al.*, 1974). As generally known in organic chemistry, formaldehyde is one of the most versatile carbon electrophiles. However, its application is often limited by its drawback a low boiling point of $\approx 19.5\text{ }^{\circ}\text{C}$. Therefore, in order to obtain formaldehyde monomer, thermal or Lewis acid pre-treatment is used to depolymerize paraformaldehyde. Environmentally friendly porous materials such as zeolites (NaX and NaY) were proven to be good storage of molecular formaldehyde by Okachi and Onaka (Okachi, T. and M. Onaka, 2004). They demonstrated that zeolite can preserve formaldehyde molecules in monomeric form for a long time at ambient temperature and can activate the formaldehyde to react with various olefins for carbonyl-ene reactions. (see Figure 77)

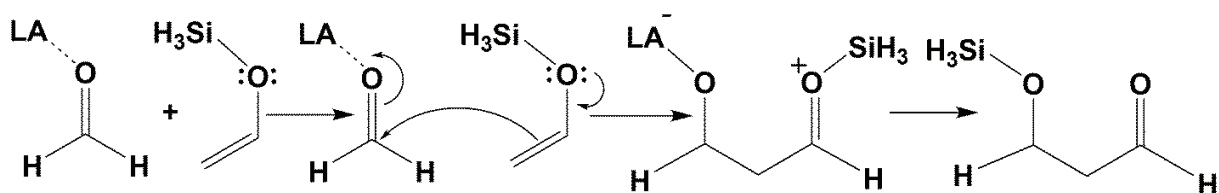


Figure 76. Mechanism for Lewis-acid (LA) catalyzed Mukaiyama aldol reaction of an aldehyde and silyl enol ether.

Zeolites are microporous molecular sieves which typically consist of interconnected tetrahedral of silicon and oxygen atoms arranged into a complex 3-dimensional arrangement of inter-connecting channels and cavities. In zeolites structures, some of the quadri-charged silicon is replaced by triple-charged aluminum, causing a deficiency of positive charge. The charge is balanced by the presence of singly- or doubly-charged atoms, such as alkaline or transition

metal, elsewhere in the structure. The question about the source of a very high activity of metal sites produced by cation exchange in a silicalite environment of framework oxygen is the important area of the research in zeolite community. One of the main points of interest in this work is the Cu^+ cation center in ZSM-5 zeolite catalyst for Mukaiyama aldol reaction. The first Cu species bonds symmetrically to two framework oxygen atoms, and the other bonds asymmetrically to three framework oxygen atoms (shown in Figure 78b). Those results agree with XAFS, IR, and UV-vis spectroscopy studies, which showed that the average coordination number of Cu is 2.5 (Lamberti, C. *et al.*, 1997).

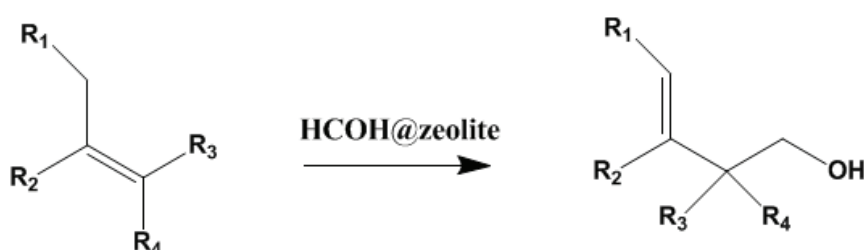
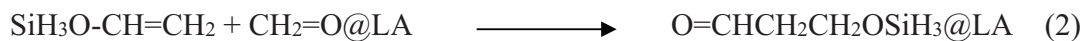


Figure 77. The carbonyl-ene reaction of various olefins and formaldehyde incorporated zeolite.

For the reaction with larger molecules, porous materials like MOFs become more advantageous because of the accessible variation of freely designed pore dimension and the systematic chemistry inside the cavity through modification of their components. In addition, MOFs can be easily synthesized under mild conditions. MOF thermal stability is known to be less optimal than conventional zeolite catalysts, but its structural flexibility, allowing tailor-made architectures to be produced, is considered a key benefit of the material.

In this work, we initially chose an open metal active MOF (Cu-MOF-505) to investigate the mechanism and catalytic efficiency with respect to the Mukaiyama aldol reaction of encapsulated formaldehyde and silyl enol ether by means of density functional calculations. We also perform an equivalent simulation within the Cu-ZSM-5 zeolite and in the gas-phase uncatalyzed system for the purpose of comparison. We suggest the fundamental steps of the reaction as follows:



where LA (Lewis Acid) = Cu-MOF-505 and Cu-ZSM-5 zeolite

Cu-MOF-505 was synthesized under analogous conditions: the solvothermal reaction of 3,3',5,5'-biphenyltetracarboxylic acid and $\text{Cu}(\text{NO}_3)_2 \cdot (\text{H}_2\text{O})_{2.5}$ in N,N-dimethylformamide (DMF)/ethanol / H_2O (3:3:2 v/v/v) at 65 °C for 24 hours gave block-shaped crystal. The compound was formulated as $[\text{Cu}_2(\text{bptc})(\text{H}_2\text{O})_2(\text{DMF})_3(\text{H}_2\text{O})]$ by elemental microanalysis and single-crystal X-ray diffraction studies. The $\text{Cu}_2(\text{CO}_2)_4$ unit is a paddlewheel unit (shown in Figure 78a) that is defined by the carboxylate carbon atoms, and the bptc⁴⁻ unit is an organic linker that is defined by the 3, 3', 5, and 5' carbon atoms. The structure consists of a cuboctahedral cage with 12 copper paddlewheels residing on the vertexes (see Figure 79).

Due to a large number of atoms per unit cell of zeolites and also MOFs, periodic ab initio calculations are computationally too demanding and expensive. Previously, we have successfully used the ONIOM approach to study several reaction mechanisms of organic molecules in zeolites and other systems of interest (Bobuatong, K. *et al.*, 2010; Boekfa, B. *et al.*, 2009; Boekfa, B. *et al.*, 2010; Kumsapaya, C. *et al.*, 2009; Maihom, T. *et al.*, 2009; Maihom, T. *et al.*, 2010; Wannakao, S. *et al.*, 2010). Therefore, we use this approach for studying the reaction mechanism of the Mukaiyama aldol reaction between the encapsulated formaldehyde molecule and silyl enol ether on MOF-505 and Cu-ZSM-5. Nonetheless, theoretical chemistry consideration of MOF as a heterogeneous catalyst is currently very limited in the literatures (Choomwattana, S. *et al.*, 2008; Yang, Q. and C. Zhong, 2005).

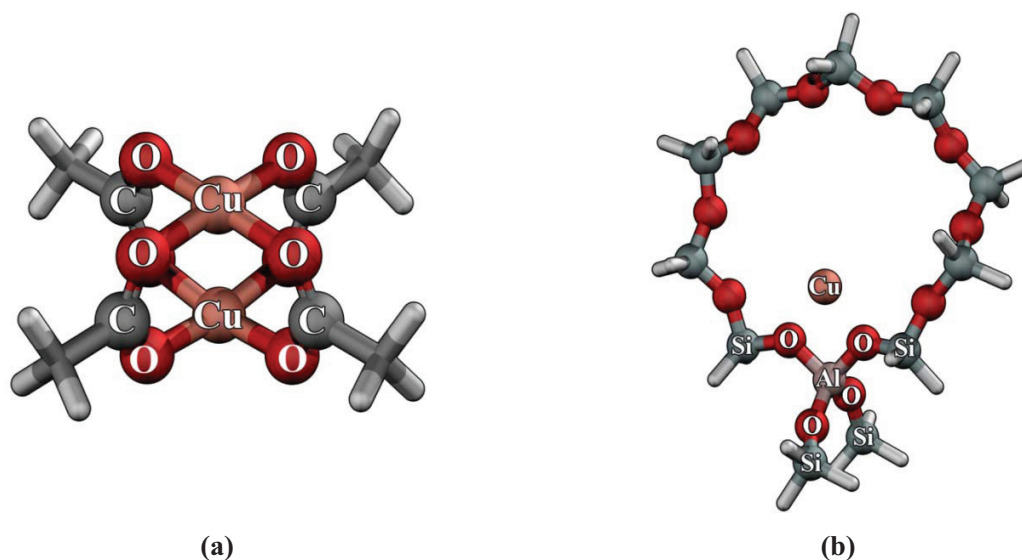


Figure 78. The structures representation of catalytic active sites of (a) Cu-MOF-505 and (b) Cu-ZSM-5

1.2 Models and Computational Methods

Both Cu-ZSM-5 and MOF-505 structures are obtained from the XRD data (Chen, B. *et al.*, 2005b, 2005a). In the ONIOM model, the system is separated into two parts. The inner cluster consists of the active region, typically treated by the density functional theory. The M06-L density functional (Zhao, Y. and D. G. Truhlar, 2008b, 2008a) with 6-31G(d,p) basis set has been employed to account for the interactions of adsorbates with the porous structure and their chemical reactions. The M06-L functional was demonstrated to give the best results for heavy-atom-transfer barrier height calculations as well as with dispersion-like interactions cases (Zhao, Y. and D. G. Truhlar, 2006). Those interactions are essential as they are relevant in our present chemical reaction studies. The outer layer represents the environmental framework, described by a UFF, to account for the van der Waals interactions between adsorbates and the extended structure of the catalytic materials. To obtain more accurate interaction energies, single-point calculations with the ONIOM(M06L/6-311++G(2df,2p):UFF) method were carried out. To estimate the basis set superposition error (BSSE), the atoms involved in the QM region of the final converged geometries, obtained from the ONIOM optimization, were terminated this active cluster with hydrogen atoms. From this model, the BSSE is estimated by calculating the single-point counterpoise correction (Boys, S. F. and F. Bernardi, 1970; Simon, S. *et al.*, 1996). With the

BSSE values of 4-10 kJ/mol for the molecular adsorption complexes, the trends of catalytic activity over these active sites are not affected. Accordingly, the BSSE correction could be neglected. Our previous publications have demonstrated that the series of this methodology can reproduce experimental results and successfully be applied in various systems of interest.

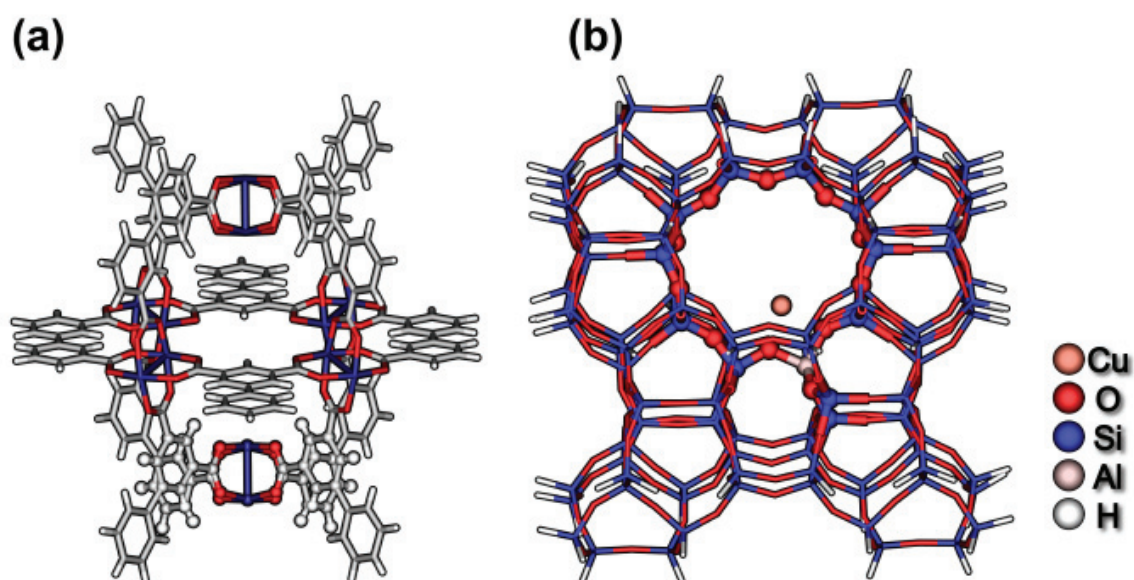


Figure 79. The computational models of (a) MOF-505 and (b) Cu-ZSM-5 in which the high layer (DFT region) is represented in ball-bond style and the low layer (UFF) is represented by line style.

The paddlewheel unit of the Lewis acid site, illustrated in Figure 79a, is assigned to be the inner layer, whereas the extended framework forming into the oval-shaped cavity (five paddlewheel units and twelve units of 3,3',5,5'-biphenyl-tetracarboxylic acid) is the outer layer. Only the active region ($\text{Cu}_2(\text{CO}_2)_4(\text{C}_6\text{H}_3)_4$) and the probe molecule are allowed to relax while the rest is kept fixed with the crystallographic structure. The framework environment constitutes the outer ONIOM layer. For the Cu-ZSM-5 crystal structure, there are twelve symmetrically nonequivalent tetrahedral framework positions known as T-sites. The active region consists of the 12T ring, representing the acidic site of zeolite and that of the reactive molecules (shown in Figure 79b), whereas the rest of the framework is included into the calculation with the universal

force field. For the MOF-505 catalyst, the monomeric Cu(II) ions have an electron spin $S=1/2$ as the doublet spin state. The electronic state of the Cu(II) ions dimers in the paddle wheel building blocks of the MOF-505 frameworks are considered both closed-shell (singlet) and open-shelled complex (triplet state). The spin state that provided the lowest energy was used as the ground state of this complex. The triplet is found to be more stable than the singlet state by about 46 kJ/mol. Therefore, the chemical reaction over this unit is considered as the triplet state which is in accordance with the experiment about the characteristic of dimeric Cu(II) paddle wheel (Pöppl, A. *et al.*, 2008). In the case of the Cu-ZSM-5 catalyst, the Cu cation compensating the negative charge in the zeolite framework has an oxidation number of +1. The ground state is thus the singlet spin state similar to that used in the literature (Nachtigall, P. *et al.*, 2000). Therefore, the spin multiplicity of all steps belonging the Cu-ZSM-5 was considered singlet state. The Wiberg bond indices (Wiberg, K. B., 1968) were computed using the natural bond orbital (NBO) method. All calculations were performed with the Gaussian 03 program (Frisch, M. J. T. *et al.*,)

1.3 Results and discussions

We separate the topics into 3 sections. In the first section we discuss the existence and reactivity of encapsulated formaldehyde in MOF-505 (HCOH@MOF-505). We predict the interactions of MOF-encapsulated formaldehyde with silyl enol ether (HCOH@MOF-505/H₃SiOHC=CH₂). In the second section, we describe the proposed mechanism of the Cu-ZSM-5 catalyzed reaction (HCOH@Cu-ZSM-5/H₃SiOHC=CH₂). Finally, in the third section we make the comparison of the two cases with the reaction without any Lewis acid catalyst. From previous work, it was proposed that the Mukaiyama aldol reaction between silyl enol ether and formaldehyde occurs via a concerted mechanism (Wong, C. T. and M. W. Wong, 2004). Therefore, we considered this mechanism in our systems.

1.3.1 MOF-505-Encapsulated Formaldehyde (HCOH@MOF-505) and Its Mukaiyama Aldol Reaction with Silyl Enol Ether (HCOH@MOF-505/H₃SiOHC=CH₂)

MOF-505 consists of Cu₂(CO₂)₄ paddlewheel units linked together by the 3,3',5,5'-biphenyl-tetracarboxylic acid units to form an oval-shaped cavity as presented in Figure 79a. From our calculation, formaldehyde initially adsorbs over the paddlewheel active site via a lone pair electron interaction with an adsorption energy of -50 kJ/mol. From Figure 80a, the Cu unit

(Cu1-Cu2) is almost unchanged upon the adsorption of formaldehyde (0.06 Å and 4° for changes in Cu1-Cu2 bond distance and O1-Cu-O3 bond angles, respectively). The carbon-oxygen bond of formaldehyde is elongated from 1.20 to 1.21 Å. According to the interaction between the hydrogen atoms of formaldehyde and the oxygen atoms of the framework, the corresponding distance between the formaldehyde oxygen and the Cu atom of MOF-505 active site is 2.32 Å (see Table 1) and the C_f-O_f...Cu/MOF angle is 112.8°. The active Cu atom moves slightly out of the paddlewheel upper plane toward the adsorbing molecule. This behavior agrees reasonably with an experimental report of the upper copper atom moving slightly out of the plane and the Cu-Cu bond lengths being elongated from 2.50 Å to 2.64 Å when absorbed with water molecules (Prestipino, C. *et al.*, 2006). Subsequently, the second reactant, silyl enol ether, binds to the complex (see Figure 80b) via a π interaction with a co-adsorption energy of -110 kJ/mol. This predicted coordinate fits the requirement necessary to allow the chemical reaction to proceed to form the 3-silyloxy-propanal. The silyl enol ether Si-O5 bond length is stretched from 1.68 to 1.76 Å, and the distance between the silicon group (Si) and the formaldehyde oxygen (O_f) is shortened from 2.91 to 2.29 Å. The C_f-O_f double bond of formaldehyde is changed from 1.22 to 1.28 Å as the distance between the silyl enol ether carbon (C1) and formaldehyde carbon (C_f) is contracted from 2.87 to 2.02 Å.

Table 1. Optimized geometric parameters of the isolated state, formaldehyde adsorption, coadsorption complex, transition state, and product of the Mukaiyama aldol reaction between formaldehyde and silyl enol ether on MOF-505 using the ONIOM (M06L/6-31G(d,p):UFF) method.

Parameter	Isolated molecule	Formaldehyde adsorption	Coadsorption complex	Transition state	Product
Distance (Å)					
Cu1-Cu2	2.53	2.59	2.60	2.63	2.60
Cu1-O1	1.95	1.95	1.97	1.97	1.95
Cu1-O2	1.95	1.97	1.97	1.99	1.96
Cu1-O3	1.95	1.97	1.95	1.96	1.97
Cu1-O4	1.95	1.95	1.96	1.96	1.97
Cu1-O _f	-	2.32	2.29	2.23	2.34
C _f -O _f	1.20	1.21	1.22	1.28	1.43
C _f -C1	-	-	2.87	2.02	1.52
C1-C2	1.33	-	1.34	1.38	1.51
C2-O5	1.36	-	1.34	1.29	1.21
O5-Si	1.68	-	1.68	1.76	4.96
O _f -Si	-	-	2.91	2.29	1.69
Angle (degrees)					
∠ O1-Cu1-O3	176.7	172.7	172.7	170.4	172.8
∠ O2-Cu2-O4	176.7	173.0	172.8	170.7	172.8

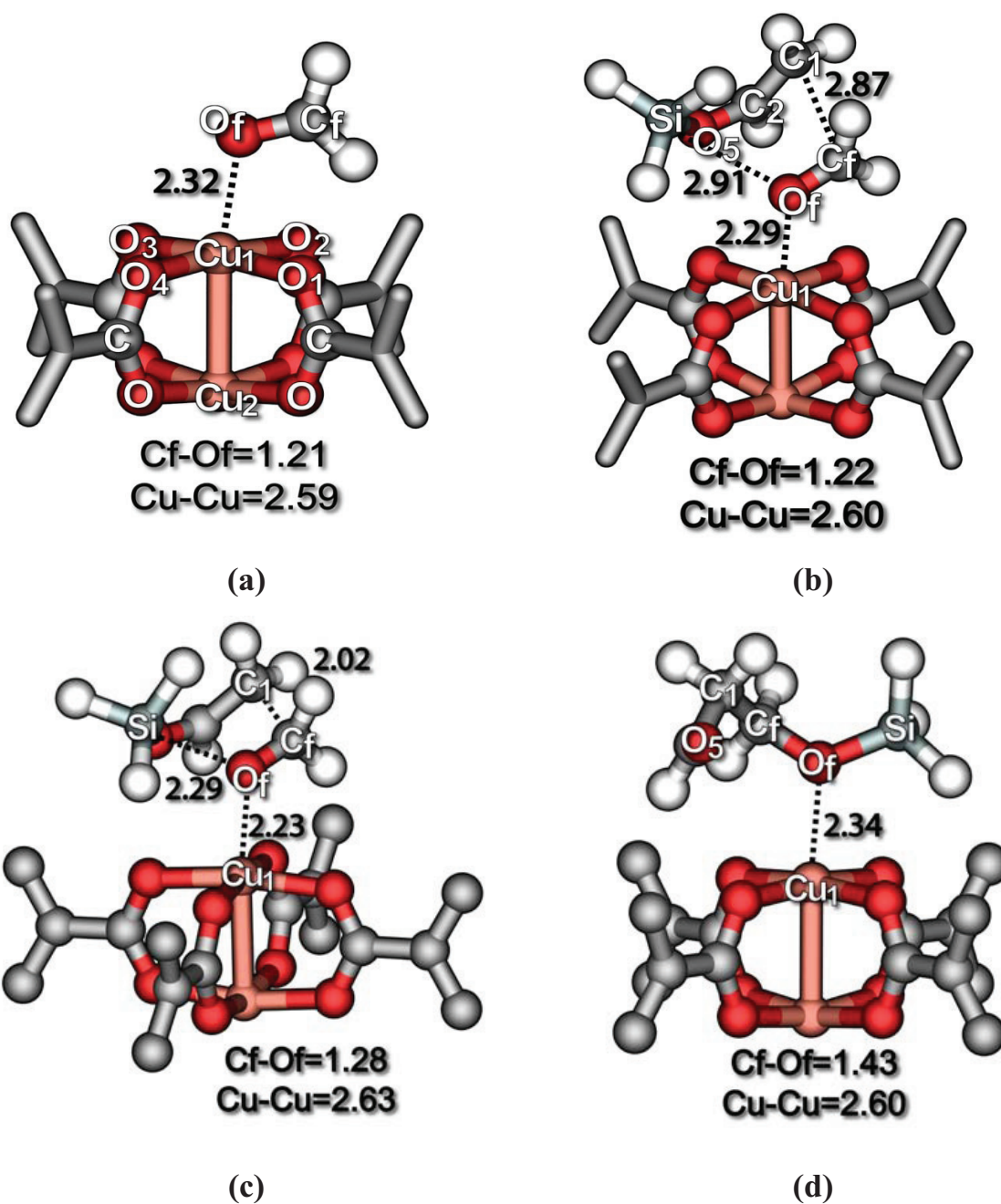


Figure 80. Optimized structures of the HCOH@MOF505/ H₃SiOHC=CH₂ (a) HCOH@MOF-505; (b) HCOH@MOF505 /H₃SiOHC=CH₂ complex; (c) transition state structure and (d) H₃SiOCH₂CH₂CHO@MOF-505 structure (distances in Å).

For all three studied scenarios (MOF-505, Cu-ZSM-5 and gas-phase) of the Mukaiyama aldol reaction, a concerted mechanism is predicted in which bond between the carbon atom of formaldehyde (C_f) and the silyl enol ether ($C1$) is formed and the silicon group transferred (as presented in Figure 80c). The proposed concerted pathway is supported by a calculated transition state with a single imaginary frequency. For MOF-505, the activation energy is 48 kJ/mol. The Mukaiyama aldol reaction is found to be exothermic by -198 kJ/mol. Finally, the adsorbed propanal requires 91 kJ/mol to desorb from the active site (see Figure 80d).

1.3.2 Cu-ZSM5-Encapsulated Formaldehyde ($HCOH@Cu-ZSM5$) and Its Mukaiyama Aldol Reaction with Silyl Enol Ether ($HCOH@Cu-ZSM5/H_3SiOHC=CH_2$)

The structure of the cation-exchange site, the location of the Al in the site, was previously explored. Ab initio studies and lattice energy minimizing calculations showed that T12 is one of the most stable sites for Al substitution and it is believed to be the active center (Alvarado-Swaisgood, A. E. *et al.*, 1991; Derouane, E. G. and J. G. Fripiat, 1985). Cu^+ was found to have a 2-fold coordination to framework O atoms when present at the intersections of the straight and sinusoidal exchange site. ZSM-5 zeolite exchanged with Cu^+ cations [$Cu(I)$ -ZSM-5] is an active catalyst (as presented in Figure 78b). X-ray adsorption fine structure (EXAFS) data shows the Cu^+ is both doubly and triply coordinated to oxygen atoms with an average coordination number of ~ 2.5 (Lamberti, C. *et al.*, 1997). Davidova et al. also suggested that Cu^+ at this configuration site is very reactive for activating chemical reaction (Davidová, M. *et al.*, 2004). Figure 81a displays the structure of adsorbed formaldehyde in the Cu-ZSM-5 zeolite framework. Formaldehyde first interacts with the active Cu^+ Lewis acid site by its lone pair electron (see Figure 81a). The carbon-oxygen bond of formaldehyde is consequently elongated from 1.20 Å to 1.23 Å (see Table 2). The intermolecular distance, measured between the formaldehyde oxygen and the Cu atom, is 1.85 Å and the corresponding adsorption energy is -159 kJ/mol. The silyl enol ether molecule then diffuses over the adsorbed formaldehyde on the Cu-ZSM-5 (see Figure 81b) with a co-adsorption energy of -270 kJ/mol. The proposed concerted pathway is supported with the calculated transition structure whose imaginary frequency belongs to the mode in which the C_f-C1 bond is formed and the silicon group is transferred (see Figure 81c). At this state, the activation energy is found to be 21 kJ/mol. The relative energy of the

adsorbed 3-silyloxy-propanal product is exothermic by -316 kJ/mol and it requires 209 kJ/mol to desorb from the active site in the final step (see Figure 81d).

Table 2. Optimized geometric parameters of the isolated state, formaldehyde adsorption, coadsorption complex, transition state, and product of the Mukaiyama aldol reaction between formaldehyde and silyl enol ether on Cu-ZSM-5 using the ONIOM (M06L/6-31G(d,p):UFF) method.

Parameters	Isolated molecule	Formaldehyde adsorption	Coadsorption complex	Transition state	Product
Distance (Å)					
Cu-O _f	-	1.85	1.89	1.88	1.95
Cu-Al	2.76	2.74	2.78	2.87	2.71
Cu-O1	1.97	1.99	2.08	1.92	2.22
Cu-O2	2.06	2.10	2.08	2.58	1.98
Al-O1	1.71	1.71	1.70	1.72	1.69
Al-O2	1.71	1.71	1.71	1.68	1.72
Si1-O1	1.61	1.61	1.60	1.61	1.60
Si2-O2	1.59	1.59	1.58	1.57	1.59
C _f -O _f	1.20	1.23	1.23	1.29	1.46
C _f -C1	-	-	2.84	1.95	1.51
C1-C2	1.33	-	1.34	1.38	1.51
C2-O3	1.36	-	1.34	1.31	1.21
O3-Si	1.68	-	1.70	1.73	3.93
O _f -Si	-	-	3.70	2.90	1.73
Angle (degrees)					
∠ Si1-O1-Al	127.4	127.1	127.6	127.7	126.1
∠ Si2-O2-Al	132.0	132.1	132.4	132.2	131.9
∠ O1-Cu-O2	75.2	73.2	72.1	65.1	71.3
∠ O1-Al-O2	91.9	91.1	91.8	93.9	91.7

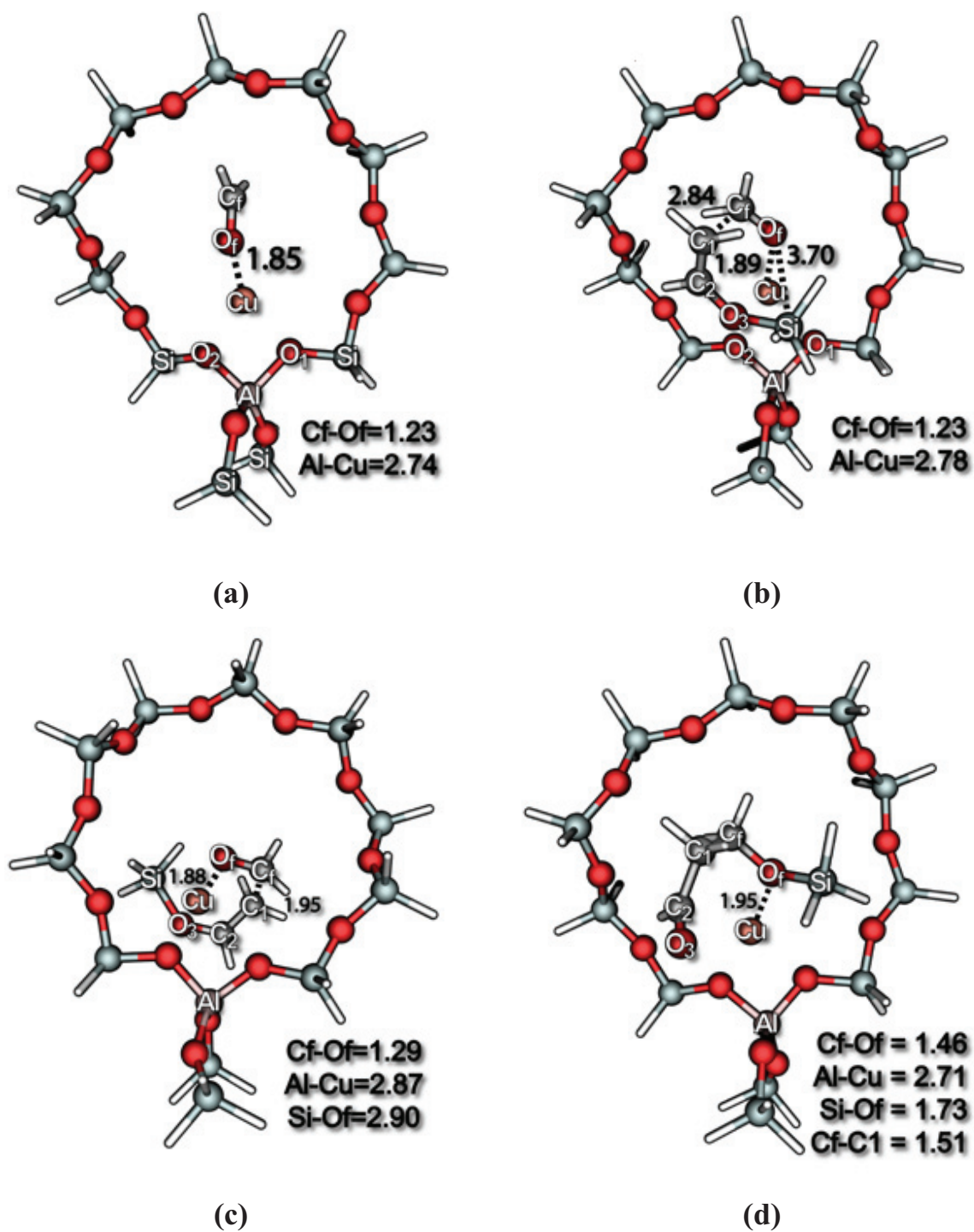


Figure 81. Optimized structures of the HCOH@Cu-ZSM-5/H₃SiOHC=CH₂ (a) HCOH@Cu-ZSM-5; (b) HCOH@Cu-ZSM-5/H₃SiOHC=CH₂ complex; (c) transition state structure and (d) H₃SiOCH₂CH₂CHO@Cu-ZSM-5 structure (distances in Å).

1.3.3 Comparison of the Two Catalyzed Cases with the Reaction without any Lewis Acid Catalyst

The energy diagrams of the three systems are given in Figure 82. The activation barriers for the MOF-505, Cu-ZSM-5, and gas-phase system are 48, 21, and 61 kJ/mol, respectively. Our prediction for the uncatalyzed gas-phase reaction agrees with the previous calculation with the MP2/6-31G(d) level of theory by Gung et al. (activation energy = 58 kJ/mol) (Gung, B. W. *et al.*, 1995)

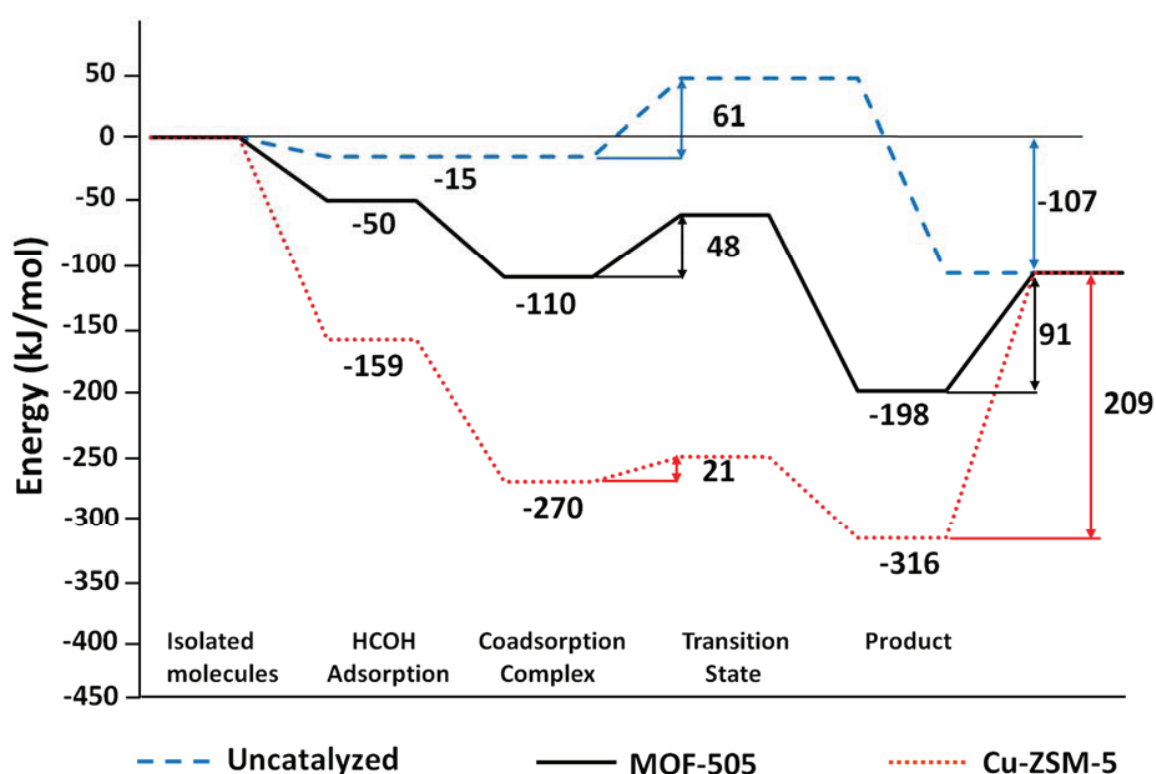


Figure 82. Calculation energy profiles (kJ/mol) for the Mukaiyama aldol reaction between formaldehyde and silyl enol ether in the MOF-505 system (solid line), the Cu-ZSM-5 system (dotted line) and the gas phase system (dashed line).

The activation energy indicates that the reaction studied here can easily occur at ambient temperature. However, the Mukaiyama aldol condensation reaction was specifically designed to prevent the undesired self condensation of formaldehyde through the use of a Lewis acid catalyst which can also impose steric constraints on the reaction. In a review concerning the uncatalyzed

reaction from previous experiments, Wong et al. found that the acidity of silicon on the silyl enol ether must be increased so that the Mukaiyama aldol reaction to proceed without a catalyst. The presence of a framework environment to envelop the reacting species not only stabilizes the reacting species but also provides a number of reaction promoting factors, such as adsorption stability, the chance enhancements of the collision in the correct orientation and the re-collision till the accumulating energy rises above the activation barrier.

From the energy diagrams in Figure 82, it is that MOF-505 and Cu-ZSM-5 can catalyze the Mukaiyama aldol reaction between the carbonyl compound and silyl enol ether. Both MOF-505 and Cu-ZSM-5 catalysts stabilize the species formed along the reaction coordinate, lowering the activation energy, compared to the uncatalyzed reaction. The Wiberg bond order as shown on Figure 83 depicted the evaluation of bond forming and bond breaking of reactants on the aldol reaction. The elongation of the C1-C2 bond of silyl enol ether from double bond character to single bond character is observed. During the C1-C2 bond breaking, the C1-C_f and the Si-O_f bond forming also occurred concurrently, leading to the single bond character at the aldol product. These observations are found on both the MOF-505 and ZSM-5 materials.

Table 3. NBO-Wiberg bond orders of reactants, transition states and products in Mukaiyama aldol reaction catalyzed by MOF-505. Values obtained at M06L/6-31G(d,p) level.

Bond types	HCOH@MOF505		Transition state structure	H ₃ SiOCH ₂ CH ₂ C HO@MOF-505
	HCOH@MOF505	/H ₃ SiOHC=CH ₂ complex		
C _f -O _f	1.866	1.771	1.359	0.882
C _f -C ₁	0.000	0.057	0.451	1.013
Si-O _f	0.000	0.024	0.138	0.570
C ₁ -C ₂	1.903	1.818	1.452	1.002

Table 4. NBO-Wiberg bond orders of reactants, transition states and products in Mukaiyama aldol reaction catalyzed by Cu-ZSM-5. Values obtained at M06L/6-31G(d,p) level.

Bond types	HCOH@Cu-ZSM-5	HCOH@ Cu-ZSM-5 /H ₃ SiOHC=CH ₂ complex	Transition state structure	H ₃ SiOCH ₂ CH ₂ CH ₂ OH@ Cu-ZSM-5
C _f -O _f	1.686	1.635	1.307	0.838
C _f -C ₁	0.000	0.081	0.497	1.023
Si-O _f	0.000	0.004	0.035	0.515
C ₁ -C ₂	1.903	1.794	1.428	0.990

As the aspect from the Wiberg bond order alterations, one may notice the more metal-assisted activation of formaldehyde in Cu-ZSM-5 than in MOF-505 (see Tables 3 and 4). The bond order of the carbonyl bond of formaldehyde is decreased significantly from 1.94 to 1.69 while a slight change is found on the MOF-505. This reveals that there is more electrophile of carbonyl carbon of H₂CO@Cu-ZSM-5 complex than that of the H₂CO@MOF-505 for condensation with the silyl enol ether. In the formaldehyde adsorption to MOF-505 and Cu-ZSM-5, both Lewis acid catalysts made a carbon atom of formaldehyde more positive, i.e., 0.248e (MOF-505) and 0.289e (Cu-ZSM-5), which can be attacked by a carbon nucleophile such as the carbon in silyl enol ether. Additionally, the oxygen atom of formaldehyde has negative charge, i.e., -0.488e (MOF-505) and -0.594e (Cu-ZSM-5). This inductive effect results in the total charge of the reacting species in the transition state of the Cu-ZSM-5 system (0.129e) being more positive than that of the MOF-505 system (0.095e) (see Figure 83). These charge distribution differences arise as a result of both the differences in the catalytic framework and the distinct variation in Cu coordination in the two materials, which is expected to affect the Lewis acid strength. The Cu cation embedded in the zeolite and was found to have a two-fold coordination (CN=2) to the framework O atoms, whereas the Cu cation in MOF-505 has a five-fold coordination (CN=5). As a consequence, the positive charge of the Cu cation is reduced due to the distribution to its connecting atoms. The larger the CN, the smaller the effective metal cation charge becomes. According to the reaction mechanism, silyl enol ether behaves as a nucleophile and attacks at the formaldehyde's carbonyl carbon. Therefore, the smaller the energy

difference between a LUMO level of formaldehyde and a HOMO level of silyl enol ether (noted as $\text{LUMO}^{\text{ele}}\text{--HOMO}^{\text{nuc}}$ energy gap) makes the electron transfer easier when the nucleophilic attack proceeds. From the orbital energy point of view, the $\text{LUMO}^{\text{ele}}\text{--HOMO}^{\text{nuc}}$ energy gap is reduced in the reaction of the MOF-505 and Cu-ZSM-5 systems. The $\text{LUMO}^{\text{ele}}\text{--HOMO}^{\text{nuc}}$ energy gap of the gas-phase system was calculated to be 3.76 eV. It is decreased to 3.15 and 2.26 eV for MOF-505 and Cu-ZSM-5 systems, respectively. As a consequence, MOF-505 and Cu-ZSM-5 were found to be good Lewis catalysts as they are more efficient in facilitating the electron transfer than the gas-phase system. The main advantage of MOFs over zeolites such as ZSM-5 is the weak adsorption of the reacting substrates. The reaction therefore requires less energy for the product desorption. The relatively weak adsorption of adsorbate-MOF has been presented in the MOF application as gas storage. Besides the promising application, MOFs can be constructed from design building blocks, the pore size depending on the size of the organic ligand. The ability to modify functional groups into porous MOFs makes them excellent candidates as heterogeneous catalysts. The well-defined pores in MOFs and zeolites have the potential to endow them with the size- and shape-selective catalysis. In these fields a comparison with zeolites can be made. Although zeolites as well as MOFs are networks, the topology of zeolites is rather limited because they are mainly constructed of tetrahedral Al and Si units. Therefore, the pores in MOFs can have different geometries and sizes compared to zeolites. Since chirality can be introduced into the reaction through the choice of appropriate building blocks, MOFs can be further developed to be chiral catalysts that improve the reaction selectively, another advantage over other conventional porous catalysts.

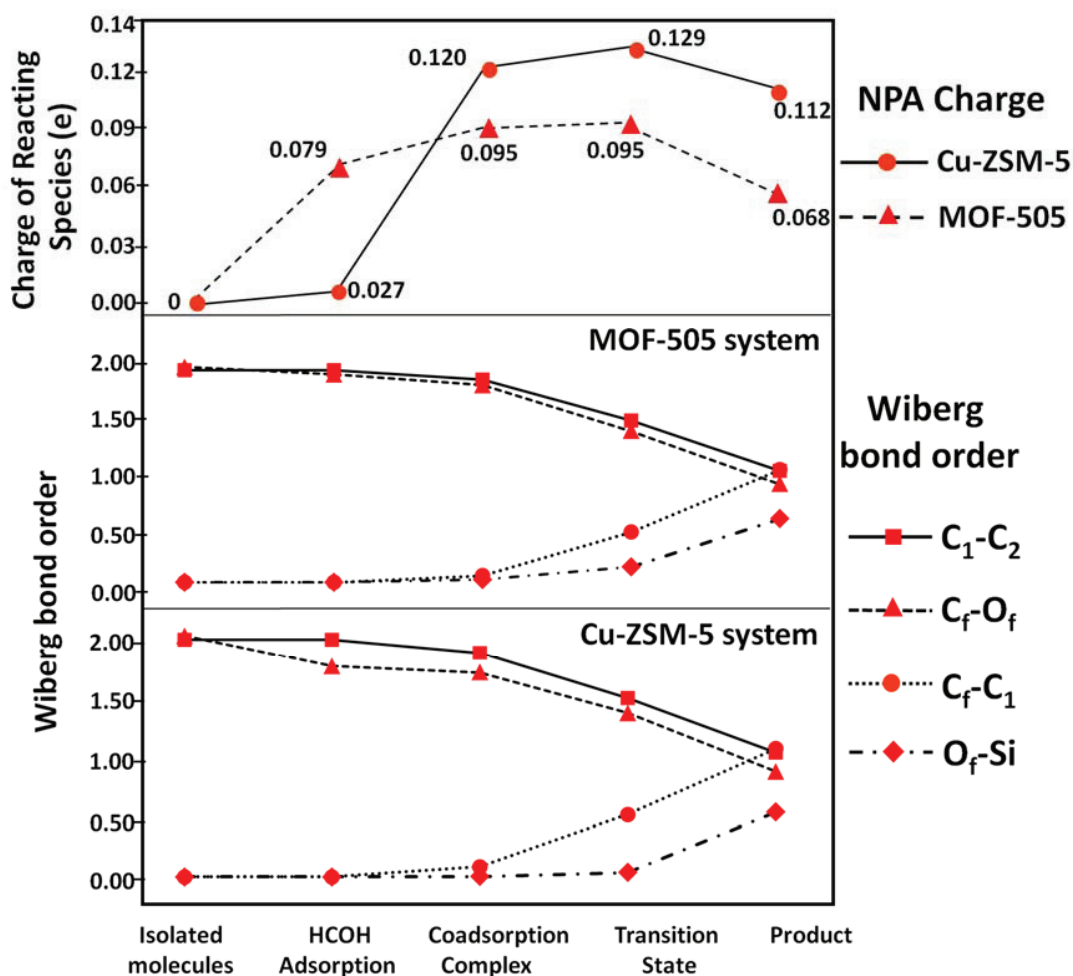


Figure 83. The natural population analysis (NPA) of the total charge of the reacting species and Wiberg bond order of the important bonds along the Mukaiyama aldol reaction catalyzed by MOF-505 and Cu-ZSM-5.

1.4 Conclusions

Density-functional theory and the ONIOM approach have been used to compare the catalytic efficiency between a metal-organic framework (MOF-505) and a zeolite (Cu-ZSM-5) on the Mukaiyama aldol reaction of formaldehyde and silyl enol ether. The reaction mechanism is proposed to be an intermediate-free, concerted process, consisting of the silyl group transfer and the carbon-carbon bond formation. Both MOF-505 and Cu-ZSM-5 contain copper cations

which behave as a Lewis acid. Not only is it the acidic character in both catalysts that is predicted to reduce the energy barrier, it was also found that environmental inclusion of the MOF and zeolite framework has a beneficial effect on the structure and energetics of the adsorption complexes. It lowers the energy barrier ($\Delta E_{\text{act}} = 48$ and 21 kJ/mol) of the reaction compared to the bare model system (61 kJ/mol). MOF-505 and Cu-ZSM-5 catalysts induce the carbon atom of formaldehyde to be more positive, which can thus be attacked more easily by the nucleophiles. The FMO analysis results confirm that both Cu-ZSM-5 and MOF-505 are good catalysts for the reaction between formaldehyde and silyl enol ether. Moreover, it was found that the total charge of the reacting species in the transition state over the Cu-ZSM-5 ($0.129e$) system were more positive than those over the MOF-505 system ($0.095e$). Therefore, Cu-ZSM-5 was also found to be a more efficient catalyst than MOF-505 in facilitating the electron transfer during the reaction.

2. Cycloaddition Reaction of Carbon Dioxide and Ethylene Oxides over Homo-metallic and Hetero-metallic Paddlewheel Clusters: A Mechanistic DFT Study

2.1 Introduction

Carbon dioxide (CO₂) is known to be the major greenhouse gas that contributes to the problem of global warming. However, it is regarded as an abundant, inexpensive and green C1 resource (Sakakura, T. *et al.*, 2007). Presently, the use of carbon dioxide as a feedstock in the chemical industry has received growing interest for economic and environmental reasons. (see in Figure 84) One of the promising processes in this field is the reaction of carbon dioxide with epoxides to produce cyclic carbonates. Cyclic carbonates are valuable chemicals, which can be used as aprotic polar solvents, fine chemical intermediate and starting materials for the synthesis of polymers and engineering plastics (Shaikh, A.-A. G. and S. Sivaram, 1996). A variety of catalysts have been developed and used in this reaction such as homogeneous catalysts of phosphonium salts, quaternary ammonium salts, alkali metal halides, ionic liquids, Schiff bases, metal complexes (Fujita, S.-i. *et al.*, 2010; He, L.-N. *et al.*, 2003; Kawanami, H. *et al.*, 2003; Kim, H. S. *et al.*, 2002; Sun, J. *et al.*, 2006; Sun, J. *et al.*, 2008; Xie, Y. *et al.*, 2007; Yasuda, H. *et al.*, 2002; Yasuda, H. *et al.*, 2005; Yasuda, H. *et al.*, 2006; Zhao, Y. *et al.*, 2007), and also heterogeneous catalysts containing metal oxides or titanosilicates in zeolites and metal-organic frameworks (MOFs) (Macias, E. E. *et al.*, 2012; Miralda, C. M. *et al.*, 2011; Song, J. *et al.*, 2009; Srivastava, R. *et al.*, 2005b; Srivastava, R. *et al.*, 2003, 2005a; Yamaguchi, K. *et al.*, 1999; Yano, T. *et al.*, 1997; Zalomaeva, O. V. *et al.*, 2013; Zhou, X. *et al.*, 2012)

In the past decades, catalysis by dinuclear transition metal paddlewheel complexes has received an increasing interest (Hansen, J. and H. M. L. Davies, 2008). Because of the unsaturated metals exposed on the surface of these complexes, they have been remarkably successfully for catalyzing reactions such as cyclopropanation, C-H functionalization, ylide formation (Doyle, M. P., 2006; Hansen, J. and H. M. L. Davies, 2008). They are also active catalysts in metal nitrene chemistry and in Lewis acid-catalyzed cycloadditions (Doyle, M. P., 2006; Hansen, J. and H. M. L. Davies, 2008). The reactivity of these metal complexes can also be enhanced by combining two different types of metal in the paddlewheel unit to form hetero-metallic catalysts, which were reported to have better performances than their homo-metallic equivalents (Wheatley, N. and P. Kalck, 1999; Yamagiwa, N. *et al.*, 2005). With a combination of metals in hetero-metallic catalyst, the stronger Lewis acid site may be found on either of the two metals. This metal site is expected to serve as a good Lewis acid active site for catalyzing the reaction of CO₂ with epoxides.

We investigate here the cycloaddition reaction mechanism of the carbon dioxide and epoxides on the homo-metallic, Mo/Mo trifluoroacetate $[\text{MoMo}(\text{O}_2\text{CCF}_3)_4]$ and Rh/Rh trifluoroacetate $[\text{RhRh}(\text{O}_2\text{CCF}_3)_4]$, and hetero-metallic, Mo/Rh trifluoroacetate $[\text{MoRh}(\text{O}_2\text{CCF}_3)_4]$ and Rh/Mo trifluoroacetate $[\text{RhMo}(\text{O}_2\text{CCF}_3)_4]$, with Density Functional

Theory (DFT) using the M06-L method (Zhao, Y. and D. G. Truhlar, 2008b, 2008a). In this system the first metal is the active site. Ethylene oxide was used as a model epoxide. The homo-metallic and hetero-metallic compounds were synthesized and characterized previously (Li, B. *et al.*, 2007). We have calculated the energy profile for all catalytic system and particularly focused on the hetero-metallic (Mo/Rh trifluoroacetate $[\text{MoRh}(\text{O}_2\text{CCF}_3)_4]$) since they demonstrated higher reactivities than the homo-metallic ones.

2.2 Models and Computational Methods

Figure 85 shows the models of the homo-metallic and hetero-metallic trifluoroacetate used in this investigation. All of them maintain the paddlewheel structural features with a $\text{M}_1\text{-M}_2$ bond, bridged over by four μ_2 -trifluoroacetate ligands. The M06-L (Zhao, Y. and D. G. Truhlar, 2008b, 2008a) density functional was used in all calculations. The 6-31G(d,p) basis set was employed for the probe molecules (ethylene oxide and CO_2), while the metal atoms were represented by the LANL2DZ pseudopotentials basis set (Hay, P. J. and W. R. Wadt, 1985). To obtain more accurate interaction energies, single-point calculations with the M06L/6-311++G(2df,2p) method were carried out. During geometry optimization, the adsorbing molecule and the entire structures of catalyst were allowed to relax.

The electronic states of the homo-metallic and hetero-metallic complexes are considered. The spin state that has the lowest energy was used as the ground state in all case. The singlet state was found lower energy in the homo-metallic systems. The quartet spin-state was employed for all calculations of the reaction coordinates in the hetero-metallic systems. Frequency calculations were performed at the same level of theory to identify the nature of all the stationary points. All calculations were performed with the Gaussian 09 code (Frisch, M. J. T. *et al.*, 2009).

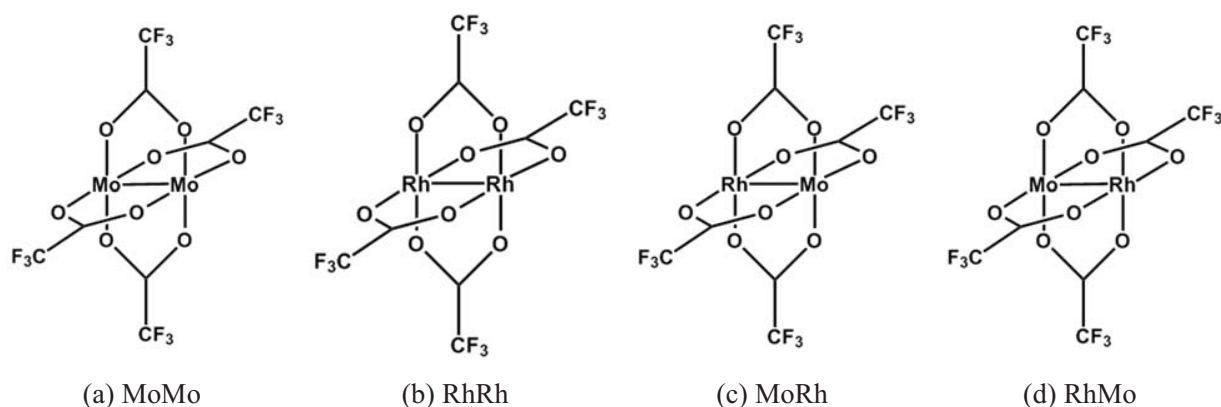


Figure 85. Schematic drawing of the homo-metallic and hetero-metallic compounds used in this investigation (a) Mo/Mo trifluoroacetate $[\text{MoMo}(\text{O}_2\text{CCF}_3)_4]$; (b) Rh/Rh trifluoroacetate $[\text{RhRh}(\text{O}_2\text{CCF}_3)_4]$; (c) Mo/Rh trifluoroacetate $[\text{MoRh}(\text{O}_2\text{CCF}_3)_4]$; and (d) Rh/Mo trifluoroacetate $[\text{RhMo}(\text{O}_2\text{CCF}_3)_4]$.

2.3 Results and discussions

2.3.1 Structure of the homo-metallic (MoMo and RhRh) and hetero-metallic trifluoroacetate (MoRh)

Figure 86 shows the optimized structures of the homo-metallic, $\text{MoMo}(\text{O}_2\text{CCF}_3)_4$, $\text{RhRh}(\text{O}_2\text{CCF}_3)_4$, and hetero-metallic trifluoroacetate, $\text{MoRh}(\text{O}_2\text{CCF}_3)_4$. (see Table 5) In the case of homo-metallic compounds, the M1-M2 bond distance is 2.13 Å for MoMo and 2.40 Å for RhRh, while the average bond length of M1-O is 2.13 Å and 2.08 Å for MoMo and RhRh systems. The average O-M1-M2 bond angle is 91.43° and 88.3° for MoMo and RhRh, respectively. For the hetero-metallic structure, the M1-M2 bond distance is 2.44 Å. The average O-M1-M2 bond angle is 85.87 and M2-M1-O bond angle is 89.55. The average bond length of M1-O and M2-O is 2.15 and 2.08 Å. These values are in a good agreement with experimental results (Li, B. *et al.*, 2007) (see Table 5). From these results, it can be claimed that the M06L functional is a well-suited methods to describe the structures of homo-metallic and hetero-metallic systems.

The natural population analysis charges of Mo and Rh in the homo-system compounds are +0.885 and +0.685 |e|, respectively. In the hetero-bimetallic system, the natural atomic population of Mo and Rh in the paddlewheel Mo/Rh trifluoroacetate are +1.105 and +0.581 |e|,

respectively. The results show a higher positive charge on the Mo site compared with the charge on the homo-metallic system. It can be expected that hetero-metallic Mo/Rh trifluoroacetate might be a better Lewis acid catalyst than the homo-metallic systems.

Table 5. Structural parameters, bond distances (Å), Angles (deg) and NPA charge analysis for Homo-metallic and Hetero-metallic, $[M_1M_2(O_2CCF_3)_4]$ (M = Mo, Rh)

	[MoMo]		[RhRh]		[MoRh]	
	calculation	experiment	calculation	experiment	calculation	experiment
M1-M2 (Å)	2.13	2.12	2.40	2.40	2.44	2.29
M1-O (Å)	2.13	2.12	2.08	2.04	2.15 (M2-O = 2.08)	2.06
O-M1-M2 (°)	91.43	91.76	88.29	88.20	85.87 (O-M2-M1 = 89.55)	89.42
Charge (e)	0.885,0.885	-	0.685,0.691	-	1.105,0.581	-

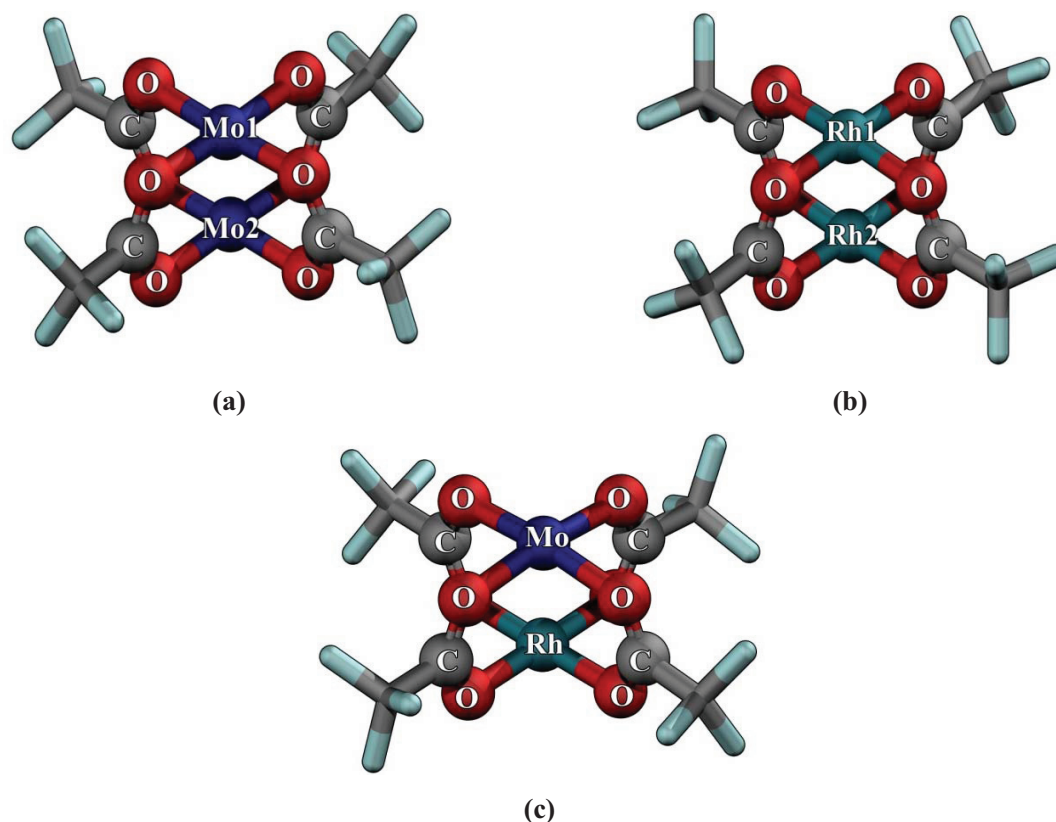


Figure 86. Optimized structures of (a) Mo/Mo trifluoroacetate $[\text{MoMo}(\text{O}_2\text{CCF}_3)_4]$, (b) Rh/Rh trifluoroacetate $[\text{RhRh}(\text{O}_2\text{CCF}_3)_4]$, (c) Mo/Rh trifluoroacetate $[\text{MoRh}(\text{O}_2\text{CCF}_3)_4]$.

2.3.2 The uncatalyzed cycloaddition reaction

The cycloaddition of CO_2 and ethylene oxide can be achieved via a concerted step, leading to the formation of ethylene carbonate. In the uncatalyzed system, for the transition state structure as compared to the coadsorption complex, the C1-O1 bond distance is elongated from 1.42 to 2.04 Å and distance between C1-O2 and C1-O3 are contracted from 3.26 to 2.26 Å and 2.76 to 1.81 Å, respectively. (see Table 6) The activation energy is 246 kJ/mol. A normal mode analysis reveals one imaginary frequency at -680.8 cm^{-1} associated with the transition state mode. This normal mode vibration confirms the connection between the adsorption complex and the cycloaddition product. It corresponds to a movement along the reaction coordinate in which the O1-C1 bond breaks and the O1-C3 and O2-C1 bonds form simultaneously. The reaction energy is -30 kJ/mol (see Figure 87).

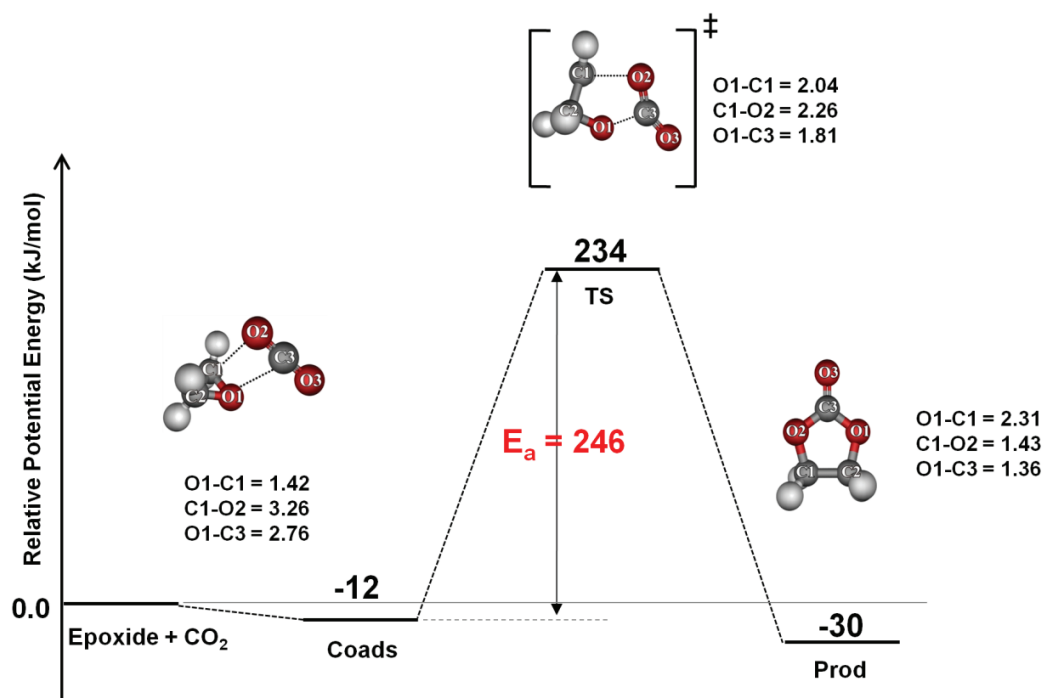


Figure 87. Energy profile for the uncatalyzed cycloaddition of CO₂ with ethylene oxide to give ethylene carbonate. Energies are in kJ/mol.

Table 6. Optimized geometric parameters of the isolated state, the coadsorption complex, the transition state, and the product of the cycloaddition between CO₂ and ethylene oxide using the M06L/6-31G(d,p) method (bond lengths in Å).

Parameter	Isolated molecule	Coadsorption complex	Transition state	Product
O ₁ -C ₁	1.417	1.422	2.040	2.306
O ₁ -C ₂	1.417	1.421	1.394	1.428
O ₂ -C ₃	1.168	1.171	1.222	1.361
O ₁ -C ₃	-	2.756	1.810	1.360
O ₂ -C ₁	-	3.174	2.259	1.428

2.3.3 Reaction mechanisms of the cycloaddition of carbon dioxide to ethylene oxide

The general mechanism of carbon dioxide cycloaddition with ethylene oxide has been reported to consist of three steps (oxidative addition, insertion, and reductive elimination). The mechanism of this reaction over the catalyst can be separated into two different routes. (see Figure 88) In route A, carbon dioxide firstly adsorbs on the active site while route B is the direct activation of ethylene oxide in a first step. In Table 7, we show a comparison of the adsorption energies between CO_2 and ethylene oxide on homo-metallic and hetero-bimetallic compounds (see Figure 89). The results show that most favorable reaction route proceeds via the ethylene oxide pathway (route B); following 3 elementary steps: (i) ethylene oxide adsorption on the catalyst and activate the ethylene oxide by single-electron transfer to cleave the ring and form a radical intermediate (ii) CO_2 co-adsorption (iii) CO_2 insertion and cyclization. In this work, we therefore use pathway B for investigating the cycloaddition mechanism of CO_2 and ethylene oxide.

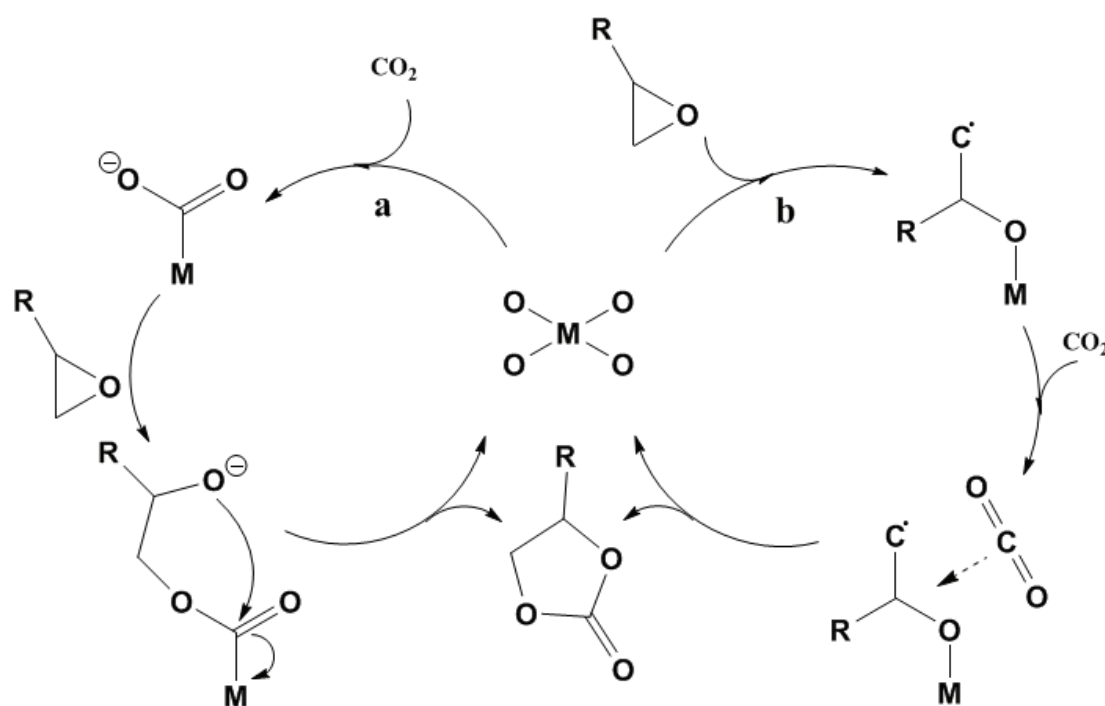


Figure 88. Reaction pathways for CO_2 with epoxides on homo-metallic and hetero-metallic systems which CO_2 activation as the first step (a) or with epoxide activation as the first step (b).

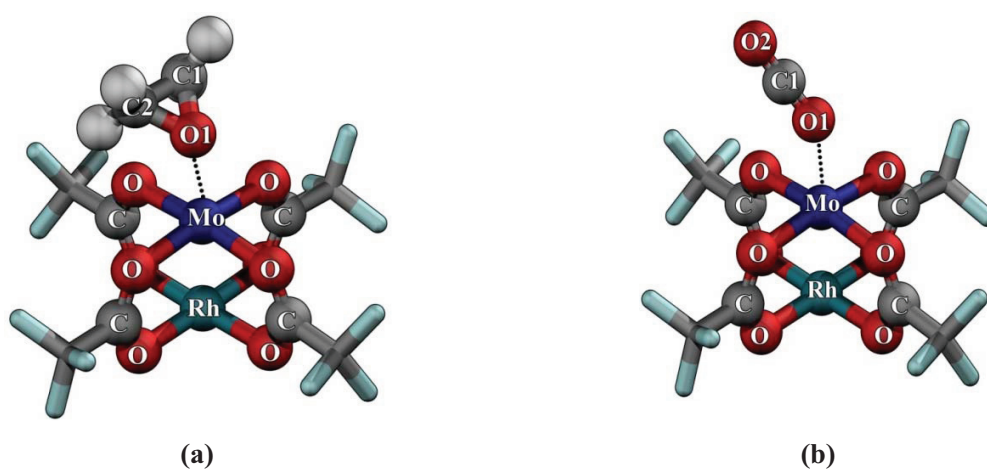


Figure 89. Optimized structures of CO₂ and ethylene oxide over Mo/Rh trifluoroacetate [MoRh(O₂CCF₃)₄]

Table 7. Optimized geometrical parameters and adsorption energies for the CO₂ and ethylene oxide adsorption over homo-metallic, MoMo(O₂CCF₃)₄ and RhRh(O₂CCF₃)₄, and hetero-metallic ,MoRh(O₂CCF₃)₄ and RhMo(O₂CCF₃)₄ compounds. Bond distances are in Å and energies are in kJ/mol.

Catalyst	ethylene oxide adsorption			CO ₂ adsorption		
	adsorption energy	Distances M1-O1 (Å)	Distances M1-M2 (Å)	adsorption energy	Distances M1-O1 (Å)	Distances M1-M2 (Å)
Mo-Mo	-59	2.52	2.14	-31	2.81	2.14
Rh-Rh	-89	2.26	2.43	-38	2.45	2.41
Mo-Rh	-104	2.31	2.46	-49	2.42	2.45
Rh-Mo	-55	2.42	2.45	-27	2.67	2.44

The catalytic cycloaddition of carbon dioxide with ethylene oxide to produce ethylene carbonate over homo-metallic and hetero-bimetallic compounds by route B are systematically investigated following two different reaction pathways: a concerted and a stepwise pathways.

2.3.3.1 Concerted Pathway

In this mechanism, the ethylene carbonate is produced by the cycloaddition of carbon dioxide to ethylene oxide in single step without any intermediate. (see Figure 90) The initial step is the adsorption of the ethylene oxide on the metal (M_I) active site via lone pair electron interaction (Ads). The adsorption energies are calculated to be -55, -59, -89 and -104 kJ/mol for RhMo, MoMo, RhRh and MoRh, respectively. (see Figure 91) Then, the carbon dioxide molecule is co-adsorbed next to the adsorbed ethylene oxide to form the coadsorption complex (Coads). The adsorption energies are -69, -73, -103, and -116 kcal/mol for RhMo, MoMo, RhRh and MoRh, respectively.

Subsequently, the ethylene carbonate product is formed via a five-membered cyclic transition state (TS_C), in which the ring-opening of ethylene oxide and the cyclization with carbon dioxide take place simultaneously. In this transition state, the O1 -C1 bond is broken and two new C-O bonds (C1-O2 and C3-O1) are formed. The activation energy for this pathway is computed to be 210, 198, 187, and 165 kJ/mol for RhMo, MoMo, RhRh and MoRh, respectively. Normal mode analysis reveals one imaginary frequency at -578.4, -432.6, -383.9 and -578.4 cm^{-1} associated with the transition states for RhMo, MoMo, RhRh and MoRh, respectively. This mode corresponds to the movement along the reaction coordinate in which the O1-C1 bond breaks and the C3-O1 and C1-O2 bonds form simultaneously. After passing through the transition state, the ethylene carbonate (prod) is formed and located on top of the active site with a relative energy of -80, -95, -108, and -133 kJ/mol for RhMo, MoMo, RhRh and MoRh, respectively. Then, the ethylene carbonate is desorbed from the active site requiring an energy of 53, 65, 78, and 103 kJ/mol for RhMo, MoMo, RhRh and MoRh, respectively. The energy profiles for the concerted reaction on all of four studied catalysts are illustrated in Figure 91. The activation barriers are 198, 187, 210, and 165 kJ/mol for RhMo, MoMo, RhRh and MoRh, respectively. The results indicate that both homo-metallic and hetero-metallic compounds can be used as a catalyst in the cycloaddition reaction between ethylene oxide and carbon dioxide. A catalysts give lower activation energies (246 kJ/mol) and also stabilize all reaction intermediates compared to the uncatalyzed reaction. Among those four systems, MoRh(O₂CCF₃)₄ shows the best performance with the lowest barrier and product energy. Therefore we choose the MoRh(O₂CCF₃)₄ hetero-metallic catalyst to investigate the stepwise pathway in detail.

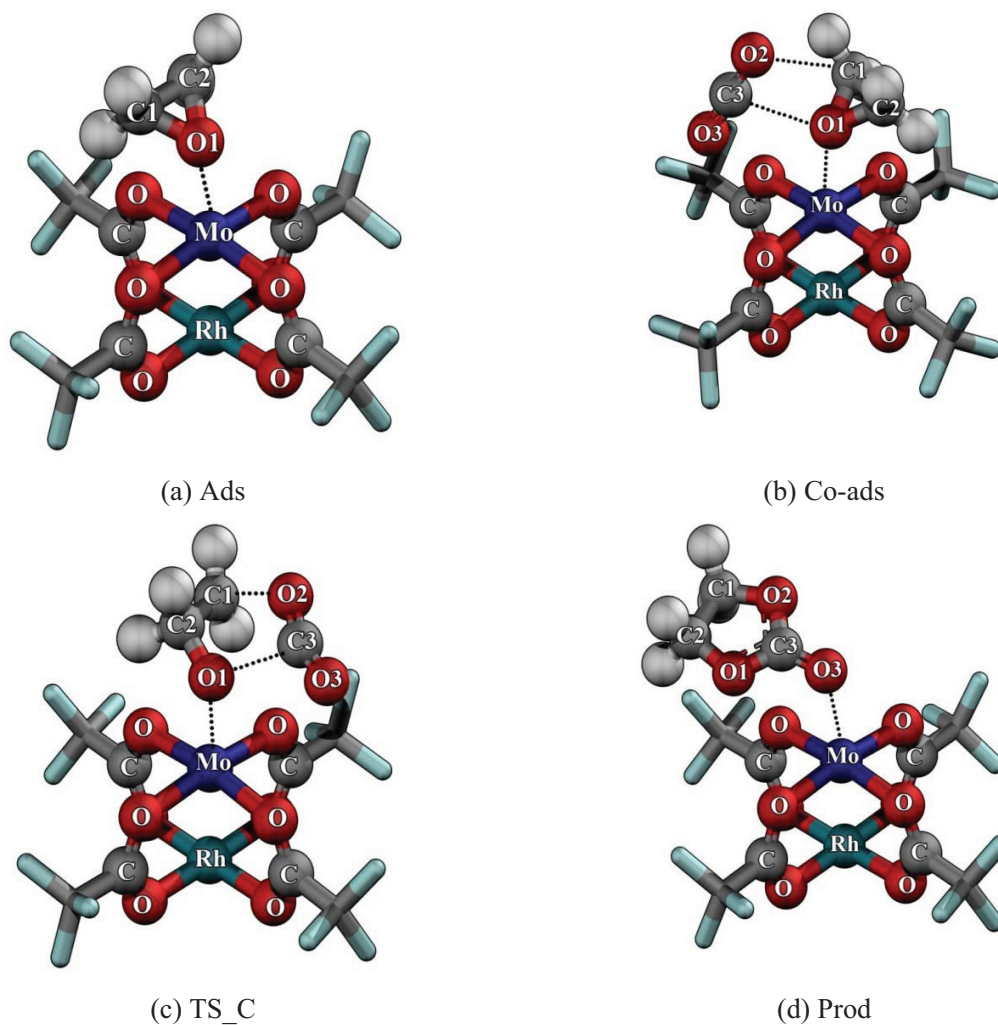


Figure 90. Optimized structures of (a) ethylene oxide adsorption (Ads) (b) the co-adsorption complex of CO₂ and ethylene oxide (Co-ads), (c) transition state (TS_C) and ethylene carbonate product (Prod_C) of concerted mechanism over Mo/Rh trifluoroacetate [MoRh(O₂CCF₃)₄].

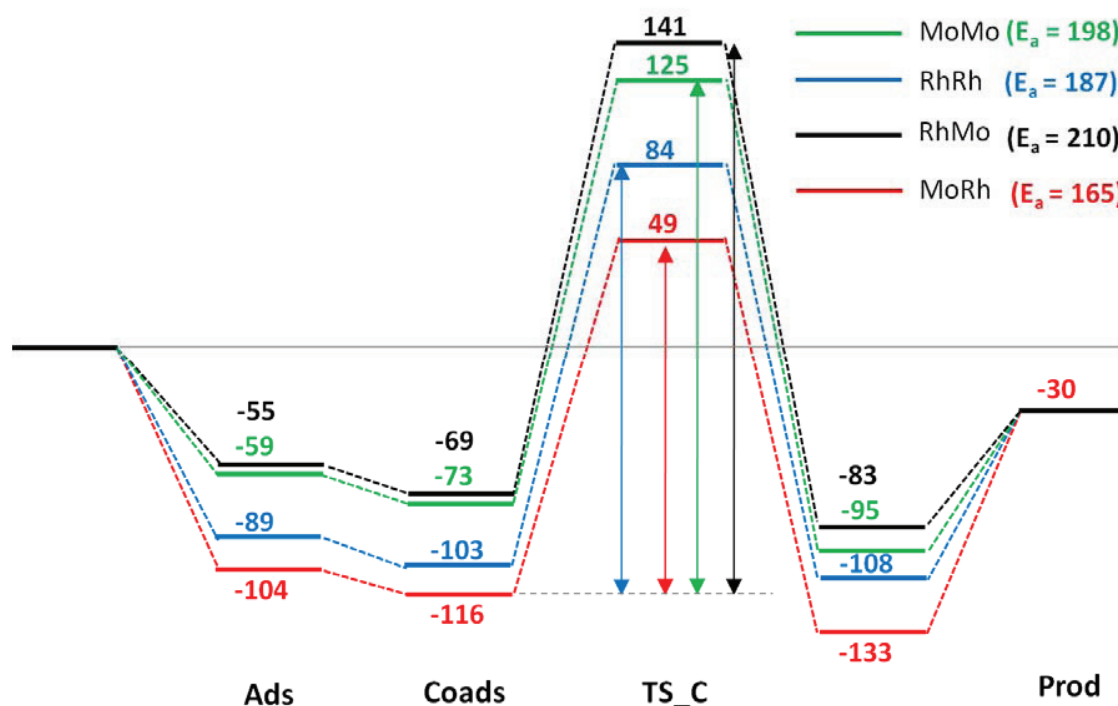


Figure 91. Energy profile (in kJ/mol) for concerted pathway mechanisms of the cycloaddition of carbon dioxide with ethylene oxide over Mo/Mo trifluoroacetate (green line), Rh/Rh trifluoroacetate (blue line), Rh/Mo trifluoroacetate (black line), and MoRh trifluoroacetate (red line).

2.3.3.2 Stepwise Pathway

The cycloaddition of CO₂ and ethylene oxide catalyzed by MoRh trifluoroacetate in the stepwise reaction can involve two possible reaction pathways: A and B (see Figure 92). In pathway A, the initial step is the coordination of the ethylene oxide to the MoRh catalyst, which forms a radical intermediate (Int1_S) followed by a CO₂ insertion into the intermediate1 (Int1_S). In this step, two C-O bonds are concurrently formed, which is rather similar to the process in the concerted pathway. In the alternative mechanism (Pathway B), the initial step consists of ethylene oxide activation and co-adsorption of CO₂ on the intermediate (Int1_S) giving co-adsorption complex. Next, an intermediate attached to CO₂ by only one C-O bond is created, leading to the formation of linear carbonate namely intermediate2 (Int2_S). The second transition state involves the formation of new C_{ethylene oxide}-O_{carbon dioxide} and Mo-O bonds. After that, the linear carbonate (Int2_S) undergoes an intramolecular ring-closing step forming a cyclic

carbonate product. Hence, in this part, we investigate these two possible pathways using MoRh trifluoroacetate as a catalyst.

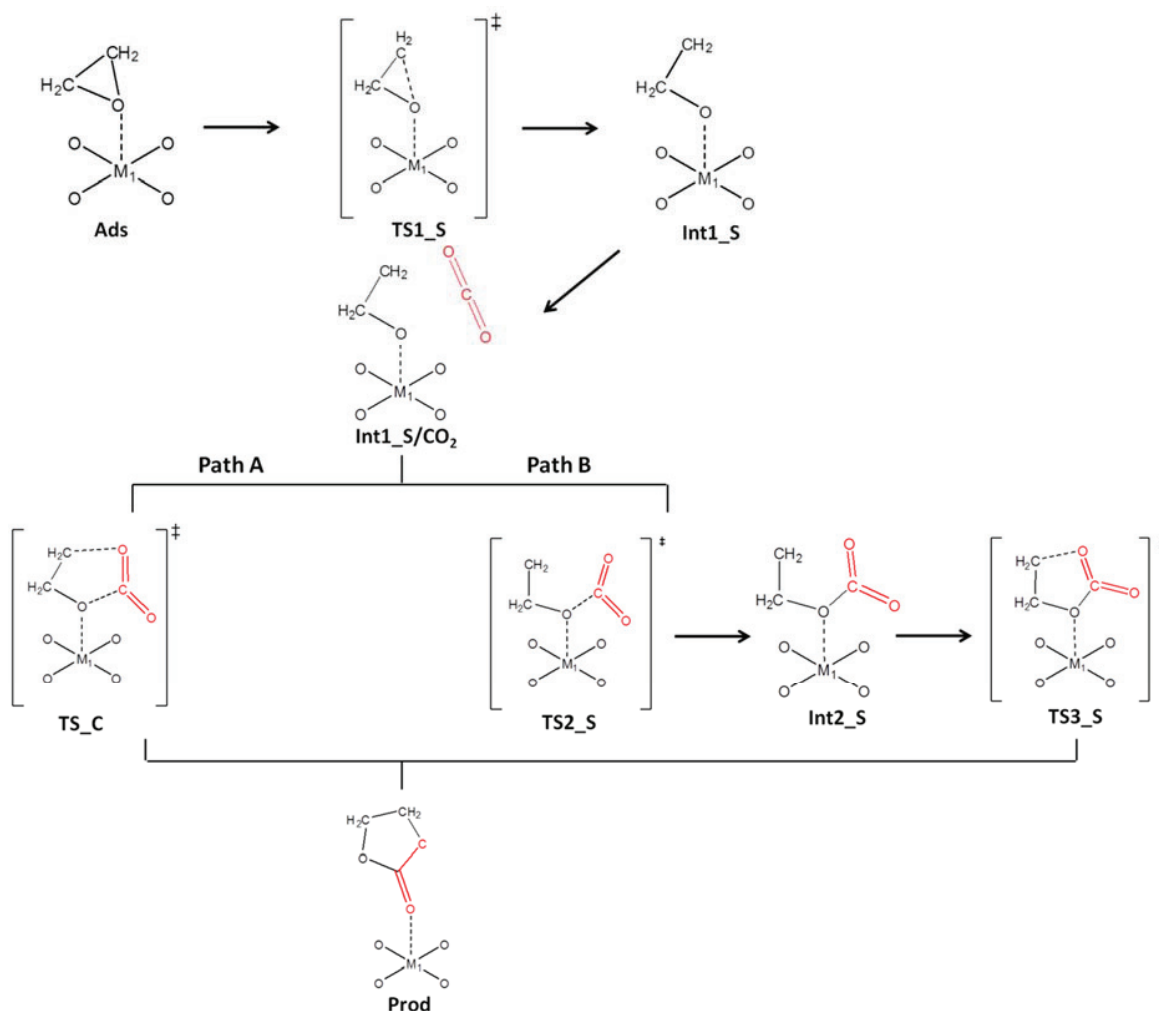


Figure 92. Possible mechanisms for the MoRh trifluoroacetate -catalyzed cycloaddition of CO₂ and ethylene oxide.

Path A

This reaction pathway is proposed to proceed as a two-step process, the ring-opening of ethylene oxide to form a Mo-O-C-C[•] radical intermediate and the subsequent cyclization of intermediate with carbon dioxide to generate the ethylene carbonate product. The reaction is started with the adsorption of ethylene oxide on the Mo active site of the [MoRh(O₂CCF₃)₄] catalyst (Ads) with an energy of -104 kJ/mol. The distance between the ethylene oxide oxygen

and the Mo atom of the active site is 2.04 Å (see appendix). This is followed by the opening of ethylene oxide ring by rupturing the C1-O1 bond via the transition state (TS1_S). At the transition state, the C1-O1 bond is broken, and the hybridization of C1 changes from tetrahedral (sp^3) to planar (sp^2). (see Figure 93a) The calculated activation energy is 88 kJ/mol. The transition state is confirmed by a frequency calculation with an imaginary frequency belonging to the vibration a mode along the C1-O1 bond broken. The imaginary frequency is at -505.9 cm^{-1} .

Then, the radical intermediate is formed (Int1_S) and adsorbed on the active site with the energy relative to the isolated reactants of -35 kJ/mol . The spin density is located at the terminal carbon atom of the ethylene oxide ($S = 1.0$). The active site (Mo) transfers an electron to the ethylene oxide, thus leading to the homolytic cleavage of the O1-C1 bond and to the formation of the Mo-O-C-C $^{\bullet}$ radical intermediate (see appendix). The spin density on the Mo active site changed from $S=2.8$ to $S=1.9$. This finding corresponds to a bond alteration of the Mo active site and the oxygen atom of the ethylene oxide. The Mo-O1 distance is shortened from 2.04 to 1.92 Å in Int1_S, supporting the covalent bond is formed between Mo and O1. The next step is the cyclization of the intermediate with carbon dioxide lead to the product. After the formation the intermediate (Int1_S), the carbon dioxide approach leading to the adsorption complex (Int1_S/CO $_2$). Its complexation energy is -53 kJ/mol relative to the isolated molecules. The transition state of this cyclization step is similar to the concerted one in which the carbon dioxide is inserted into the intermediate by forming new C3-O1 and C1-O2 bonds as confirmed by unique imaginary frequency. The activation energy for this step is computed to be 102 kJ/mol, which is larger than in the first step. This step is thus considered to be the rate-determining one of the stepwise pathway A. The ethylene carbonate product is adsorbed on the Mo active site of the [MoRh(O $_2$ CCF $_3$) $_4$] catalyst with an energy of -133 kJ/mol . Finally, it can be desorbed with the energy of 103 kJ/mol. (see Figure 95)

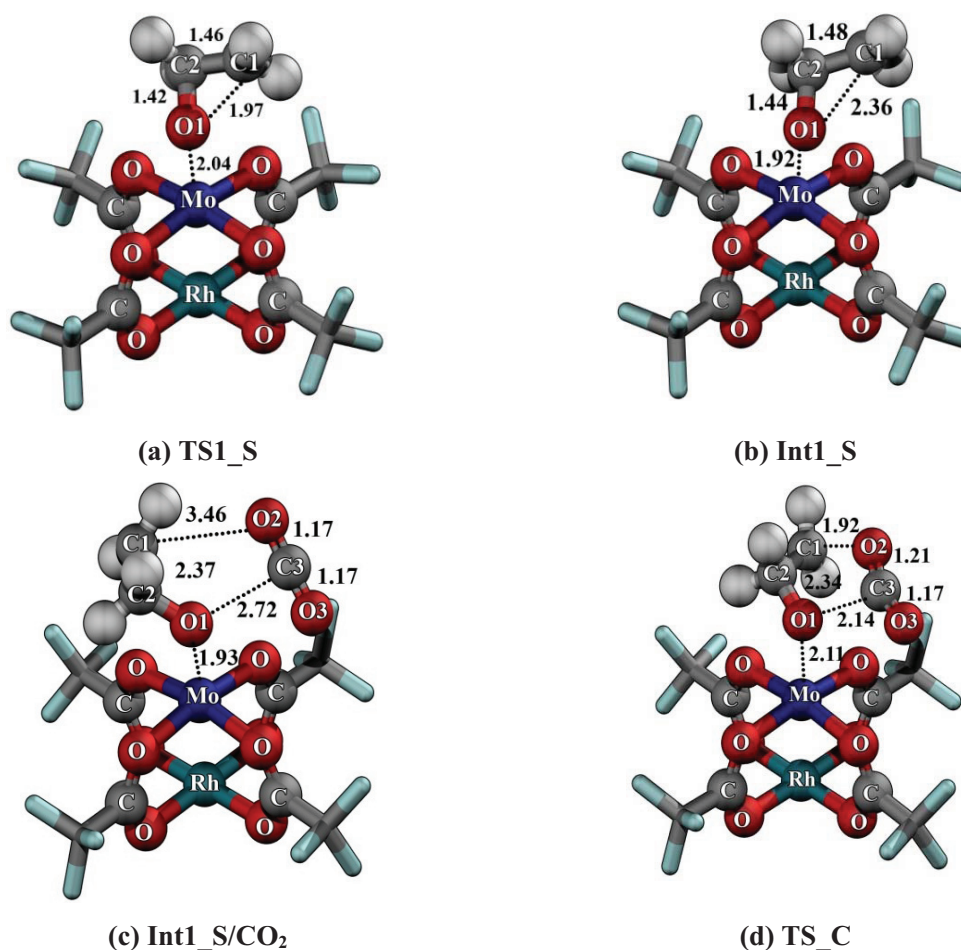


Figure 93. Optimized structures of (a) transition state (TS1_S) (b) intermediate (Int1_S) (c) complex of Int_S and CO₂ (Int_C/CO₂) and (d) transition state (TS2_S) of the step mechanism A over Mo/Rh trifluoroacetate [MoRh(O₂CCF₃)₄].

Path B

Reaction pathway B is proposed as a three-step process, containing the ring-opening ethylene oxide to form a Mo-O-C-C^{*} radical intermediate, bond formation between the intermediate and CO₂ and the intra-molecular cyclization of the intermediate to generate the ethylene carbonate product. (see Figure 94 and Table 8) The first step involves the coordination of ethylene oxide to the MoRh(O₂CCF₃)₄. The catalyst polarizes the C1-O1 epoxide bond thereby facilitating the ring-opening step. This is followed by the opening of ethylene oxide ring by rupturing the C1-O1 bond via the transition state. Then, the radical intermediate is formed and

adsorbed on the active site with an energy relative to the isolated reactants of -35 kJ/mol. In the next step, the carbon dioxide moves to bind to the radical intermediate leading to the adsorption complex (Int1_S/CO₂). This step is similar to what has been seen in the stepwise path A. The complexation energy is -53 kJ/mol. In the subsequent step, the second transition state (TS2_S) involves the formation of new O1-C3 and Mo-O3 bonds that involve the CO₂ molecule. This step is confirmed by the calculated transition structure the imaginary frequency of which belongs to the vibration mode in which the O1-C3 bond forms. The imaginary frequency is at -341.2 cm⁻¹. The calculated activation energy barrier is 68 kJ/mol. After that, the radical intermediate (Int2_S) is formed and adsorbed on the active site with an energy relative to isolated reactants of -12 kJ/mol. The spin density is again located at the terminal carbon atom of the ethylene oxide ($S = 1.0$) and an electron is also transfer from Mo to the reacting species (from $S = 2.8$ to $S = 1.8$). After that, an intramolecular ring-closing step occurs with an energy of 45 kJ/mol⁻¹. The ethylene carbonate product is adsorbed on the Mo active site catalyst with an energy of -133 kJ/mol and it is finally desorbed requiring an energy of 103 kJ/mol.

From the comparison of all pathways in the reaction profile, it can be concluded that the coupling reaction of ethylene oxide and carbon dioxide to produce ethylene carbonate preferably occurs via the stepwise pathway B.

Table 8. Optimized geometry parameter of the cycloaddition reaction between CO₂ and ethylene oxide over the hetero-metallic (MoRh(O₂CCF₃)₄). Bond distances are in Å.

	Bond Distances (Å)								
	Isolate molecules	Ads	TS1_S	Int1_S	Int1_S/CO ₂	TS2_S	Int2_S	TS3_S	Prod
M ₁ -M ₂	2.44	2.46	2.48	2.49	2.49	2.51	2.50	2.47	2.47
M ₁ -O ₁	-	2.31	2.04	1.92	1.93	2.06	2.22	3.53	3.45
O ₁ -C ₁	1.42	1.44	1.97	2.36	2.37	2.36	2.45	2.41	2.32
O ₁ -C ₂	1.42	1.45	1.42	1.44	1.44	1.45	1.48	1.44	1.44
C ₁ -C ₂	-	1.46	1.46	1.48	1.48	1.47	1.47	1.47	1.53
O ₂ -C ₃	1.17	-	-	-	1.17	1.18	1.20	1.23	1.33
O ₃ -C ₃	1.17	-	-	-	1.17	1.22	1.29	1.30	1.22
O ₁ -C ₃	-	-	-	-	2.72	1.82	1.43	1.35	1.33
O ₂ -C ₁	-	-	-	-	3.46	3.48	3.16	2.34	1.44

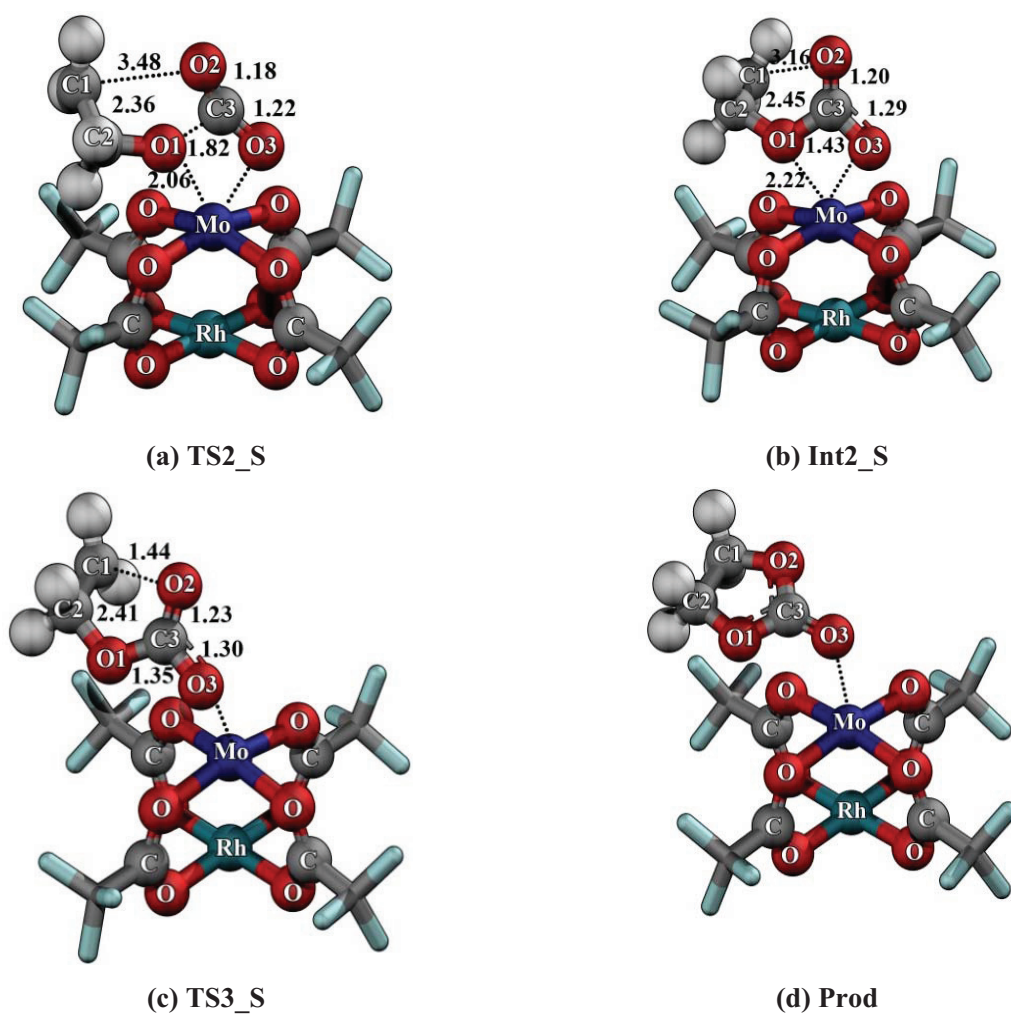


Figure 94. Optimized structures of (a) transition state (TS2_S) (b) intermediate (Int2_S) (c) transition state (TS3_S) and (d) product of the step mechanism B over Mo/Rh trifluoroacetate $[\text{MoRh}(\text{O}_2\text{CCF}_3)_4]$.

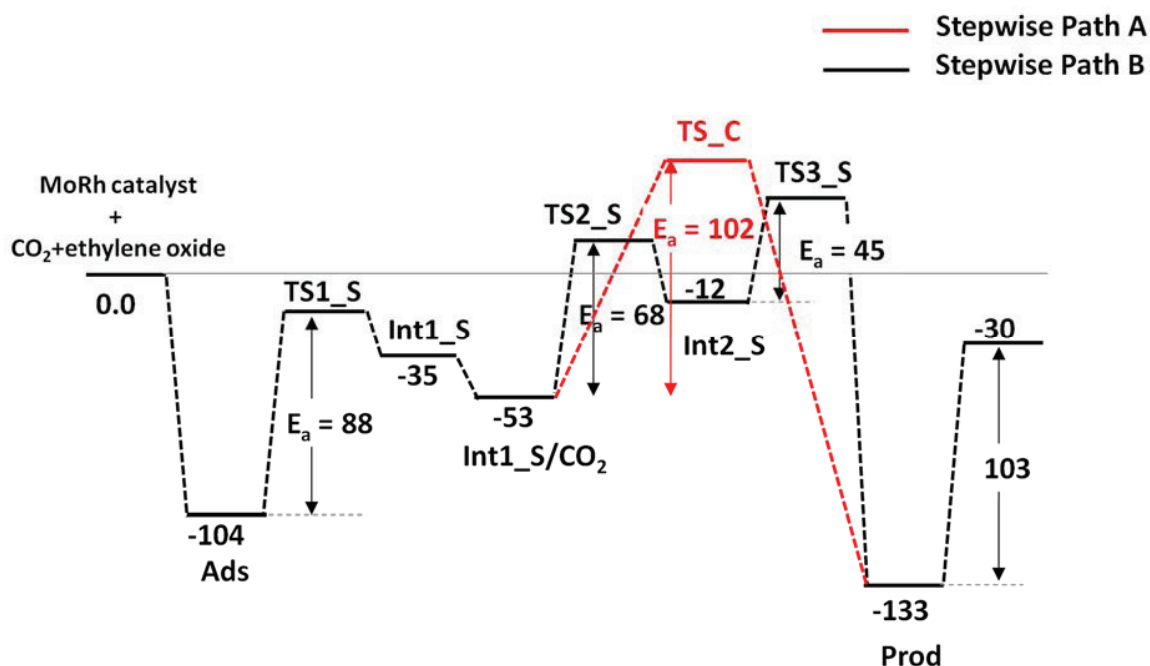


Figure 95. Energy profile (in kJ/mol) of the cycloaddition of carbon dioxide with ethylene oxide over Mo/Rh trifluoroacetate [MoRh(O₂CCF₃)₄] : stepwise pathway A (red line) and stepwise pathway B (black line).

2.4 Conclusions

We study the cycloaddition of ethylene oxide with CO₂ over homo-metallic (Mo/Mo trifluoroacetate and Rh/Rh trifluoroacetate) and hetero-metallic (Mo/Rh trifluoroacetate and Rh/Mo trifluoroacetate) compounds with density-functional theory using the M06L method. We study for the reaction mechanism two processes, concerted and stepwise. The stepwise process can be further subdivided into two pathways (called A and B). First, we show a comparison of the catalytic activity of homo-metallic and hetero-metallic compounds in the concerted pathway. In this mechanism, the reaction occurs in a single step of simultaneous ethylene oxide ring-opening and carbon dioxide cyclization with an activation barrier of 210, 198, 187, and 165 kJ/mol for RhMo, MoMo, RhRh and MoRh, respectively. We see clearly that the cycloaddition of CO₂ and ethylene oxide proceeds more easily in presence of a hetero-metallic than a homo-metallic system, especially Mo/Rh trifluoroacetate. Therefore we choose the MoRh hetero-metallic catalyst to investigate the stepwise pathway.

In the stepwise pathway A, the reaction proceeds via the activation of the ethylene oxide to open the epoxide ring, resulting in the formation of an intermediate with an activation energy of 88 kJ/mol. Consequently, a CO₂ molecule is inserted nearby to form the ethylene carbonate product. The activation energy of this step is calculated to be 103 kJ/mol.

In the stepwise pathway B, after the intermediate 1, a molecule of CO₂ reacts with the negatively charged oxygen atom (insertion) of intermediate 1, leading to the formation of intermediate 2. The calculated activation energy barrier is 68 kJ/mol. Finally, intermediate 2 undergoes an intramolecular ring-closing step with an activation energy of 45 kcal/mol. From the entire reaction profile of this reaction, it can be concluded that the discussed reaction preferably occurs via the stepwise path B. We expect the hetero-metallic (Mo/Rh trifluoroacetate) to exhibit a good performance. It was also found to be a more efficient catalyst than homo-metallic systems.

CHAPTER IV. CONCLUDING REMARKS

In this work, indirect bipolar electrocrodposition (IBED), which is considered as a simple and rapid synthesis technique, was developed and employed for the first time to prepare two representative MOF materials including ZIF-8 and HKUST-1 on metal substrates (zinc wire and copper bead, respectively) at room temperature in a straightforward and site selective way. The crystal size and morphology can be tuned in a facile manner through the modulation of linker concentration, electrodeposition time and the amplitude of the external electric field. This cheap and green synthesis concept is expected to be able to be generalized for other MOF compounds, leading to new generations of MOF-based Janus-type composites with applications in catalysis, separation, storage and sensing.

Designed hierarchical macro-/microporous HKUST-1 electrodes were prepared via an electrochemical dissolution-deposition technique with the motivation to overcome the diffusion limits that are typically occurring in the cases of the conventional microporous MOFs. Silica spheres with monodisperse and narrow size distribution were prepared via the Stöber method. Then, a colloidal crystal of these silica spheres was prepared on gold substrates by the Langmuir–Blodgett (LB) technique. Macroporous copper (Cu) electrodes with controlled numbers of porous layers were prepared via an electrochemical technique by using the template. After the removal of the template, the synthesis of HKUST-1 was performed via the anodic dissolution of the copper surface of the electrodes in the presence of the organic linker, leading to the deposition of the HKUST-1 on the electrode surface with the designed macroporous structure. The macroporous Cu electrodes do not only behave as the structural template but also as the Cu source of the formation of MOFs. The applied potential and deposition time plays an important role for the amount of product and its characteristics. The developed synthesis approach is rapid, thus being very practical, and opens up MOFs for various applications including catalysis, separation and sensors.

With the aim to obtain new hybrid materials containing MOFs for applications in catalysis, MIL-101-supported noble metal nanoparticles (Au, Pd and Pt) were prepared via a simple colloidal deposition followed by calcination. The size-controlled noble metal nanoparticles (gold (Au), palladium (Pd) and platinum (Pt)) stabilized by poly(N-vinyl-2-pyrrolidone) and a MOF material (MIL-101) possessing a large surface area, large pore size and

good chemical resistance (prepared via the hydrothermal synthesis) were used as the starting materials. The results show that, via the employed technique, Au and Pd nanoparticles were deposited onto the external surface of MIL-101, while Pt nanoparticles were deposited both in the porous structure of MIL-101 and onto its external surface. The highly dispersed particles were in the MIL-101 pores while the aggregated particles were on the external surface. The preparation technique used in this study is expected to be able to be generalized for the synthesis of other metal nanoparticle/MOF composites, and should allow to improve the catalytic efficiency of MOF structures.

Apart from the experimental study, the catalytic behavior of a MOF with open metal active sites (Cu-MOF-505) was theoretically investigated by means of density functional calculations with respect to another catalyst, Cu-ZSM-5 zeolite, for the Mukaiyama aldol reaction of encapsulated formaldehyde and silyl enol ether. For comparison, the gas phase (non-catalyzed) reaction was also investigated. The concerted mechanism consisting of the steps of the silyl group transfer and the carbon-carbon bond formation was proposed for the reaction. Our results confirm that both Cu-ZSM-5 and MOF-505 are good catalysts for the Mukaiyama aldol reaction. Both catalysts behave as Lewis acid catalysts, inducing the carbon atom of formaldehyde to be more positive, and thus, being attacked more easily by the nucleophile reactant. This results in the decrease in the energy barriers.

In the last part of the study, the catalytic behavior of metal complexes that represent the metal clusters in some MOF materials, including homo-metallic clusters (Mo/Mo trifluoroacetate and Rh/Rh trifluoroacetate) and hetero-bimetallic clusters (Mo/Rh trifluoroacetate) were theoretically investigated for the synthesis of cyclic carbonate via the cycloaddition of CO₂ to epoxide. The reaction mechanisms are proposed to occur via two different pathways, concerted and stepwise. The hetero-metallic complex exhibits superior catalytic behavior compared to the homo-metallic one. The findings obtained from the calculations provide an insight into the design of MOF catalysts with good catalytic behavior.

REFERENCES

- Aguirre-Diaz, L.M., M. Iglesias, N. Snejko, E. Gutierrez-Puebla and M.A. Monge. 2013. Indium Metal-Organic Frameworks as Catalysts in Solvent-Free Cyanosilylation Reaction. **CrystEngComm**. 15(45): 9562-9571.
- Allendorf, M.D., C.A. Bauer, R.K. Bhakta and R.J.T. Houk. 2009. Luminescent Metal-Organic Frameworks. **Chem. Soc. Rev.** 38(5): 1330-1352.
- Allendorf, M.D., A. Schwartzberg, V. Stavila and A.A. Talin. 2011. A Roadmap to Implementing Metal–Organic Frameworks in Electronic Devices: Challenges and Critical Directions. **Chemistry – A European Journal**. 17(41): 11372-11388.
- Alvarado-Swaisgood, A.E., M.K. Barr, P.J. Hay and A. Redondo. 1991. Ab Initio Quantum Chemical Calculations of Aluminum Substitution in Zeolite Zsm-5. **J. Phys. Chem.** 95(24): 10031-10036.
- Ameloot, R., L. Stappers, J. Fransaer, L. Alaerts, B.F. Sels and D.E. De Vos. 2009. Patterned Growth of Metal-Organic Framework Coatings by Electrochemical Synthesis. **Chem. Mater.** 21(13): 2580-2582.
- Ameloot, R., E. Gobechiya, H. Uji-i, J.A. Martens, J. Hofkens, L. Alaerts, B.F. Sels and D.E. De Vos. 2010. Direct Patterning of Oriented Metal–Organic Framework Crystals Via Control over Crystallization Kinetics in Clear Precursor Solutions. **Adv. Mater.** 22(24): 2685-2688.
- Batten Stuart, R., R. Champness Neil, X.-M. Chen, J. Garcia-Martinez, S. Kitagawa, L. Öhrström, M. O’Keeffe, M. Paik Suh and J. Reedijk. (2013) Terminology of Metal–Organic Frameworks and Coordination Polymers (Iupac Recommendations 2013). *Pure Appl. Chem.* pp. 1715-1724.

- Bobuatong, K., M. Probst and J. Limtrakul. 2010. Structures and Energetics of the Methylation of 2-Methylnaphthalene with Methanol over H-Bea Zeolite. **J. Phys. Chem. C.** 114(49): 21611-21617.
- Boekfa, B., S. Choomwattana, P. Khongpracha and J. Limtrakul. 2009. Effects of the Zeolite Framework on the Adsorptions and Hydrogen-Exchange Reactions of Unsaturated Aliphatic, Aromatic, and Heterocyclic Compounds in Zsm-5 Zeolite: A Combination of Perturbation Theory (MP2) and a Newly Developed Density Functional Theory (M06-2x) in Oniom Scheme. **Langmuir.** 25(22): 12990-12999.
- Boekfa, B., P. Pantu, M. Probst and J. Limtrakul. 2010. Adsorption and Tautomerization Reaction of Acetone on Acidic Zeolites: The Confinement Effect in Different Types of Zeolites. **J. Phys. Chem. C.** 114(35): 15061-15067.
- Bordiga, S., L. Regli, F. Bonino, E. Groppo, C. Lamberti, B. Xiao, P.S. Wheatley, R.E. Morris and A. Zecchina. 2007. Adsorption Properties of HKUST-1 toward Hydrogen and Other Small Molecules Monitored by IR. **PCCP.** 9(21): 2676-2685.
- Boutin, A., F.o.-X. Coudert, M.-A. Springuel-Huet, A.V. Neimark, G.r. Férey and A.H. Fuchs. 2010. The Behavior of Flexible Mil-53(Al) Upon Ch₄ and Co₂ Adsorption. **J. Phys. Chem. C.** 114(50): 22237-22244.
- Boyer, D., P. Tamarat, A. Maali, B. Lounis and M. Orrit. 2002. Photothermal Imaging of Nanometer-Sized Metal Particles among Scatterers. **Science.** 297(5584): 1160-1163.
- Boys, S.F. and F. Bernardi. 1970. The Calculation of Small Molecular Interactions by the Differences of Separate Total Energies. Some Procedures with Reduced Errors. **Mol. Phys.** 19(4): 553-566.
- Bradley, J.-C. and Z. Ma. 1999. Contactless Electrodeposition of Palladium Catalysts. **Angew. Chem. Int. Ed.** 38(11): 1663-1666.

- Bradley, J.-C., H.-M. Chen, J. Crawford, J. Eckert, K. Ernazarova, T. Kurzeja, M. Lin, M. McGee, W. Nadler and S.G. Stephens. 1997. Creating Electrical Contacts between Metal Particles Using Directed Electrochemical Growth. **Nature**. 389(6648): 268-271.
- Bradley, J.C., S. Babu and P. Ndungu. 2005. Contactless Tip - Selective Electrodeposition of Palladium onto Carbon Nanotubes and Nanofibers. **Fullerenes Nanotubes Carbon Nanostruct.** 13(3): 227-237.
- Bradshaw, D., A. Garai and J. Huo. 2012. Metal-Organic Framework Growth at Functional Interfaces: Thin Films and Composites for Diverse Applications. **Chem. Soc. Rev.** 41(6): 2344-2381.
- Bradshaw, D., S. El-Hankari and L. Lupica-Spagnolo. 2014. Supramolecular Templating of Hierarchically Porous Metal-Organic Frameworks. **Chem. Soc. Rev.** 43(16): 5431-5443.
- Burda, C., X. Chen, R. Narayanan and M.A. El-Sayed. 2005. Chemistry and Properties of Nanocrystals of Different Shapes. **Chem. Rev.** 105(4): 1025-1102.
- Burgoyne, A. and R. Meijboom. 2013. Knoevenagel Condensation Reactions Catalysed by Metal-Organic Frameworks. **Catal. Lett.** 143(6): 563-571.
- Castillejos, E., P.-J. Debouttière, L. Roiban, A. Solhy, V. Martinez, Y. Kihn, O. Ersen, K. Philippot, B. Chaudret and P. Serp. 2009. An Efficient Strategy to Drive Nanoparticles into Carbon Nanotubes and the Remarkable Effect of Confinement on Their Catalytic Performance. **Angew. Chem. Int. Ed.** 48(14): 2529-2533.
- Champion, J.A., Y.K. Katare and S. Mitragotri. 2007. Making Polymeric Micro- and Nanoparticles of Complex Shapes. **Proc. Natl. Acad. Sci.** 104(29): 11901-11904.

- Chen, B., N.W. Ockwig, A.R. Millward, D.S. Contreras and O.M. Yaghi. 2005a. High H₂ Adsorption in a Microporous Metal–Organic Framework with Open Metal Sites. **Angew. Chem. Int. Ed.** 44(30): 4745-4749.
- Chen, B., N.W. Ockwig, A.R. Millward, D.S. Contreras and O.M. Yaghi. 2005b. High H₂ Adsorption in a Microporous Metal–Organic Framework with Open Metal Sites. **Angew. Chem.** 117(30): 4823-4827.
- Chen, S., R.S. Ingram, M.J. Hostetler, J.J. Pietron, R.W. Murray, T.G. Schaaff, J.T. Khoury, M.M. Alvarez and R.L. Whetten. 1998. Gold Nanoelectrodes of Varied Size: Transition to Molecule-Like Charging. **Science.** 280(5372): 2098-2101.
- Choi, K.M., H.J. Jeon, J.K. Kang and O.M. Yaghi. 2011. Heterogeneity within Order in Crystals of a Porous Metal–Organic Framework. **J. Am. Chem. Soc.** 133(31): 11920-11923.
- Choomwattana, S., T. Maihom, P. Khongpracha, M. Probst and J. Limtrakul. 2008. Structures and Mechanisms of the Carbonyl-Ene Reaction between Mof-11 Encapsulated Formaldehyde and Propylene: An Oniom Study. **J. Phys. Chem. C.** 112(29): 10855-10861.
- Chui, S.S.-Y., S.M.-F. Lo, J.P.H. Charmant, A.G. Orpen and I.D. Williams. 1999. A Chemically Functionalizable Nanoporous Material [Cu₃(TMA)₂(H₂O)₃]_n. **Science.** 283(5405): 1148-1150.
- Cravillon, J., S. Münzer, S.-J. Lohmeier, A. Feldhoff, K. Huber and M. Wiebcke. 2009. Rapid Room-Temperature Synthesis and Characterization of Nanocrystals of a Prototypical Zeolitic Imidazolate Framework. **Chem. Mater.** 21(8): 1410-1412.

- Cravillon, J., C.A. Schröder, R. Nayuk, J. Gummel, K. Huber and M. Wiebcke. 2011a. Fast Nucleation and Growth of ZIF-8 Nanocrystals Monitored by Time-Resolved in Situ Small-Angle and Wide-Angle X-Ray Scattering. **Angew. Chem.** 123(35): 8217-8221.
- Cravillon, J., C.A. Schröder, R. Nayuk, J. Gummel, K. Huber and M. Wiebcke. 2011b. Fast Nucleation and Growth of ZIF-8 Nanocrystals Monitored by Time-Resolved in Situ Small-Angle and Wide-Angle X-Ray Scattering. **Angew. Chem. Int. Ed.** 50(35): 8067-8071.
- Cravillon, J., R. Nayuk, S. Springer, A. Feldhoff, K. Huber and M. Wiebcke. 2011c. Controlling Zeolitic Imidazolate Framework Nano- and Microcrystal Formation: Insight into Crystal Growth by Time-Resolved in Situ Static Light Scattering. **Chem. Mater.** 23(8): 2130-2141.
- Crossley, S., J. Faria, M. Shen and D.E. Resasco. 2010. Solid Nanoparticles That Catalyze Biofuel Upgrade Reactions at the Water/Oil Interface. **Science.** 327(5961): 68-72.
- Cuenya, B.R. 2010. Synthesis and Catalytic Properties of Metal Nanoparticles: Size, Shape, Support, Composition, and Oxidation State Effects. **Thin Solid Films.** 518(12): 3127-3150.
- Dapprich, S., I. Komáromi, K.S. Byun, K. Morokuma and M.J. Frisch. 1999. A New Oniom Implementation in Gaussian98. Part I. The Calculation of Energies, Gradients, Vibrational Frequencies and Electric Field Derivatives. **J. Mol. Struct. THEOCHEM.** 461–462(0): 1-21.
- Davidová, M., D. Nachtigallová, P. Nachtigall and J. Sauer. 2004. Nature of the Cu⁺—No Bond in the Gas Phase and at Different Types of Cu⁺ Sites in Zeolite Catalysts. **J. Phys. Chem. B.** 108(36): 13674-13682.

- Davydovskaya, P., R. Pohle, A. Tawil and M. Fleischer. 2013. Work Function Based Gas Sensing with Cu-Btc Metal-Organic Framework for Selective Aldehyde Detection. **Sens. Actuator B: Chem.** 187(0): 142-146.
- Derouane, E.G. and J.G. Fripiat. 1985. Non-Empirical Quantum Chemical Study of the Siting and Pairing of Aluminium in the Mfi Framework. **Zeolites.** 5(3): 165-172.
- Dhakshinamoorthy, A., M. Alvaro and H. Garcia. 2010. Aerobic Oxidation of Benzylic Alcohols Catalyzed by Metal–Organic Frameworks Assisted by Tempo. **ACS Catalysis.** 1(1): 48-53.
- Dhakshinamoorthy, A., M. Alvaro and H. Garcia. 2011. Metal-Organic Frameworks as Heterogeneous Catalysts for Oxidation Reactions. **Catalysis Science & Technology.** 1(6): 856-867.
- Doherty, C.M., G. Greci, R. Riccò, J.I. Mardel, J. Reboul, S. Furukawa, S. Kitagawa, A.J. Hill and P. Falcaro. 2013. Combining Uv Lithography and an Imprinting Technique for Patterning Metal-Organic Frameworks. **Adv. Mater.** 25(34): 4701-4705.
- Doyle, M.P. 2006. Perspective on Dirhodium Carboxamidates as Catalysts. **J. Org. Chem.** 71(25): 9253-9260.
- Du, Y., R.Z. Chen, J.F. Yao and H.T. Wang. 2013. Facile Fabrication of Porous ZnO by Thermal Treatment of Zeolitic Imidazolate Framework-8 and Its Photocatalytic Activity. **J. Alloys Compd.** 551(0): 125-130.
- Eddaoudi, M., D.B. Moler, H. Li, B. Chen, T.M. Reineke, M. O'Keeffe and O.M. Yaghi. 2001. Modular Chemistry: Secondary Building Units as a Basis for the Design of Highly Porous and Robust Metal–Organic Carboxylate Frameworks. **Acc. Chem. Res.** 34(4): 319-330.

- Eddaoudi, M., J. Kim, N. Rosi, D. Vodak, J. Wachter, M. O'Keeffe and O.M. Yaghi. 2002. Systematic Design of Pore Size and Functionality in Isoreticular MOFs and Their Application in Methane Storage. **Science**. 295(5554): 469-472.
- El-Shall, M.S., V. Abdelsayed, A.E.R.S. Khder, H.M.A. Hassan, H.M. El-Kaderi and T.E. Reich. 2009. Metallic and Bimetallic Nanocatalysts Incorporated into Highly Porous Coordination Polymer MIL-101. **J. Mater. Chem.** 19(41): 7625-7631.
- Fattah, Z., J. Roche, P. Garrigue, D. Zigah, L. Bouffier and A. Kuhn. 2013. Chemiluminescence from Asymmetric Inorganic Surface Layers Generated by Bipolar Electrochemistry. **ChemPhysChem**. 14(10): 2089-2093.
- Fattah, Z., G. Loget, V. Lapeyre, P. Garrigue, C. Warakulwit, J. Limtrakul, L. Bouffier and A. Kuhn. 2011. Straightforward Single-Step Generation of Microswimmers by Bipolar Electrochemistry. **Electrochim. Acta**. 56(28): 10562-10566.
- Férey, G., C. Mellot-Draznieks, C. Serre, F. Millange, J. Dutour, S. Surblé and I. Margiolaki. 2005. A Chromium Terephthalate-Based Solid with Unusually Large Pore Volumes and Surface Area. **Science**. 309(5743): 2040-2042.
- Fleischmann, M., J. Ghoroghchian, D. Rolison and S. Pons. 1986. Electrochemical Behavior of Dispersions of Spherical Ultramicroelectrodes. **J. Phys. Chem.** 90(23): 6392-6400.
- Fosdick, S.E., K.N. Knust, K. Scida and R.M. Crooks. 2013. Bipolar Electrochemistry. **Angew. Chem. Int. Ed.** 52(40): 10438-10456.
- Frisch, M.J.T., G. W.; Schlegel, H. B.; Scuseria, G. E.; Robb, M. A.; Cheeseman, J. R.; Montgomery, Jr., J. A.; Vreven, T.; Kudin, K. N.; Burant, J. C.; Millam, J. M.; Iyengar, S. S.; Tomasi, J.; Barone, V.; Mennucci, B.; Cossi, M.; Scalmani, G.; Rega, N.; Petersson, G. A.; Nakatsuji, H.; Hada, M.; Ehara, M.; Toyota, K.; Fukuda, R.; Hasegawa, J.; Ishida, M.; Nakajima, T.; Honda, Y.; Kitao, O.; Nakai, H.; Klene, M.; Li, X.; Knox, J.

E.; Hratchian, H. P.; Cross, J. B.; Bakken, V.; Adamo, C.; Jaramillo, J.; Gomperts, R.; Stratmann, R. E.; Yazyev, O.; Austin, A. J.; Cammi, R.; Pomelli, C.; Ochterski, J. W.; Ayala, P. Y.; Morokuma, K.; Voth, G. A.; Salvador, P.; Dannenberg, J. J.; Zakrzewski, V. G.; Dapprich, S.; Daniels, A. D.; Strain, M. C.; Farkas, O.; Malick, D. K.; Rabuck, A. D.; Raghavachari, K.; Foresman, J. B.; Ortiz, J. V.; Cui, Q.; Baboul, A. G.; Clifford, S.; Cioslowski, J.; Stefanov, B. B.; Liu, G.; Liashenko, A.; Piskorz, P.; Komaromi, I.; Martin, R. L.; Fox, D. J.; Keith, T.; Al-Laham, M. A.; Peng, C. Y.; Nanayakkara, A.; Challacombe, M.; Gill, P. M. W.; Johnson, B.; Chen, W.; Wong, M. W.; Gonzalez, C.; and Pople, J. A.; . A. *Gaussian 03*, Revision B.05; Gaussian, Inc.: Wallingford, Ct, 2004.

Frisch, M.J.T., G. W.; Schlegel, H. B.; Scuseria, G. E.; Robb, M. A.; Cheeseman, J. R.; Scalmani, G.; Barone, V.; Mennucci, B.; Petersson, G. A.; Nakatsuji, H.; Caricato, M.; Li, X.; Hratchian, H. P.; Izmaylov, A. F.; Bloino, J.; Zheng, G.; Sonnenberg, J. L.; Hada, M.; Ehara, M.; Toyota, K.; Fukuda, R.; Hasegawa, J.; Ishida, M.; Nakajima, T.; Honda, Y.; Kitao, O.; Nakai, H.; Vreven, T.; Montgomery, J. A., Jr.; Peralta, J. E.; Ogliaro, F.; Bearpark, M.; Heyd, J. J.; Brothers, E.; Kudin, K. N.; Staroverov, V. N.; Kobayashi, R.; Normand, J.; Raghavachari, K.; Rendell, A.; Burant, J. C.; Iyengar, S. S.; Tomasi, J.; Cossi, M.; Rega, N.; Millam, M. J.; Klene, M.; Knox, J. E.; Cross, J. B.; Bakken, V.; Adamo, C.; Jaramillo, J.; Gomperts, R.; Stratmann, R. E.; Yazyev, O.; Austin, A. J.; Cammi, R.; Pomelli, C.; Ochterski, J. W.; Martin, R. L.; Morokuma, K.; Zakrzewski, V. G.; Voth, G. A.; Salvador, P.; Dannenberg, J. J.; Dapprich, S.; Daniels, A. D.; Farkas, Ö.; Foresman, J. B.; Ortiz, J. V.; Cioslowski, J.; Fox, D. J. Gaussian, Inc., Wallingford CT. 2009. Gaussian 09, Revision A.02.

Friscic, T. and L. Fabian. 2009. Mechanochemical Conversion of a Metal Oxide into Coordination Polymers and Porous Frameworks Using Liquid-Assisted Grinding (LAG). **CrystEngComm**. 11(5): 743-745.

- Fujita, S.-i., M. Nishiura and M. Arai. 2010. Synthesis of Styrene Carbonate from Carbon Dioxide and Styrene Oxide with Various Zinc Halide-Based Ionic Liquids. **Catal. Lett.** 135(3-4): 263-268.
- Furukawa, S., K. Hirai, K. Nakagawa, Y. Takashima, R. Matsuda, T. Tsuruoka, M. Kondo, R. Haruki, D. Tanaka, H. Sakamoto, S. Shimomura, O. Sakata and S. Kitagawa. 2009a. Heterogeneously Hybridized Porous Coordination Polymer Crystals: Fabrication of Heterometallic Core–Shell Single Crystals with an in-Plane Rotational Epitaxial Relationship. **Angew. Chem.** 121(10): 1798-1802.
- Furukawa, S., K. Hirai, K. Nakagawa, Y. Takashima, R. Matsuda, T. Tsuruoka, M. Kondo, R. Haruki, D. Tanaka, H. Sakamoto, S. Shimomura, O. Sakata and S. Kitagawa. 2009b. Heterogeneously Hybridized Porous Coordination Polymer Crystals: Fabrication of Heterometallic Core–Shell Single Crystals with an in-Plane Rotational Epitaxial Relationship. **Angew. Chem. Int. Ed.** 48(10): 1766-1770.
- Giesche, H. 1994. Synthesis of Monodispersed Silica Powders I. Particle Properties and Reaction Kinetics. **J. Eur. Ceram. Soc.** 14(3): 189-204.
- Guerrette, J.P., S.J. Percival and B. Zhang. 2012a. Fluorescence Coupling for Direct Imaging of Electrocatalytic Heterogeneity. **J. Am. Chem. Soc.** 135(2): 855-861.
- Guerrette, J.P., S.M. Oja and B. Zhang. 2012b. Coupled Electrochemical Reactions at Bipolar Microelectrodes and Nanoelectrodes. **Anal. Chem.** 84(3): 1609-1616.
- Gung, B.W., Z. Zhu and R.A. Fouch. 1995. Transition State of the Silicon-Directed Aldol Reaction: An Ab Initio Molecular Orbital Study. **J. Org. Chem.** 60(9): 2860-2864.
- Hansen, J. and H.M.L. Davies. 2008. High Symmetry Dirhodium(Ii) Paddlewheel Complexes as Chiral Catalysts. **Coord. Chem. Rev.** 252(5–7): 545-555.

- Hara, N., M. Yoshimune, H. Negishi, K. Haraya, S. Hara and T. Yamaguchi. 2014. Diffusive Separation of Propylene/Propane with ZIF-8 Membranes. **J. Membr. Sci.** 450(0): 215-223.
- Haruta, M. 1997. Size- and Support-Dependency in the Catalysis of Gold. **Catal. Today.** 36(1): 153-166.
- Hashmi, A.S.K. and G.J. Hutchings. 2006. Gold Catalysis. **Angew. Chem. Int. Ed.** 45(47): 7896-7936.
- Hay, P.J. and W.R. Wadt. 1985. Ab Initio Effective Core Potentials for Molecular Calculations. Potentials for the Transition Metal Atoms Sc to Hg. **J. Chem. Phys.** 82(1): 270-283.
- He, L.-N., H. Yasuda and T. Sakakura. 2003. New Procedure for Recycling Homogeneous Catalyst: Propylene Carbonate Synthesis under Supercritical CO₂ Conditions. **Green Chemistry.** 5(1): 92-94.
- Hermes, S., M.-K. Schröter, R. Schmid, L. Khodeir, M. Muhler, A. Tissler, R.W. Fischer and R.A. Fischer. 2005. Metal@MOF: Loading of Highly Porous Coordination Polymers Host Lattices by Metal Organic Chemical Vapor Deposition. **Angew. Chem. Int. Ed.** 44(38): 6237-6241.
- Hod, I., W. Bury, D.M. Karlin, P. Deria, C.-W. Kung, M.J. Katz, M. So, B. Klahr, D. Jin, Y.-W. Chung, T.W. Odom, O.K. Farha and J.T. Hupp. 2014. Directed Growth of Electroactive Metal-Organic Framework Thin Films Using Electrophoretic Deposition. **Adv. Mater.** n/a-n/a.
- Horcajada, P., R. Gref, T. Baati, P.K. Allan, G. Maurin, P. Couvreur, G. Férey, R.E. Morris and C. Serre. 2011. Metal–Organic Frameworks in Biomedicine. **Chem. Rev.** 112(2): 1232-1268.

- Hu, Y., H. Kazemian, S. Rohani, Y. Huang and Y. Song. 2011. In Situ High Pressure Study of Zif-8 by Ftir Spectroscopy. **Chem. Commun.** 47(47): 12694-12696.
- Hu, Y., Z. Liu, J. Xu, Y. Huang and Y. Song. 2013. Evidence of Pressure Enhanced CO₂ Storage in Zif-8 Probed by Ftir Spectroscopy. **J. Am. Chem. Soc.** 135(25): 9287-9290.
- Huang, X.-X., L.-G. Qiu, W. Zhang, Y.-P. Yuan, X. Jiang, A.-J. Xie, Y.-H. Shen and J.-F. Zhu. 2012. Hierarchically Mesostructured MIL-101 Metal-Organic Frameworks: Supramolecular Template-Directed Synthesis and Accelerated Adsorption Kinetics for Dye Removal. **CrystEngComm.** 14(5): 1613-1617.
- Huxford, R.C., J. Della Rocca and W. Lin. 2010. Metal–Organic Frameworks as Potential Drug Carriers. **Curr. Opin. Chem. Biol.** 14(2): 262-268.
- Hwang, Y.K., D.-Y. Hong, J.-S. Chang, S.H. Jhung, Y.-K. Seo, J. Kim, A. Vimont, M. Daturi, C. Serre and G. Férey. 2008. Amine Grafting on Coordinatively Unsaturated Metal Centers of MOFs: Consequences for Catalysis and Metal Encapsulation. **Angew. Chem. Int. Ed.** 47(22): 4144-4148.
- Jeremias, F., S.K. Henninger and C. Janiak. 2012. High Performance Metal-Organic-Framework Coatings Obtained Via Thermal Gradient Synthesis. **Chem. Commun.** 48(78): 9708-9710.
- Jhung, S.H., J.H. Lee, J.W. Yoon, C. Serre, G. Férey and J.S. Chang. 2007. Microwave Synthesis of Chromium Terephthalate MIL-101 and Its Benzene Sorption Ability. **Adv. Mater.** 19(1): 121-124.
- Jiang, H.-L., B. Liu, T. Akita, M. Haruta, H. Sakurai and Q. Xu. 2009. Au@ZIF-8: Co Oxidation over Gold Nanoparticles Deposited to Metal–Organic Framework. **J. Am. Chem. Soc.** 131(32): 11302-11303.

- Jiang, S and Granick, S. (Editor) 2012. **Janus Particle Synthesis Self-Assembly and Applications**. The Royal Society of Chemistry, London,
- Kato, H., T. Minami, T. Kanazawa and Y. Sasaki. 2004. Mesopores Created by Platinum Nanoparticles in Zeolite Crystals. **Angew. Chem. Int. Ed.** 43(10): 1251-1254.
- Kawanami, H., A. Sasaki, K. Matsui and Y. Ikushima. 2003. A Rapid and Effective Synthesis of Propylene Carbonate Using a Supercritical CO₂-Ionic Liquid System. **Chem. Commun.** (7): 896-897.
- Khan, N.A., I.J. Kang, H.Y. Seok and S.H. Jung. 2011. Facile Synthesis of Nano-Sized Metal-Organic Frameworks, Chromium-Benzenedicarboxylate, MIL-101. **Chem. Eng. J.** 166(3): 1152-1157.
- Kida, K., M. Okita, K. Fujita, S. Tanaka and Y. Miyake. 2013. Formation of High Crystalline ZIF-8 in an Aqueous Solution. **CrystEngComm.** 15(9): 1794-1801.
- Kim, H.S., J.J. Kim, H.N. Kwon, M.J. Chung, B.G. Lee and H.G. Jang. 2002. Well-Defined Highly Active Heterogeneous Catalyst System for the Coupling Reactions of Carbon Dioxide and Epoxides. **J. Catal.** 205(1): 226-229.
- Kim, S.-H., J.Y. Sim, J.-M. Lim and S.-M. Yang. 2010. Magnetoresponse Microparticles with Nanoscopic Surface Structures for Remote-Controlled Locomotion. **Angew. Chem. Int. Ed.** 49(22): 3786-3790.
- Kitagawa, S., R. Kitaura and S.-i. Noro. 2004. Functional Porous Coordination Polymers. **Angew. Chem. Int. Ed.** 43(18): 2334-2375.
- Klinowski, J., F.A. Almeida Paz, P. Silva and J. Rocha. 2011. Microwave-Assisted Synthesis of Metal-Organic Frameworks. **Dalton Trans.** 40(2): 321-330.

- Krawiec, P., M. Kramer, M. Sabo, R. Kunschke, H. Fröde and S. Kaskel. 2006. Improved Hydrogen Storage in the Metal-Organic Framework $\text{Cu}_3(\text{BTC})_2$. **Adv. Eng. Mater.** 8(4): 293-296.
- Kreno, L.E., K. Leong, O.K. Farha, M. Allendorf, R.P. Van Duyne and J.T. Hupp. 2011. Metal–Organic Framework Materials as Chemical Sensors. **Chem. Rev.** 112(2): 1105-1125.
- Kumsapaya, C., K. Bobuatong, P. Khongpracha, Y. Tantirungrotechai and J. Limtrakul. 2009. Mechanistic Investigation on 1,5- to 2,6-Dimethylnaphthalene Isomerization Catalyzed by Acidic B Zeolite: Oniom Study with an M06-L Functional. **J. Phys. Chem. C.** 113(36): 16128-16137.
- Lamberti, C., S. Bordiga, M. Salvalaggio, G. Spoto, A. Zecchina, F. Geobaldo, G. Vlaic and M. Bellatreccia. 1997. XAFS, Ir, and UV–Vis Study of the Cui Environment in Cu-ZSM-5. **J. Phys. Chem. B.** 101(3): 344-360.
- Lee, J., O.K. Farha, J. Roberts, K.A. Scheidt, S.T. Nguyen and J.T. Hupp. 2009. Metal-Organic Framework Materials as Catalysts. **Chem. Soc. Rev.** 38(5): 1450-1459.
- Lee, K.J., J. Yoon, S. Rahmani, S. Hwang, S. Bhaskar, S. Mitragotri and J. Lahann. 2012. Spontaneous Shape Reconfigurations in Multicompartmental Microcylinders. **Proc. Natl. Acad. Sci.** 109(40): 16057-16062.
- Li, B., H. Zhang, L. Huynh, M. Shatruk and E.V. Dikarev. 2007. Mo/Rh Carboxylate: Heterometallic Compound Built of Homometallic Paddlewheel Units. **Inorg. Chem.** 46(22): 9155-9159.
- Li, J.-R., R.J. Kuppler and H.-C. Zhou. 2009. Selective Gas Adsorption and Separation in Metal-Organic Frameworks. **Chem. Soc. Rev.** 38(5): 1477-1504.

- Li, M. and M. Dincă. 2011. Reductive Electrosynthesis of Crystalline Metal–Organic Frameworks. **J. Am. Chem. Soc.** 133(33): 12926-12929.
- Li, M. and M. Dinca. 2014. Selective Formation of Biphasic Thin Films of Metal-Organic Frameworks by Potential-Controlled Cathodic Electrodeposition. **Chemical Science.** 5(1): 107-111.
- Lin, Y., X. Cui, C. Yen and C.M. Wai. 2005. Platinum/Carbon Nanotube Nanocomposite Synthesized in Supercritical Fluid as Electrocatalysts for Low-Temperature Fuel Cells. **J. Phys. Chem. B.** 109(30): 14410-14415.
- Liu, H., Y. Liu, Y. Li, Z. Tang and H. Jiang. 2010. Metal–Organic Framework Supported Gold Nanoparticles as a Highly Active Heterogeneous Catalyst for Aerobic Oxidation of Alcohols. **J. Phys. Chem. C.** 114(31): 13362-13369.
- Liu, Q., L. Ning, S. Zheng, M. Tao, Y. Shi and Y. He. 2013. Adsorption of Carbon Dioxide by Mil-101(Cr): Regeneration Conditions and Influence of Flue Gas Contaminants. **Sci. Rep.**
- Loget, G. and A. Kuhn. 2010. Propulsion of Microobjects by Dynamic Bipolar Self-Regeneration. **J. Am. Chem. Soc.** 132(45): 15918-15919.
- Loget, G. and A. Kuhn. 2011a. Shaping and Exploring the Micro- and Nanoworld Using Bipolar Electrochemistry. **Anal Bioanal Chem.** 400(6): 1691-1704.
- Loget, G. and A. Kuhn. 2011b. Electric Field-Induced Chemical Locomotion of Conducting Objects. **Nat Commun.** 2:535.
- Loget, G. and A. Kuhn. 2012. Bipolar Electrochemistry for Cargo-Lifting in Fluid Channels. **Lab on a Chip.** 12(11): 1967-1971.

- Loget, G., J. Roche, E. Gianessi, L. Bouffier and A. Kuhn. 2012. Indirect Bipolar Electrodeposition. **J. Am. Chem. Soc.** 134(49): 20033-20036.
- Loget, G., D. Zigah, L. Bouffier, N. Sojic and A. Kuhn. 2013. Bipolar Electrochemistry: From Materials Science to Motion and Beyond. **Acc. Chem. Res.** 46(11): 2513-2523.
- Loget, G., V. Lapeyre, P. Garrigue, C. Warakulwit, J. Limtrakul, M.-H. Delville and A. Kuhn. 2011. Versatile Procedure for Synthesis of Janus-Type Carbon Tubes. **Chem. Mater.** 23(10): 2595-2599.
- Loget, G., G. Larcade, V. Lapeyre, P. Garrigue, C. Warakulwit, J. Limtrakul, M.H. Delville, V. Ravaine and A. Kuhn. 2010. Single Point Electrodeposition of Nickel for the Dissymmetric Decoration of Carbon Tubes. **Electrochim. Acta.** 55(27): 8116-8120.
- Lordi, V., N. Yao and J. Wei. 2001. Method for Supporting Platinum on Single-Walled Carbon Nanotubes for a Selective Hydrogenation Catalyst. **Chem. Mater.** 13(3): 733-737.
- Lu, G. and J.T. Hupp. 2010. Metal–Organic Frameworks as Sensors: A Zif-8 Based Fabry–Pérot Device as a Selective Sensor for Chemical Vapors and Gases. **J. Am. Chem. Soc.** 132(23): 7832-7833.
- Lu, G., O.K. Farha, W. Zhang, F. Huo and J.T. Hupp. 2012. Engineering ZIF-8 Thin Films for Hybrid Mof-Based Devices. **Adv. Mater.** 24(29): 3970-3974.
- Ma, L., C. Abney and W. Lin. 2009. Enantioselective Catalysis with Homochiral Metal–Organic Frameworks. **Chem. Soc. Rev.** 38(5): 1248-1256.
- Macias, E.E., P. Ratnasamy and M.A. Carreon. 2012. Catalytic Activity of Metal Organic Framework $\text{Cu}_3(\text{BTC})_2$ in the Cycloaddition of CO_2 to Epichlorohydrin Reaction. **Catal. Today.** 198(1): 215-218.

- Maihom, T., P. Pantu, C. Tachakritikul, M. Probst and J. Limtrakul. 2010. Effect of the Zeolite Nanocavity on the Reaction Mechanism of N-Hexane Cracking: A Density Functional Theory Study. **J. Phys. Chem. C.** 114(17): 7850-7856.
- Maihom, T., B. Boekfa, J. Sirijaraensre, T. Nanok, M. Probst and J. Limtrakul. 2009. Reaction Mechanisms of the Methylation of Ethene with Methanol and Dimethyl Ether over H-ZSM-5: An Oniom Study. **J. Phys. Chem. C.** 113(16): 6654-6662.
- Maillard, M., P. Huang and L. Brus. 2003. Silver Nanodisk Growth by Surface Plasmon Enhanced Photoreduction of Adsorbed $[Ag^+]$. **Nano Lett.** 3(11): 1611-1615.
- Mao, Y., L. shi, H. Huang, W. Cao, J. Li, L. Sun, X. Jin and X. Peng. 2013. Room Temperature Synthesis of Free-Standing HKUST-1 Membranes from Copper Hydroxide Nanostrands for Gas Separation. **Chem. Commun.** 49(50): 5666-5668.
- Martinez Joaristi, A., J. Juan-Alcañiz, P. Serra-Crespo, F. Kapteijn and J. Gascon. 2012. Electrochemical Synthesis of Some Archetypical Zn^{2+} , Cu^{2+} , and Al^{3+} Metal Organic Frameworks. **Cryst. Growth Des.** 12(7): 3489-3498.
- Mavré, F.o., R.K. Anand, D.R. Laws, K.-F. Chow, B.-Y. Chang, J.A. Crooks and R.M. Crooks. 2010. Bipolar Electrodes: A Useful Tool for Concentration, Separation, and Detection of Analytes in Microelectrochemical Systems. **Anal. Chem.** 82(21): 8766-8774.
- Meilikhov, M., K. Yusenko, D. Esken, S. Turner, G. Van Tendeloo and R.A. Fischer. 2010. Metals@MOFs – Loading Mofs with Metal Nanoparticles for Hybrid Functions. **Eur. J. Inorg. Chem.** 2010(24): 3701-3714.
- Millange, F., C. Serre and G. Ferey. 2002. Synthesis, Structure Determination and Properties of Mil-53as and Mil-53ht: The first Cr^{III} hybrid inorganic–organic microporous solids: $Cr^{III}(OH) \cdot \{O_2C-C_6H_4-CO_2\} \cdot \{HO_2C-C_6H_4-CO_2H\}_x$. **Chem. Commun.** 8: 822-823.

- Miralda, C.M., E.E. Macias, M. Zhu, P. Ratnasamy and M.A. Carreon. 2011. Zeolitic Imidazole Framework-8 Catalysts in the Conversion of CO_2 to Chloropropene Carbonate. **ACS Catalysis**. 2(1): 180-183.
- Morris, R.E. and P.S. Wheatley. 2008. Gas Storage in Nanoporous Materials. **Angew. Chem. Int. Ed.** 47(27): 4966-4981.
- Mueller, U., M. Schubert, F. Teich, H. Puetter, K. Schierle-Arndt and J. Pastre. 2006. Metal-Organic Frameworks-Prospective Industrial Applications. **J. Mater. Chem.** 16(7): 626-636.
- Müller, U. (BASF AG). 2005. Method for electrochemical production of a crystalline porous metal organic skeleton material **Patent** WO 2005/049892.
- Mukaiyama, T., K. Banno and K. Narasaka. 1974. New Cross-Aldol Reactions. Reactions of Silyl Enol Ethers with Carbonyl Compounds Activated by Titanium Tetrachloride. **J. Am. Chem. Soc.** 96(24): 7503-7509.
- Nachtigall, P., D. Nachtigallová and J. Sauer. 2000. Coordination Change of Cu^+ Sites in Zsm-5 on Excitation in the Triplet State: Understanding of the Photoluminescence Spectra. **J. Phys. Chem. B.** 104(8): 1738-1745.
- Okachi, T. and M. Onaka. 2004. Formaldehyde Encapsulated in Zeolite: A Long-Lived, Highly Activated One-Carbon Electrophile to Carbonyl-Ene Reactions. **J. Am. Chem. Soc.** 126(8): 2306-2307.
- Opelt, S., S. Türk, E. Dietzsch, A. Henschel, S. Kaskel and E. Klemm. 2008. Preparation of Palladium Supported on Mof-5 and Its Use as Hydrogenation Catalyst. **Catal. Commun.** 9(6): 1286-1290.

- Ordoñez, M.J.C., K.J. Balkus Jr, J.P. Ferraris and I.H. Musselman. 2010. Molecular Sieving Realized with ZIF-8/Matrimid® Mixed-Matrix Membranes. **J. Membr. Sci.** 361(1–2): 28-37.
- Pan, Y., B. Yuan, Y. Li and D. He. 2010. Multifunctional Catalysis by Pd@MIL-101: One-Step Synthesis of Methyl Isobutyl Ketone over Palladium Nanoparticles Deposited on a Metal-Organic Framework. **Chem. Commun.** 46(13): 2280-2282.
- Pan, Y., Y. Liu, G. Zeng, L. Zhao and Z. Lai. 2011. Rapid Synthesis of Zeolitic Imidazolate Framework-8 (ZIF-8) Nanocrystals in an Aqueous System. **Chem. Commun.** 47(7): 2071-2073.
- Park, K.S., Z. Ni, A.P. Côté, J.Y. Choi, R. Huang, F.J. Uribe-Romo, H.K. Chae, M. O’Keeffe and O.M. Yaghi. 2006. Exceptional Chemical and Thermal Stability of Zeolitic Imidazolate Frameworks. **Proc. Natl. Acad. Sci.** 103(27): 10186-10191.
- Park, T.-H., K.J. Lee, S. Hwang, J. Yoon, C. Woell and J. Lahann. 2014. Spatioselective Growth of Metal-Organic Framework Nanocrystals on Compositionally Anisotropic Polymer Particles. **Adv. Mater.** 26(18): 2883-2888.
- Pathan, N.B., A.M. Rahatgaonkar and M.S. Chorghade. 2011. Metal-Organic Framework Cu₃(BTC)₂(H₂O)₃ Catalyzed Aldol Synthesis of Pyrimidine-Chalcone Hybrids. **Catal. Commun.** 12(12): 1170-1176.
- Peng, L., J. Zhang, J. Li, B. Han, Z. Xue and G. Yang. 2012. Surfactant-Directed Assembly of Mesoporous Metal-Organic Framework Nanoplates in Ionic Liquids. **Chem. Commun.** 48(69): 8688-8690.
- Pham, M.-H., G.-T. Vuong, A.-T. Vu and T.-O. Do. 2011a. Novel Route to Size-Controlled Fe–MIL-88b–NH₂ Metal–Organic Framework Nanocrystals. **Langmuir.** 27(24): 15261-15267.

- Pham, M.-H., G.-T. Vuong, F.-G. Fontaine and T.-O. Do. 2011b. A Route to Bimodal Micro-Mesoporous Metal–Organic Frameworks Nanocrystals. **Cryst. Growth Des.** 12(2): 1008-1013.
- Philip, M. 2001. Nanostructured Materials. **Rep. Prog. Phys.** 64(3): 297.
- Pichon, A., A. Lazuen-Garay and S.L. James. 2006. Solvent-Free Synthesis of a Microporous Metal-Organic Framework. **CrystEngComm.** 8(3): 211-214.
- Pöpl, A., S. Kunz, D. Himsl and M. Hartmann. 2008. Cw and Pulsed ESR Spectroscopy of Cupric Ions in the Metal–Organic Framework Compound $\text{Cu}_3(\text{BTC})_2$. **J. Phys. Chem. C.** 112(7): 2678-2684.
- Prestipino, C., L. Regli, J.G. Vitillo, F. Bonino, A. Damin, C. Lamberti, A. Zecchina, P.L. Solari, K.O. Kongshaug and S. Bordiga. 2006. Local Structure of Framework Cu(II) in HKUST-1 Metallorganic Framework: Spectroscopic Characterization Upon Activation and Interaction with Adsorbates. **Chem. Mater.** 18(5): 1337-1346.
- Qiu, L.-G., Z.-Q. Li, Y. Wu, W. Wang, T. Xu and X. Jiang. 2008a. Facile Synthesis of Nanocrystals of a Microporous Metal-Organic Framework by an Ultrasonic Method and Selective Sensing of Organoamines. **Chem. Commun.** 31): 3642-3644.
- Qiu, L.-G., T. Xu, Z.-Q. Li, W. Wang, Y. Wu, X. Jiang, X.-Y. Tian and L.-D. Zhang. 2008b. Hierarchically Micro- and Mesoporous Metal–Organic Frameworks with Tunable Porosity. **Angew. Chem. Int. Ed.** 47(49): 9487-9491.
- Reboul, J., S. Furukawa, N. Horike, M. Tsotsalas, K. Hirai, H. Uehara, M. Kondo, N. Louvain, O. Sakata and S. Kitagawa. 2012. Mesoscopic Architectures of Porous Coordination Polymers Fabricated by Pseudomorphic Replication. **Nat Mater.** 11(8): 717-723.

- Reetz, M.T., R. Breinbauer and K. Wanninger. 1996. Suzuki and Heck Reactions Catalyzed by Preformed Palladium Clusters and Palladiumnickel Bimetallic Clusters. **Tetrahedron Lett.** 37(26): 4499-4502.
- Sachse, A., R. Ameloot, B. Coq, F. Fajula, B. Coasne, D. De Vos and A. Galarneau. 2012. In Situ Synthesis of Cu-Btc (HKUST-1) in Macro-/Mesoporous Silica Monoliths for Continuous Flow Catalysis. **Chem. Commun.** 48(39): 4749-4751.
- Sakakura, T., J.-C. Choi and H. Yasuda. 2007. Transformation of Carbon Dioxide. **Chem. Rev.** 107(6): 2365-2387.
- Sayle, D.C., J.A. Doig, S.C. Parker and G.W. Watson. 2003. Metal Oxide Encapsulated Nanoparticles. **J. Mater. Chem.** 13(9): 2078-2089.
- Schlesinger, M., S. Schulze, M. Hietschold and M. Mehring. 2010. Evaluation of Synthetic Methods for Microporous Metal–Organic Frameworks Exemplified by the Competitive Formation of $[\text{Cu}_2(\text{BTC})_3(\text{H}_2\text{O})_3]$ and $[\text{Cu}_2(\text{BTC})(\text{OH})(\text{H}_2\text{O})]$. **Microporous Mesoporous Mater.** 132(1–2): 121-127.
- Shaikh, A.-A.G. and S. Sivaram. 1996. Organic Carbonates†. **Chem. Rev.** 96(3): 951-976.
- Shao, Y., G. Yin, Y. Gao and P. Shi. 2006. Durability Study of Pt/C and Pt/Cnts Catalysts under Simulated Pem Fuel Cell Conditions. **J. Electrochem. Soc.** 153(6): A1093-A1097.
- Shekhah, O., J. Liu, R.A. Fischer and C. Woll. 2011. MOF Thin Films: Existing and Future Applications. **Chem. Soc. Rev.** 40(2): 1081-1106.
- Simon, S., M. Duran and J.J. Dannenberg. 1996. How Does Basis Set Superposition Error Change the Potential Surfaces for Hydrogen - Bonded Dimers? **J. Chem. Phys.** 105(24): 11024-11031.

- Song, J., Z. Zhang, S. Hu, T. Wu, T. Jiang and B. Han. 2009. MOF-5/N-Bu₄NBr: An Efficient Catalyst System for the Synthesis of Cyclic Carbonates from Epoxides and CO₂ under Mild Conditions. **Green Chemistry**. 11(7): 1031-1036.
- Srivastava, R., D. Srinivas and P. Ratnasamy. 2003. Synthesis of Polycarbonate Precursors over Titanosilicate Molecular Sieves. **Catal. Lett.** 91(1-2): 133-139.
- Srivastava, R., D. Srinivas and P. Ratnasamy. 2005a. Zeolite-Based Organic–Inorganic Hybrid Catalysts for Phosgene-Free and Solvent-Free Synthesis of Cyclic Carbonates and Carbamates at Mild Conditions Utilizing CO₂. **Appl. Catal. A: Gen.** 289(2): 128-134.
- Srivastava, R., T.H. Bennur and D. Srinivas. 2005b. Factors Affecting Activation and Utilization of Carbon Dioxide in Cyclic Carbonates Synthesis over Cu and Mn Peraza Macrocyclic Complexes. **J. Mol. Catal. A: Chem.** 226(2): 199-205.
- Stavitski, E., E.A. Pidko, S. Couck, T. Remy, E.J.M. Hensen, B.M. Weckhuysen, J. Denayer, J. Gascon and F. Kapteijn. 2011. Complexity Behind CO₂ Capture on NH₂-MIL-53(Al). **Langmuir**. 27(7): 3970-3976.
- Stöber, W., A. Fink and E. Bohn. 1968. Controlled Growth of Monodisperse Silica Spheres in the Micron Size Range. **J. Colloid Interface Sci.** 26(1): 62-69.
- Stock, N. and S. Biswas. 2011. Synthesis of Metal-Organic Frameworks (MOFs): Routes to Various Mof Topologies, Morphologies, and Composites. **Chem. Rev.** 112(2): 933-969.
- Sun, J., S. Zhang, W. Cheng and J. Ren. 2008. Hydroxyl-Functionalized Ionic Liquid: A Novel Efficient Catalyst for Chemical Fixation of CO₂ to Cyclic Carbonate. **Tetrahedron Lett.** 49(22): 3588-3591.

- Sun, J., L. Wang, S. Zhang, Z. Li, X. Zhang, W. Dai and R. Mori. 2006. ZnCl_2 /Phosponium Halide: An Efficient Lewis Acid/Base Catalyst for the Synthesis of Cyclic Carbonate. **J. Mol. Catal. A: Chem.** 256(1–2): 295-300.
- Suresh, M., B. David Raju, K.S. Rama Rao, K. Raveendranath Reddy, M. Kantam and P. Srinivasu. 2014. Metal Organic Framework MIL-101(Cr) for Dehydration Reactions. **J Chem Sci.** 126(2): 527-532.
- Tan, C.G., B.D. Bowen and N. Epstein. 1987. Production of Monodisperse Colloidal Silica Spheres: Effect of Temperature. **J. Colloid Interface Sci.** 118(1): 290-293.
- Taylor-Pashow, K.M.L., J.D. Rocca, Z. Xie, S. Tran and W. Lin. 2009. Postsynthetic Modifications of Iron-Carboxylate Nanoscale Metal–Organic Frameworks for Imaging and Drug Delivery. **J. Am. Chem. Soc.** 131(40): 14261-14263.
- Tosheva, L. and V.P. Valtchev. 2005. Nanozeolites: Synthesis, Crystallization Mechanism, and Applications. **Chem. Mater.** 17(10): 2494-2513.
- Tranchemontagne, D.J., J.R. Hunt and O.M. Yaghi. 2008. Room Temperature Synthesis of Metal-Organic Frameworks: MOF-5, MOF-74, MOF-177, MOF-199, AND IRMOF-0. **Tetrahedron.** 64(36): 8553-8557.
- Tranchemontagne, D.J., J.L. Mendoza-Cortes, M. O'Keeffe and O.M. Yaghi. 2009. Secondary Building Units, Nets and Bonding in the Chemistry of Metal-Organic Frameworks. **Chem. Soc. Rev.** 38(5): 1257-1283.
- Tsunoyama, H., H. Sakurai and T. Tsukuda. 2006. Size Effect on the Catalysis of Gold Clusters Dispersed in Water for Aerobic Oxidation of Alcohol. **Chem. Phys. Lett.** 429(4–6): 528-532.

- Tsunoyama, H., H. Sakurai, Y. Negishi and T. Tsukuda. 2005. Size-Specific Catalytic Activity of Polymer-Stabilized Gold Nanoclusters for Aerobic Alcohol Oxidation in Water. **J. Am. Chem. Soc.** 127(26): 9374-9375.
- Tsunoyama, H., N. Ichikuni, H. Sakurai and T. Tsukuda. 2009. Effect of Electronic Structures of Au Clusters Stabilized by Poly(N-Vinyl-2-Pyrrolidone) on Aerobic Oxidation Catalysis. **J. Am. Chem. Soc.** 131(20): 7086-7093.
- Tsunoyama, H., H. Sakurai, N. Ichikuni, Y. Negishi and T. Tsukuda. 2004. Colloidal Gold Nanoparticles as Catalyst for Carbon–Carbon Bond Formation: Application to Aerobic Homocoupling of Phenylboronic Acid in Water. **Langmuir**. 20(26): 11293-11296.
- Ulrich, C., O. Andersson, L. Nyholm and F. Björefors. 2008a. Formation of Molecular Gradients on Bipolar Electrodes. **Angew. Chem.** 120(16): 3076-3078.
- Ulrich, C., O. Andersson, L. Nyholm and F. Björefors. 2008b. Formation of Molecular Gradients on Bipolar Electrodes. **Angew. Chem. Int. Ed.** 47(16): 3034-3036.
- Van Hyning, D.L. and C.F. Zukoski. 1998. Formation Mechanisms and Aggregation Behavior of Borohydride Reduced Silver Particles. **Langmuir**. 14(24): 7034-7046.
- Venna, S.R. and M.A. Carreon. 2009. Highly Permeable Zeolite Imidazolate Framework-8 Membranes for CO₂/CH₄ Separation. **J. Am. Chem. Soc.** 132(1): 76-78.
- Venna, S.R., J.B. Jasinski and M.A. Carreon. 2010. Structural Evolution of Zeolitic Imidazolate Framework-8. **J. Am. Chem. Soc.** 132(51): 18030-18033.
- Vishnyakov, A., P.I. Ravikovitch, A.V. Neimark, M. Bülow and Q.M. Wang. 2003. Nanopore Structure and Sorption Properties of Cu–Btc Metal–Organic Framework. **Nano Lett.** 3(6): 713-718.

- Wan, Y., Y. Shi and D. Zhao. 2007. Designed Synthesis of Mesoporous Solids Via Nonionic-Surfactant-Templating Approach. **Chem. Commun.** 9): 897-926.
- Wang, F., H. Guo, Y. Chai, Y. Li and C. Liu. 2013. The Controlled Regulation of Morphology and Size of Hkust-1 by “Coordination Modulation Method”. **Microporous Mesoporous Mater.** 173(0): 181-188.
- Wang, H., X. Qiao, J. Chen and S. Ding. 2005. Preparation of Silver Nanoparticles by Chemical Reduction Method. **Colloids Surf., A.** 256(2–3): 111-115.
- Wannakao, S., B. Boekfa, P. Khongpracha, M. Probst and J. Limtrakul. 2010. Oxidative Dehydrogenation of Propane over a VO₂-Exchanged Mcm-22 Zeolite: A DFT Study. **ChemPhysChem.** 11(16): 3432-3438.
- Warakulwit, C., T. Nguyen, J. Majimel, M.-H. Delville, V. Lapeyre, P. Garrigue, V. Ravaine, J. Limtrakul and A. Kuhn. 2008. Dissymmetric Carbon Nanotubes by Bipolar Electrochemistry. **Nano Lett.** 8(2): 500-504.
- Wee, L.H., C. Wiktor, S. Turner, W. Vanderlinden, N. Janssens, S.R. Bajpe, K. Houthoofd, G. Van Tendeloo, S. De Feyter, C.E.A. Kirschhock and J.A. Martens. 2012. Copper Benzene Tricarboxylate Metal–Organic Framework with Wide Permanent Mesopores Stabilized by Keggin Polyoxometallate Ions. **J. Am. Chem. Soc.** 134(26): 10911-10919.
- Wheatley, N. and P. Kalck. 1999. Structure and Reactivity of Early–Late Heterobimetallic Complexes. **Chem. Rev.** 99(12): 3379-3420.
- Wiberg, K.B. 1968. Application of the Pople-Santry-Segal CNDO Method to the Cyclopropylcarbanyl and Cyclobutyl Cation and to Bicyclobutane. **Tetrahedron.** 24(3): 1083-1096.

- Wong, C.T. and M.W. Wong. 2004. Facile Uncatalyzed Mukaiyama Aldol Reactions: An Ab Initio Study of the Effects of Substituents. **J. Org. Chem.** 70(1): 124-131.
- Wu, D., Z. Guo, X. Yin, Q. Pang, B. Tu, L. Zhang, Y.-G. Wang and Q. Li. 2014. Metal–Organic Frameworks as Cathode Materials for Li–O₂ Batteries. **Adv. Mater.** 26(20): 3258-3262.
- Wu, Y.-n., F. Li, W. Zhu, J. Cui, C.-a. Tao, C. Lin, P.M. Hannam and G. Li. 2011. Metal–Organic Frameworks with a Three-Dimensional Ordered Macroporous Structure: Dynamic Photonic Materials. **Angew. Chem. Int. Ed.** 50(52): 12518-12522.
- Xian-Wen, W., Z. Guo-Xing, X. Chuan-Jun and Y. Yin. 2006. A Solution Phase Fabrication of Magnetic Nanoparticles Encapsulated in Carbon. **Nanotechnology.** 17(17): 4307.
- Xie, Y., Z. Zhang, T. Jiang, J. He, B. Han, T. Wu and K. Ding. 2007. CO₂ Cycloaddition Reactions Catalyzed by an Ionic Liquid Grafted onto a Highly Cross-Linked Polymer Matrix. **Angew. Chem. Int. Ed.** 46(38): 7255-7258.
- Yamagiwa, N., H. Qin, S. Matsunaga and M. Shibasaki. 2005. Lewis Acid–Lewis Acid Heterobimetallic Cooperative Catalysis: Mechanistic Studies and Application in Enantioselective Aza-Michael Reaction. **J. Am. Chem. Soc.** 127(38): 13419-13427.
- Yamaguchi, K., K. Ebitani, T. Yoshida, H. Yoshida and K. Kaneda. 1999. Mg–Al Mixed Oxides as Highly Active Acid–Base Catalysts for Cycloaddition of Carbon Dioxide to Epoxides. **J. Am. Chem. Soc.** 121(18): 4526-4527.
- Yáñez-Sedeño, P. and J.M. Pingarrón. 2005. Gold Nanoparticle-Based Electrochemical Biosensors. **Anal Bioanal Chem.** 382(4): 884-886.

- Yang, Q. and C. Zhong. 2005. Understanding Hydrogen Adsorption in Metal–Organic Frameworks with Open Metal Sites: A Computational Study. **J. Phys. Chem. B.** 110(2): 655-658.
- Yang, Q., C. Xue, C. Zhong and J.-F. Chen. 2007. Molecular Simulation of Separation of CO₂ from Flue Gases in Cu-Btc Metal-Organic Framework. **AIChE J.** 53(11): 2832-2840.
- Yano, T., H. Matsui, T. Koike, H. Ishiguro, H. Fujihara, M. Yoshihara and T. Maeshima. 1997. Magnesium Oxide-Catalysed Reaction of Carbon Dioxide with an Epoxide with Retention of Stereochemistry. **Chem. Commun.** 12): 1129-1130.
- Yasuda, H., L.-N. He and T. Sakakura. 2002. Cyclic Carbonate Synthesis from Supercritical Carbon Dioxide and Epoxide over Lanthanide Oxychloride. **J. Catal.** 209(2): 547-550.
- Yasuda, H., L.-N. He, T. Sakakura and C. Hu. 2005. Efficient Synthesis of Cyclic Carbonate from Carbon Dioxide Catalyzed by Polyoxometalate: The Remarkable Effects of Metal Substitution. **J. Catal.** 233(1): 119-122.
- Yasuda, H., L.-N. He, T. Takahashi and T. Sakakura. 2006. Non-Halogen Catalysts for Propylene Carbonate Synthesis from CO₂ under Supercritical Conditions. **Appl. Catal. A: Gen.** 298(0): 177-180.
- Yuan, B., Y. Pan, Y. Li, B. Yin and H. Jiang. 2010. A Highly Active Heterogeneous Palladium Catalyst for the Suzuki–Miyaura and Ullmann Coupling Reactions of Aryl Chlorides in Aqueous Media. **Angew. Chem. Int. Ed.** 49(24): 4054-4058.
- Zalomaeva, O.V., A.M. Chibiryayev, K.A. Kovalenko, O.A. Kholdeeva, B.S. Balzhinimaev and V.P. Fedin. 2013. Cyclic Carbonates Synthesis from Epoxides and CO₂ over Metal–Organic Framework Cr-MIL-101. **J. Catal.** 298(0): 179-185.

- Zhang, D.-W., C.-H. Chen, J. Zhang and F. Ren. 2008. Fabrication of Nanosized Metallic Copper by Electrochemical Milling Process. **J Mater Sci.** 43(4): 1492-1496.
- Zhang, Z., S. Huang, S. Xian, H. Xi and Z. Li. 2011. Adsorption Equilibrium and Kinetics of Co₂ on Chromium Terephthalate MIL-101. **Energy & Fuels.** 25(2): 835-842.
- Zhao, Y. and D.G. Truhlar. 2006. A New Local Density Functional for Main-Group Thermochemistry, Transition Metal Bonding, Thermochemical Kinetics, and Noncovalent Interactions. **J. Chem. Phys.** 125(19): 194101-194118.
- Zhao, Y. and D.G. Truhlar. 2008a. Density Functionals with Broad Applicability in Chemistry. **Acc. Chem. Res.** 41(2): 157-167.
- Zhao, Y. and D.G. Truhlar. 2008b. Benchmark Data for Interactions in Zeolite Model Complexes and Their Use for Assessment and Validation of Electronic Structure Methods. **J. Phys. Chem. C.** 112(17): 6860-6868.
- Zhao, Y., J.-S. Tian, X.-H. Qi, Z.-N. Han, Y.-Y. Zhuang and L.-N. He. 2007. Quaternary Ammonium Salt-Functionalized Chitosan: An Easily Recyclable Catalyst for Efficient Synthesis of Cyclic Carbonates from Epoxides and Carbon Dioxide. **J. Mol. Catal. A: Chem.** 271(1-2): 284-289.
- Zhao, Y., M. Padmanabhan, Q. Gong, N. Tsumori, Q. Xu and J. Li. 2011. Co Catalytic Oxidation by a Metal Organic Framework Containing High Density of Reactive Copper Sites. **Chem. Commun.** 47(22): 6377-6379.
- Zhou, X., Y. Zhang, X. Yang, L. Zhao and G. Wang. 2012. Functionalized IRMOF-3 as Efficient Heterogeneous Catalyst for the Synthesis of Cyclic Carbonates. **J. Mol. Catal. A: Chem.** 361-362(0): 12-16.

- Zhu, M., D. Srinivas, S. Bhogeswararao, P. Ratnasamy and M.A. Carreon. 2013. Catalytic Activity of ZIF-8 in the Synthesis of Styrene Carbonate from CO₂ and Styrene Oxide. **Catal. Commun.** 32(0): 36-40.
- Zhu, Y., H. Qian and R. Jin. 2010a. An Atomic-Level Strategy for Unraveling Gold Nanocatalysis from the Perspective of Aun(SR)_m Nanoclusters. **Chemistry – A European Journal**. 16(37): 11455-11462.
- Zhu, Y., H. Qian, M. Zhu and R. Jin. 2010b. Thiolate-Protected Aun Nanoclusters as Catalysts for Selective Oxidation and Hydrogenation Processes. **Adv. Mater.** 22(17): 1915-1920.
- Zybaylo, O., O. Shekhah, H. Wang, M. Tafipolsky, R. Schmid, D. Johannsmann and C. Woll. 2010. A Novel Method to Measure Diffusion Coefficients in Porous Metal-Organic Frameworks. **PCCP**. 12(28): 8093-8098.

APPENDIX

Table S1. Optimized geometrical parameter of cycloaddition reaction between CO₂ and ethylene oxide over the MoMo(O₂CCF₃)₄ via concerted pathway using M06L/6-31G(d,p) method. Bond distances are in Å.

Bonds	Bond Distances (Å)				
	Isolated molecules	Ads	Coads	TS_C	Prod
Mo-Mo	2.13	2.15	2.15	2.16	2.14
Mo1-O ₁	-	2.52	2.56	2.30	3.94
O ₁ -C ₁	1.42	1.43	1.44	2.35	2.32
O ₁ -C ₂	1.42	1.43	1.43	1.33	1.44
C ₁ -C ₂	-	1.46	1.46	1.44	1.52
O ₂ -C ₃	1.17	-	1.17	1.20	1.34
O ₃ -C ₃	1.17	-	1.17	1.16	1.21
O ₁ -C ₃	-	-	2.70	2.38	1.34
O ₂ -C ₁	-	-	3.44	1.98	1.44

Table S2. Optimized geometrical parameter of cycloaddition reaction between CO₂ and ethylene oxide over the RhRh(O₂CCF₃)₄ via concerted pathway using M06L/6-31G(d,p) method. Bond distances are in Å.

Bonds	Bond Distances (Å)				
	Isolated molecules	Ads	Coads	TS_C	Prod
Rh-Rh	2.40	2.43	2.42	2.45	2.42
Rh1-O ₁	-	2.26	2.25	2.16	3.41
O ₁ -C ₁	1.42	1.44	1.44	2.38	2.33
O ₁ -C ₂	1.42	1.44	1.44	1.34	1.43
C ₁ -C ₂	-	1.46	1.45	1.45	1.53
O ₂ -C ₃	1.17	-	1.17	1.20	1.34
O ₃ -C ₃	1.17	-	1.17	1.16	1.22
O ₁ -C ₃	-	-	2.85	2.51	1.34
O ₂ -C ₁	-	-	3.41	1.97	1.44

Table S3. Optimized geometrical parameter of cycloaddition reaction between CO₂ and ethylene oxide over the MoRh(O₂CCF₃)₄ via concerted pathway using M06L/6-31G(d,p) method. Bond distances are in Å.

Bonds	Bond Distances (Å)				
	Isolated molecules	Ads	Coads	TS_C	Prod
Mo-Rh	2.44	2.46	2.46	2.49	2.47
Mo1-O ₁	-	2.31	2.31	2.12	3.45
O ₁ -C ₁	1.42	1.44	1.44	2.34	2.32
O ₁ -C ₂	1.42	1.45	1.45	1.39	1.44
C ₁ -C ₂	-	1.46	1.46	1.47	1.53
O ₂ -C ₃	1.17	-	1.17	1.21	1.33
O ₃ -C ₃	1.17	-	1.17	1.17	1.22
O ₁ -C ₃	-	-	2.75	2.14	1.33
O ₂ -C ₁	-	-	3.54	1.92	1.44

Table S4. Optimized geometrical parameter of cycloaddition reaction between CO₂ and ethylene oxide over the RhMo(O₂CCF₃)₄ via concerted pathway using M06L/6-31G(d,p) method. Bond distances are in Å.

Bonds	Bond Distances (Å)				
	Isolated molecules	Ads	Coads	TS_C	Prod
Rh-Mo	2.44	2.45	2.45	2.47	2.45
Rh1-O ₁	-	2.42	2.41	2.31	3.55
O ₁ -C ₁	1.42	1.43	1.44	2.36	2.32
O ₁ -C ₂	1.42	1.43	1.44	1.33	1.43
C ₁ -C ₂	-	1.46	1.46	1.44	1.52
O ₂ -C ₃	1.17	-	1.17	1.20	1.34
O ₃ -C ₃	1.17	-	1.17	1.16	1.21
O ₁ -C ₃	-	-	2.83	2.34	1.34
O ₂ -C ₁	-	-	3.34	2.01	1.43

Table S5. Optimized geometrical parameter of cycloaddition reaction between CO₂ and ethylene oxide over the MoRh(O₂CCF₃)₄ via stepwise pathway A using M06L/6-31G(d,p) method. Bond distances are in Å.

Bonds	Bond Distances (Å)						
	Isolated molecules	Ads	TS1_S	Int1_S	Int1_S/CO ₂	TS_C	Prod
M1-M2	2.44	2.46	2.48	2.49	2.49	2.49	2.47
M1-O1	-	2.31	2.04	1.92	1.93	2.12	3.45
O1-C1	1.42	1.44	1.97	2.36	2.37	2.34	2.32
O1-C2	1.42	1.45	1.42	1.44	1.44	1.39	1.44
C1-C2	-	1.46	1.46	1.48	1.48	1.47	1.53
O2-C3	1.17	-	-	-	1.17	1.21	1.33
O3-C3	1.17	-	-	-	1.17	1.17	1.22
O1-C3	-	-	-	-	2.72	2.14	1.33
O2-C1	-	-	-	-	3.46	1.92	1.44

Table S6. Spin density of cycloaddition reaction between CO₂ and ethylene oxide over the MoRh(O₂CCF₃)₄ via stepwise pathway A using M06L/6-31G(d,p) method.

Atoms	Spin Density						
	Isolated molecules	Ads	TS1_S	Int1_S	Int1_S/CO ₂	TS_C	Prod
Mo	2.839	2.86	2.438	1.928	1.935	2.660	2.859
Rh	0.087	0.138	0.252	0.117	0.113	0.127	0.132
O1	-	-0.014	-0.072	-0.026	-0.027	-0.008	0.002
C1	-	0.004	0.401	1.037	1.034	0.221	0
C2	-	0.004	-0.019	-0.025	-0.025	-0.002	0.001
C3	-	-	-	-	0.001	0.019	0.012
O2	-	-	-	-	0.001	-0.001	0.003
O3	-	-	-	-	0	0.002	-0.02

Table S7. Spin density of cycloaddition reaction between CO₂ and ethylene oxide over the MoRh(O₂CCF₃)₄ via stepwise pathway B using M06L/6-31G(d,p) method.

Atoms	Spin Density								
	Isolate molecules	Ads	TS1_S	Int1_S	Int1_S/CO ₂	TS2_S	Int2_S	TS3_S	Prod
Mo	2.839	2.86	2.438	1.928	1.935	1.807	1.825	2.235	2.859
Rh	0.087	0.138	0.252	0.117	0.113	0.151	0.145	0.054	0.132
O1		-0.014	-0.072	-0.026	-0.027	0.073	0.04	0.02	0.002
C1		0.004	0.401	1.037	1.034	1.062	1.062	0.782	0
C2		0.004	-0.019	-0.025	-0.025	-0.035	-0.031	-0.041	0.001
C3					0.001	0.002	0.002	0.024	0.012
O2					0.001	0.002	0.009	-0.051	0.003
O3					0	-0.013	-0.004	-0.025	-0.02

CURRICULUM VITAE

NAME : Ms. Sudarat Yadnum

BIRTH DATE : July 28, 1984

BIRTH PLACE : Kamphaeng Phet, Thailand

EDUCATION	:	<table border="0" style="width: 100%;"> <tr> <td style="text-align: center;"><u>YEAR</u></td> <td style="text-align: center;"><u>INSTITUTE</u></td> <td style="text-align: center;"><u>DEGREE/DIPLOMA</u></td> </tr> <tr> <td>2008</td> <td>Kasetsart University</td> <td>M.Sc.(Chemistry), Major Physical Chemistry</td> </tr> <tr> <td>2006</td> <td>Naresuan University</td> <td>B.Sc. (Chemistry)</td> </tr> </table>	<u>YEAR</u>	<u>INSTITUTE</u>	<u>DEGREE/DIPLOMA</u>	2008	Kasetsart University	M.Sc.(Chemistry), Major Physical Chemistry	2006	Naresuan University	B.Sc. (Chemistry)
<u>YEAR</u>	<u>INSTITUTE</u>	<u>DEGREE/DIPLOMA</u>									
2008	Kasetsart University	M.Sc.(Chemistry), Major Physical Chemistry									
2006	Naresuan University	B.Sc. (Chemistry)									

SCHOLARSHIPS

2006 – 2007 : The American Chamber of Commerce in Thailand (AMCHAM)

2008 – 2009 : The Postgraduate Education and Research on Petroleum and Petrochemical Technology (MUA-ADB)

2009 – 2014 : The Royal Golden Jubilee (RGJ) Ph.D. Program, the scholarship for Ph.D student, from the Thailand Research Fund, Thailand

2013 : French Government's scholarship contribution to the RGJ-Ph. D. Program

PUBLICATIONS

1. Warakulwit, C.; Yadnum, S.; Paluka, V.; Phuakkong, O.; Niemlaem, M.; Pongpaisanseree, K.; Chareonpanich, M.; Sinthupinyo, S.; Limtrakul, J., Controlled Production of Carbon Nanofibers over Cement Clinker via Oxidative Dehydrogenation of Acetylene by Intrinsic Carbon Dioxide, *Chemical Engineering Journal*, **2014** (Accepted)
2. Yadnum, S.; Roche, J.; Lebraud, E.; Négrier, P.; Garrigue, P.; Bradshaw, D.; Warakulwit, C.; Limtrakul, J.; Kuhn, A., Site-Selective Synthesis of Janus-type Metal-Organic Framework Composites, *Angewandte Chemie International Edition*, **2014**, 53, 1–6.
3. Wattanakit, C.; Côme, Y. B. S.; Lapeyre, V.; Bopp, P.A.; Heim, M.; Yadnum, S.; Nokbin, S.; Warakulwit, C.; Limtrakul, J.; Kuhn, A., Enantioselective recognition at mesoporous chiral metal surfaces, *Nature Communications*, **2014**, | 5:3325 | DOI: 10.1038/ncomms4325.
4. Yadnum, S.; Choomwattana, S.; Khongpracha, P.; Sirijaraensre, J.; and Limtrakul, J., Comparison of Cu-ZSM-5 Zeolites and Cu-MOF-505 Metal-Organic Frameworks as Heterogeneous Catalysts for the Mukaiyama Aldol Reaction: A DFT Mechanistic Study, *ChemPhysChem* **2013**, 14, 923 – 928.

CONFERENCE PROCEEDING

1. Yadnum, S.; Choomwattana, S.; Kongpracha, P.; Limtrakul, J., Mechanism of MOF-505 and Cu-ZSM-5 Promoted Mukaiyama Aldol Reaction: An ONIOM study. *NSTI-Nanotech* **2009**, 3, 308–311.
2. Yadnum, S.; Kongpracha, P.; Warakulwit, C.; Limtrakul, J., Precisely Size-controlled Metal Nanoparticles (Au, Pd and Pt) Inserted into Metal-Organic Frameworks (MOFs): Synthesis and Catalytic Properties, *Preprints- American Chemical Society Division of Petroleum Chemistry*, 56, 2; 197-200.

CONFERENCE PARTICIPATIONS

1. Warakulwit, C., Yadnum, S., Paluka, V., Phuakkong, O., Niemlaem, M., Pongpaisanseree, K., Chareonpanich, M., Sinthupinyo, S., Limtrakul, J. , Controlled Production of Carbon Nanofibers over Cement Clinker via Oxidative Dehydrogenation of Acetylene by Intrinsic Carbon Dioxide, 23rd International Symposium on Chemical Reaction Engineering (ISCRE 23) and Asia Pacific Chemical Reaction Engineering Symposium (APCRE) for its 7th symposium, Centara Grand & Bangkok Convention Centre, Bangkok, Thailand, September 7-10, 2014 (Poster presentation)
2. Yadnum, S., Impeng, S., Maihom, T., Boekfa, B., Limtrakul, J., Cycloaddition reaction of carbon dioxide and ethylene oxides over heterometallic paddlewheel carboxylates: A mechanistic study, 247th ACS National Meeting and Exposition, Dallas, Texas, March 16-20, 2014 (Poster presentation)
3. Yadnum, S., Warakulwit, C., Khongpracha, P., Limtrakul, J., Precisely Size-controlled Metal Nanoparticles (Au, Pd and Pt) Inserted into Metal-Organic Frameworks (MOFs), 1st Chemistry Postgraduate Symposium (ChPGS), Department of Chemistry, Kasetsart University, Thailand August 8, 2012 (Poster presentation)
4. Yadnum, S., Khongpracha, P., Warakulwit, C., Limtrakul, J., Precisely Size-controlled Metal Nanoparticles (Au, Pd and Pt) Inserted into Metal-Organic Frameworks (MOFs), RGJ – Ph.D. Congress XIII (The Thailand Research Fund), Jomtien Palm Beach Resort, Chonburi, Thailand, April 6-8, 2012 (Poster presentation)
5. Yadnum, S., Choomwatana, S., Khongpracha, P., Warakulwit, C., Limtrakul, J., Precisely Size-Controlled Metal Nanoparticles (Au, Pd and Pt) Inserted into Metal-Organic Frameworks (MOFs): Synthesis and Catalytic Properties, 242nd ACS National Meeting and Exposition, Denver, Colorado, USA, August 28-September 1, 2011 (Oral presentation)

6. Yadnum, S., Choomwatana, S., Khongpracha, P., Warakulwit, C., Limtrakul, J., Synthesis of Metal-Organic Frameworks (MOFs) Supported by Metal Nanoparticles (Au, Pd and Pt) as Highly Active Catalyst for Oxidation of Alcohols, The 2nd Research Symposium on Petroleum, Petrochemicals, and Advanced Materials and the 17th PPC Symposium on Petroleum, Petrochemicals, and Polymer, Bangkok, Thailand, April, 26, 2011 (Poster presentation)
7. Yadnum, S., Choomwatana, S., Khongpracha, P., Warakulwit, C., Limtrakul, J., DFT Analysis of the Catalyzed Ring-Opening Reaction of Epoxide: An Important Process in Alkoxy Alcohol Synthesis, Nanothailand 2010: Nanotechnology for a Sustainable World, Bangkok, Thailand, November, 18-20, 2010 (Poster presentation)
8. Yadnum, S., Choomwatana, S., Khongpracha, P., Limtrakul, J., Density Functional Study of Epoxide Ring-Opening Reaction with Methanol Promoted by Dicopper Carboxylate in Metal-Organic Framework, The 239th ACS National Meeting and Exposition, San Francisco, California, USA, March, 21-25, 2010 (Poster presentation)
9. Yadnum, S., Choomwatana, S., Khongpracha, P., Limtrakul, J., Structures and Mechanism of Metal-Organic Frameworks and Cu-ZSM-5 Promoted Mukaiyama Aldol Reaction: An ONIOM study, Sokendai Asian Winter School, Molecular Science-Central Role in Multidisciplinary Fields, Okazaki, Japan, December 1-4, 2009 (Poster presentation)
10. Yadnum, S., Choomwatana, S., Khongpracha, P., Limtrakul, J., Mechanism of MOF-505 and Cu-ZSM-5 Promoted Mukaiyama Aldol Reaction: An ONIOM study, The 2009 NSTI Nanotechnology Conference and Trade Show, Houston, United States of America, May 1-8, 2009 (Poster presentation)
11. Yadnum, S., Choomwatana, S., Khongpracha, P., Limtrakul, J., Structures and Mechanism of the Mukaiyama Aldol Reactions between Metal Organic Frameworks-505 Encapsulated Formaldehyde and Silyl Enol Ether: An ONIOM study, Pure and Applied Chemistry International Conference (PACCON), Pitsanulok, Thailand, January 14-16, 2009 (Poster presentation)